

# Hierarchical Zeolites for Improved Separation Performance: Synthesis, Characterization, Growth Mechanism and Applications

By

**Fatin A Hasan**

A dissertation submitted for the degree of Doctor of Philosophy

**Department of Chemical Engineering**

**Monash University**

**Supervisor**

**Prof. Paul A Webley**

**August 2012**

# **Declaration**

This thesis contains no material which has been accepted for the award of any other degree or diploma in any university or institution. I affirm that, to the best of my knowledge and belief, the thesis contains no material previously published or written by another person, except where due references is made in the text of the thesis.

*Fatin Hasan*

*Department of Chemical engineering*

*Monash University*

*August, 2012*

## **Notice 1**

Under the Copyright Act 1968, this thesis must be used only under the normal conditions of scholarly fair dealing. In particular no results or conclusions should be extracted from it, nor should it be copied or closely paraphrased in whole or in part without the written consent of the author. Proper written acknowledgement should be made for any assistance obtained from this thesis.

## **Notice 2**

I certify that I have made all reasonable efforts to secure copyright permissions for third-party content included in this thesis and have not knowingly added copyright content to my work without the owner's permission.

## **Acknowledgments**

First of all, I would like to express my deep gratitude to my supervisor Prof. Paul Webley for his valuable advice, kind guidance and extensive experience. Since the early stages of my study, Paul has been motivating, encouraging and unlimitedly supportive. The gentle gaudiness and excellent working atmosphere he provides are the keys to the extraordinary achievements of his group. Also I will always be indebted to him for giving me this opportunity of working on this project and for supporting me to be awarded the Department of Chemical Engineering scholarship.

Many thanks go in particular to Dr. Ranjeet Singh who is always willing to help and provide advice. Her extensive knowledge, valuable assistance, constant encouragement, and most importantly her friendship were crucial for me to proceed smoothly in achieving this task.

I would also like to acknowledge the support of Dr. Penny Xiao. Her constant encouragement, help and extensive discussions helped me significantly to conduct the processing and simulation part of my research.

I gratefully acknowledge all the former and current Paul Webley's group members, especially Dr. Liying Liu (Vicky), Dr. Gongkui Xiao (James), Dr. Gang Li (Kevin), Jin Shang (Eric), Huamei Duan, Dr. Dong Xu (Edward), Dr. Xinyi Zhang, Dr. Zhangxiong Wu (William) and Dr. Na Hao. Their constant support and willingness to share their ideas have provided me with a good and smooth basis to my PhD.

I am especially obliged to Ms Lilyanne Price for her willingness to help unconditionally and for her friendly and caring personality. Many thanks go to the staff in the Department of Chemical Engineering, Jill Crisfield, Gary Thunder and Chloe Priebee for their kind assistance in administration matters during my study period. I would also like to acknowledge the support of Ron Graham, Kim Phu and Gamini Ganegoda for their constant help in technical issues.

Finally, I wholeheartedly thank my family starting from my loving, supportive, encouraging, and patient husband Firas. I am extraordinary fortunate for having him in my life. Special appreciation and love go to my daughters Mina and Basma and my son Jaber for their

unconditional support, love and patience. I am also sincerely grateful to my sister Rayya and my brother in law Riadh for supporting me and my family since our first day in Melbourne and also for encouraging me to pursue this degree. Lastly I would like thank my beloved mother for her unconditional love and prayers.

Thank you all,

*Fatin Hasan*

*August 2012*

# ***Table of Contents***

<b>Declaration .....</b>	<b>I</b>
<b>Acknowledgments.....</b>	<b>II</b>
<b>Table of Contents.....</b>	<b>IV</b>
<b>Abstract .....</b>	<b>IX</b>
<b>List of Figures .....</b>	<b>XII</b>
<b>List of Tables.....</b>	<b>XVII</b>
<b>List of Schemes .....</b>	<b>XVIII</b>
<b>Abbreviations.....</b>	<b>XX</b>
<b>Chapter 1: Introduction.....</b>	<b>1</b>
<b>Chapter 2: Literature Review .....</b>	<b>5</b>
2.1 Overview.....	5
2.2 Introduction to zeolites .....	5
2.2.1 Zeolite structure and chemical composition .....	5
2.2.2 Zeolite characteristics.....	8
2.3 Zeolite applications.....	9
2.4 Problems associated to zeolite applications.....	11
2.5 Strategies used to decrease the diffusion limitation and pressure drop .....	12
2.5.1 Decrease the size of zeolite crystals to nano-scale.....	12
2.5.2 Fabricating hierarchical porous zeolites structures .....	13
2.5.2.1 Hierarchical zeolite single crystals .....	14

2.5.2.2 Nano-zeolite crystals/substrate hierarchical structures.....	14
2.5.2.3 Self standing hierarchical zeolite structures .....	15
2.6 Techniques used to synthesize hierarchical zeolites.....	15
2.6.1 Solid-template synthesis.....	15
2.6.2 Supramolecular-template synthesis (Soft Template) .....	23
2.6.3 Dual-template synthesis .....	25
2.6.4 Vapor Phase Transport (VPT).....	27
2.6.5 Emulsion droplets-template synthesis.....	28
2.6.6 Non-templating technique .....	31
2.7 Fabrication of hierarchical microscopic zeolite structures for better adsorption characteristics.....	33
2.7.1 Synthesis of micro-mesoporous zeolite via supramolecular templating technique .....	34
2.7.1.1 <i>Direst crystallization of zeolite in presence of surfactant micelles</i> .....	34
2.7.1.2 Surfactant-mediated assembly of zeolite seeds into mesoporous structures ...	35
2.7.2 Factors influence the formation of hierarchical zeolites in presence of surfactant micelles.....	36
2.7.2.1 The influence of temperature on the surfactant behavior:.....	36
2.7.2.2 The infleuence of the size of surfacatnt micelles .....	38
2.8 Self standing hierarchical zeolite structures as adsorbents .....	40
2.8.1 Zeolite/substrate monoliths .....	41
2.8.2 Binder free self standing monoliths .....	43
2.8.3 Zeolite/binder self standing monoliths.....	44
2.9 Scope of the present work.....	45
<b>Chapter 3: Characterization and testing techniques .....</b>	<b>47</b>
3.1 Powder X-Ray Diffraction (PXRD).....	47

3.2 Scanning Electron Microscopy (SEM) .....	47
3.3 Transmission Electron Microscopy (TEM) .....	47
3.4 Dynamic Light Scattering (DLS).....	48
3.5 Fourier Transform Infrared (FTIR).....	48
3.6 Solid State Nuclear Magnetic Resonance (NMR) .....	48
3.7 Thermogravimetric Analysis (TGA) .....	48
3.8 Cryogenic Temperature Transmission Electron Microscopy (Cryo-TEM).....	49
3.9 Nitrogen Adsorption-Desorption Analysis .....	49
3.10 Mercury Intrusion Porosimetry (MIP).....	50
3.11 Gas adsorption characteristics at low pressure .....	50
3.12 Gas adsorption capacity at high pressure.....	50
3.13 Breakthrough measurements.....	50
3.14 Pressure drop.....	51
<b>Chapter 4: Direct Synthesis of Hierarchical LTA Zeolite via a Low Crystallization and Growth Rate Technique in the Presence of Cetyltrimethylammonium Bromide (CTAB).....</b>	<b>53</b>
4.1 Introduction.....	53
4.2 Experimental work.....	55
4.2.1 Materials.....	55
4.2.2 Synthesis .....	55
4.3 Results and discussion .....	58
4.3.1 Influence of direct addition of CTAB or CTAB with different concentrations of swelling agent to Na-A zeolite gel .....	58
4.3.2 Influence of chain length of the swelling agent on the mesopore size distribution .....	69
4.3.3 Influence of aging period on the mesopore size distribution .....	71

4.3.4 Influence of CTAB concentration on the mesopore size distribution .....	73
4.3.5 Influence of the addition of two organic expanders to the zeolite / CTAB gel.....	75
4.3.6 The effect of calcination conditions on the pore size distribution .....	79
4.3.7 Colloidal stability of synthesized mesoporous Na-A zeolite aqueous suspensions .....	82
4.3.8 Ethylene adsorption-desorption measurements.....	83
4.3.9 The hydrothermal stability of the synthesized micro-mesoporous NaA zeolite .....	84
4.4 Conclusion .....	91

**Chapter 5: Formation of LTA Zeolite Crystals with Multi-hollow Polycrystalline Core-shell Structure via Aggregation- recrystallization Route in the presence of Emulsion Droplets .....**

5.1 Introduction.....	93
5.2 Experimental work.....	95
5.2.1 Materials.....	95
5.2.2 Synthesis .....	95
5.2.1 Ca <sup>+2</sup> ion-exchange .....	97
5.3 Results and discussion .....	97
5.3.1. First stage crystal growth: Formation of multi-hollow polycrystalline aggregates ..	104
5.3.2. Second stage of crystallization: Formation of multi-hollow polycrystalline core-shell particles .....	110
5.3.3 Third stage of crystallization: Aging for longer than 14 days.....	116
5.3.4 Growth mechanism .....	121
5.4 Conclusion .....	123

**Chapter 6: Zeolite monoliths with channel structure mimicking a tree's vascular system: High effective diffusivity, low pressure drop and high adsorption capacity .....**

6.1 Introduction.....	125
-----------------------	-----

6.2 Experimental section.....	126
6.2.1 Synthesis .....	126
6.2.1.1 <i>Synthesis of micro-mesoporous 4A zeolite</i> .....	126
6.2.1.2 $\text{Ca}^{+2}$ ion-exchange .....	127
6.2.1.3 Preparation of hierarchical ZACa monoliths.....	127
6.2.2 Processing work .....	130
6.2.2.1 Adsorption isotherms.....	130
6.2.2.2 Pressure drop .....	131
6.2.2.3 $\text{CO}_2$ breakthrough measurements .....	132
6.3 Results and discussion .....	134
6.3.1 Micro-mesoporous primary building units.....	134
6.3.2 Physical Characterization of monoliths .....	136
6.3.3 Adsorption isotherms .....	144
6.3.4 Processing work .....	146
6.3.4.1 Breakthrough profiles .....	146
6.3.4.2 Pressure drop .....	151
6.4 Conclusion .....	153
<b>Chapter 7: Conclusion and recommendations for future work.....</b>	<b>155</b>
7.1 Conclusion .....	155
7.2 Recommendations for future work .....	157
<b>References.....</b>	<b>159</b>
<b>Appendix-Relevant Publications.....</b>	<b>177</b>

## **Abstract**

Zeolites are highly crystalline materials with well-defined micropores that have the ability to strongly adsorb certain molecules and completely exclude others. Zeolites are widely used as adsorbents in gas separation by adsorption processes. Gas separation by zeolites might occur *via* three different routes; namely, equilibrium separation, molecular sieving and kinetic selectivity. However, the small size of zeolite pores (0.2 – 1.3 nm), hinders the large molecules from accessing the zeolite structure cavities and even the small molecules may exhibit very limited diffusion speeds within these pores. Accordingly, there has been considerable interest in synthesizing zeolite with larger pores for better adsorption characteristics.

In this thesis, a new strategy described as slow crystallization and growth rate at room temperature in the presence of surfactant micelles was used to synthesize hierarchical Na-A zeolites. The surfactant used in this work is cetyltrimethylammonium bromide – CTAB which is cheap and commercially available. The sluggish formation and growth of the zeolite crystals in this system due to the moderate synthesis conditions was responsible for retaining the surfactant micelles within the crystallization domain. After the removal of CTAB template, the products showed large mesopores which were attributed to the interstitial voids between the aggregated zeolite nanocrystallites. The size of the mesopores can be further expanded by using linear hydrocarbon (*n*-dodecane) as a swelling agent. Increasing the amount of *n*-dodecane in the synthesis mixture resulted in increasing the size of the mesopores. Conversely, the size of the mesopores decreased when a swelling agent with shorter hydrocarbon chain than *n*-dodecane, such as *n*-hexane was used. The effects of the aging period and the concentration of CTAB in the synthesis mixture on the pore size distribution were also investigated. Additionally, the effect of combining two swelling agents in one system on the textural properties of the synthesized mesoporous Na-A zeolite was also examined. Different calcination conditions and the hydrothermal stability of the resultant material were also studied. The colloidal suspension of the synthesized zeolite showed negative zeta potential in the entire range of pH. The mesoporous Na-A zeolite synthesized in this work showed higher ethylene adsorption capacity as compared to the conventional microporous Na-A zeolite.

For fundamental understanding of the formation of the resultant micro-mesoporous Na-A zeolite, a detailed study of the formation and growth of the zeolite particles was necessary. In

this study, the concentration of *n*-dodecane was raised in the system until high internal phase emulsion (HIPE) was formed. The characterization showed that Na-A zeolite crystals consisting of thin crystalline polyhedral shell and multi-hollow polycrystalline core were formed following a reverse crystallization mechanism. A systematic investigation of the crystal growth over different crystallization stages indicates that these extraordinary crystals were formed *via* two step crystallization. Initially, *n*-dodecane droplets stabilized with a thin layer of cetyltrimethylammonium bromide enhance the formation of aggregates of amorphous nanoparticle which later transform into polycrystalline aggregates by local crystallization of each nanoparticle into a crystallite. Crystallized islands are built on the surface of the polycrystalline aggregates which are then extended and merged resulting in typical cubic morphology of LTA zeolite. Surface recrystallization continues towards the core *via* Oswald ripening process increasing the thickness of the shell. During the entire growth process, the *n*-dodecane droplets are retained inside the polycrystalline aggregates, probably due to slow crystallization rate at room temperature. The removal of the *n*-dodecane droplets and cetyltrimethylammonium bromide molecules results in Na-A zeolite particles with core-shell structure. The shell is highly crystalline Na-A zeolite and the core comprises of multi-hollow polycrystalline aggregates. The product shows mesoporosity with large size distribution attributed to polycrystalline aggregates that are free of the crystallized shell. This part of our work demonstrates two points; the synthesis of new kind of mesoporous Na-A with multi-hollow polycrystalline morphology and also demonstrates, for the first time, formation of LTA zeolite crystal *via* reverse crystallization route while retaining the identity of LTA zeolite.

The resultant micro-mesoporous zeolite particles were ion exchanged to 5A zeolite and used as primary building units for construction of walls of 5A monolithic structures with novel channeling design that mimics a tree's vascular system. The performance of these monoliths on CO<sub>2</sub> separation was examined and compared to conventional 5A beads. Three different sizes of channels were introduced into the monoliths body; large parallel channels (500  $\mu\text{m}$ ) which are interconnected *via* their walls to medium and small scale channels. The medium (85 – 20  $\mu\text{m}$ ) and small (9 – 1  $\mu\text{m}$ ) scale channels are abundantly distributed throughout the walls of the monoliths. The effects of the number of the parallel channels (cell density per square inch), the concentration of medium scale channels and the concentration of the binder in the monoliths were investigated. Monoliths with high cell density (209 cpsi) showed sharper CO<sub>2</sub> breakthrough

front compared to the low cell density monolith (88 cpsi). Additionally, increasing the concentration of the medium scale channels in the walls of the monolith resulted in a significant reduction in the width of CO<sub>2</sub> breakthrough curve suggesting even gas flow distribution and lower mass transfer resistance. The pressure drop per unit length measured across bed loaded with the prepared monoliths was 1.3 times less than 5A beads packed bed. The experimental data were simulated and the results showed that the effective diffusivity of CO<sub>2</sub> molecules in beds of monoliths was six times faster than in 5A packed bed. On the other hand, the concentration of the binder concentration in the monoliths body did not show a noticeable influence on the trend of the breakthrough front or the pressure drop measurement. The high effective diffusivity and low pressure drop in addition to a considerable adsorption capacity in our monoliths indicates that they are competitive alternatives for conventional 5A beads and promising adsorbents for CO<sub>2</sub> separation by adsorption processes.

# List of Figures

Figure 2.1: (a) Representation of silica $[\text{SiO}_4]^{-4}$ and alumina $[\text{AlO}_4]^{-5}$ tetrahedra; (b) tetrahedra linked sharing oxygen atom to create three dimensional structure <sup>27</sup> .....	6
Figure 2.2: LTA frameworkType <sup>31</sup> .....	7
Figure 2.3 Faujasite framework Type <sup>26</sup> .....	8
Figure 2.4 SEM image of macroporous monolith with filament interconnections of zeolite Na-Y/silica composite using dextran <sup>74</sup> .....	19
Figure 2.5 SEM image of zeolite foams with different macroporosity synthesized with polymers contained different compositions <sup>73</sup> .....	20
Figure 2.6 SEM images of a calcined macroporous silicalite monolith prepared from a starch-silicalite gel template <sup>80</sup> .....	21
Figure 2.7 SEM image of calcined micro-patterned silicalite film fabricated by Evaporation Induced Self Assembly (EISA) method <sup>83</sup> .....	32
Figure 2.8 The optical image of the cuttlebone monolith (a), SEM image of washed cuttlebone, top view of the pillars (b) and NaX honeycomb monolith prepared by flow coating, scale bar 400 mm (c). .....	42
Figure 2.9 SEM image of the original silica monolith (a) and (c), and its pseudomorphic transformation in SOD monolith <sup>136</sup> .....	43
Figure 2.10 SEM images of precursor silica gel (a and b), optical picture of silicalite monolith and SEM images of silicalite monolith (d – f) <sup>138</sup> .....	44
Figure 4.1 XRD patterns of Na-A zeolites synthesized with different molar ratios of <i>n</i> -dodecane as micellar swelling agent. ....	58
Figure 4.2 Particle size distribution (PDS) curves obtained from DLS for MZ-0.14C-0 (A), MZ-0.14C-0.14D (B), MZ-0.14C-1.1D (C), MZ-0.14C-2.75D (D) and ZA-st (E). ....	59
Figure 4.3 SEM images of MZ-0.14C-0 (A and inset), MZ-0.14C-0.14D (B), MZ-0.14C-1.1D (C) and MZ-0.14C-2.75D (D). The scale of images A-D and insets is 100 nm.....	61

Figure 4.4 SEM images of ZA-st (A), ZA (B) and CZA (C). The scale of images A is 100 nm, while of image B and C is 1 $\mu$ m.....	62
Figure 4.5 N <sub>2</sub> adsorption-desorption isotherms at 77 K of ZA-st (A), MZ-0.14C-0 (B), MZ- 0.14C-0.14D (C), MZ-0.14C-1.1D (D) and MZ-0.14C-2.75D (E). The inset with each plot is the corresponding BJH mesopore size distribution obtained from the adsorption branch. ....	63
Figure 4.6 High and low magnification images of MZ-0.14C-0 (A-1, A-2), MZ-0.14C-0.14D (B- 1, B-2), MZ-0.14C-1.1D (C-1, C-2) and MZ-0.14C-2.75D (D-1, D-2). The insets on the bottom right corner in images B-1 and D-1 are the corresponding SAED patterns. The white arrows in images A-1, B-1, C-1 and D-1 mark the intracrystalline mesopores. The black arrows A-2, B-2, C-2 and D-2 show the lattice fringes.....	66
Figure 4.7 <sup>29</sup> Si NMR spectra of the samples; ZA-st, MZ-0.14C1.1D and MZ-0.14C-0.....	67
Figure 4.8 FTIR spectra of ZA-st (A), MZ-0.14C-0 (B), MZ-0.14C-0.14D (C), MZ-0.14C-1.1D (D) and MZ-0.14C-2.75D (E). .....	69
Figure 4.9 PXRD patterns (A), N <sub>2</sub> adsorption-desorption isotherms (B), and BJH pore size distribution (C) of the mesoporous Na-A zeolites synthesized with <i>n</i> -hexane (MZ- 0.14C-1.1H) and <i>n</i> -octane (MZ-0.14C-1.1O). .....	70
Figure 4.10 PXRD patterns (A), N <sub>2</sub> adsorption-desorption isotherms (B), and BJH pore size distribution (C) of MZ-0.14C-8.2D-14, MZ-0.14C-8.2D-17 and MZ-0.14C-8.2D-19. .....	72
Figure 4.11 PXRD patterns (A), N <sub>2</sub> adsorption-desorption isotherms (B), and BJH pore size distribution (C) of MZ-0.14C-8.2D, MZ-0.07C-8.2D and MZ-0.21C-8.2D.....	74
Figure 4.12 XRD patterns of samples synthesized in presence of two micellar expanders; <i>n</i> - dodecane and TMB.....	76
Figure 4.13 N2 adsorption-desorption isotherms of MZ-0.14C-1.1D-0.73T (A), MZ-0.14C-1.1D- 1.1T (B), MZ-0.14C-1.1D-2.2T (C) and MZ-0.14C-2.2T (D). The inset of each plot is the corresponding BJH pore size distributions measured from the adsorption branch. .....	77

Figure 4.14 N <sub>2</sub> adsorption-desorption isotherms (A, C and E) and BJH pore size distribution (B, D and F) of samples synthesized at two different calcinations conditions.....	80
Figure 4.15 Zeta potential as a function of pH of MZ-0.14C-0.14D and CZA.....	83
Figure 4.16 Isotherms of ethylene gas adsorption on Mz-0.14C-0.14D and CZA at 0 °C and 850 kPa. ....	84
Figure 4.17 XRD patterns of sample MZ-0.14-0 and sample MZ-0.14C-0-HS. ....	85
Figure 4.18 Low and high magnification SEM images of sample MZ-0.14C-0-HS. The scale of images (A) and (B) is 100 nm. ....	86
Figure 4.19 N <sub>2</sub> adsorption-desorption isotherms (A) and BJH pore size distribution (B) of sample MZ-0.14C-0 and sample MZ-0.14C-0-HS.....	87
Figure 5.1 Wide and small (inset) angle XRD patterns of MZ-14d-cryst. Indicated peaks can be linked to the literature <sup>140</sup> .....	98
Figure 5.2 N <sub>2</sub> adsorption-desorption isotherms at (-196 °C) of MZ-14d-cryst and ZA-st. BJH mesopores size distribution obtained from the adsorption branch of sample MZ-14-cryst (inset). ....	98
Figure 5.3 N <sub>2</sub> adsorption desorption isotherm at -196 °C (A); (B) Pore size distribution obtained from BJH method using the adsorption branch of MZ-14d-cryst-Ca; inset- micropore size distribution calculated by Horvath-Kawazoe .....	100
Figure 5. 4 FTIR spectra of MZ-14d-cryst and ZA-st.....	101
Figure 5. 5 <sup>27</sup> Al MAS NMR (left) and <sup>29</sup> SI MAS NMR (right) for ZA-st and MZ-14d-cryst. ....	101
Figure 5.6 SEM images of a group of particles (A) and focused on a single particle (B) of MZ-14d-cryst. The scale of images is 100 nm. ....	102
Figure 5.7 TEM images of two different particles in the sample MZ-14d-cryst (A and B). The inset in image A shows the SAED pattern for the sample. The inset in image B shows the high magnification TEM image of the edge of the particle in (B) as marked by the rectangle.....	103
Figure 5.8 TEM images for the aliquots taken from CTAB/gel (A) and CTAB/Dod/gel (B). ...	104
Figure 5.9 Cryo-TEM image of a drop taken from the fresh emulsion.....	105

Figure 5.10 Relative weight loss by TGA of as synthesized samples taken from CTAB/gel and CTAB/Dod/gel samples.....	105
Figure 5.11 TEM images for samples taken after 48 h (A), 6 days (B) and 9 days aging (C). Cryo-TEM image for the gel sample taken after 9 days aging (D).....	107
Figure 5.12 SEM images for samples taken after 6d (A), 9 days (B) 12 days (C) and 14 days aging (D).....	108
Figure 5.13 Powder X-ray diffraction patterns of Na-A zeolite samples collected at different aging periods, 5 (A), 7 (B), 9 (C), 12 (D), 14 (E) days and also the pattern of the sample crystallized at elevated temperature after 14 days aging MZ-14d-crys (F). Indicated peaks can be linked to the literature <sup>140</sup> .....	109
Figure 5.14 Low and high magnification images of a particle from MZ-12d (A, B). Corresponding SAED pattern of the same particle (B-inset). TEM image of another group of particles from MZ-12d (C) with corresponding SAED pattern (C-inset)....	111
Figure 5.15 N <sub>2</sub> adsorption-desorption isotherms (A, C and E) and corresponding pore size distribution (B, D and F) of the samples aged for 6, 7, 8, 9, 12 and 14 days and of samples MZ-14d-cryst, MZ-17d-cryst, MZ-19d-cryst and MZ-44d-cryst.....	113
Figure 5.16 FTIR spectra of series of samples taken after different aging periods; 48 h and 6, 9 and 14 days. ....	115
Figure 5.17 XRD pattern of sample MZ-44d-cryst. The peaks marked with star correspond the FAU phase. ....	117
Figure 5.18 SEM images of samples MZ-14d-cryst (A and B), MZ-17d-cryst (C and D) and MZ-19d-cryst (E and F). ....	118
Figure 5.19 SEM images of sample MZ-44d-cryst. ....	120
Figure 6.1 XRD patterns of the ZANa (A), ZACa powder (B), 5A zeolite beads (C) and M8 monolith after being crushed to powder (D). ....	134
Figure 6.2 N <sub>2</sub> adsorption-desorption isotherm for ZANa zeolite at -196 °C (A) and pore size distribution (inset). ....	135
Figure 6.3 SEM images of a group of particles (A) and a single particle (B) of ZANa zeolite..	136

Figure 6.4 Thermogravimetry and differential thermogravimetry curves of pure resin (A) and as synthesized M8 monolith (B).....	137
Figure 6.5 SEM images of a top view of a fragment taken from M8 monolith (A), image of a parallel channel cross sectioned along its length (B), high magnification image of the area marked with a rectangle in image B (C), high magnification image for the area marked with a square in image C (D), high magnification image for the area marked with a circle in image C (E), SEM image of another area on the surface of M8 monolith (F).....	139
Figure 6.6 SEM images of methyl cellulose fiber (A), 5A commercial beads (B) and high magnification image of the surface of 5A beads (C).....	140
Figure 6.7 N <sub>2</sub> adsorption-desorption isotherms (A) and the corresponding pore size distribution (B) of M8 and M9 monoliths and 5A beads.....	142
Figure 6.8 Pore size distribution of M7, M8 and M9 as determined by mercury (Hg) porosimetry. .....	144
Figure 6.9 CO <sub>2</sub> and N <sub>2</sub> isotherms at 0, 30 and 40°C of M8 M9 and 5A beads. The experimental data are labeled by symbols and the simulation data are labeled by solid lines.....	145
Figure 6.10 CO <sub>2</sub> breakthrough curves determined experimentally at 0.18 L·min <sup>-1</sup> of Blank, M6, M7, M8, M9 and 5A beads.....	147
Figure 6.11 The experimental (symbols) and simulation (solid lines) CO <sub>2</sub> breakthrough profiles of samples M8, M9 and 5A beads at 0.18 L · min <sup>-1</sup> . Black arrow on each plot highlights the corresponding time to reach 50 % of final concentration.....	149
Figure 6.12 The experimental results of the pressure drop across beds of monoliths or 5A beads measured at gas flow at two different superficial velocities; 0.71 (A) or 1.24 (B) m · sec <sup>-1</sup> .....	151

## ***List of Tables***

Table 4.1 List of samples and their gel compositions .....	57
Table 4.2 Particle diameter as determined by SEM and DLS for the synthesized mesoporous and reference zeolites.....	60
Table 4.3 Textural properties for the samples synthesized in the work .....	64
Table 4.4 The elemental analyses of samples MZ-0.14C-0.14D and conventional zeolite A (CZA) .....	68
Table 4.5 Experimental details of the samples synthesized to investigate the effects of incorporating two expander agents to zeolite/CTAB gel. ....	75
Table 4.6 Textural properties obtained from N <sub>2</sub> -adsorption-desorption analysis of MZ-0.14C-1.1D-0.73T, MZ-0.14C-1.1D-1.1T, MZ-0.14C-1.1D-2.2T and MZ-0.14C-2.2T .....	78
Table 4.7 Textural and porosity characteristics of samples calcined at two different calcination methods.....	81
Table 5.1 Textural properties of reference Na-A zeolite (ZA-st), samples collected after various aging periods; 9, 12, 14 days and of MZ-14d-cryst-Ca <sup>+2</sup> .....	114
Table 5.2 Particle diameter as determined by SEM for samples aged for 14, 17, 19 and 44 days before being undertaken a high temperature crystallization.....	119
Table 6.1 Characteristics of the monoliths prepared in the experiments.....	130
Table 6.2 Pore structural properties as measured by N <sub>2</sub> adsorption-desorption analysis at (-196 °C).....	143
Table 6.3 Dual-site Langmuir isotherm parameters for CO <sub>2</sub> and N <sub>2</sub> .....	146
Table 6.4 Samples characteristics for breakthrough and pressure drop experiments.....	148
Table 6.5 Summary of CO <sub>2</sub> adsorption properties extracted from breakthrough curves. ....	150
Table 6.6 Summary of pressure drop measurements obtained experimentally ( $\Delta P_{exp}$ ) and theoretically ( $\Delta P_{equ}$ ) at two different superficial velocities of gas flow across monoliths and packed beds.....	152

## List of Schemes

Scheme 2.1 Schematic diagram of synthesizing zeolite nanocrystals by using thermoreversible polymer hydrogel <sup>65</sup> .....	12
Scheme 2.2 Schematic diagram shows the zeolite crystal growth inside the pores and around the carbon matrix (left). TEM image of a single large mesoporous crystal (right) and corresponding diffraction pattern (inset) <sup>5</sup> .....	16
Scheme 2.3 Schematic representation of the process for the preparation of hollow sicalite-1 sphere and bodies with a regular system of macrocavities <sup>75</sup> .....	17
Scheme 2.4 Schematic representation of the growth of ZSM-5 crystals inside the mesopores of carbon aerogel generating bimodal ZSM-5 monolith <sup>9</sup> .....	20
Scheme 2.5 A Schematic representation of normal micelles (oil in water) (a) and inverse micelles (water in oil) (b).....	23
Scheme 2.6 Schematic diagram of mesopore generation in LTA zeolite: (A) as-synthesized zeolite, (B) methanol-washed sample, (C) calcined sample <sup>67</sup> .....	25
Scheme 2.7 Schematic diagram for the synthesis of micro-mesoporous zeolite microspheres by introducing dual templates, poly-methyl methacrylate (PMMA) nano-particles and tetra-propylammonium hydroxide (TPAOH), to zeolite system <sup>58</sup> .....	26
Scheme 2.8 schematic representation of the formation of hollow NaP particles (Route A) and macroporous NaP zeolite monoliths (Route B) <sup>103</sup> .....	28
Scheme 2.9 Schematic representation of the suggested formation process of mesoporous ZSM-5 zeolite with hollow capsular structure <sup>57</sup> .....	31
Scheme 2.10 A schematic representation of the proposed growth mechanism for LTA zeolite at room temperature <sup>125</sup> .....	37
Scheme 2.11 Schematic representation of a micelle of surfactant molecules (a) in absence of alkane molecules as expansion agent, (b) with alkanes with $n = 5 - 8$ , (c) with alkane with $n = 9 - 15$ <sup>127</sup> .....	39

Scheme 3.1 Apparatus used for pressure drop and breakthrough experiments.....	51
Scheme 4.1 (A) Proposed mechanisms for the synthesis of mesoporous Na-A zeolite by using CTAB micelles at room temperature, (B) swelling the CTAB micelles by linear chain alkane molecules to enlarge the mesopores size in the produced Na-A zeolite .....	91
Scheme 5.1 Proposed mechanism for the synthesis of Na-A zeolite crystals with multi-hollow polycrystalline core.....	122
Scheme 6.1 Schematic diagram of the homemade die used to fabricate the monoliths.....	129
Scheme 6.2 Overall picture of one of the synthesized monoliths (A) and schematic diagram of top view of a monolith with 21 parallel channels.....	129

## ***Abbreviations***

<b>CTAB:</b>	Cetyltrimethylammonium bromide
<b>LTA:</b>	Linde Type A
<b>FAU:</b>	Faujasite
<b>SOD:</b>	Sodalite
<b>D4R:</b>	4-membered double ring
<b>D6R:</b>	6-membered double ring
<b>IUPAC:</b>	International Union of Pure and Applied Chemistry organization
<b>FCC:</b>	Fluid Catalytic Cracking
<b>LbL:</b>	Layer-by-Layer
<b>VPT:</b>	Vapor Phase Transport
<b>HIPE:</b>	High Internal Phase Emulsion
<b>O/W:</b>	Oil in Water emulsion
<b>W/O:</b>	Water in Oil emulsion
<b>W/O/W:</b>	Water in Oil in Water emulsion
<b>EISA:</b>	Evaporation Induced Self Assembly
<b>LCT:</b>	Liquid Crystal Tmplate
<b>TPAOH:</b>	Tetrapropylammonium hydroxide
<b>MS:</b>	Mesoporous silica
<b>CA :</b>	Cellulose Acetate
<b>PMMA:</b>	Poly-methyl methacrylate
<b>PEG:</b>	Polyethylene glycol
<b>TEOS:</b>	Triethyl orthosilicate
<b>Al (PrO)<sub>3</sub>:</b>	Aluminium isopropoxide

<b>PDMS:</b>	Polydimethylsilane
<b>TMAOH:</b>	Tetramethylammonium hydroxide
<b>TMB:</b>	1,3,5-trimethylbenzene
<b>CTACl:</b>	Cetyltrimethylammonium chloride
<b>TMS:</b>	Tetramethyl silane
<b>PBS:</b>	Phosphate buffered saline
<b>cpsi:</b>	cell per square inch
<b>BFDH:</b>	Bravais-Friedel-Donnay-Harker law
<b>XRD:</b>	X-Ray Diffraction
<b>SEM:</b>	Scanning Electron Microscopy
<b>EDX:</b>	Energy Dispersive X-ray spectroscopy
<b>TEM:</b>	Transmission Electron Microscopy
<b>Cryo-TEM:</b>	Cryogenic Temperature Transmission Electron Microscopy
<b>SAED:</b>	Selected Electron Diffraction
<b>TGA:</b>	Thermogravimetric Analysis
<b>FTIR:</b>	Fourier Transform Infrared
<b>MIP:</b>	Mercury Intrusion Porosimetry
<b>NMR:</b>	Solid State Nuclear Magnetic Resonance
<b>MAS:</b>	Magic angle spinning probe
<b>DLS:</b>	Dynamic Light Scattering
<b>PSD:</b>	Particle Size Distribution
<b>PDI:</b>	Polydispersity index
<b><math>\xi</math>-potential:</b>	zeta potential
<b>IEP:</b>	Iso-Electric Point
<b>ASAP:</b>	Accelerated Surface Area and Porosimetry system

**BET:** Brunauer-Emmett-Teller

**S<sub>BET</sub>:** Specific surface area

**P/P<sub>0</sub>:** Relative pressure

**BJH:** Barrett-Joyner-Halenda

**HK:** Horvath-Kawazoe method



# **Chapter 1: Introduction**

Zeolites are a class of microporous crystalline aluminosilicates consisting of interconnected tetrahedral units of  $\text{AlO}_4^-$  and  $\text{SiO}_4$  which are coordinated in a three dimensional framework structures<sup>1-3</sup>. The frameworks are very open and contain interconnected channels and cavities which are occupied by cations (to balance the negative framework charge introduced by each  $\text{AlO}_4^-$  unit) and water molecules. More than 130 different frameworks have been reported and characterized in the literature. Because of the high surface area, high void volume (20 to 50 % of the entire solid crystal), uniform size of pores, exchangeable cations, thermal and hydrothermal stability, and strong acidity, zeolites have been widely applied in areas like adsorption, separation, catalysis, purification, ion exchange and sensing<sup>4</sup>. However, the relatively small micropores (0.2 – 1.3 nm) in the zeolite structure strongly restrict the mass transfer of the guest molecules to and from the pores and thus reduce their efficiency.

Research has shown that zeolite diffusion limitation can be overcome either by decreasing the size of zeolite particles to nano-scale or by increasing the size of the pores<sup>5-9</sup>. The former strategy suffers from difficulties in separation and recovery of the nanoparticles. The latter strategy is more flexible and has potential to synthesize zeolite structures with micro and meso pores or with micro and macropores or with micro-meso and macropores. However, some of these techniques are either complicated with multi-steps or require particular synthesis strategies which make them impractical for large scale application<sup>10-12</sup>.

Numerous studies have reported that highly ordered mesoporous silicate materials with controllable pores have been synthesized following supramolecular templating technique<sup>13-15</sup>. In these techniques, surfactant molecules are directly added to the precursors and then the mixture is subjected to hydrothermal treatment at high temperature. The advantage of this technique is that many of the surfactants are cheap and commercially available which is extremely desirable if they are going to be used at industrial scale. Also, the procedure used to synthesize the hierarchical silicate materials was simple and conducted in a one-pot method. Hence, it would be of considerable interest to investigate the possibility of synthesizing micro-mesoporous zeolite in one-pot procedure *via* direct addition of a cheap and commercially available surfactant to the synthesis mixture.

The huge interest in the synthesis of zeolites with hierarchical structures, which has emerged over the past decade, has imposed a necessity to understand the synthesis mechanism. Two basic crystal growth mechanisms have been reported for zeolite systems; the first one is Ostwald ripening in which nuclei are born in the early stage of the gel evolution and then these nuclei grow to the final crystal habit *via* atom by atom addition<sup>16, 17</sup>. In the second growth mechanism, which is called oriented aggregation process, meso, micro or nano-structured building units are formed in the early stage of the crystal growth and then are recrystallized forming single crystalline structures<sup>18, 19</sup>. Hence, an advanced understanding of the formation and growth of zeolite crystals will surely benefit the design and the fabrication of novel hierarchical zeolite structures with controllable pore size distribution.

The literature reported<sup>20-23</sup> that highly ordered hierarchical zeolites have been synthesized following different synthesis techniques; however, the products are powders with particles less than 10 micrometer in size. To overcome the huge pressure drop and mass transfer resistance that might accompany using zeolites in the form of a powder in a packed bed or a reactor, novel zeolite assemblies such as membranes and monoliths are fabricated. In some studies, zeolite particles are synthesized in nano-scale then deposited as a thin film or membrane on a surface of a particular monolithic support. The produced zeolite-support structures were examined in adsorption processes and showed low pressure drop. However, the adsorption capacity per unit weight of the adsorbent was very low. Other studies focused on the fabrication of self standing zeolite monoliths which consisted of pure zeolite or zeolite plus a binder. The reported results indicated that the pressure drop reduced and the equilibrium adsorption improved, but the diffusivity coefficient was very low<sup>24</sup>. This highlights the need to further investigate the possibility of fabricating zeolite monoliths which show low pressure drop, high diffusivity and a comparable adsorption capacity to commercial beads.

The goal of this research is to synthesize hierarchical zeolite structures with three types of pores (macro-meso and micro) for better adsorption characteristics. Micro-mesoporous zeolite particles are synthesized and then can be used as primary building units to fabricate self standing monoliths. In order to obtain efficient hierarchical zeolite monoliths, many parameters such as cell density per square inch, channels distributions and binder concentration were considered. Chapter 2 in this thesis reviews the relevant literature on zeolites, crystal growth mechanisms in zeolite systems and the strategies and techniques used to synthesize hierarchical zeolite

structures. Chapter 3 describes the characterization techniques employed in this study. Chapter 4 describes direct synthesis of micro-mesoporous LTA zeolite following a novel technique which is low temperature crystallization and growth rate in the presence of the commercially available surfactant, cetyltrimethylammonium bromide. Chapter 5 presents a detailed study of the growth mechanism of the synthesized micro-mesoporous LTA zeolite particles. Chapter 6 describes the fabrication of macro-meso-microporous LTA zeolite monoliths with a channeling design that provides even and smooth flow for the guest molecules. Finally the conclusion from the study and suggestions for future work are summarized in chapter 7.



# ***Chapter 2: Literature Review***

## **2.1 Overview**

The first part of this literature review provides a summary of zeolites characteristics and highlights the problems associated with their applications. The strategies that have been suggested by numerous studies to synthesize zeolite structures with better diffusion and less pressure drop are also reviewed. An extensive review of the techniques used to synthesize hierarchical zeolites is included. In particular, the literature relevant to the supramolecular-templating technique and the factors that hinder the formation of hierarchical zeolites *via* direct presence of ordinary surfactant micelles is provided. Furthermore, this chapter summarizes the recent studies in which different categories of hierarchical zeolite monolithic structures were fabricated and their performance as gas adsorbents as compared to commercial beads. The last part of this literature review outlines the technique that is used in the current research to synthesize micro-mesoporous zeolite particles which are then subsequently used as building units for tri-modal porous zeolite monolithic structures. Finally the format of this thesis is presented.

## **2.2 Introduction to zeolites**

### ***2.2.1 Zeolite structure and chemical composition***

Zeolites are crystalline aluminosilicates with well-defined three dimensional framework structures. The primary building units of zeolite crystals consist of  $[\text{SiO}_4]^{-4}$  and  $[\text{AlO}_4]^{-5}$  tetrahedra connected to each other by oxygen atoms (Figure 2.1a)<sup>1, 3, 25</sup>. Adjacent primary building units are linked together by sharing the oxygen atoms located at their corners and thus generate infinite lattices consisting of identical building blocks called unit cells (Figure 2.1b)<sup>1</sup>. The highest possible symmetry of these unit cells forms the framework structure of the zeolite<sup>2</sup>. Accordingly, the framework type describes the aluminosilicate skeleton which is normally open

with three dimensional interconnected channels and cages<sup>1-3</sup>. More than 130 unique framework types of zeolites have been classified and labeled with a three letter code by the International Zeolite Association<sup>26</sup>. Each of these framework types has its own distinct pore size and shape which are strictly uniform. The sizes of these pores range between 0.2 to 1.3 nm.

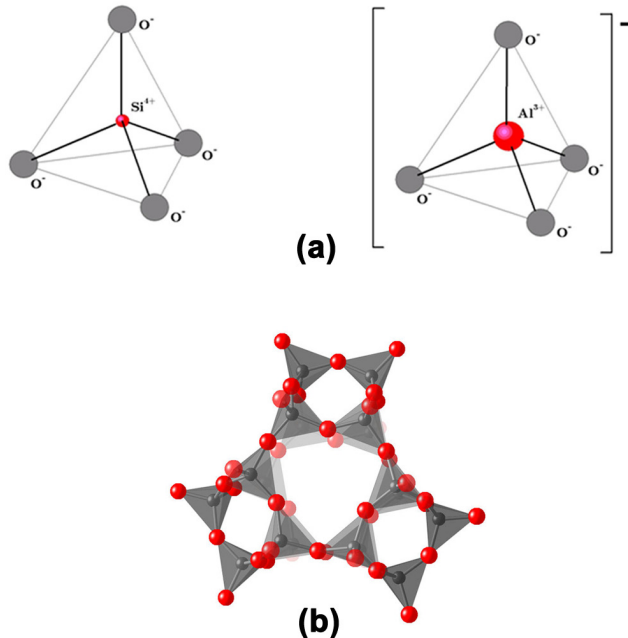
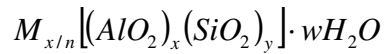


**Figure 2.1: (a) Representation of silica  $[SiO_4]^{4-}$ <sup>4</sup> and alumina  $[AlO_4]^{5-}$ <sup>5</sup> tetrahedra; (b) tetrahedra linked sharing oxygen atom to create three dimensional structure<sup>27</sup>.**

The aluminosilicate framework has a negative charge because the isomorphous substitution of Al<sup>3+</sup> for Si<sup>4-</sup> generates a residual negative charge on the oxygen which is normally neutralized by a small metal cation ( i.e. Na<sup>+1</sup>, K<sup>+1</sup>, Ca<sup>+2</sup>, Mg<sup>+2</sup>) <sup>1</sup>. Hence, a cation resides on every tetrahedron of zeolite framework that has aluminium at its center. The remaining space in the channels and cages of zeolite structure is occupied by water molecules. Thus the structural formula of zeolite can best be described as follows <sup>3, 25</sup>:



Where  $M$  is the cation with valence  $n$ ,  $w$  is the number of water molecules and  $x$  and  $y$  represent the number of alumina and silica tetrahedra in the unit cell; respectively. The ratio of Si: Al in zeolite framework is usually  $\geq 1$ .

Herein we include the basic descriptions of some types of zeolites which are widely used in industrial applications:

Zeolite A: this type of zeolite exhibits Linde Type A (LTA) framework (Figure 2.2). The unit cell in Type A zeolite is cubic with an edge of  $12.3 \text{ \AA}$  and consists of eight cubic arrangements or called double 4-membered ring-D4R (each comprises of eight tetrahedral), and eight  $\beta$ -cages or called sodalite cages (each comprised of 24 tetrahedra) that enclose cavities of diameters  $6.6 \text{ \AA}$ <sup>2, 3, 28, 29</sup>. The center of the unit cell is a large cavity with a diameter of  $11.4 \text{ \AA}$ . The size of the aperture of the large cavity is  $5 \text{ \AA}$  which represents the pore size of the unit cell. The Si: Al ratio in the unit cell is 1:1 because it contains 24 tetrahedra;  $12 \text{ AlO}_4$  and  $12 \text{ SiO}_4$ . The void fraction in this type of zeolite is 0.47<sup>1</sup>. Based on the type of the cation in the framework structure, three types of LTA zeolite are known; 5A, 4A and 3A with  $\text{Ca}^{+2}$ ,  $\text{Na}^{+1}$  and  $\text{K}^{+1}$ , respectively as the charge balancing cations. The numbers 5, 4 and 3 demonstrate the pore size in  $\text{\AA}$ <sup>28, 30</sup>.

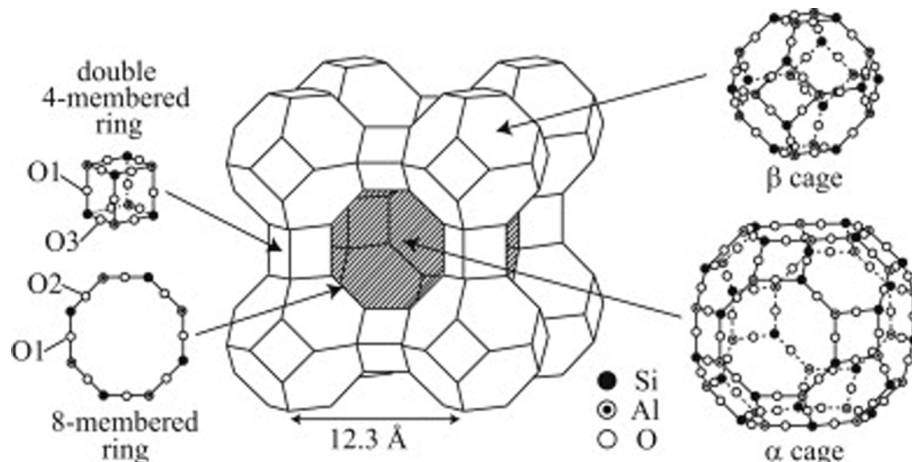
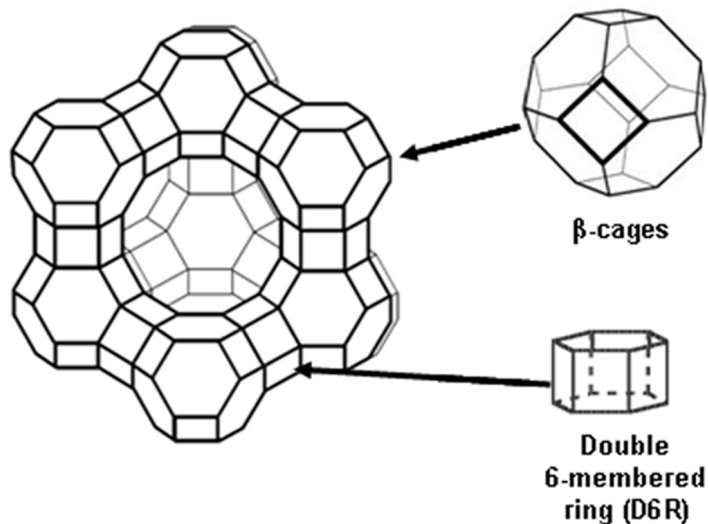


Figure 2.2: LTA framework Type<sup>31</sup>

Zeolite X and Y: These types of zeolites have framework type Faujasite (Figure 2.3) or FAU. This type of framework structure has a cubic unit cell with dimension of  $24.3 \text{ \AA}$  which consists of ten  $\alpha$  cages or Sodalite (diameter  $6.6 \text{ \AA}$ ) connected through hexagonal prisms (or called double 6-ring - D6R)<sup>26</sup>. The cage enclosed in the center of the unit cell has diameter of  $12.5 \text{ \AA}$  which is the largest of any zeolite<sup>3, 26</sup>. This framework structure contains three types of pores

arranged perpendicularly. The diameter of the aperture of the center void, or in other words the pore of the unit cell, is relatively large at 7.4 Å. The fraction of the void space in Faujasite unit cell is 0.53<sup>1</sup>. The Si: Al ratio in zeolite X ranges between 1 to 1.5 and for Y ranges between 1.5 to 3<sup>3, 32</sup>. This type of zeolite can also be prepared with different type of cations; Na<sup>+1</sup>, K<sup>+1</sup>, Ca<sup>+2</sup>... etc and is designated NaX, CaX, etc. or NaY, CaY, etc.



**Figure 2.3 Faujasite framework Type<sup>26</sup>**

### 2.2.2 Zeolite characteristics

Zeolites have unique characteristics arising from their distinctive molecular framework structures which make them suitable for a wide range of technical applications including separation by adsorption<sup>28, 33-35</sup>, heterogeneous catalysis particularly in the field of oil and petrochemistry<sup>36-38</sup>, purification, ion exchange, desiccation and also new emerging applications like chromatographic application for the separation of biomolecules<sup>39</sup>.

Some of these unique characteristic are listed below:

- A wide varieties variety of zeolite framework structures, each with a distinctive regular 1D, 2D, or 3D interconnected channels and pores. Thus, zeolites are capable of shape and size selectivity (molecular sieving)<sup>25</sup>.

- The charge balancing cations that are abundantly distributed in their micropores generate high gradient electrical fields and thus attract particular molecules based on the dipole, quadrupole, or other electronic properties of these molecules<sup>40</sup>.
- The multi-dimensional interconnected channels and cages that are distributed uniformly in the entire volume of zeolite crystals endows them with a very high surface area which can be utilized for adsorption and catalysis applications<sup>3</sup>.
- The cations neutralizing the negative charge of aluminum tetrahedra in the framework of zeolite are mobile and can easily be exchanged with other types of cations without causing defects in the framework structure<sup>41</sup>. The size of the cations and the positions they occupy in the unit cell, i.e. near the apertures of the cell or in the center, determine the effective sizes of the pores. In addition, in some zeolites, the aluminum atom can be removed and replaced by silicon thus decreasing the number of the cations<sup>25, 29</sup>. In other words, different window sizes can be obtained for the same framework type by varying the type and the number of the cations.
- Thermal stability up to over 600 °C<sup>1</sup>.
- The cages and channels in zeolites structures are filled with water molecules which can be removed easily by heating or evacuation leaving the aluminosilicate skeleton with a void fraction between 0.2 to 0.5<sup>25</sup>.
- Strong acidity which allows zeolites to play a crucial role in catalysis applications such as in fluid catalytic cracking (FCC) of heavy petroleum distillates<sup>38</sup>.

## 2.3 Zeolite applications

The unique characteristics of zeolite structures besides the availability of a wide variety of these structures make zeolites suitable for many applications such as:

- Separation by adsorption: zeolites have been used widely in separating a particular component, gas or liquid, from a mixture<sup>42, 43</sup>. Gas separation by adsorption using zeolites may occur *via* one or more of the following three routes:
  - 1) The electrostatic interactions between the dipole/quadrupole moments of the gas molecules and the charge inside the zeolite micropores generated by the charge balancing

cations. Thus the type of the cations in collaboration with the framework structure controls the adsorption process. This type of separation is called “equilibrium separation”<sup>40, 43-46</sup>.

- 2) The second route is named molecular sieving or size and shape selectivity because some gas molecules, with diameter smaller than the size of the zeolite window, are allowed access while the larger molecules are excluded<sup>25</sup>.
- 3) Some gas molecules in the mixture can diffuse through zeolite channels faster than other molecules. This type of adsorption is called “Kinetic selectivity”<sup>40, 43</sup>.

The adsorption capacity and selectivity for a particular gas are determined by the framework type of the unit cell of the used zeolite because some types of zeolites have larger windows as compared to others; i.e. Faujasite zeolite has a window with 7.4 Å diameter; LTA zeolite with 4.1 Å and Chabazite with 3.8 Å. Furthermore, the type and the density of the cations and also the positions they occupy in the voids of the framework structure of a zeolite significantly affect the adsorption capacity and selectivity<sup>47</sup>. For example, zeolite X with Li<sup>+1</sup> cation (LiX) shows the highest selectivity for N<sub>2</sub> compared to O<sub>2</sub>. Also, Zeolite X with Na<sup>+1</sup> is well known as an excellent adsorbent with high adsorption capacity for CO<sub>2</sub><sup>48</sup>. Furthermore, Chabazite with K<sup>+1</sup> cation (K-CHA) shows better O<sub>2</sub>/Ar selectivity as compared to Ca-CHA<sup>49</sup>.

- Catalysis: zeolites are considered as the most important discovery in the history of catalysis because the availability of a wide range of zeolite structures with different micropore designs enables them to be used as shape selective catalysts<sup>50-52</sup>. Normally, during the catalysis process the reaction occurs in the micropores of the zeolite framework structure; thus the shape and the size of the pores control the access of the reactants and the products. Accordingly, zeolite is called as a “shape selective catalyst”<sup>38</sup>.

For example; zeolite X and Y have been used as catalysts on an industrial scale in fluid catalytic cracking (FCC) of heavy petroleum distillates<sup>38</sup>. Additionally, zeolites catalysts have been used in hydrocracking processes of heavy petroleum distillates, isomerization of xylenes to produce *para*-xylene and also in the enhancement of Octane number of light gasoline by isomerization.

- The other unique property of zeolite *viz.* loosing and gaining water molecules readily without destroying the framework structure, makes zeolites an efficient drying agent<sup>3</sup>.

- Due to the ion exchanging ability, zeolites are used for purifying the exhausting gases of internal combustion engine, purifying water, and as additives for detergents, soil improving, and in the animal feed industry.

## 2.4 Problems associated to zeolite applications

The sole presence of the micropores with a relatively small diameter (0.2 – 1.3 nm) in zeolites structures considerably retards the mass transport of the guest molecules, especially with applications associated with large molecules. Nevertheless, even the small molecules with diameter less than the diameter of the micropore must diffuse through these windows and cages to reach to the active adsorption/reaction sites. Therefore, it is often not possible to explore the full potential of zeolite crystals<sup>7-9, 20, 53-58</sup>.

Furthermore, in catalysis applications, if zeolite could transform the reactants into the desirable products at a rate faster than the diffusion of the reactants/products through the small windows of the zeolite pores, then the overall reaction rate will be reduced<sup>7, 59</sup>.

This diffusion issue imposes significant limitations on the range of adsorption/catalysis processes that might be performed efficiently by using these unique products.

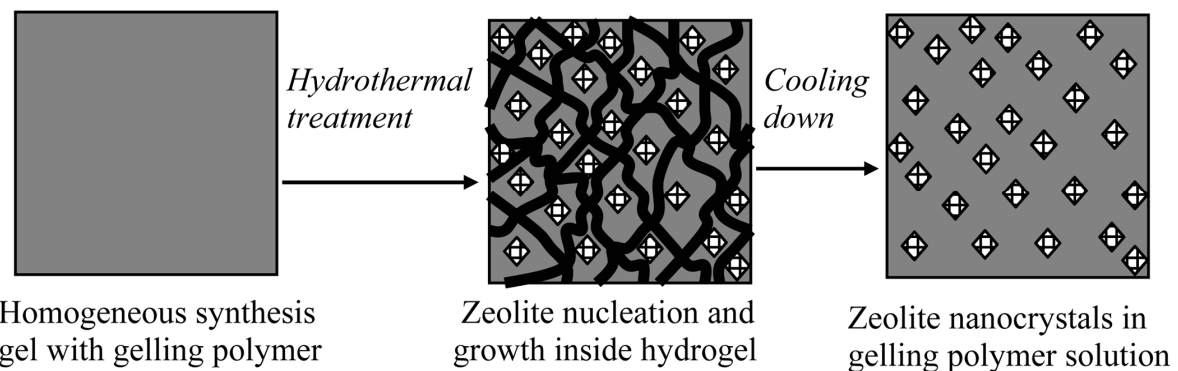
Zeolites are synthesized as fine powders with particle diameters of less than 10 micrometers. It is not practical to use them in this form in a packed bed reactor or adsorber as this will cause a very large pressure drop. Most commonly in industrial applications, zeolite powders are mixed with an inorganic binder; such as clay or silicate, granulated forming paste and then shaped as beads or pellets with a size of several millimeters<sup>40, 60-62</sup>. These beads are then packed randomly in a bed or reactor. Such processes, normally, are accompanied with moderate pressure drop but high mass transfer resistance through the macropores formed in the pelleted materials.. Also, the clay binder in the beads is regarded as an impurity and may cause blockage to the zeolite pores decreasing their effective surface area. Consequently zeolite efficiency will be reduced significantly<sup>20, 21, 63</sup>.

## 2.5 Strategies used to decrease the diffusion limitation and pressure drop

In the past two decades, significant efforts have been devoted to developing solutions to overcome the diffusion limitation and the pressure drop problems associated with zeolite applications. Two main strategies have emerged and have been investigated intensively:

### 2.5.1 Decrease the size of zeolite crystals to nano-scale

Normally, zeolite crystals are of micron size. As described earlier, the small size of the channels and pores in the zeolite framework structure imposes diffusion limitation to the guest molecules. Thus, long diffusion paths that the relatively large crystals offer imposes further limitations to the mass transport rate of guest molecules inhibiting them from reaching the active sites in the center of the crystal. Consequently, the potential efficiency of the zeolite will be reduced. On the other hand, zeolite nanocrystals offer shorter diffusion paths, fewer blocked channels, higher surface area and more exposed active acidic sites<sup>6, 64, 65</sup>.



**Scheme 2.1 Schematic diagram of synthesizing zeolite nanocrystals by using thermoreversible polymer hydrogel<sup>65</sup>**

Several schemes have been used to synthesize zeolite nanocrystals with tailored size distribution. A novel method named “confined space synthesis” is the most attractive approach<sup>6</sup>. In this method, the crystallization of zeolite gel is conducted inside the pores of inert matrices. For example, Jacobsen *et. al.*<sup>6</sup> used mesoporous carbon black matrix to synthesize nanocrystals of zeolites; Beta, X and A. The nanocrystal size was controlled by the pore size distribution of the mesoporous carbon matrix<sup>6</sup>. The zeolite gel was impregnated into the mesopores of the

matrix by sequential incipient wetness. After the crystallization, the zeolite nanoparticles were recovered by controlled combustion of the carbon matrix.

By following the same concept of a space-confined nanoreactor, Yan *et. al.* synthesized Na-A and Na-X zeolite nanocrystals by using thermoreversible polymer hydrogel (Scheme 2.1) <sup>65</sup>. This type of polymer has a reversible response to temperature; at elevated temperature it is gelled forming the three dimensional network of polymer chains and by decreasing the temperature to room temperature it returns to solution. The thermoreversible polymer hydrogel that was introduced into the zeolite system was methylcellulose which was gelled with increasing the temperature offering controlled space for zeolite gel to crystallize. After a sufficient time for zeolite crystallization, the system was cooled to room temperature and hence the methylcellulose returned to solution again. The synthesized zeolite nanocrystals were collected by centrifugation.

However, using zeolite nanocrystals at industrial scale is difficult and impractical because the nanoparticles are colloidal. Thus to separate and recover them from a solution requires centrifugation. Jacobsen *et. al.* reported that they synthesized zeolite nanoparticles inside the mesopores of carbon matrix and they were able to wash and ion exchange the produced nanoparticles while they are embedded inside the matrix. However, this can only be done once; to recycle them the separation and recovery problem arises again.

### ***2.5.2 Fabricating hierarchical porous zeolites structures***

The second strategy that has been considered as a promising solution for the diffusion limitation and pressure drop is synthesizing zeolite with hierarchical porosity. Hierarchically porous structures are a type of material that contains pores at different length scales, e.g., micropores, meso-pores and macropores. According to International Union of Pure and Applied Chemistry (IUPAC) organization, porous materials are classified into three types based on their pore size. Microporous materials have pores with diameter range between 0.2 to 2 nm, mesoporous materials contain pores with size of 2 – 50 nm and finally macroporous materials have pores with diameter >50 nm <sup>66</sup>. Such zeolites are attractive since they retain the adsorption and reaction properties while improving their transportation properties.

Four categories of hierarchical zeolites structures were developed namely:

### **2.5.2.1 Hierarchical zeolite single crystals**

Hierarchical zeolite crystal are the ordinary zeolite crystals but with additional porosity. In other words, each individual zeolite crystal contains another type of pores with larger size beside the micropores which are associated with the framework of crystal structure. Hierarchical zeolite crystals could be micro-mesoporous or micro-macroporous. Hierarchical zeolite crystals would further extend the potential applications of zeolites because they combine the benefits of all types of pores. The micropores provide the shape and size selectivity and the meso or macro pores provide the easy access to the active adsorption/reaction sites.

Numerous studies have been conducted to synthesize zeolite crystals that contain micropores and mesopores in one phase, however only few were successful. Micro-mesoporous single zeolite crystals were obtained by using a certain type of surfactant that contains a methoxysilyl moiety<sup>53, 54, 67</sup> or by post-synthesis treatment such as steaming, dealumination or desalination<sup>68</sup>; or by embedding a mesoporous carbon matrix in the synthesis mixture of zeolite, the nucleation and growth of zeolite crystals occurs inside the mesopores and around matrix<sup>69</sup>.

### **2.5.2.2 Nano-zeolite crystals/substrate hierarchical structures**

Supported nano-crystals is a description of a structure containing nano-sized zeolite crystals deposited as a thin film or membrane on a surface of a particular support. The shape, size and pore size distribution of the final nano-zeolite/support composite depend on the substrate. Bi-modal (micro-meso or micro macro) and tri-modal (micro-meso-macro) hierarchical zeolite structures can be fabricated following this procedure. The microporosity is solely attributed to the zeolite framework structure. The mesoporosity is either due to the intercrystalline voids between the deposited nanocrystals or the substrate itself could be mesoporous. The macropores are normally determined by the nature of the substrate<sup>70, 71</sup>.

The film or the membrane in the composite comprises of either a pure zeolite or zeolite with a binder. The deposition of the nano-zeolite crystals on the surface of a substrate is performed by wash-coating, dip-coating or slip-coating<sup>60, 72</sup>.

The advantage of this approach is combining the benefits of the nanocrystals and the porous substrate together. The nanocrystals provide short diffusion path, high surface area and active

sites. The intercrystalline pores and the pores in the substrate enhance the molecules diffusion rate. However, zeolite-substrate structures have a disadvantage of a possible separation of zeolite film/membrane from the substrate due to the difference between their thermal expansion coefficients<sup>73</sup>. Also, this type of hierarchical zeolite structure suffers from low zeolite loading which in consequence will decrease the total capacity per unit weight.

#### **2.5.2.3 Self standing hierarchical zeolite structures**

The difference between this type of hierarchical zeolite structure and the zeolite/support structures is that they are built on removable substrates; hence the final structure is a replica to the parent substrate. A wide range of substrates with different shapes, sizes and nature were used to generate hierarchical zeolite structures. The self standing hierarchical zeolite structures are either comprised of pure zeolite or zeolite with a binder. The former suffers from low mechanical stability which results from the weak interaction among the zeolite crystals on their walls. On the other hand, the latter show better strength and mechanical stability but the binder normally is considered as an impurity<sup>74-76</sup>.

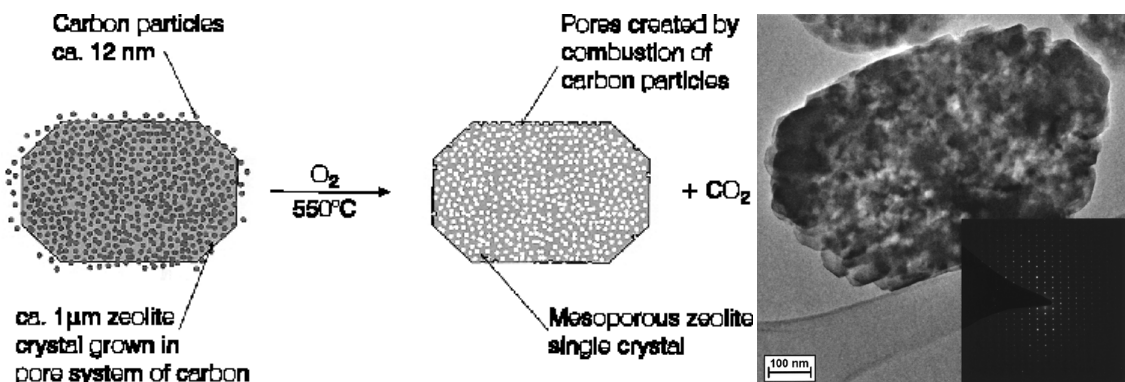
## **2.6 Techniques used to synthesize hierarchical zeolites**

### **2.6.1 Solid-template synthesis**

In this route, a solid template is used as a substrate on which zeolite species are grown or deposited. Initially the substrate is charged oppositely to the negative zeolite species and in consequence the zeolite species are self assembled on the substrate surface driven by the electrostatic forces. Subsequent removal of this substrate generates a zeolite structure which is replica to it. With non-removable substrates, zeolite deposition forms a film/substrate composite. This technique offers considerable potential due to its flexibility in preparing a wide variety of shapes, structures and sizes of porous materials i.e. hollow spheres, core shell composites, membrane, monoliths, foams or any desirable shape or structure.

Large single mesoporous crystals of ZSM-5 zeolite were synthesized by using carbon matrix as a template (Scheme 2.2). The carbon matrix contains pores of a size that provide a sufficient space for the nucleation and growth of zeolite crystals. Excess of zeolite gel with adequate

concentration was used to ensure that zeolite crystallization occurs inside the pores as well as around the matrix. Subsequent removal of the carbon particles produces large particles of mesoporous ZSM-5 zeolite<sup>5</sup>.

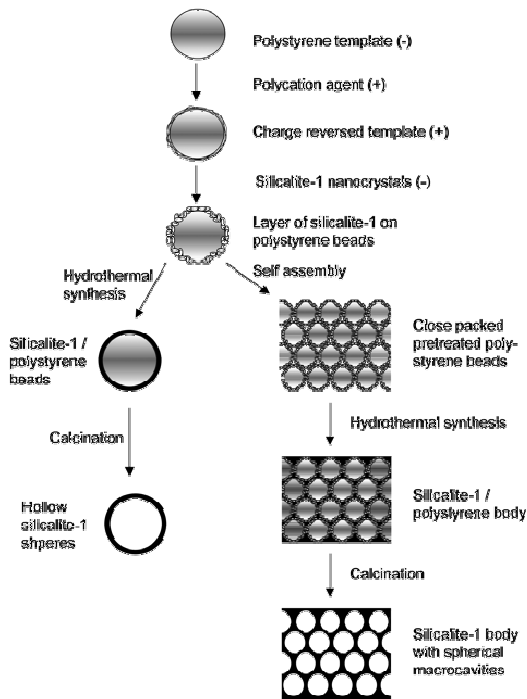


**Scheme 2.2** Schematic diagram shows the zeolite crystal growth inside the pores and around the carbon matrix (left). TEM image of a single large mesoporous crystal (right) and corresponding diffraction pattern (inset)<sup>5</sup>.

Numerous studies have focused on polystyrene beads as substrates<sup>22, 75</sup>. Several types of zeolite (LTA, FAU, BEA and MFI) with hollow sphere morphology have been prepared by using “Layer-by-Layer” (LbL) self assembly technique<sup>20</sup>. The procedure includes charging the micro sized polystyrene beads positively with polycation agent. Then these beads are immersed into a suspension of pre-prepared zeolite nano-seeds. An electrostatic attraction occurs between the beads and the negatively charged zeolite seeds resulting in producing a core shell composite. Subsequent repetition of this process produces the desired shell thickness. Calcination of the composites produces hollow zeolite spheres. However, most of the produced hollow spheres were damaged, probably due to the weak interaction between the shell building units (zeolites nanoseeds) or due to the inhomogeneity of the zeolite layer over the beads.

To improve the mechanical stability and the homogeneity of the shell of the hollow spheres, Valtchev and Mitova, combined the LbL (layer by layer) strategy with hydrothermal synthesis (Scheme 2.3)<sup>75</sup>. They applied this combination in synthesizing silicalite-1 as hollow micro sized spheres and as macroporous structure of arrays of the hollow spheres. After adsorbing one layer of nanosized silicalite-1 crystals, the beads are subjected to hydrothermal synthesis conditions. The characterization shows that the walls of the spheres and the structure are continuous and they comprise well inter-grown particles, which indicate the absence of interconnectivity

between them. Even though the inter-grown particles in the shell indicate higher mechanical stability, the results show some broken spheres, which according to the authors was due to the incomplete formation of the seeding layer. Wang et al suggest that by adjusting the pH, the strength of the ions in the colloidal solution, and the sizes of the beads and the seeds would increase the percentage of the intact hollow particles of zeolite BEA and silicalite-1<sup>22</sup>.



**Scheme 2.3 Schematic representation of the process for the preparation of hollow silicalite-1 sphere and bodies with a regular system of macropores**<sup>75</sup>

Large zeolite spheres ~ 500 µm were prepared by in situ crystallization of zeolite in the matrix of ion exchange resins<sup>4</sup>. The produced spheres have 3-dimensional porous structures of silicalite-1. During the hydrothermal synthesis, the silicalite-1 nanocrystals are grown inside the pores of the resins. Therefore, removing the resins by calcination leaves structures which are identical to the parent resins and consist of primary nanocrystals of silicalite-1 aggregated with each other. However, the XRD characterizations reveal that the produced silicalite-1 microspheres were not completely crystallized and an amorphous phase was present.

Dong *et al.* synthesized a mechanically stable zeolite monolith with three dimensional ordered closed macropores. Initially the charge of the template, mesoporous silica spheres-MS, was modified with polymer, and then the template was seeded electrostatically with zeolite

nanocrystals. The gel was left under ambient conditions allowing the MS to naturally sediment in three dimensional arrays on the bottom of the reactor and finally hydrothermal treatment was applied. Interestingly, the entire silica species in the MS and in the synthesis solution were transformed into zeolite producing monolith with closed macro holes. This monolith showed mechanical stability during sonication<sup>77</sup>. Modification on this procedure by Wang and Caruso resulted in membranes of zeolite with well interconnected macropores. They started with preparing membranes of packed MS by natural sedimentation followed by the seeding step. The interconnected points between the MS packed particles remain unseeded which ultimately became the windows between the macropores after the hydrothermal treatment<sup>78</sup>.

Wang et al has used a cellulose acetate membrane (CA) as a template to produce hierarchical zeolite<sup>79</sup>. The produced zeolite membrane consists of connected tubes with micro scale diameter and these tubes comprise micro-channels inside them. The charge of CA membrane was modified and then seeded with silicalite nanocrystals. A homogeneous layer of silicalite nanocrystals was built on the surface of the membrane. Removal of the CA membrane by calcination generates sicalite-1 membranes which are replicas to the parent template. However, the produced membrane is not stable mechanically due to the considerable shrinkage during calcination. Therefore the authors investigated two strategies to optimize the characteristics of the synthesized membrane. First, by vapor phase transport (VPT), which improved the mechanical stability of the product but the external surface area was decreased and the interconnectivity with the channels inside the microtubes almost disappeared. In the second method, the seeded membrane was subjected to hydrothermal treatment and the produced zeolite membrane showed enhanced mechanical strength, higher external surface area and better interconnectivity with the inner channels.

Walsh et al. produced a macroporous monolith with filament interconnections of zeolite Na-Y/silica composite using dextran (Figure 2.6)<sup>74</sup>. Dissolving the dextran in a suspension of Na-Y and silica crystals produces a paste. Steam and carbon dioxide were blown into the paste to produce foam. Afterwards the removal of the dextran produced a centimeter sized monolith made of Na-Y zeolite and silica composite. The high temperature required for producing this monolith (about 470°C) and the easy rupturing of the structure are the disadvantages of this method.

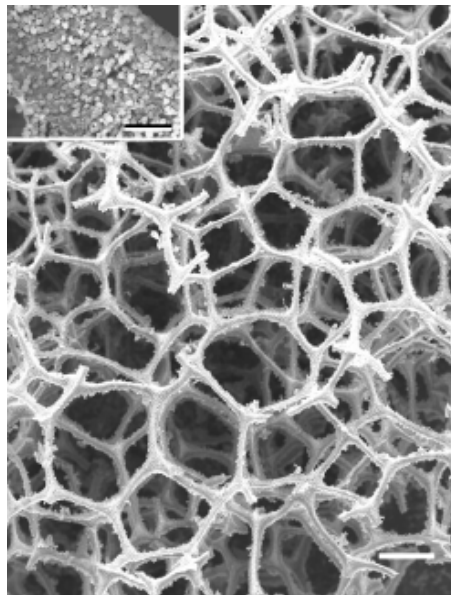


**Figure 2.4 SEM image of macroporous monolith with filament interconnections of zeolite Na-Y/silica composite using dextran<sup>74</sup>.**

Lee et al. and Yoon et al, prepared foams of zeolites with macro/micro pores (Figure 2.7)<sup>21, 76</sup>. The suitable templates for this strategy are polymers that release organic amines in basic medium such as, polyurethane, polyamide, polyimide.etc. They found that the polyurethane foam was transformed completely into zeolite foam when they were treated hydrothermally in zeolite synthesis mixture. When the polyurethane foam was deposited into the zeolite reaction gel, it was hydrolysed generating alcohol and organic amines. These amines attracted the zeolite species electrostatically and acted as structure directing agent for them. The zeolite layer growth and the hydrolysis process occurred simultaneously. If the polymer is entirely decomposed, the zeolite layer thickness would stop increasing unless there is excess of zeolite species in the reaction gel. The generated zeolite foam was tested and found to be mechanically stable.

In another study Lee and Yoon reported that this stability can considerably be affected by the chemical composition of the polymer<sup>73</sup>. For example polyurethane foam containing ester groups produced zeolite foam which was more mechanically stable than the one produced by polyurethane containing ether groups. The reason is that the ester-polyurethane hydrolyses faster than the ether type, which means the zeolite crystallization is also faster. Due to the rapid operation, the size of the zeolite seeds on the template could not increase significantly allowing more zeolite species in the gel to access the remote points where the decomposition process was

occurring. In contrast, with ether-polyurethane the zeolite layer thickness increased from the outer surface; whereas in the inner area, the polymer decomposition continued leaving a hollow structure.

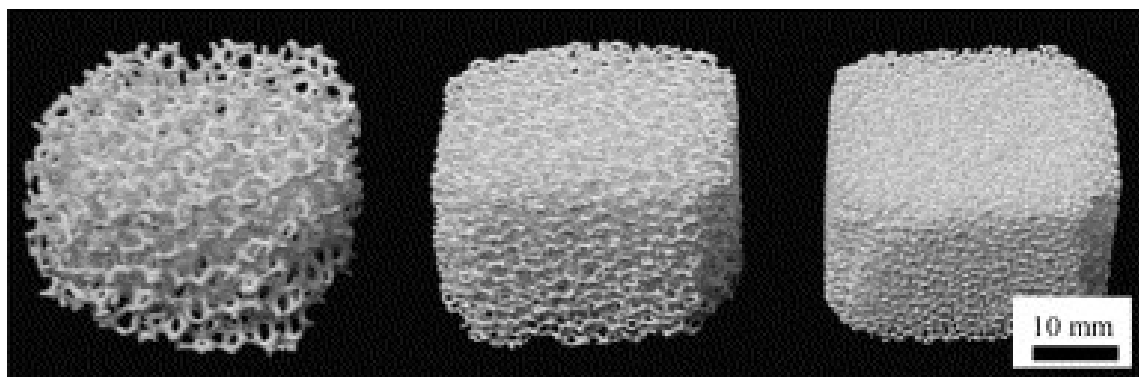
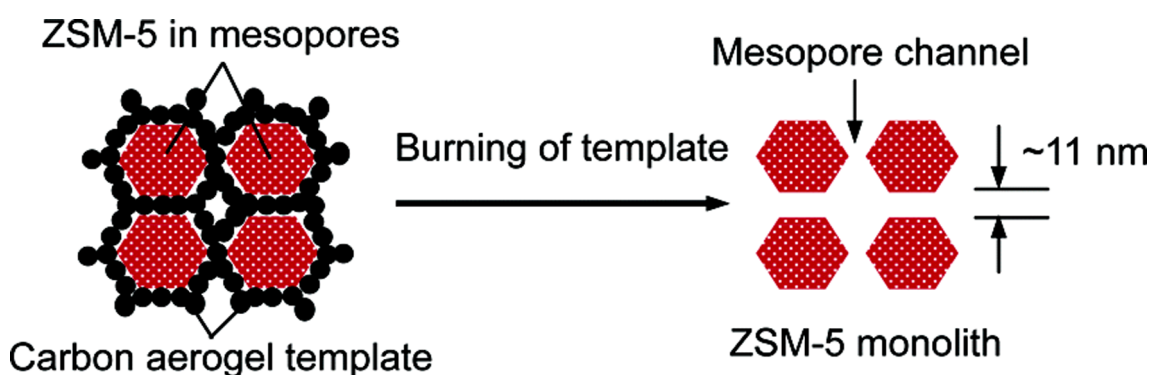


**Figure 2.5 SEM image of zeolite foams with different macroporosity synthesized with polymers contained different compositions<sup>73</sup>.**

Bimodal ZSM-5 monolith with uniform mesopores of average diameter of 11 nm was synthesized by using carbon aerogel with uniform mesopores as a template<sup>9</sup>. The carbon aerogel consists of uniform carbon particles which are interconnected forming relatively large mesopores of 23 nm. The size of these mesopores was sufficient for zeolite crystals to nucleate and grow until they fill the space inside these mesopores. Then the aerogel was removed by calcination leaving micro-mesoporous highly crystalline ZSM-5 monolith (Scheme 2.4).



**Scheme 2.4 Schematic representation of the growth of ZSM-5 crystals inside the mesopores of carbon aerogel generating bimodal ZSM-5 monolith<sup>9</sup>.**

A silicalite monolith with macro-meso-micropores and a silicalite film with meso-micropores were prepared by starch templating<sup>80</sup>. A suspension of pre-prepared silicalite nanocrystals (50 nm) was homogenized with a starch gel and formed as a film. Whereas for the monolith, pre-prepared cationic silicalite nanocrystals (50 nm) were assembled electrostatically on the anionic walls of a starch sponge. Then the starch was removed by combustion and a silicalite monolith/film was obtained. Although starch has advantages of availability, low cost and environmental compatibility, the produced monolith suffered from rupturing due to the shrinkage during calcination (Figure 2.8).

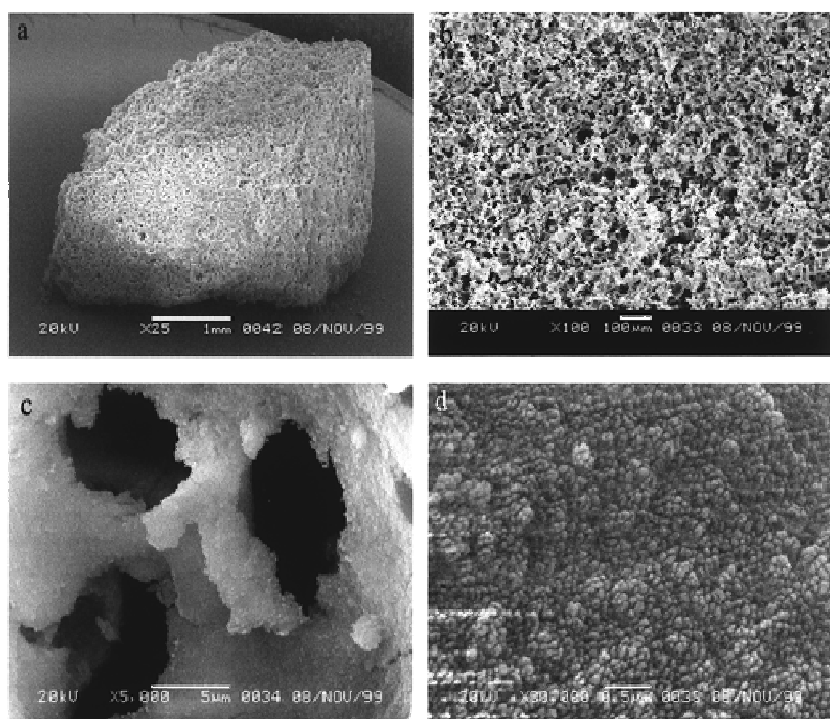


**Figure 2.6 SEM images of a calcined macroporous silicalite monolith prepared from a starch-silicalite gel template<sup>80</sup>.**

In another study, bread templating was used to prepare meso-microporous ZSM-5 zeolite structure<sup>81</sup>. The high porosity of the bread and the hydrophobic starch content contribute to fabricating hierarchical ZSM-5.

Due to the abundance and reproducibility of the natural templates, they have attracted considerable attention. For example, wood tissues were used as a template for tailoring hierarchical silicalite monoliths<sup>23</sup>. The procedure comprised of the same steps of solid templating which were: charge modification, seeding, hydrothermal synthesis and calcination.

The generated zeolite monolith showed three types of pores namely; macropores which were attributed to the structure of the wood tissue, mesopores due to the interstitial voids between the aggregated crystals and finally the micropores were associated to the zeolite nanocrystals.

A desirable size and shape of zeolite structure may be produced by growing zeolite nanocrystals on varying types, shapes and sizes of non-removable supports. Holmes et al. have used a stainless steel mesh as a substrate on which  $1\mu\text{m}$  thin film of silicalite nanocrystals was grown<sup>82</sup>. They started with coating the mesh with layer of silicalite seeds by sonication, followed by introducing the seeded mesh in a silicalite synthesis solution and then subjected to a hydrothermal treatment. The produced film was homogeneous and crack free.

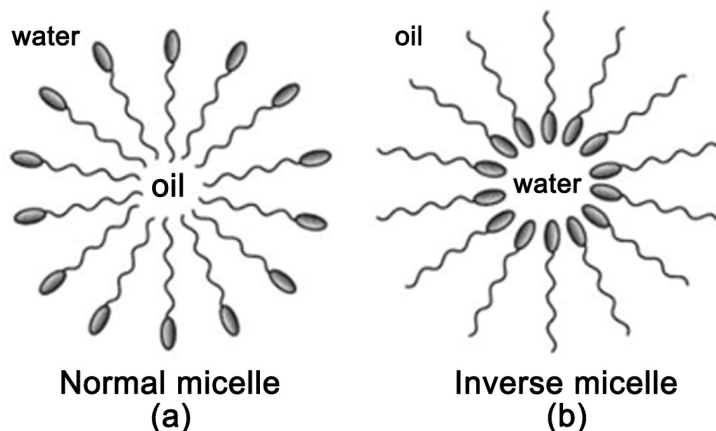
Mintova and Bein have applied the spin coating technique for growing a thin film of ZSM-5 zeolite on different shapes and types of templates; such as square silicon wafer support and round shape gold support<sup>72</sup>. They reported that the thickness and the homogeneity of the grown film are not affected by the type of the support but by the solid concentration in the suspension and the number of spin coating cycles.

This technique offers flexibility in fabricating hierarchical zeolite structures with different shapes, sizes and pores distribution; such as hollow spheres<sup>75, 83</sup>, membrane/support<sup>23, 82</sup>, monoliths and foams<sup>21, 76, 84</sup>. However, the produced structures can possibly collapse due to the significant shrinkage that might occur during the template removal by calcination<sup>80</sup>. The second disadvantage is the incompatibility between the thermal expansion coefficient of the solid template and of zeolite may cause the film to separate from the substrate under heat exposure<sup>76</sup>. Holmes et al. verify that using a low ramp rate in heating may prevent this separation<sup>82</sup>. But it is not guaranteed that the repeated exposure to chemical conditions during practical applications would not affect the film continuity. Further, wastage of bulk zeolite occurs during the seeding step, and finally the final zeolite weight in the film compared with the total weight of zeolite/substrate composite is very low<sup>76</sup>. Also, the synthesis procedure consists of many steps including charge modification of the solid template, seeding, hydrothermal synthesis and calcination<sup>4, 20</sup>. Additionally, the charge modification of the solid template and the seeding steps has to be repeated several times in order to obtain thicker walls and consequently higher stability.

## 2.6.2 Supramolecular-template synthesis (Soft Template)

This technique is based on inclusion of surfactant molecules into the zeolite synthesis mixture. Surfactants have a unique characteristic of self assembly forming micelles within certain concentration ranges<sup>85</sup>. These micelles are dispersed in the reaction solution of the zeolite and act as supramolecular templates around which the zeolite crystals are grown, and hence the removal of these micelles leaves mesoporous zeolites.

Surfactants are large organic compounds which can also be named as amphiphiles because their molecules contain two groups, hydrophilic head (polar) and hydrophobic tail (non-polar) of variable length. Introducing the surfactant molecules into a polar solvent like water, induces these molecules to self assemble forming regular aggregates or micelles<sup>85, 86</sup>. Normal micelles (oil in water) are formed if the surfactant has strong hydrophilic groups and inverse micelles (water in oil) are formed if the hydrophobic groups of the surfactant molecules are strong (Schematic 2.5)<sup>86</sup>.



**Scheme 2.5 A Schematic representation of normal micelles (oil in water) (a) and inverse micelles (water in oil) (b).**

Introducing the surfactants into a synthesis mixture of inorganic materials; like silica molecular sieves, induces condensation and polymerization of an inorganic source of silica around the micelles of surfactant. A supramolecular assembly of charged surfactant ( $S^+$  or  $S^-$ ) with charged inorganic precursors ( $\Gamma$  or  $\Gamma^+$ ) driven by electrostatic forces<sup>87, 88</sup>.

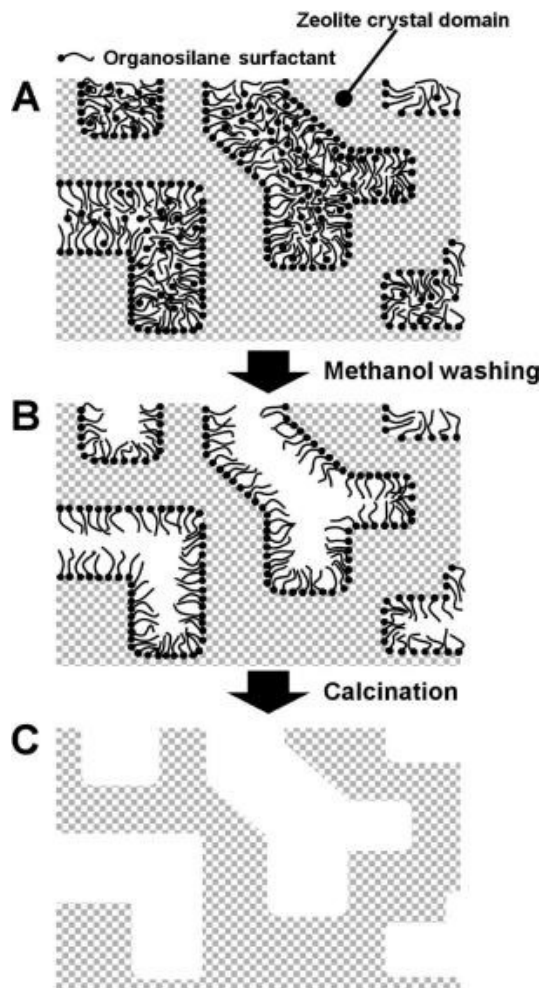
Surfactants are classified into four categories namely: anionic, cationic, nonionic and amphoteric<sup>85</sup>. The surfactant of interest is hexadecyltrimethylammonium bromide or can also be called cetyltrimethylammonium bromide (CTAB)<sup>15, 89, 90</sup>. CTAB is a cationic surfactant which dissociates in water according to path shown below:



CTAB has been used widely in industry because it is cheap and easily available. Also in research area, CTAB has been the most popular surfactant used as a template to synthesize mesoporous materials such as: MCM-41, MCM-48 and M41S<sup>87, 91, 92</sup>.

This technique has been applied extensively on silicate and aluminosilicate systems. Structures of ordered mesoporous silica such as: MCM-41 and SBA-15 have been prepared by adding different types of surfactants directly to the precursor mixtures<sup>13, 93-95</sup>. The prepared mesoporous silica is amorphous and has defects of low hydrothermal stability and low acidity. Therefore, to enhance the crystallinity of the produced structures, surfactants have been added to suspensions of pre-prepared zeolite seeds<sup>96, 97</sup>. The resulting materials show a little improvement in terms of stability and the acidity, but the XRD patterns show absence of any crystalline phase.

However, no mesoporous zeolite has been obtained by following the same procedure probably due to the weak interactions between the surfactant and large aluminosilicate species, which results in exclusion of the surfactant micelles during the crystallization and growth of zeolites. Recently, however, Choi *et al.* have synthesized MFI and LTA zeolites containing micro- and mesopores in one phase by direct addition of amphiphilic organosilane surfactant into the synthesis mixture<sup>54</sup>. In addition to quaternary ammonium and alkyl chain groups which are the characteristic of common surfactants, the molecule contains a methoxysilyl moiety (Scheme 2.6). This hydrolysable moiety has the ability to interact strongly through covalent bonds with aluminosilicate species in the growing crystals<sup>53, 54, 67, 98</sup>. Nevertheless, the shortcoming of this procedure is the high price and the non-availability of this type of surfactant commercially. This type of synthesis technique is discussed elaborately in section 2.7.1 because it is the technique of interest in this thesis.



**Scheme 2.6 Schematic diagram of mesopore generation in LTA zeolite: (A) as-synthesized zeolite, (B) methanol-washed sample, (C) calcined sample<sup>67</sup>.**

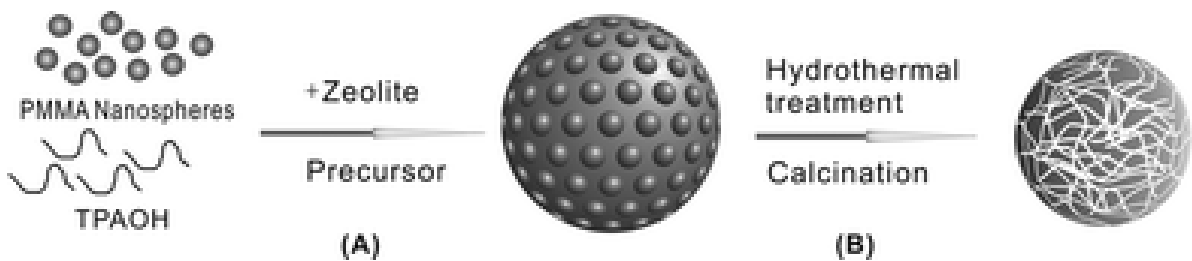
### 2.6.3 Dual-template synthesis

Some researchers have combined the supramolecular and the hard templating techniques in one process in order to generate well ordered three dimensional hierarchical zeolite and zeotype materials. For instance, Holland *et al.* prepared zeolite structure containing nano- meso- and macropores by introducing polystyrene spheres (PS) into silicalite – TPAOH solution <sup>99</sup>. The silicalite nanoparticles were assembled on the PS spheres forming core shell structures. The thickness of silicalite – TPAOH layer in the core shell structures was controlled by following the layer by layer route. Next, the obtained core shell structures were close-packed forming structures at macroscopic dimensions. The polystyrene spheres and the other organics were removed by calcination. The advantage of this method is that the wall thickness can be

controlled by the number of silicalite layers in the core shell structure. On the other hand, in other studies where layer by layer pathway was involved, the wall thickness was limited by the void spaces between the packed pre-seeded spheres<sup>20, 75, 77</sup>.

Based on the same technique, ordered macro-meso-microporous silica was produced by Sen *et al.*<sup>100</sup>. They used close-packed polystyrene, to generate the macropores, and tri-block copolymer surfactant to form the micro and mesopores. In a recent study, Hua and Han added directly certain amounts of the tri-block copolymer and styrene to the reaction gel of silicalite-1 and ZSM-5 zeolites<sup>101</sup>. During the hydrothermal synthesis, the styrene was polymerised and integrated with zeolite nanocrystals constituting the micro spheres. Subsequent calcination produced macro-meso-microporous zeolite micro-spheres. Also they reported that the macroporosity can be governed by the quantity of the styrene.

Further, Zhao *et al.* introduced poly-methyl methacrylate (PMMA) nano-particles and tetra-propylammonium hydroxide (TPAOH) in zeolite synthesis composition<sup>58</sup>. The PMMA nanoparticles were assembled spontaneously forming spherical particles which were stabilized by TPAOH and penetrated by zeolite synthesis solution. Afterward, these spheres were subjected to hydrothermal conditions for zeolite crystallization, followed by carbonization for PMMA removal. The synthesized ZSM-5 has micro-sphere shape with micropores from the framework of zeolite and mesopores attributed to the removed PMMA (Scheme 2.7).



**Scheme 2.7 Schematic diagram for the synthesis of micro-mesoporous zeolite microspheres by introducing dual templates, poly-methyl methacrylate (PMMA) nano-particles and tetra-propylammonium hydroxide (TPAOH), to zeolite system<sup>58</sup>.**

In very recent work, Yang *et al.* implemented this technique to prepare a hierarchical (meso-macro) aluminosilicate monolith<sup>102</sup>. Tri-block copolymer (Pluronic 123) was used as a supramolecular template, and water soluble polymer (Polyethylene glycol-PEG) as a gelation initiator. The main idea of this study was the simultaneous gelation and phase separation in order

to produce well-interconnected hierarchical monolith rather than spherical aggregated particles. They report that the Si/Al ratio and the water concentration in the precursor mixture have a vital role in controlling the timing of these two processes. Additionally, they reported that the hierarchical monolith can be formed by enhancing the aluminium quantity and decreasing the water concentration in the reaction solution.

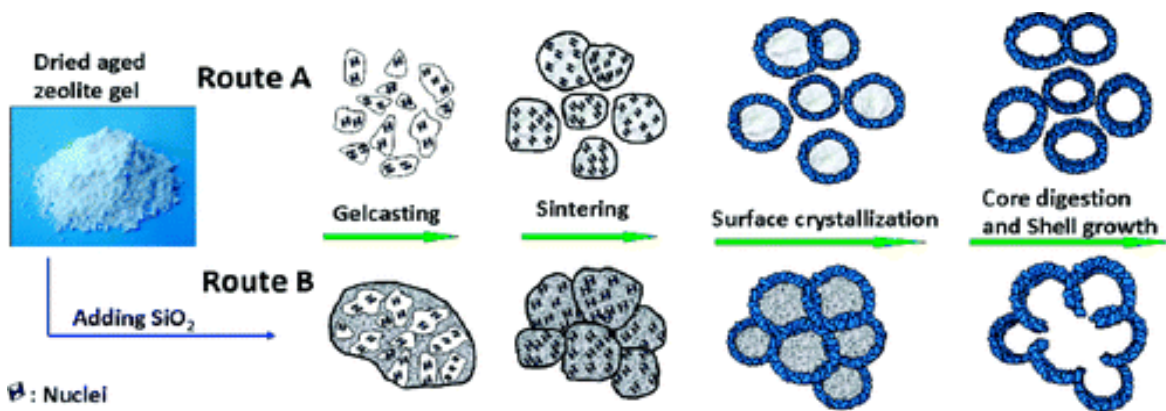
#### **2.6.4 Vapor Phase Transport (VPT)**

This technique is based on converting pre-fabricated amorphous hierarchical structures; i.e. monoliths, membrane, etc into zeolites by exposing them to vapors of organic templating agents and water. In a study conducted by Nishiyama *et al.*, aluminosilicate membranes were built on alumina support by a dipping technique<sup>10</sup>. Then the aluminosilicate membrane/ alumina support was placed into an autoclave with organic compounds (trimethylamine and ethylenediamine) and water as vapor sources. The results showed that fully crystallized MOR zeolite membrane was formed on the alumina support.

In another study, prefabricated bimodal silica skeleton was converted into ZSM-5 monoliths with MFI framework structure<sup>11</sup>. The macro-mesoporous silica gel monolith was first soaked in a SOD solution with tetrpropylammonium hydroxide (TPAOH) and then placed in an autoclave and heated with saturated water vapor. The textural properties of the produced monolith showed macro- and microporosities indicating that the macroporosity of the parent skeleton was maintained, while the mesoporosity disappeared. Although the prepared ZSM-5 monolith showed some stiffness some parts of it were fragile.

Huang *et al.* followed a gel casting technique to form monolith of sufficiently aged zeolite gel with colloidal silica (as binder)<sup>103</sup>. Then the monolith was crystallized *in situ* under vapor of water producing NaP zeolite monolith composed of interconnected hollow NaP zeolite particles. The hollow particles were formed due to the conversion of the core of zeolite gel particles into a crystalline shell following surface to core crystallization mechanism (Scheme 2.8). The authors reported that without the silica binder, only dispersible hollow NaP zeolite particle were formed.

Although following this strategy maintains the shape of the monoliths or the membranes, the pores size has changed significantly after the crystallization. In addition, the necessity for pressured vessel (autoclave) reduces the effectiveness of this technique in practical applications.



**Scheme 2.8** schematic representation of the formation of hollow NaP particles (Route A) and macroporous NaP zeolite monoliths (Route B)<sup>103</sup>.

### 2.6.5 Emulsion droplets-template synthesis

Emulsion consists of two immiscible liquids, one of them is a continuous/external phase and the other is a dispersed/internal phase<sup>85, 104</sup>. Emulsions can be either oil in water (O/W) or water in oil (W/O) or water in oil in water (W/O/W). The conventional method to prepare a stable emulsion is by dissolving emulsifier (surfactant or solid particles) into the continuous phase, followed by adding the dispersed phase drop by drop under a continuous stirring.

Employing this type of templating in the preparation of porous materials has been explored intensively. In this technique the reaction solution is considered as an external phase in which droplets of oil are dispersed, these droplets act as templates. The species of the produced material are assembled around these droplets, subsequent polymerization or sol-gel process followed by droplets removal generates porous structures.

For instance, Imhof *et al.* proposed that macroporous structures of titania, silica and zirconia with controlled and uniform spherical pores can be synthesized by using evenly sized droplets of mono-dispersed emulsion as templates<sup>104-106</sup>. They followed the repeated fractionation technique reported by Bibette in order to obtain the required consistent size of droplets<sup>107</sup>. Also, Yi and Yang used emulsion of silicon oil in water which was emulsified by sodium dodecyl sulfate to synthesize a macroporous silica matrix<sup>108</sup>. They reported that if the gelation does not occur at the same time or at least during a short period in every region of the continuous phase, the droplets will move to a remote area and cause inhomogeneous droplet distribution. Consequently, the produced silica matrix suffered from a non-uniform macropore distribution.

Further, silica with macro-mesoporous hollow spheres was prepared by emulsion templating<sup>109</sup>. The spheres comprised micrometer sized hollow surrounded with mesoporous hexagonal ordered walls. The authors used a nonionic surfactant which performed dual jobs *viz.* stabilizing the emulsion and forming micelles around the droplets. Silicate species in the syntheses mixture were aggregated around the micelles which themselves were assembled on the surface of the droplets. The micelles formed the mesopores and the droplets were responsible for the macropore formation.

In another study, by Das *et al.*, coffin shaped silicalite-1 nano-crystals were produced inside the water droplets in W/O emulsion<sup>110</sup>. The synthesis solution of silicalite-1 was added drop-wise to the continuous phase (Hexane) which was stabilized by nonionic surfactant. After crystallization and separation, silicalite-1 crystals with coffin shape are produced.

The O/W micro-emulsion was included in the preparation of low silica zeolite type L<sup>111</sup>. The research reveals that the emulsion composition controls the shape and the size of the produced zeolite crystals. Zeolite L crystals prepared in a conventional procedure show a rod shape with length per diameter (L/D) ratio around 1.5, while with emulsion the ratio enhances to 42 depending on the composition of the emulsion. A micro-emulsion of O/W/nonionic surfactant/co-surfactant was employed by Lee and Shantz in synthesizing silicalite-1<sup>112</sup>. Two different morphologies were produced *viz.* spherical particles and plates and both of them consisted of nanosized coffin shaped silicalite crystals aggregated with each other. The study discussed the factors that might influence the morphology, quality and the size of the product, i.e. emulsion concentration, the type and quantity of the surfactant, surfactant/co-surfactant ratio and finally the temperature.

Monoliths of inorganic materials were fabricated by employing an emulsion templating technique. Hierarchical silica monoliths with macro and mesopores were prepared and investigated by Carn *et al.*<sup>113</sup>. The silica synthesis solution was considered as the aqueous phase of an emulsion in which the surfactant was dissolved and the oil droplets were dispersed. The macropores were formed due to the oil droplets and the mesopores were obtained because of the micelles of the surfactant. The authors demonstrate that the volume and concentration of the oil controls the pores size in the monolith.

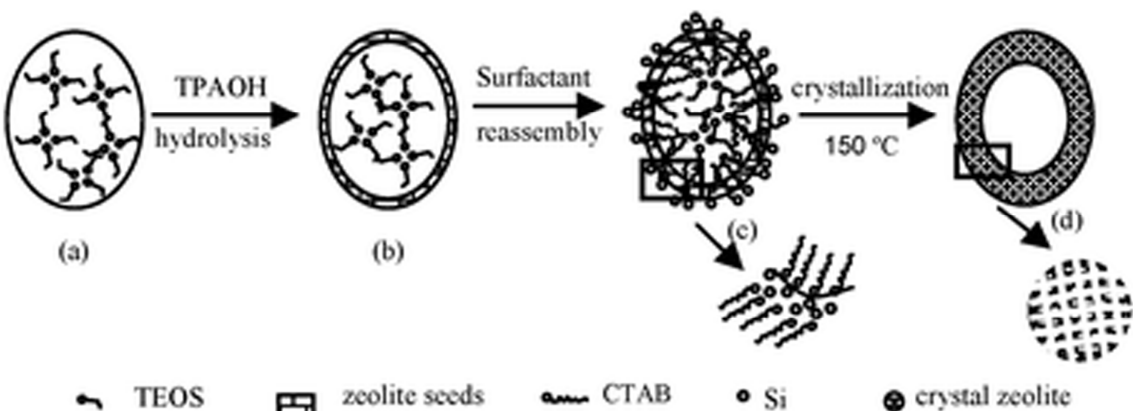
The above studies showed that hierarchical structures of silica and inorganic oxides can easily be obtained by direct introduction of the emulsion droplets into the synthesis mixture. On the other hand, no hierarchical zeolite structures were obtained *via* this type of template synthesis. Nevertheless, droplets of emulsion can be used as a nanoreactor in which nano-scale zeolite crystals with controllable shape and size can be synthesized.

Compared to the solid templating technique, the emulsion templating offers better chances to produce intact hierarchical structures. The reason stems from the deformability of the emulsion droplets because they are liquid; thus the product can adapt to the shrinkage that occurs during the gelation and drying<sup>114</sup>. Also the template can easily be removed by dissolution in a solvent or by evaporation<sup>104, 105</sup>. However, only a few studies investigated the possibility of synthesizing hierarchical zeolite structures by employing this type of template.

Cheng *et al.* conducted a study to prepare hollow microspheres with ZSM-5 zeolite shells<sup>115</sup>. They combine sol-gel strategy with W/O/W emulsion templating to prepare amorphous aluminosilicate hollow micro-spheres. Afterwards, by VPT (Vapor Phase Transport) technique, the amorphous aluminosilicate micro-spheres were transformed into ZSM-5. Three types of pores were presented in the generated ZSM-5 hollow microspheres *viz.* macropores which were represented by the hollow inside the spheres, mesopores were attributed to the interstitial voids between the crystals that compose the shell of the spheres and finally the micropores which were associated with the structure of the crystals in the shell. The only disadvantage of this method stems from the high temperature VPT technique which means more energy consumption and higher cost.

In another study conducted by Zhao *et al.*, O/W emulsion technique was involved in synthesizing a mesoporous ZSM-5 zeolite with hollow capsular structure<sup>57</sup>. In this work, oil (triethyl orthosilicate [TEOS]) in water (aqueous solution containing aluminium isopropoxide [(Al(PrO)<sub>3</sub>]) was firstly prepared followed by drop wise addition of alkaline solution containing TPAOH and NaOH under stirring at low temperature. At this stage, zeolite nano-seeds were formed and condensed under the direction of TPAOH along the interface of the droplets. Next, the obtained emulsion was added to the surfactant cetyltrimethylammonium bromide (CTAB) solution, the CTAB molecules were enriched at oil-water interface contributing in stabilizing the emulsion droplets. During the last step, the hydrothermal step, the TEOS was hydrolyzed and

diffused outwards from the center of the droplets leaving behind a hollow core (Scheme 2.9). However, the size of the obtained mesopores is relatively small at ~ 3nm.



**Scheme 2.9 Schematic representation of the suggested formation process of mesoporous ZSM-5 zeolite with hollow capsular structure<sup>57</sup>.**

### 2.6.6 Non-templating technique

In this technique, hierarchical porous zeolite structure can be obtained without the addition of any type of templates.

Complex porous architectures; such as micropatterned zeolite films, self standing zeolite membrane, long fiber, and micro-macroporous zeolite structures were constructed by using zeolite nanoparticles as building units following the distinctive strategy named “Evaporation Induced Self Assembly (EISA)”<sup>83</sup>. Silicalite nanocrystals with adjustable diameter (30 – 80 nm) and narrow size distribution were dispersed in ethanol at room temperature (Figure 2.9). Then a drop of nanosilicalite/ethanol suspension was placed on a silicon wafer, followed by applying a patterned polydimethylsilane (PDMS) stamp with a compression pressure. The mould was removed after 12 hours which was a sufficient period for ethanol to evaporate. The obtained structure indicated that the nanoparticles were self organized into a continuous close-packed network. The theory behind this strategy is that due to the ethanol evaporation, the nanoparticles were compacted closely driven by capillary forces and then hydrogen bonds were formed keeping the crystals attached. Further, during calcination, the silanol groups on the external surface of the nanosilicalite crystals were condensed and covalent (Si–O–Si) bonds were formed which further cross-linked the nanocrystals.

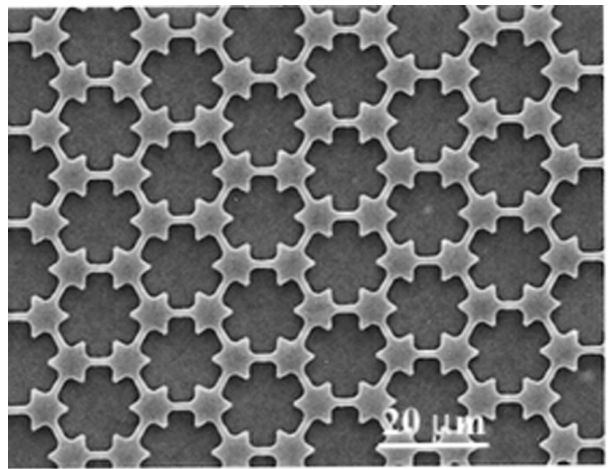


**Figure 2.7 SEM image of calcined micro-patterned silicalite film fabricated by Evaporation Induced Self Assembly (EISA) method<sup>83</sup>.**

Natural diatomite is a type of siliceous biologic sedimentary rock with unique macro-sized channels with size ranging from sub-microns to several tens of microns. Natural diatomite was used as a precursor to synthesize different types of zeolites<sup>116</sup>. The high silica diatomite was used as a raw material for synthesizing MFI zeolite structures. Further, due to intrinsic macroporosity and high silica content in the natural diatomite, it was utilized in fabricating hierarchical zeolite with a micro and macro-pore model<sup>116</sup>. In a study performed by Anderson *et al.*, diatomite with hollow tube shape particles and macroporous walls were converted to zeolite forming meso-microporous zeolite diatomite composite<sup>117</sup>. In another study, the addition of the diatomite to a solution of sodium chloride and structure directing agent followed by a hydrothermal treatment produced MFI zeolite with microspheric morphology<sup>116</sup>. Each sphere consists of an aggregation of nano sized zeolite crystals with meso sized interstitial voids between them. Using the natural diatomite in synthesizing hierarchical zeolite is tempting because it is abundantly available and cheap. However, the high quality diatomite naturally contains more than 90 wt % silica and some other oxides which may be considered as impurities. Also, its natural composition has restricted its utility to produce zeolite with high silica ratio<sup>116, 117</sup>.

Huang *et al.* synthesized hierachically porous NaY zeolite particles consisting of aggregated nano-crystallites (20 – 80 nm) by following three-stage temperature control<sup>64</sup>. N<sub>2</sub> sorption results indicate that the synthesized aggregates contain micro and mesopores. The size of the nanocrystallites and the size of the intercrystalline pores were controlled by varying the water to

silica contents in the reaction gel. The hierarchical NaY aggregates remained intact after several hours ultrasonication indicating the mechanical stability of these particles.

Groen *et al.* prepared mesoporous ZSM-5 crystals by following the post synthesis desalination method<sup>118</sup>. They obtained large crystals which showed homogeneous distribution of aluminium in the framework and accessible interconnected intra-crystalline mesopores with preserved crystallinity. The desalination shortened the diffusion path considerably. Thus, the produced hierarchical crystals showed a remarkably improved diffusion of neopentane to about 2 orders faster than the microporous crystals.

## **2.7 Fabrication of hierarchical microscopic zeolite structures for better adsorption characteristics**

The above literature review demonstrated the distinctive properties of zeolites structures which make them suitable for a wide variety of applications in industry and medicine. However, the sole presence of micropore imposes diffusion limitations, especially when large molecules are involved in the application. Also, the small size of the zeolite crystals/beads causes a large pressure drop when fluid molecules flow through the spaces between these crystals in a packed bed.

Extensive research has been conducted to investigate the possible solutions for the diffusion limitation and the pressure drop in order to improve the zeolites performance and extend their range of applications. According to the literature, two main strategies were investigated: namely, decreasing the crystal size and fabricating hierarchical microscopic zeolite structures.

In our work we are focusing on zeolites as adsorbents to be used for gas separation by adsorption. Therefore, the synthesis technique should be practical, not complicated and eco-friendly. Also, the synthesized structure should compete with the commercial beads and show high adsorption capacity, better diffusivity and less pressure drop. Accordingly, a self standing hierarchical zeolite structure with tri-modal interconnected pore network could be a promising adsorbent. The macropores can be constructed in the body of the self standing hierarchical

structure. The building units of the walls of the macropores can be micro-mesoporous zeolite nanocrystals because they offer higher surface area and better transport path to the active sites. The technique of interest is the supramolecular-template synthesis because it offers one pot method and also some surfactants (eg. CTAB) are cheap, available and already have been used in industry.

### ***2.7.1 Synthesis of micro-mesoporous zeolite via supramolecular templating technique***

The direct synthesis of hierarchical porous zeolites by using the supramolecular templating technique is still considered a challenge which requires more investigation. It is tempting to investigate the possibility of synthesizing hierarchical zeolite simply by direct addition of an ordinary surfactant *i.e.* CTAB to the synthesis mixture.

#### ***2.7.1.1 Direct crystallization of zeolite in presence of surfactant micelles***

Many studies have reported that highly ordered mesoporous silicate materials with controllable pores have been successfully synthesized simply by direct addition of surfactant molecules into the synthesis mixture<sup>13-15</sup>. The advantage of this technique is that many of the surfactants are cheap and commercially available which is extremely desirable if they are going to be used at industrial scale. Also, the procedure used to synthesize the hierarchical silicate materials were simple and conducted in one-pot.

However, crystalline zeolite containing both micro and mesoporous structures in one phase could not be obtained by straightforward addition of ordinary surfactant to the aluminosilicate gel. This is probably due to the weak interactions between the surfactant and large aluminosilicate building blocks which results in exclusion of the surfactant micelles during the crystallization and growth of zeolite. This reason was emphasized when Ryoo *et al.* synthesized micro-mesoporous MFI<sup>54</sup>, LTA<sup>67</sup> and AlPO<sub>4</sub><sup>55</sup> zeolites by using the surfactant containing methoxysilyl moiety which can form covalent bonds with the aluminosilicate species. Consequently, the surfactants were not expelled from the aluminosilicate gel particle during the crystallization and make it possible for zeolite crystal to grow into a mesoporous structure. The

non-availability and the high price of this surfactant reduce its applicability at the industrial scale.

Another reason for not obtaining mesoporous zeolite structures by direct addition of ordinary surfactant to the synthesis mixture is that the hydrothermal treatment for zeolite crystallization is normally performed at high temperature. According to Huo *et al.*, the probability of forming organized surfactant aggregates in silicate systems reduces at high temperature ( $>50$  °C)<sup>119</sup>. The reason is that, at high temperature, the kinetics of inorganic condensation becomes favorable because the ion interactions and solvation effects becomes less pronounced and the hydrolysis rate increases and as a result the kinetics of organized organic arrays reduces.

### **2.7.1.2 Surfactant-mediated assembly of zeolite seeds into mesoporous structures**

This strategy emerged as a promising alternative to synthesize mesoporous zeolite structures. This strategy is based on two steps: the first step involves the synthesis of zeolite nanoclusters or can also be called “zeolite seeds”, and the second step involves the assembly of these nano seeds into meso-porous structures under the directing effect of surfactant<sup>120, 121</sup>.

This technique was first suggested by Liu *et al.* in the work that included the synthesis of hexagonal Al-MCM-41 starting from NaY zeolite nano-clusters<sup>120</sup>. Initially, they prepared proto- zeolitic nano-clusters that normally nucleate the crystallization of micro-porous zeolite. Introducing the surfactant (CTAB) induced the assembly of these nano-seeds into hexagonal meso-structures. The produced mesopores Al-MCM-41 showed high acidity and hydrothermal stability that begins to approach zeolites. Even though the primary building units used in this work were NaY zeolite seeds, no long range atomic order was detected in the XRD pattern due to the relatively small size of the assembled zeolite seeds, less than XRD detection limit. On the other hand, larger zeolite seeds cannot be assembled under the direction of the surfactant due to the weak charge density or the relatively small size of the micelles (2 – 4 nm).

Accordingly, it has become crucial to investigate the conditions that maintain the surfactant micelles within the crystallization domain during the crystallization and growth of zeolite crystals.

## **2.7.2 Factors influence the formation of hierarchical zeolites in presence of surfactant micelles**

Two vital factors are to be taken into consideration for direct synthesis of hierarchical zeolite via supramolecular templating technique: namely, the reaction temperature and the micelle size.

### **2.7.2.1 The influence of temperature on the surfactant behavior:**

Many studies have investigated the influence of the synthesis temperature on the interaction between the silicate species and surfactant molecules<sup>92, 122, 123</sup>.

Beck *et al.* obtained mesoporous silica MCM-41 at 100 °C in the presence of self assembled aggregates of cetyltrimethylammonium bromide as templates<sup>92</sup>. Increasing the reaction temperature to 150 °C enhanced the MCM-41 crystallinity, but at 200 °C only an amorphous material was obtained. They reported that at low temperatures, the formation of ordered aggregates of surfactant molecules is favorable while at high temperatures the preformed micelles were decomposed and thus the surfactant molecules acted as single molecule structure-directing agents.

Furthermore, Chen, *et al.* described the behavior of surfactants in the silicate – cetyltrimethylammonium bromide (CTAB) – water system at different temperature<sup>123</sup>. Increasing the hydrothermal synthesis temperature from room temperature to 100 °C resulted in the formation of well-defined mesoporous hexagonal silicate structure (MCM-41) with high surface area and pore volume. Increasing the temperature to 135 °C decreased the long range order on the product. Further increasing the temperature to 170 °C resulted in changing the structure of the produced material to micro-porous MFI framework. In other words, the structures of the materials obtained due to the interaction between the surfactant and the silicate species change with changing the hydrothermal temperature. Increasing the temperature from 100 to 135 and then to 170 °C changes the product structure from hexagonal to lamellar and then to micro-porous zeolite with MFI framework structure.

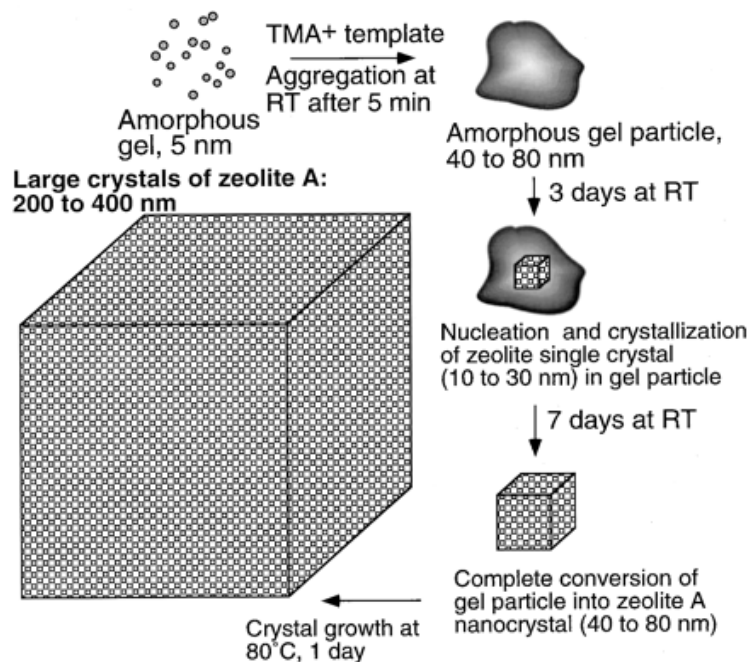
Moreover, Huo *et al.* stated that the condensation of inorganic species becomes slow at low temperature *i.e.* room temperature<sup>119</sup>.

These findings suggest a possible approach to produce hierarchical zeolite in presence of surfactant micelles is low temperature crystallization. At low temperature, the micelle formation becomes dominant and the condensation of aluminosilicate species becomes slower which probably results in retaining the micelles within the crystallization domain.

Several successful attempts were published in which microporous zeolite-type materials were crystallized at room temperature<sup>16, 124-126</sup>

### **2.7.2.1.1 Zeolite formation at room temeparture**

It has been reported that LTA and FAU zeolite can be crystallized at room temeprature<sup>16, 124-126</sup>. The aluminosilicate gel of LTA zeolite was transformed completely into crystalline phase after 7 days while the amorphous gel of FAU required 21 days for complete crystallization.



**Scheme 2.10** A schematic representation of the proposed growth mechanism for LTA zeolite at room temeparture<sup>125</sup>.

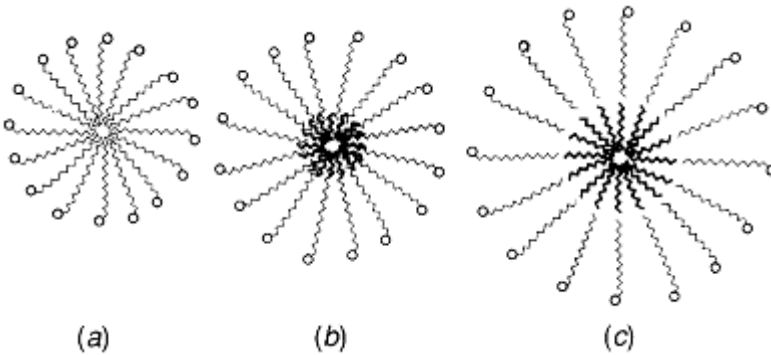
Directly after mixing the presurors of LTA zeolite system, amorphous gel particles with size of 40 – 80 nm are formed<sup>125</sup>. These gel particles comprised of the aggregated spheres of aluminosilicate species with size of 5 to 10 nm which were condensed due to the addition of the organic template, tetramethylammonium hydroxide (TMAOH). After three days of room temperature synthesis, tiny zeolite A crystallites were obsereveed embeded inside the amorphous

gel aggregates. The growth of these crystallites continued at the expense of the amorphous gel particles following solution-mediated mechanism. The growth continued until the entire amorphous gel aggregates were consumed. Zeolite A nanocrystals with size of 40 to 80 nm were formed after 7 days of room temperature synthesis. Subsequent hydrothermal treatment at high temperature (80°C), resulted in further increase in the size of the obtained crystals to 200 – 400 nm (Scheme 2.10).

### 2.7.2.2 The influence of the size of surfacatnt micelles

As presented earlier, numerous studies have investigated the synthesis of silicates with different mesoporous structures and pore size distribution by using supramolecular surfactant aggregates as template or as named by Beck; “Liquid Crystal Tmplate” (LCT) <sup>91</sup>. The structure and the pore dimensions of the synthesized mesoporous silicates *i.e.* MCM-41 and M41S are linked to the properties of the surfactant, for example, the chain length and the solution chemistry<sup>91</sup>. Furthermore, Beck *et al.* stated that the inclusion of an expander agent into the synthesis mixture contributes to increasing the size of the organic aggregates (micelles) and hence the diameter of the pores in the mesoporous structures. They demonstrated that, the pore size of MCM-41 can be tuned by adding 1,3,5-trimethylbenzene (TMB) at different concentrations <sup>91</sup>. Hua *et al.* observed that the alkylated aromatic expander (swelling agent), TMB, dissolves in the hydrophobic tail of the surfactant, cetyltrimethylammonium chloride (CTACl). The organic inorganic molecules are organized with the organic TMB molecules as a cosolvent for the hydrophobic part of the synthesis mixture <sup>119</sup>.

Normal alkanes,  $C_nH_{2n+2}$ , have also been investigated as expander (swelling) agents for the organized aggregates of alkyltrimethylammonium bromide surfactants in silica systems <sup>88, 127-130</sup>. Ulagappan and Rao presented that a progressive increase in the diameter of the mesoporous silica can be observed with the increase of the chain length of the alkane. The authors revealed that the alkanes with  $n = 5 - 8$  might dissolve between the tails of the surfactant molecules, thus they do not contribute to the formation of the micelles with their entire length (Scheme 2.11b). However, the alkane with  $n = 9 - 15$  added their entire length to the micelle diameter suggesting that molecule to molecule interaction had occurred (Scheme 2.11c).



**Scheme 2.11 Schematic representaion of a micelle of surfactant molecules (a) in absence of alkane molecules as expension agent, (b) with alkanes with  $n = 5 - 8$ , (c) with alkane with  $n = 9 - 15$** <sup>127</sup>.

In another study conducted by Blin and Su, the alkanes were incorporated in a silica/surfactant system as swelling agents<sup>88</sup>; however however, their behavior was different than results obtained by Ulagappan and Rao<sup>127</sup>. They reported that pentane and hexane did not show a noticeable increase on the pore diameter, probably because their boiling points are close to the temperature of the micelle solution preparation. Alkanes with  $n = 7 - 10$  showed a linear relationship between the pore diameter and the number of carbon atoms of the alkanes. With further increase in the number of carbon atoms to  $n = 10$ , the maximum expansion was observed suggesting that alkane molecules were incorporated into the core of the micelles increasing their volumes. However, alkane with  $n = 11$  and 12 were dissolved between the tails of the surfactant and as a result only part of them incorporated in the core of the micelles increasing their sizes.

Even though both studies included alkanes as expander agents in silica systems and both maintain the surfactant : alkane ratio at 1 : 1, the results suggest that the behavior of the alkanes changes according to the system conditions.

Expanding the size the surfactant micelles has been considered in a zeolite system by Gu *et al.*<sup>121</sup>. The authors proposed that the small size of micelles is a hindrance to the relatively large pre-formed zeolite seeds to be assembled around these micelles. They expanded the CTAB micelles by TMB and enhanced the charge density of the micelles by introducing tert-butyl alcohol as a co-solvent. However, they obtained mesoporous zeolite only at a certain concentration while at all other compositions they investigated; their product was a composite of NaY zeolite and silica. Further, no mesoporous phase was obtained when only CTAB (without swelling agent) was introduced to the system.

## **2.8 Self standing hierarchical zeolite structures as adsorbents**

As described earlier, zeolites have been widely used in gas separation by adsorption processes due to their unique framework structure and uniform pores size which allow molecules with a particular size to diffuse while excluding others. In addition, the charge balancing cations that are abundantly distributed in their micropores generate an electrical field and thus attract the adsorbate molecules based on the quadrupole properties of these molecules.

In a comparison between the performance of 13X zeolite and activated carbon as adsorbents for CO<sub>2</sub> from flue gas at two different CO<sub>2</sub> concentrations, 13X zeolite was considered as a better adsorbent than activated carbon in non-isothermal and adiabatic PSA process <sup>48</sup>. Although the heat of adsorption of CO<sub>2</sub> on activated carbon less than on 13X zeolite, the latter yielded high purity CO<sub>2</sub> (over 99 %) and higher recoveries, at 53 % from the low CO<sub>2</sub> concentration flue gas and at 70 % from high CO<sub>2</sub> concentration flue gas. In addition to the higher CO<sub>2</sub> adsorption capacity of 13X zeolite compared to activated carbon, it also showed higher equilibrium selectivity for CO<sub>2</sub> over N<sub>2</sub>. Thus, to select a good adsorbent for PSA process, 13X zeolite is preferred compared to activated carbon because the high adsorption capacity, high equilibrium selectivity and low purge gas requirement are more effective in PSA process than heat effects.

Additionally, enormous efforts have been devoted to study the adsorption of different gases on zeolites, namely, produce oxygen enriched air by using 5A zeolite <sup>131</sup>, propane and propylene adsorption on 4A zeolite <sup>24</sup> adsorption of O<sub>2</sub>, N<sub>2</sub> and Ar on potassium chabazite <sup>49</sup>, CO<sub>2</sub> capture on chabazite <sup>132</sup>, CO<sub>2</sub> capture from high humidity flue gas on 13X zeolite <sup>45</sup> ..etc.

In conventional gas separation processes, zeolite pellets / beads are randomly packed into the adsorption column. Then the gas mixture flows through the packed bed wherein the molecules of interest diffuse into the adsorbent pores and the other components leave the column through the outlet stream. However, the adsorption process by using a packed bed column has the drawback of high pressure drop and heat and mass transfer limitations which results in high energy consumption and thus high capital cost <sup>60, 76, 133, 134</sup>. Furthermore, beads, normally have a size of several millimeters; therefore it is difficult to obtain uniform reactivity at uniform reaction temperature because the temperature in the inner part of the beads is different than the temperature at the external surface <sup>76</sup>.

Therefore, over the past decade, enormous efforts have been devoted to develop and optimize different configurations of structured adsorbents for better performance with low pressure drop, high mass transfer coefficient and high adsorption capacity<sup>40, 60-62, 71, 135</sup>. Monoliths, laminates and foams are examples of these structured adsorbents.

Monoliths are structured materials with parallel channels. The shape and the diameter of the channels and their density per cross sectional area can be controlled. Additionally, the monoliths themselves can be produced with different geometrical shapes and sizes. Zeolite monolithic structures can either be zeolite-substrate monoliths which are prepared by depositing layer or film of zeolite or zeolite plus binder on monolithic substrates (normally made of alumina or ceramic), or can be zeolite monoliths which are prepared by directly moulding a paste of pure zeolite or zeolite and a binder into monolithic structures.

### **2.8.1 Zeolite/substrate monoliths**

A thin film of 13X zeolite was grown on porous cordierite monoliths (400 cpsi) and the performance of this film on CO<sub>2</sub> adsorption was examined and compared with commercial 13X beads<sup>40</sup>. The prepared 13X zeolite-substrate monoliths exhibited 100 times less pressure drop and 67 times lower CO<sub>2</sub> adsorption capacity compared to the 13X beads. The low adsorption capacity was attributed to low zeolite loading per unit mass of the monolith. Increasing the zeolite loading ratio by depositing thicker layer of zeolite on the substrates might enhance the adsorption capacity but on the other hand the mass transfer resistance will increase.

Gang *et al.* reported the synthesis of zeolite honeycombs by depositing NaX or silicalite crystallites on the surface of cuttlebone skeleton (Figure 2.10). A biomorphic honeycomb monolith with exceptionally high cell density of 16 000 cpsi was prepared by *in situ* hydrothermal growth of zeolite on the walls of the cuttlebone skeleton<sup>71</sup>. The authors used a novel flow coating technique to allow the zeolite gel to circulate through the channels of the cuttlebone. Flow coating method resulted in more uniform zeolite deposition in the capillary channels than the dip coating. The XRD and N<sub>2</sub> adsorption-desorption results indicate that pure mesoporous zeolite film was deposited on the surface of cuttlebone skeleton. The mesoporosity was attributed to the intercrystalline voids between the crystals that form the film. Although the

zeolite honeycombs performance showed lower pressure drop, it also showed less adsorption capacity than the pellets.

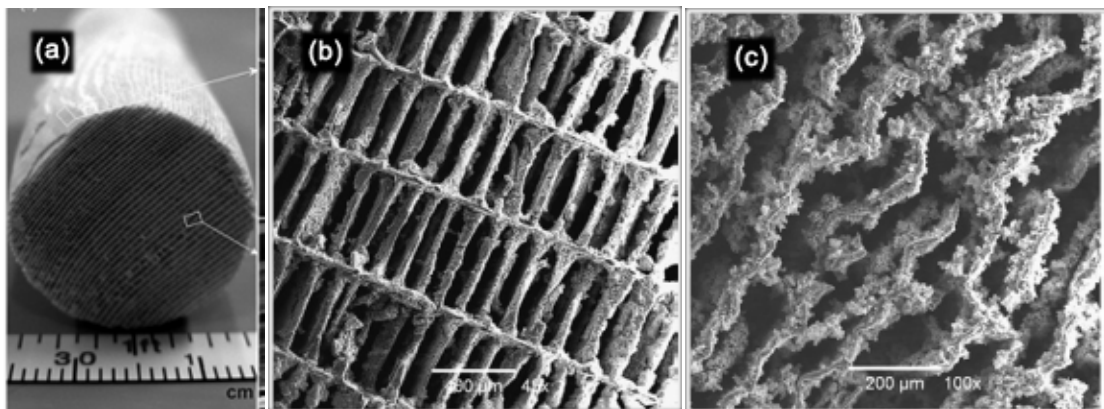


**Figure 2.8 The optical image of the cuttlebone monolith (a), SEM image of washed cuttlebone, top view of the pillars (b) and NaX honeycomb monolith prepared by flow coating, scale bar 400 mm (c).**

Another option to optimize the performance of zeolite-substrate monolith structures is by using a substrate with higher cell density. Accordingly, the performance of 13X zeolite films with 1.6  $\mu\text{m}$  thickness grown on cordierite substrates with 900 and 400 cpsi were studied<sup>135</sup>. The CO<sub>2</sub> isotherms of 13X zeolite-substrate monoliths with cell density of 900 cpsi showed higher adsorption capacity than 13X zeolite-substrate monoliths with 400 cpsi due to higher zeolite loading per unit mass in the former sample. However, the former sample exhibited broader CO<sub>2</sub> breakthrough curves compared to the latter which is an indication of higher mass transfer resistance or probably non-uniform distribution of the gas into the channels<sup>135</sup>.

Further disadvantages of zeolite-substrate monoliths is the difference between the thermal expansion coefficients of zeolite film and the monolithic support which might cause the separation of the film from the substrate upon frequent heating for activation<sup>73, 133</sup>. Also, film-substrate monoliths suffer from single-sided mass transport characteristics because monolithic substrates can be considered as a bundle of isolated parallel channels without mutual interconnection<sup>73</sup>.

To overcome all the above mentioned problems associated with the zeolite-substrate monolithic structures, one is tempted to focus on developing self standing zeolite monoliths that consists of only zeolite or zeolite plus a binder, with a channel structure which offer even mass distribution of the adsorbate molecules. These types of zeolite monoliths are expected to show

high adsorption capacity due to high zeolite loading in addition to low pressure drop (the main advantage of monolithic structures).

### 2.8.2 Binder free self standing monoliths

Sechse *et al.* have established a synthesis procedure to fabricate a self standing zeolite monolith which was crack free and contained a homogeneous macro-porous network which makes such monolith useful as a catalyst for liquid phase reactions under flow conditions<sup>136</sup>. Their procedure based on pseudomorphic transformation of the walls of macro-porous silica monolith into sodalite (SOD). The pre-prepared silica monolith was impregnated in a solution containing an appropriate template (TPAOH) in a Teflon-lined stainless steel autoclave. The small amount of TPAOH (template) prevented the SOD crystals from growing and hence enhanced the stability of the monolith which remained as one piece with the same shape after the pseudomorphic transformation (Figure 2.11 ).

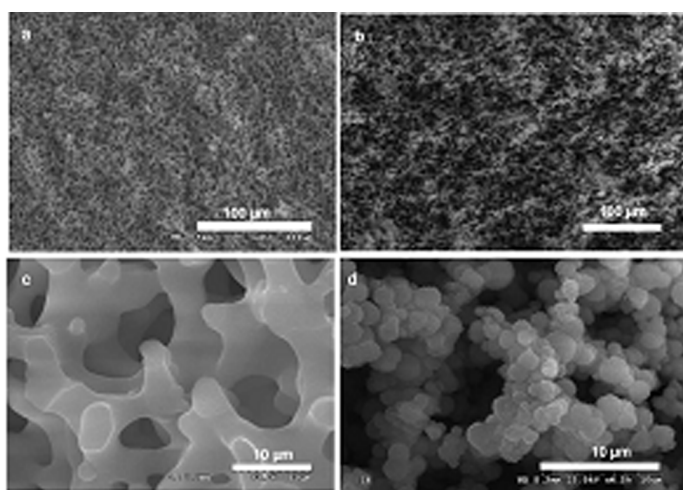


**Figure 2.9** SEM image of the original silica monolith (a) and (c), and its pseudomorphic transformation in SOD monolith<sup>136</sup>.

Tong *et al.* have fabricated self standing micro-meso-macroporous zeolite beta monolith following a novel procedure based on the transformation of amorphous walls of silica into crystalline zeolite using carbon as transitional template<sup>137</sup>. The pre-prepared silica monolith was first immersed in sucrose/sulfuric acid solution and then carbonized to obtain carbon/silica composite. Then this composite was impregnated with a clear solution of beta zeolite and transferred into an autoclave for further treatment at high temperature. Then the carbon template

was removed by calcinations. The channels of the silica monolith were maintained during the conversion of the amorphous walls into zeolite due to the presence of the carbon inside them which acted as a transitional template.

Silicalite monolith with micrometer-sized honeycomb structure was synthesized following ice templating method<sup>138</sup>. Initially, silica hydrogel was prepared and frozen undirectionally. Rod like ice crystals were formed within the gel and act as a template for the macropores. Then these ice crystals were removed by thawing by freeze drying and the resultant precursor silica gel contained well-ordered channels. By using a steam treatment at high temperature and pressure in presence of a structure directing agent, the walls of the precursor silica gel were transformed into crack free crystalline silicalite monolith.

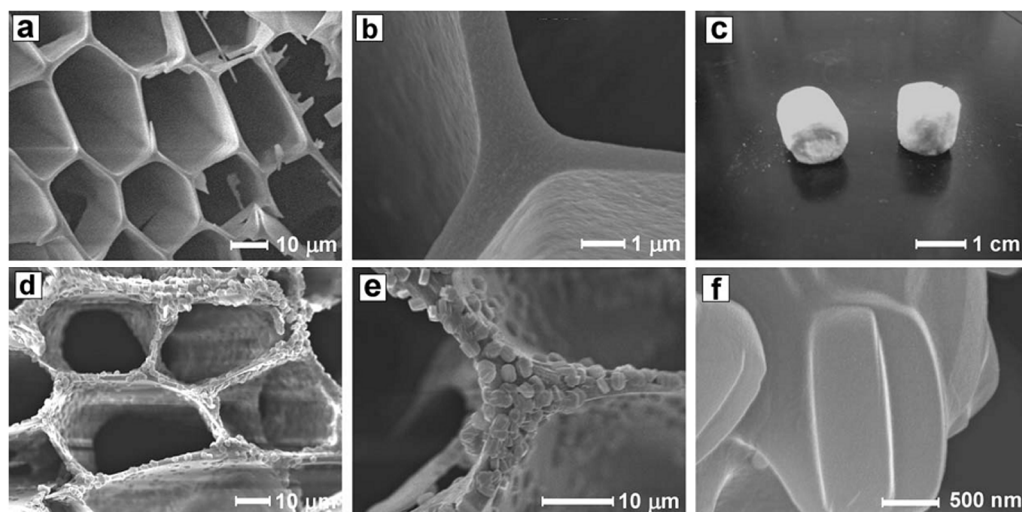


**Figure 2.10** SEM images of precursor silica gel (a and b), optical picture of silicalite monolith and SEM images of silicalite monolith (d – f)<sup>138</sup>.

In spite of the interesting strategies that have been proposed in the above described studies, the necessity of autoclave for transformation of the amorphous walls of silica monoliths into crystalline zeolite reduces their efficiency for industrial scale.

### 2.8.3 Zeolite/binder self standing monoliths

Different shapes and sizes of zeolite monoliths consisting of a desired number of parallel channels (cell density) can easily be prepared by extruding a paste of zeolite powder and a binder using a die extruder. A square channel 5A zeolite monolith consisting Na-bentonite as a binder at

concentration of 25 wt % was fabricated for air separation using constant volume method <sup>131</sup>. Although the authors suggested that the prepared monoliths might produce less pressure drop compared to beads if they were used for pressure swing adsorption air separation processes, the work does not include pressure drop results. In another study, a square channel 4A honeycomb monolith with 424 cpsi cell density was prepared and their behavior in terms of adsorbing propane and propylene gases was measured and compared to commercial extrudates <sup>24</sup>. The results of equilibrium adsorption of pure gases were in agreement with commercial extrudates, however, the values of diffusivity coefficients were three orders of magnitude smaller due to the partial blocking of the micropores by the binders.

The main aim for fabricating hierarchical zeolite structures is to find efficient alternatives to beads for industrial applications. Accordingly, the synthesis procedure of the zeolite monoliths should be practical and applicable for large scale mass production. Also, these monoliths should show adsorption characteristics which are competitive or better than commercial beads.

## 2.9 Scope of the present work

The literature review highlighted the necessity to fabricate zeolite architectures with interconnected hierarchical pore/channel system for better adsorption characteristics. The primary building units for the hierarchical architectures are suggested to be micro-mesoporous zeolite particles because they offer high surface area and high accessibility to the active sites. The technique of interest to synthesize the building units is supramolecular-templating because it represents a challenge as all the attempts to synthesize mesoporous zeolite by direct inclusion of ordinary surfactant in the synthesis mixture failed. The influence of temperature on the growth rate of zeolite crystals in the presence of surfactant micelles has not been studied before. Constructing a self standing zeolite monolith with a particular channeling system and with walls built of the micro-mesoporous zeolite particles has a potential of better diffusion and less pressure drop compared to commercial beads. The main aim of this study is to improve the adsorption characteristics of zeolites by following a practical technique.

The aims of this study with the corresponding chapters are listed as follows:

- Synthesis of micro-mesoporous zeolite particles by direct addition of a commercially available surfactant to the synthesis mixture. Low temperature crystallization is the reaction conditions to be used because it offers low growth rate of zeolite crystals and more stable micelles. (Chapter 4)
- Increase the size of the mesopores pores by using micellar expansion agent. (Chapter 4)
- Investigate the effects of the parameters involved in the synthesis techniques on the pore size distribution; for example the concentration of the surfactant and the micelle expansion agent. (Chapter 4)
- Detailed study of the formation and growth mechanism of zeolite crystals in the system. (Chapter 5)
- Using the pre-prepared hierarchical building units to fabricate a self standing zeolite monolith with channeling system to be designed in a particular way that offer even gas distribution and better adsorption. (Chapter 6)

Examine the performance of the fabricated hierarchical zeolite monoliths on CO<sub>2</sub> adsorption. The isotherms, pressure drop and breakthrough fronts will be measured and the experimental results will be simulated using modeling software to estimate the performance of the monoliths compared to the commercial beads. (Chapter 6).

## ***Chapter 3: Characterization and testing techniques***

The properties and the characteristics of the prepared samples have been investigated using the following techniques:

*Note:* All the characterizations were carried out on calcined samples unless noted otherwise.

### **3.1 Powder X-Ray Diffraction (PXRD)**

The crystallinity of the synthesized samples was characterized by powder X-ray diffraction (PXRD). The wide angle diffraction patterns were recorded by a Phillips PW1140/90 diffractometer using Cu K $\alpha$  radiation. The x-ray diffraction scanning was performed at ambient conditions at  $2\theta$  from 4 to  $60^\circ$  in steps of  $0.05^\circ$  and a scan rate of  $1^\circ \text{ min}^{-1}$ .

The low angle diffraction patterns were obtained on Scintag PAD V diffractometer with carbon monochrometor.

### **3.2 Scanning Electron Microscopy (SEM)**

The morphology and the size of the produced particles were determined using field emission scanning electron microscopy images obtained using a JEOL 7001F FEG instrument at 15 kV. The samples were crushed, sprinkled on carbon tape and mounted on a metal stub and coated with 1 nm layer of platinum metal.

The energy dispersive x-ray spectrometer (EDXS) attached to the JEOL 7001F FEG SEM instrument was used to conduct elemental analysis of the samples. The quantitative element results were recorded and analyzed using Oxford INCA software. The final quantity of each element was obtained by taking the average of a number of measurements at different spots.

### **3.3 Transmission Electron Microscopy (TEM)**

The detailed features of the produced particles and the structural evolution of the gel were investigated by transmission electron microscopy (TEM) type CM20 equipped with a LaB<sub>6</sub> electron gun and operated at 200 kV accelerating voltage. The samples were finely crushed, then

dispersed in ethanol and sonicated for 10 min. Thereafter a drop of this suspension was dispersed on a Cu grid coated with a thin layer of carbon.

### **3.4 Dynamic Light Scattering (DLS)**

The average particle size, particle size distribution (PSD) and zeta potential were determined by dynamic light scattering measurements on a Zetasizer Nano ZS (Malvern Instrument). The polydispersity index (PDI) was used as qualitative indicator of the particle size distribution. The colloidal stability of the synthesized material was determined by measuring the zeta potential ( $\xi$ -potential) as a function of pH. The medium used was 0.01 M phosphate buffered saline (PBS) with pH 7.4 and contained NaCl 0.138 M and KCl 0.0027 M. The measurements were conducted on wide pH ranges which were obtained by adjusting the PBS pH by NaOH and HCl solutions.

### **3.5 Fourier Transform Infrared (FTIR)**

The Fourier transform infrared (FTIR) spectra were recorded on a Perkin Elmer 100 FT-IR spectrometer in the wavelength range of 400 – 1400 cm<sup>-1</sup> with a resolution of 4 cm<sup>-1</sup> using KBr pellets.

### **3.6 Solid State Nuclear Magnetic Resonance (NMR)**

The <sup>29</sup>Si and <sup>27</sup>Al solid state nuclear magnetic resonance (MAS-NMR) spectra were performed at room temperature on a Bruker Avance 300 spectrometer equipped with a 4 mm magic angle spinning (MAS) probe at spinning speeds of 10–14 kHz with resonance frequency of 59.6 MHz for <sup>29</sup>Si and 78.2 MHz for <sup>27</sup>Al. The spectra were collected in single pulse mode with 10 s recycle delay and 3  $\mu$ s excitation pulse. The standards used for chemical shifts referring are tetramethyl silane (TMS) for <sup>29</sup>Si and aluminium nitrate solution for <sup>27</sup>Al.

### **3.7 Thermogravimetric Analysis (TGA)**

Weight changes and temperatures for organics removal were monitored using thermogravimetric analyses (TGA) on Mettler Toledo TGA/SDTA851 in oxygen flow of 20 ml min<sup>-1</sup> and at heating rate of 10 °C min<sup>-1</sup> to 900 °C.

### **3.8 Cryogenic Temperature Transmission Electron Microscopy (Cryo-TEM)**

The emulsion features and the droplet size were characterized by using cryogenic temperature transmission electron microscope (cryo-TEM) type Tecnai F30 -FEI equipped with an anti-contaminator and cold stage that allows imaging of quick frozen samples. The samples for the cryo-TEM analyses were prepared by plunge freezing. Briefly, a drop of the emulsion was placed on Holey carbon film supported by a copper TEM grid. The drop was blotted gently with filter paper from both sides of the grids to remove the excess liquid and form a thin film of sample spanning the holes of the support film. The sample was vitrified by plunging in liquid ethane. The vitrified specimens were transferred and loaded into the TEM cryo-holder under liquid nitrogen at (-196 °C). The temperature of the specimens was maintained under (-170 °C) throughout the TEM examination which was operated at 300 kV.

### **3.9 Nitrogen Adsorption-Desorption Analysis**

The textural properties of the synthesized samples were characterized by N<sub>2</sub> adsorption-desorption measurements at 77 K using a Micromeritics ASAP 2020 accelerated surface area and porosimetry system. All samples were degassed at 350 °C for 15 h under vacuum before analysis. The Brunauer-Emmett-Teller (BET) method was utilized to calculate the specific surface area ( $S_{\text{BET}}$ ) using the adsorption data collected over a relative pressure ( $P/P_0$ ) range of 0.05 – 0.3. The total pore volume was calculated by the amount of N<sub>2</sub> adsorbed at the highest relative pressure,  $P/P_0 = 0.992$ . The mesopore diameter distribution was measured by the Barrett-Joyner-Halenda (BJH) algorithm using the adsorption branch. The mesopore volume was calculated by subtraction from the total pore volume derived by the amount of N<sub>2</sub> adsorbed at  $P/P_0 = 0.992$  of the micropore volume calculated by *t*-plot method. The Horvath-Kawazoe (HK) method was used to determine the size and the distribution of the micropores in the samples.

### **3.10 Mercury Intrusion Porosimetry (MIP)**

The macropore size distribution was recorded by using mercury intrusion porosimetry using a Macromeritics Autopore III porosimeter which was operated over a pressure range of 1.4 – 379200 kPa.

### **3.11 Gas adsorption characteristics at low pressure**

The equilibrium adsorption capacities of pure gases on the synthesized samples and the commercial beads were measured at low pressure (100 kPa) using a Micromeritics ASAP 2010 accelerated surface area and porosimetry system. The equilibrium adsorption isotherms were collected over range of temperatures, 273.15, 303.15 and 313.15K. The samples were degassed at 350 °C for 15 h under vacuum before the analysis.

### **3.12 Gas adsorption capacity at high pressure**

The equilibrium adsorption capacity of a large molecule gas (ethylene) on the samples were measured at 273.15K and at pressure up to 850 kPa by a Micromeritics ASAP 2050 Xtended Pressure Sorption analyzer.

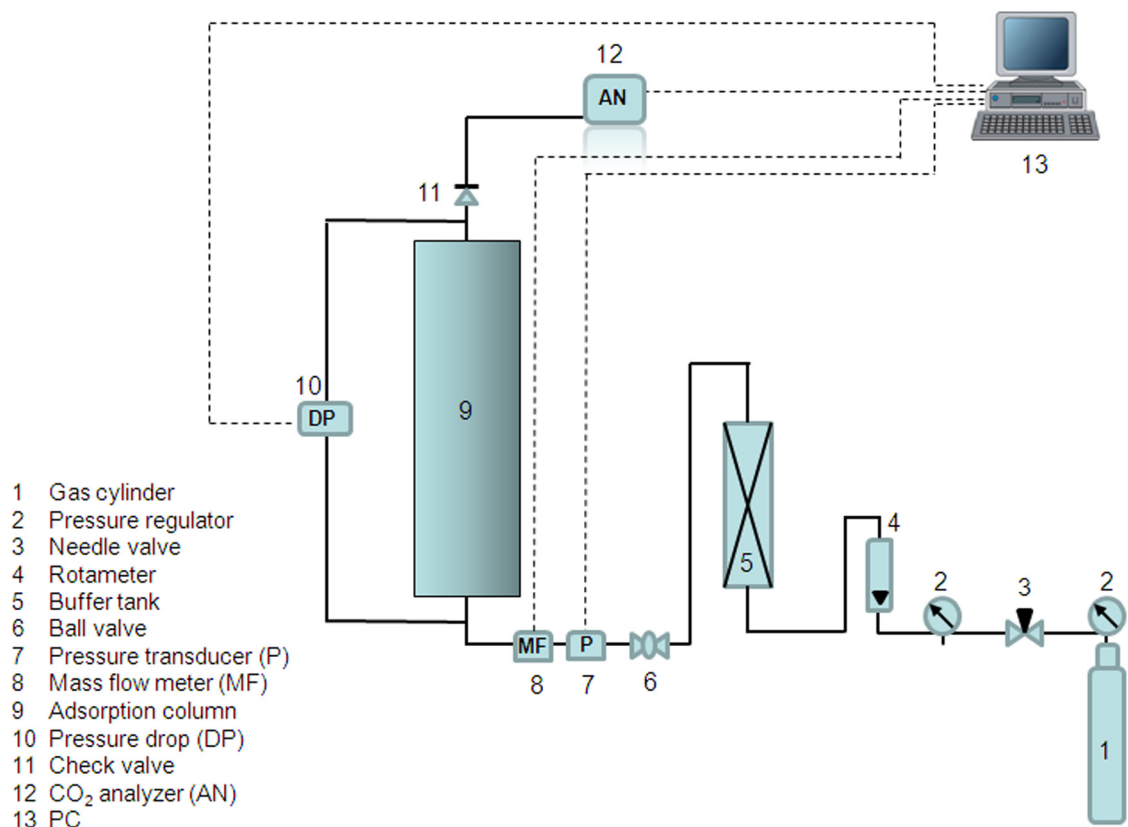
### **3.13 Breakthrough measurements**

The adsorption characteristics of the porous structured adsorbents fabricated in this work were characterized by breakthrough experiments. Scheme 3.1 demonstrates the instrument used for these experiments. The pressure regulator, rotameter, buffer tank, ball valve, pressure transducer and mass flow meter were used in order to obtain stable flow and pressure inside the system.

The adsorbents were loaded into the adsorption column and then an inert gas was fed into the system (Scheme 3.1). Afterward a feed stream (15% CO<sub>2</sub> and 85% N<sub>2</sub>) was introduced into the adsorbent at a particular flowrate and at 1.2 bar pressure and room temperature. The concentration of the adsorbate was measured as function of time at the exit of the column. More details about the breakthrough experiment conditions are given in chapter 6.

### 3.14 Pressure drop

The pressure drop over a bed of packed structured porous adsorbents was measured between the inlet and the outlet of the adsorption column using the same system used for the breakthrough experiments and demonstrated in scheme 3.1. Details of these experiments are presented in chapter 6.



Scheme 3.1 Apparatus used for pressure drop and breakthrough experiments



# ***Chapter 4: Direct Synthesis of Hierarchical LTA Zeolite via a Low Crystallization and Growth Rate Technique in the Presence of Cetyltrimethylammonium Bromide (CTAB)***

## **4.1 Introduction**

The previous chapter highlighted the necessity of synthesizing hierarchical zeolites with multi modal pore size distribution in order to enhance their diffusivity and thus broaden the range of their applications. Many techniques have been investigated which resulted in very unique results<sup>22, 58, 71, 83</sup>. However, some disadvantages in implementation of these techniques reduce their applicability in industry. For instance, shrinkage during the removal of the template in the hard templating technique results in rupturing of the fabricated structure. Other techniques require multiple steps for synthesis or centrifugation for product collection and/or an autoclave for crystallization. The technique of interest in this thesis is a supramolecular templating technique because it can be conducted in one pot by direct addition of surfactant molecules into the synthesis mixture. Furthermore, many types of surfactants are cheap and commercially available which enhances the applicability of this technique in industry. However, the direct inclusion of a surfactant like CTAB into the zeolite system produces micropores and mesopores in one phase has been not reported yet. This is probably due to the weak interactions between the surfactant and large aluminosilicate building block species which results in repulsion of the surfactant micelles during the crystallization and growth of zeolites.

Recently, however, Choi *et al.* have successfully synthesized MFI and LTA zeolites containing micro- and mesopores in one phase by using the amphiphilic organosilane surfactant which has ability to interact strongly through covalent bonds with aluminosilicate species

because it contains methoxysilyl moiety<sup>54, 55</sup>. The disadvantage of this procedure is the surfactant is unavailable and expensive. In another study, the authors aged the zeolite gel for a sufficient time for zeolites nano seeds to be formed<sup>120</sup>. Then the gel was added to a pre-prepared surfactant solution followed by hydrothermal treatment. The zeolite seeds were assembled on the pre-formed micelle aggregates producing well-ordered mesoporous structures built of zeolite nanoclusters. However, no long range atomic order of crystalline zeolites was detected in the XRD pattern. This is probably due to the relatively small size of the assembled zeolite seeds, less than XRD detection limit. On the other hand, larger zeolite seeds cannot be assembled under the direction of the surfactant due to the weak charge density or the relatively small size of the micelles (2 – 4 nm).

The literature review (in chapter 2) also highlighted the influence of the high temperature on the micelles stability which is probably another reason that hinder the formation of mesoporous phase in zeolite structure in presence of the surfactant micelles. Beck *et al.* reported that at low temperatures, the formation of ordered aggregates of surfactant molecules is favorable while at high temperatures the preformed micelles decomposed and thus the surfactant molecules acted as single molecule structure-directing agents<sup>92</sup>. These findings suggest that a possible approach to produce hierarchical zeolite is low temperature crystallization of zeolites in the presence of surfactant micelles. Several successful attempts were published in which microporous zeolite-type materials were crystallized at room temperature<sup>16, 124-126</sup>.

This chapter discusses the synthesis of micro-mesoporous Na-A zeolite by direct addition of a commercially available surfactant (CTAB) into the synthesis mixture which then was aged at room temperature for 14 days before being crystallized at high temperature. The size of the mesopores was increased by adding alkane as a micellar expansion (swelling) agent to the synthesis mixture. Under such moderate conditions and a slowly developing system, we anticipate the swollen micelles will be retained and not expelled from the crystallization domain. The effects of the synthesis parameters on the pore size distribution were investigated: such as, the amount of the expansion agent, the length of the hydrocarbon chain of the alkanes, CTAB concentration, the aging step and the length of the aging period, simultaneous incorporation of two expanders in one system and two different calcination conditions. Moreover, the stability of the colloidal suspension and the hydrothermal stability of the synthesized materials were tested.

Finally, the chapter also includes the adsorption capability of the micro-mesoporous LTA zeolite of ethylene gas.

## 4.2 Experimental work

### 4.2.1 Materials

The chemicals used for the synthesis of mesoporous Na-A zeolite were: sodium silicate solution (~ 26.5 % SiO<sub>2</sub>, ~ 10.6 % Na<sub>2</sub>O, Sigma Aldrich), sodium aluminate (50 – 56 % Al<sub>2</sub>O<sub>3</sub>, 40 – 45 % Na<sub>2</sub>O, Sigma Aldrich), sodium hydroxide ( $\geq$  99 %, Merck), cetyltrimethylammonium bromide (CTAB-Ajax Finechem), *n*-dodecane (99 %, Merck), *n*-octane (99 %, Merck), *n*-hexane (97 %, Sigma Aldrich), 1,3,5-Trimethylbenzene (98%, Sigma Aldrich), and ethanol (< 0.002 % water, Sigma-Aldrich). All chemicals were used without any further purification.

### 4.2.2 Synthesis

The initial gel of Na-A zeolite was prepared according to the procedure reported in the literature <sup>139</sup>. A typical synthesis procedure started by dissolving 2 g of sodium hydroxide in 37.6 g of deionized water. Then one half of this alkaline solution was mixed with 3.9 g of sodium aluminate under stirring until a clear solution was obtained. The other half of the alkaline solution was mixed with 8.7 g of sodium silicate. The two solutions were mixed and stirred vigorously by a mechanical stirrer until the gel was homogenized. Then 1.04 g of the cationic surfactant CTAB was added to the initial gel under stirring. The molar composition of the final gel was 1.0Al<sub>2</sub>O<sub>3</sub>: 1.9SiO<sub>2</sub>: 3.2Na<sub>2</sub>O: 120H<sub>2</sub>O: 0.14CTAB. A calculated amount of the swelling agent (*i.e.* *n*-dodecane, or *n*-octane, or *n*-hexane) was then added drop by drop under stirring which continued for several minutes before the resultant homogenized gel was stored in a sealed polypropylene bottle and aged at room temperature for two weeks. Finally the gel was heated in an oven at 99 °C for 4 h. The product was collected by filtration, washed repeatedly with ethanol and water and then dried at 70 °C overnight. The surfactant was removed by calcination at 550 °C using a ramp rate of 2 °C/min in N<sub>2</sub> flow for 1 h and then in air flow for 4 h.

The final samples were denoted as MZ-0.14C-*x*D, where MZ represented the initial gel of the reactants, 0.14C indicated the molar ratio of CTAB, and *x* was the molar ratio of *n*-dodecane (D). For investigating the influence of the hydrocarbon chain length on the pore size distribution; *n*-

octane and *n*-hexane were used instead of *n*-dodecane and the samples were denoted as MZ-0.14C-1.1O and MZ-0.14C-1.1H, respectively.

Zeolite gel with composition of MZ-0.14C-1.1D was prepared and crystallized directly at 99 °C for 4 h without aging at room temperature. The aim of this experiment was to investigate whether mesoporous Na-A zeolite would be formed by only introducing CTAB and *n*-dodecane into the reaction mixture without room temperature aging. This sample was named ZA.

Furthermore, to investigate whether aging the Na-A zeolite gel without the inclusion of CTAB and *n*-dodecane would form the mesopores; conventional gel was prepared and aged at room temperature for two weeks prior being crystallized at 99 °C for 4 h. The product was collected by filtration under vacuum, washed frequently with water and dried at 70 °C overnight. The obtained zeolite was denoted as ZA-st in this work.

In addition to 14 days aging, two more aging periods were studied *viz*; 17 and 19 days. For this purpose, gel with molar composition 1.0Al<sub>2</sub>O<sub>3</sub>: 1.9SiO<sub>2</sub>: 3.2Na<sub>2</sub>O: 120H<sub>2</sub>O: 0.14CTAB: 8.5*n*-dodecane was used. The samples were named MZ-0.14C-8.2D-*t*, where *t* represented the number of days the gel was aged.

The influence of CTAB concentration on the pore size distribution was also investigated. The gel used for this purpose was 1.0Al<sub>2</sub>O<sub>3</sub>: 1.9SiO<sub>2</sub>: 3.2Na<sub>2</sub>O: 120H<sub>2</sub>O: *y* CTAB: 8.5*n*-dodecane, where *y* was 0.07, 0.14 and 0.21. The samples were named MZ-0.07-8.2D, MZ-0.14C-8.2D and MZ-0.21C-8.2D.

For comparison purposes, conventional Na-A zeolite was prepared according to the procedure reported in the literature<sup>139</sup>. The prepared sample was named CZA in this work.

All prepared samples with their gels compositions are listed in Table 4.1

**Table 4.1 List of samples and their gel compositions**

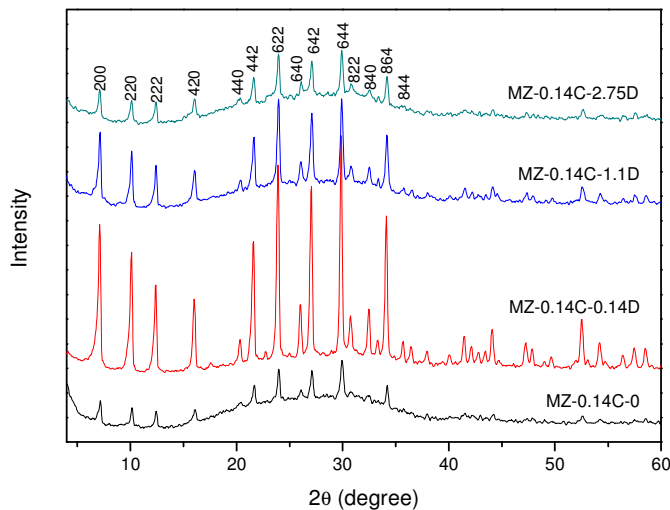
Sample name	Type of swelling agent	Al <sub>2</sub> O <sub>3</sub> : SiO <sub>2</sub> : Na <sub>2</sub> O: H <sub>2</sub> O (mole)	CTAB (mole)	Swelling agent (mole)	Aging (days)
MZ-0.14C-0 <sup>a</sup>	–	1.0: 1.9: 3.2: 120	0.14	–	14
MZ-0.14C-0.14D <sup>b</sup>	<i>n</i> -Dodecane	1.0: 1.9: 3.2: 120	0.14	0.14	14
MZ-0.14C-1.1D <sup>b</sup>	<i>n</i> -Dodecane	1.0: 1.9: 3.2: 120	0.14	1.1	14
MZ-0.14C-2.75D <sup>b</sup>	<i>n</i> -Dodecane	1.0: 1.9: 3.2: 120	0.14	2.75	14
MZ-0.14C-1.1H <sup>c</sup>	<i>n</i> -Hexane	1.0: 1.9: 3.2: 120	0.14	1.1	14
MZ-0.14C-1.1O <sup>c</sup>	<i>n</i> -Octane	1.0: 1.9: 3.2: 120	0.14	1.1	14
MZ-0.14C-8.5D-14 <sup>d,j</sup>	<i>n</i> -Dodecane	1.0: 1.9: 3.2: 120	0.14	8.5	14
MZ-0.14C-8.5D-17 <sup>d</sup>	<i>n</i> -Dodecane	1.0: 1.9: 3.2: 120	0.14	8.5	17
MZ-0.14C-8.5D-19 <sup>d</sup>	<i>n</i> -Dodecane	1.0: 1.9: 3.2: 120	0.14	8.5	19
MZ-0.07C-8.5D <sup>e</sup>	<i>n</i> -Dodecane	1.0: 1.9: 3.2: 120	0.07	8.5	14
MZ-0.21C-8.5D <sup>e</sup>	<i>n</i> -Dodecane	1.0: 1.9: 3.2: 120	0.21	8.5	14
ZANa (0.3C-0.3D) <sup>f</sup>	<i>n</i> -Dodecane	1.0: 1.9: 3.2: 120	0.3	0.3	14
ZACa (0.3C-0.3D) <sup>f</sup>	<i>n</i> -Dodecane	1.0: 1.9: 3.2: 120	0.3	0.3	14
CZA <sup>g</sup>	–	1.0: 1.9: 3.2: 120	–	–	–
ZA-st <sup>h</sup>	–	1.0: 1.9: 3.2: 120	–	–	14
ZA <sup>i</sup>	<i>n</i> -Dodecane	1.0: 1.9: 3.2: 120	0.14	1.1	–

<sup>a</sup> Sample synthesized with CTAB only . <sup>b</sup> Samples synthesized with different *n*-dodecane concentration. <sup>c</sup> Samples synthesized using *n*-Hexane or *n*-Octane as a swelling agent. <sup>d</sup> Samples synthesized with different aging periods. <sup>e</sup> Samples synthesized from gel containing different CTAB concentrations. <sup>f</sup> Conventional NaA zeolite synthesized following literature method <sup>139</sup>. <sup>g</sup> Sample synthesized from gel with composition similar to conventional zeolite, but crystallized after 14 days room temperature ageing. <sup>h</sup> Sample has final composition similar to sample MZ-0.14C-1.1D, but crystallized at elevated without aging at room temperature. <sup>i</sup> This sample (MZ-0.14C-8.5D-14) is also named as MZ-0.14C-8.5D in the text.

## 4.3 Results and discussion

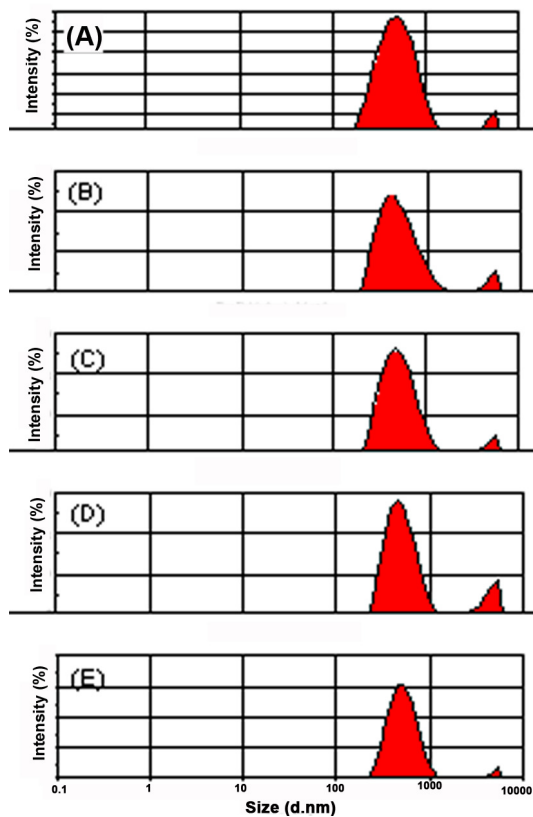
### 4.3.1 Influence of direct addition of CTAB or CTAB with different concentrations of swelling agent to Na-A zeolite gel

Figure 4.1 shows the wide angle XRD patterns of Na-A zeolites synthesized with CTAB and different molar ratios of *n*-dodecane ( $x = 0, 0.14, 1.1, 2.75$ ) as a swelling agent. All the samples exhibited diffraction peaks that match the characteristics of LTA zeolite as compared to the standard crystal data published by International Zeolite Association of the face-centred cubic (*fcc*) unit cell with  $a = 24.61 \text{ \AA}$ <sup>140</sup>.



**Figure 4.1** XRD patterns of Na-A zeolites synthesized with different molar ratios of *n*-dodecane as micellar swelling agent.

The sample prepared without swelling agent (MZ-0.14C-0) showed broad diffraction peaks and relatively high proportion of amorphous phase, suggesting partial transformation of the gel into zeolite. Figure 4.1 indicates that the addition of *n*-dodecane with equal molar ratio to CTAB in the sample MZ-0.14C-0.14D enhanced the crystallinity of the produced Na-A zeolite. However, the crystallinity decreased gradually with increasing the *n*-dodecane concentration as shown in XRD patterns for the samples MZ-0.14C-1.1D and MZ-0.14C-2.75D.



**Figure 4.2 Particle size distribution (PDS) curves obtained from DLS for MZ-0.14C-0 (A), MZ-0.14C-0.14D (B), MZ-0.14C-1.1D (C), MZ-0.14C-2.75D (D) and ZA-st (E).**

The average diameter of particles of MZ-0.14C-0, MZ-0.14C-0.14D, MZ-0.14C-1.1D and MZ-0.14C-2.75D were 492, 511, 520 and 595 nm; respectively. On the other hand, the sample named ZA-st, synthesized from conventional gel of LTA zeolite that was aged for 14 days at room temperature before being crystallized at high temperature, shows an average particle diameter of 569 nm (Table 4.2). The DLS measurements show high polydispersity index (PDI) in the range 0.25 – 0.3 suggesting multimodal particle size distribution. This can also be deduced from the PDS curve of each sample (Figure 4.2) which shows a broad peak extending from ~ 200 to ~ 1000 nm.

Figure 4.3 A-D and inset show the SEM images of the zeolite samples synthesized using only CTAB or CTAB with various amounts of *n*-dodecane in the synthesis composition. These images show some particles with cubic morphology and others which consist of closely aggregated nanoparticles forming irregular spherical aggregates.

**Table 4.2 Particle diameter as determined by SEM and DLS for the synthesized mesoporous and reference zeolites.**

Sample	Average diameter / SEM (nm)		Mean diameter/ DLS (nm)
	Aggregates	Cubes	
MZ-0.14C-0	200±25 – 375±25	200±2 – 375±25	492
MZ-0.14C-0.14D	125±25 – 250±25	200 – 570	511
MZ-0.14C-1.1D	125±25 – 250±25	200 – 570	520
MZ-0.14C-2.75D	300±25 – 600±50	300±25–600±50	595
ZA-st	-	250 – 850	569
CZA	-	6000	-

In general these spherical aggregates exhibit smaller size compared to the particles with cubic habit, except for the samples MZ-0.14C-0 and MZ-0.14C-2.75D, where both types of particles lie in a similar size range, which is between  $200 \pm 25$  to  $375 \pm 25$  nm for the former and between  $300 \pm 25$  to  $600 \pm 50$  nm for the latter. Also the SEM results for these two samples show that the major proportion of the particles are spherical aggregations and few cube-like particles. For MZ-0.14C-0.14D and MZ-0.14C-1.1D, the aggregates size ranges from  $125 \pm 25$  to  $250 \pm 25$  nm and the size of the cube-like particles ranges from 200 to about 570 nm. Generally the nanoparticles within the aggregates are about 15 – 20 nm in size except for a few of size about 40 – 50 nm (confirmed later by TEM).

In general, the average particle diameter obtained from the DLS for every sample, except MZ-0.14C-0, lie within the range of the particle size distribution determined by the SEM (Table 4.2). The SEM investigation (Figure 4.3B-D) also shows that crystalline islands were developed on the surface of some of the polycrystalline aggregates suggesting that surface recrystallization had probably taken place <sup>19, 141</sup>.

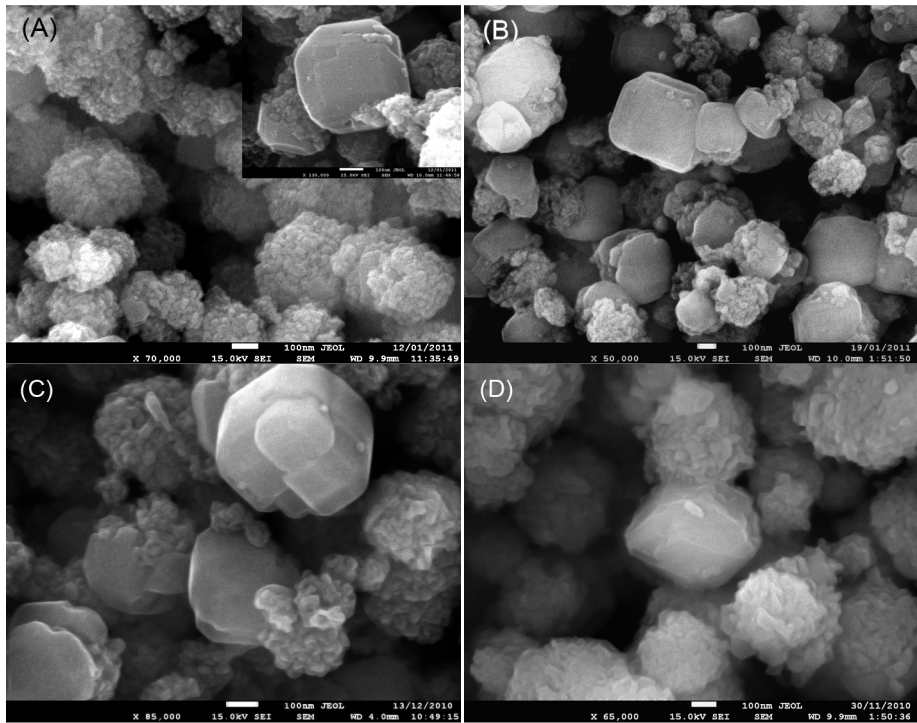


**Figure 4.3 SEM images of MZ-0.14C-0 (A and inset), MZ-0.14C-0.14D (B), MZ-0.14C-1.1D (C) and MZ-0.14C-2.75D (D).** The scale of images A-D and insets is 100 nm.

The SEM image of ZA-st shows that the sample consists of cubic crystals in size range from 250 to 850 nm (Figure 4.4A). On the other hand, cubic crystals with size around 3 – 6  $\mu\text{m}$  can be observed in the SEM images of samples ZA (Figure 4.4B) and CZA (Figure 4.4C). The small size of Na-A zeolite crystals in ZA-st compared to ZA and CZA is attributed to the room temperature aging, as the role of room temperature aging in enhancing the number of the nuclei and thus reducing the crystals size has been reported<sup>17, 142</sup>. According to SEM investigations, the nanoparticle aggregates were absent in the samples named ZA, ZA-st and CZA.

The XRD and SEM findings indicate that aging the synthesis mixture without introducing CTAB and *n*-dodecane produces cubes of zeolite Na-A with submicron size (sample ZA-st). Further, the Na-A zeolite synthesized from a mixture included CTAB and *n*-dodecane and then crystallized directly without aging contains cubes in micron-scale size (ZA). The absence of the nanoparticle aggregates in the ZA-st and ZA suggests that both factors, aging and CTAB and *n*-dodecane addition, induced the formation of the nanoparticle aggregates of Na-A zeolite.

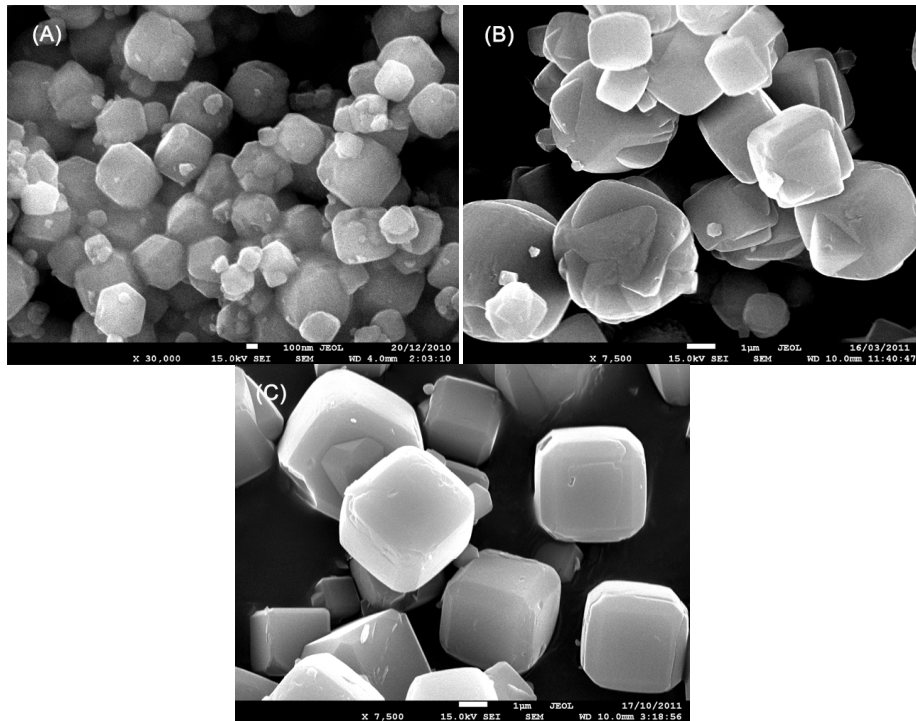


**Figure 4.4 SEM images of ZA-st (A), ZA (B) and CZA (C). The scale of images A is 100 nm, while of image B and C is 1 $\mu$ m.**

It is well known that conventional Na-A zeolite does not adsorb N<sub>2</sub> at 77 K due to pore blockage by Na<sup>+</sup> cations in the unit cell structure. These Na<sup>+</sup> cations occupy positions close to the pore apertures reducing their size from 4.4 Å to less than 3.1 Å and thus prohibiting the admission of nitrogen molecules (kinetic radius ~ 3.4 Å) into the super-cages <sup>29, 142</sup>. Accordingly the low surface area presented in Table 4.3 is not an indication of the presence of amorphous phase but because it only represents the mesopore area. The adsorption-desorption isotherms of ZA-st in Figure 4.5A shows very little adsorption which can be attributed to adsorption of the N<sub>2</sub> molecules on the external surface of the crystals. In contrast, the isotherms of Na-A zeolites synthesized from gels that contained a constant amount of CTAB but varying amount of *n*-dodecane; MZ-0.14C-0, MZ-0.14C-0.14D, MZ-0.14C-1.1D and MZ-0.14C-2.75D, show a steep increase in the adsorption amount over the relative pressure range between 0.6 – 0.99 which is attributed to capillary condensation of N<sub>2</sub> within the mesopores (Figure 4.5B-E). The isotherms for these samples are of type IV with H3 hysteresis, without a plateau at high relative pressure (close to unity) which suggests that the products are comprised of aggregated crystallites <sup>64, 143</sup>. The highest mesopore volume recorded was 0.27 cm<sup>3</sup>·g<sup>-1</sup> (Table 4.3) which was obtained when

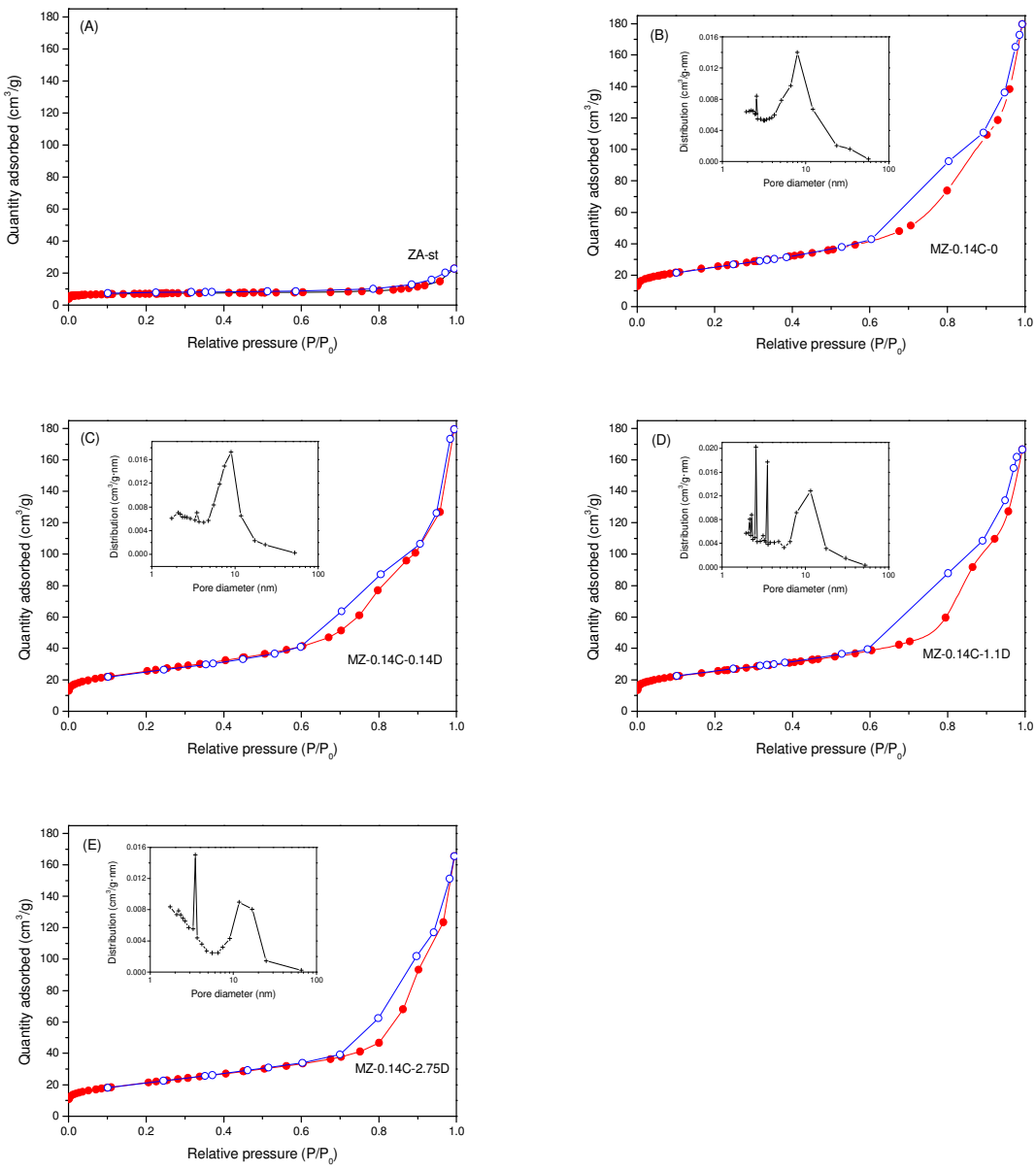


**Figure 4.5**  $\text{N}_2$  adsorption-desorption isotherms at 77 K of ZA-st (A), MZ-0.14C-0 (B), MZ-0.14C-0.14D (C), MZ-0.14C-1.1D (D) and MZ-0.14C-2.75D (E). The inset with each plot is the corresponding BJH mesopore size distribution obtained from the adsorption branch.

CTAB was introduced into the reaction gel (sample MZ-0.14C-0) and when CTAB: *n*-dodecane molar ratio is 1:1 (sample MZ-0.14C-0.14D). To the best of our knowledge, synthesizing mesoporous zeolites by direct addition of CTAB to the reaction gel has not been achieved to date. The mesopore volume decreased slightly to about  $0.25 \text{ cm}^3 \cdot \text{g}^{-1}$  with increasing the *n*-dodecane molar ratio to 1.1 and 2.75. Table 4.3 and the insets in Figure 4.5B-E show two mesopore size distributions; small mesopores in the range 1.9 – 3.5 nm and large mesopores in

the range 7.9 – 13 nm. The influence of *n*-dodecane molar ratio is more pronounced in the large mesopore domain, as BJH pore size distribution show narrow peaks centered on 7.9, 9.0, 11.5 and 13.0 nm for samples with 0, 0.14, 1.1 and 2.75 *n*-dodecane molar ratios, respectively.

**Table 4.3 Textural properties for the samples synthesized in the work**

Sample	$S_{\text{BET}}$ ( $\text{m}^2 \cdot \text{g}^{-1}$ ) <sup>a</sup>	$V_{\text{meso}}$ <sup>b</sup> ( $\text{cm}^3 \cdot \text{g}^{-1}$ )	$d_{\text{meso}}$ <sup>c</sup> (nm)
MZ-0.14C-0	89	0.27	2.5 , 7.9
MZ-0.14C-0.14D	89	0.27	2.0 , 3.5 , 9.0
MZ-0.14C-1.1D	87	0.25	2.1, 2.2, 2.5 , 3.5 , 11.5
MZ-0.14C-2.75D	75	0.25	3.5 , 13.0
MZ-0.14C-1.1H	73	0.21	2.5, 3.5, ~9.0
MZ-0.14C-1.1O	58	0.20	2.0, 11.7
MZ-0.14C-8.5D-14 <sup>d</sup>	76	0.17	2 – 4, ~9.1
MZ-0.14C-8.5D-17	41	0.17	2 – 4, 6.9, 13
MZ-0.14C-8.5D-19	28	0.08	3.3, 4.3, 7.2
MZ-0.07C-8.5D	54	0.19	2.7, 3.7, 9.5
MZ-0.21C-8.5D	62	0.16	1.8, 2.1, 13.4
CZA	-	-	-
ZA-st	22	-	-

<sup>a</sup> Surface area obtained at relative pressure range of 0.05 – 0.3. <sup>b</sup> Mesopore volume was collected on pore size range between about 1.7 to 50 nm. <sup>c</sup> Mesopore size distribution was measured by BJH adsorption  $dV/dD$  pore volume. <sup>d</sup> This sample (MZ-0.14C-8.5D-14) was also named as MZ-0.14C-8.5D in the text.

In general, a progressive increase in the mesopore size could be detected with increasing the amount of *n*-dodecane in the synthesis gel. In contrast, no N<sub>2</sub> adsorption was measured on ZA which was synthesized from the gel contained 0.14C: 1.1D molar ratio and crystallized directly without aging at room temperature (results not provided). The results obtained from N<sub>2</sub> adsorption-desorption analysis, in agreement with the SEM, reveal that the presence of CTAB micelles in the synthsis gel is not effective in terms of forming the mesoporous Na-A zeolite without the aging at room temeprature and vice versa.

Figure 4.6A-1 and the inset display TEM images of MZ-0.14C-0 at high and low magnification respectively, which exhibits relative uniform nanoparticles with size of 15 – 25 nm (marked with black arrows in A-1) agglomerated to form spherical aggregates with average overall size around 300 nm.

The images also show the mesopores which are represented by the interstitial voids (marked with white arrows in A-1) between the aggregated nanoparticles. On the other hand, the TEM investigations of the samples MZ-0.14C-0.14D, MZ-0.14C-1.1D and MZ-0.14C-2.75D show the three types of particles: single cubic particles, spherical aggregates and also show some aggregates which are partially transforming into cubes (Figure 4.6 images B-1, C-1 and D-1).

In agreement with the SEM results, the TEM images indicate that the spherical aggregates comprise of 15 – 20 nm sized particles that are closely compacted confining mesoscopic voids which represent the mesopores. The SAED patterns shown in the insets in the images (Figure 4.6B-1 and D-1) confirm the crystallinity observed by the XRD patterns for MZ-0.14C-0.14D and MZ-0.14C-2.75D.

The TEM findings support the XRD, SEM and N<sub>2</sub>-adsorption-desorption analysis indicating that the products are mesoporous materials with three types of particles, cubes, nanoparticle aggregates, and aggregates which are partially transforming into cubes. Further, the mesoporosity is represented by the voids confined between the compacted nanoparticles in the aggregates. However, all the above results do not provide direct evidence whether the aggregated nanoparticles are pure zeolite A or other mesoporous phase was formed. Therefore, the lattice fringes of 15 – 20 nm crystallites within the nanoparticle aggregates were observed by high magnification TEM. Figures 4.6A-2, B-2, C-2 and D-2 show the lattice fringes resolved on the nanoparticles of samples MZ-0.14C-0, MZ-0.14C-0.14D, MZ-0.14C-1.1D and MZ-0.14C-2.75D, respectively. These images show single oriented lattice fringes, indicating that these nanoparticles are zeolite A crystallites, which started forming from a single nucleus in one isolated amorphous gel particle<sup>125</sup>. The lattice fringes in image 4.6A-2 for sample MZ-0.14C-0 corresponds to d-spacing 8.5 which matches with the (220) plane in LTA zeolite structure. Similarly for the other samples, their lattice fringes (shown in images 4.6B-2, C-2 and D-2) correspond to d-spacing 8.1, 12.0, and 3.7 Å and match well with the (220), (200) and (622)

planes in LTA zeolite structure, respectively. These results reveal that the nanoparticles within the mesoporous aggregates are Na-A zeolite crystallites.

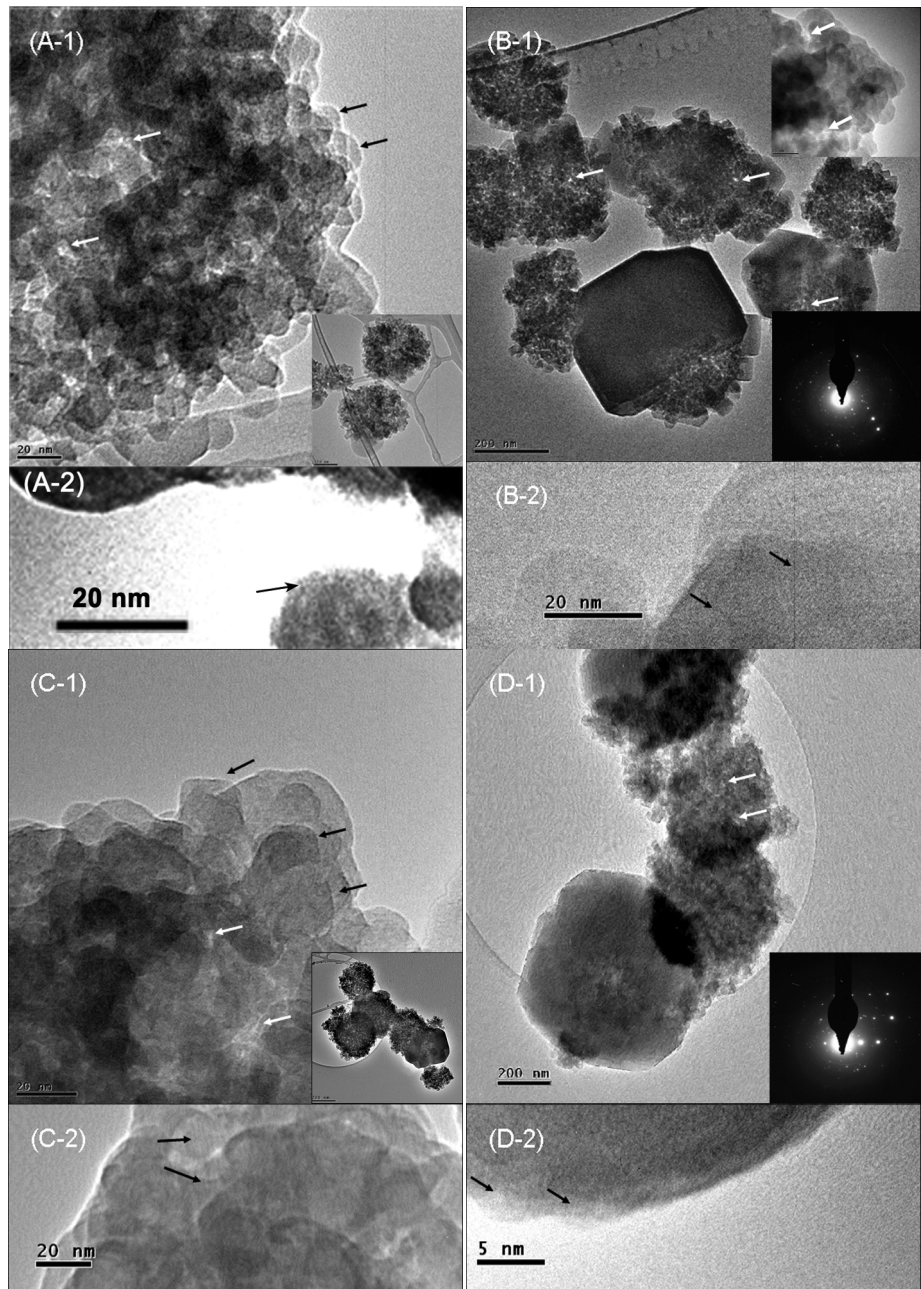


**Figure 4.6** High and low magnification images of MZ-0.14C-0 (A-1, A-2), MZ-0.14C-0.14D (B-1, B-2), MZ-0.14C-1.1D (C-1, C-2) and MZ-0.14C-2.75D (D-1, D-2). The insets on the bottom right corner in images B-1 and D-1 are the corresponding SAED patterns. The white arrows in images A-1, B-1, C-1 and D-1 mark the intercrystalline mesopores. The black arrows A-2, B-2, C-2 and D-2 show the lattice fringes.

To further confirm that the produced mesoporous material is a pure phase of LTA zeolite,  $^{29}\text{Si}$  NMR spectra were obtained. In Figure 4.7, the  $^{29}\text{Si}$  NMR spectrum of ZA-st shows a single resonance signal centered at  $\delta = -89.2$  ppm which is assigned to Si (4Al). Also a low intensity shoulder appeared at  $\delta = -94.5$  ppm which is attributed to coexistence of Si (3Al). These results indicate that the sample contains a less ordered region in which  $\text{SiO}_4$  tetrahedra are linked to three Al and one Si. This behavior is consistent with studies conducted by Lippmaa *et al.* and Melchior *et al.* on zeolite <sup>144, 145</sup>.

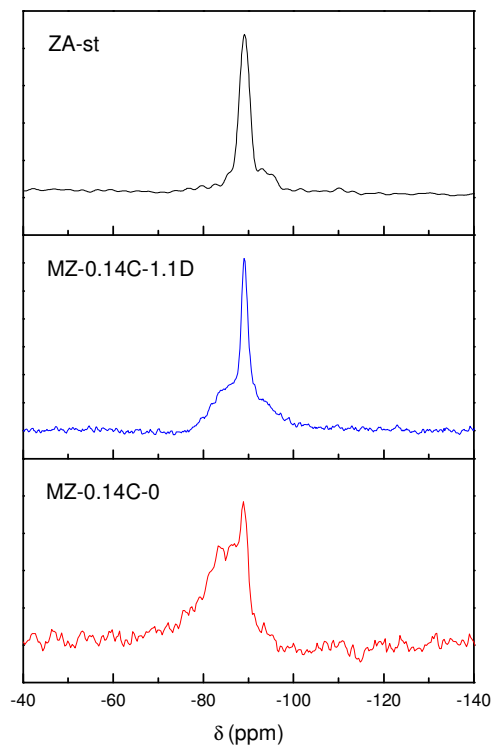


**Figure 4.7**  $^{29}\text{Si}$  NMR spectra of the samples; ZA-st, MZ-0.14C1.1D and MZ-0.14C-0.

The  $^{29}\text{Si}$  NMR spectra for the MZ-0.14C-0 and MZ-0.14C-1.1D samples indicate the presence of different environment in the lattice of the synthesized mesoporous Na-A zeolites (Figure 4.7). The spectrum of the sample MZ-0.14C-0 synthesized with only CTAB is broad and shows extra resonances at  $\delta = -83.3$  and  $-86.9$  ppm in addition to the Si(4Al) peak which is also shifted down to  $-88.8$  ppm rather than  $-89.5$  ppm. On the other hand, the sample MZ-0.14C-1.1D shows sharp resonance at  $\delta = -89.0$  ppm and also a wide region which extends from  $\delta = -78$  to  $-105$  ppm.

86 ppm, but with very low intensity. Similar resonances were observed by Greere *et al.* in  $^{29}\text{Si}$  NMR spectra of zeolite A and they attributed them to lower polymerized Si species <sup>19</sup>. These results show the absence of any other phase except pure LTA type zeolite in the synthesized samples.

Furthermore, SEM-EDX was used to measure the concentration of Si, Al, Na and O on the surface of the nanoparticle aggregates in sample MZ-0.14C-0.14D and also the concentration of these elements on the surface of cubic particles in the same sample (Table 4.4). The results show consistency in the concentration of all elements in both types of particles suggesting that both, the cubic particles and the nanoparticles, are comprised of the same material.

**Table 4.4 The elemental analyses of samples MZ-0.14C-0.14D and conventional zeolite A (CZA)**

Sample	Si % mole	Al % mole	Na % mole	O % mole
MZ-0.14C-0.14D (nanoparticle aggregates)	16.52	14.97	8.66	59.84
MZ-0.14C-0.14D (cubes)	16.70	14.80	8.57	59.91
CZA	14.86	13.60	13.67	57.51

A complementary IR study was performed on standard microporous Na-A zeolite (ZA-st) and mesoporous Na-A zeolites synthesized in the presence of CTAB only as well as CTAB with various amounts of *n*-dodecane. The absorption bands were assigned on the basis of previous studies <sup>146, 147</sup>. All IR spectra show bands at around 464, 560, 670, and 1000 cm<sup>-1</sup> (Figure 4.8). The absorption bands centered at 1000 and 670 cm<sup>-1</sup> are assigned to the internal vibration of Al-O and Si-O asymmetric and symmetric stretching, respectively <sup>146, 147</sup>. The corresponding internal bending of Al-O and Si-O bonds is represented by the bands centered at 464 cm<sup>-1</sup>. Moreover, the characteristic of Na-A zeolite structure is represented by the absorption band at 560 cm<sup>-1</sup> which is attributed to the external vibration of the tetrahedron of the secondary building units (4DR).

The results obtained from high magnification TEM,  $^{29}\text{Si}$  NMR, SEM-EDX and FTIR reveal that the produced mesoporous material consists of one phase which is a pure Na-A zeolite with

Si/Al ratio =1.1. The results also show that concentrations of the elements (Al, Si O and Na) in the cubic particles are exactly similar to the concentrations of the elements in the nanoparticles within the aggregates (Table 4.4). However, the number of  $\text{Na}^+$  cations in the structure of MZ-0.14C-0.14D is less than in CZA. The reason is probably the early involvement of CTAB molecules in zeolite gel which then was aged to evolve slowly, some of the  $\text{Na}^+$  cations were probably superseded by the cationic ammonium group from the CTAB molecules. Then during calcination, ammonium groups were decomposed totally leaving Na-A zeolite crystals with less number of  $\text{Na}^+$  cations.

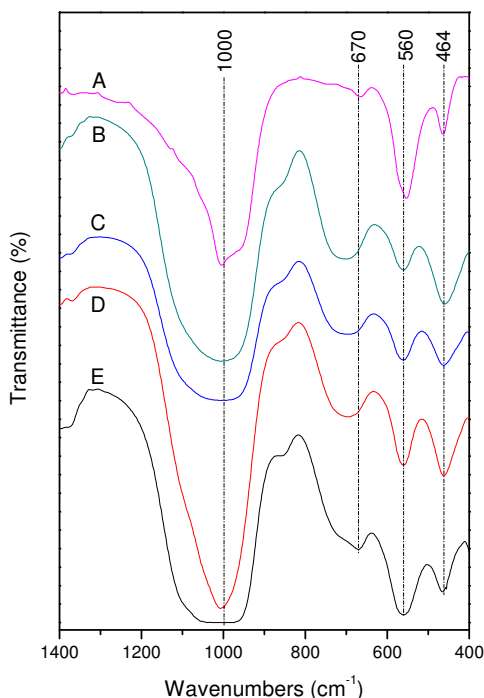


**Figure 4.8** FTIR spectra of ZA-st (A), MZ-0.14C-0 (B), MZ-0.14C-0.14D (C), MZ-0.14C-1.1D (D) and MZ-0.14C-2.75D (E).

#### 4.3.2 Influence of chain length of the swelling agent on the mesopore size distribution

Other alkanes with different hydrocarbon chain length were introduced into the Na-A zeolite – CTAB system to examine the influence of the chain length on the micelle expansion. Figure

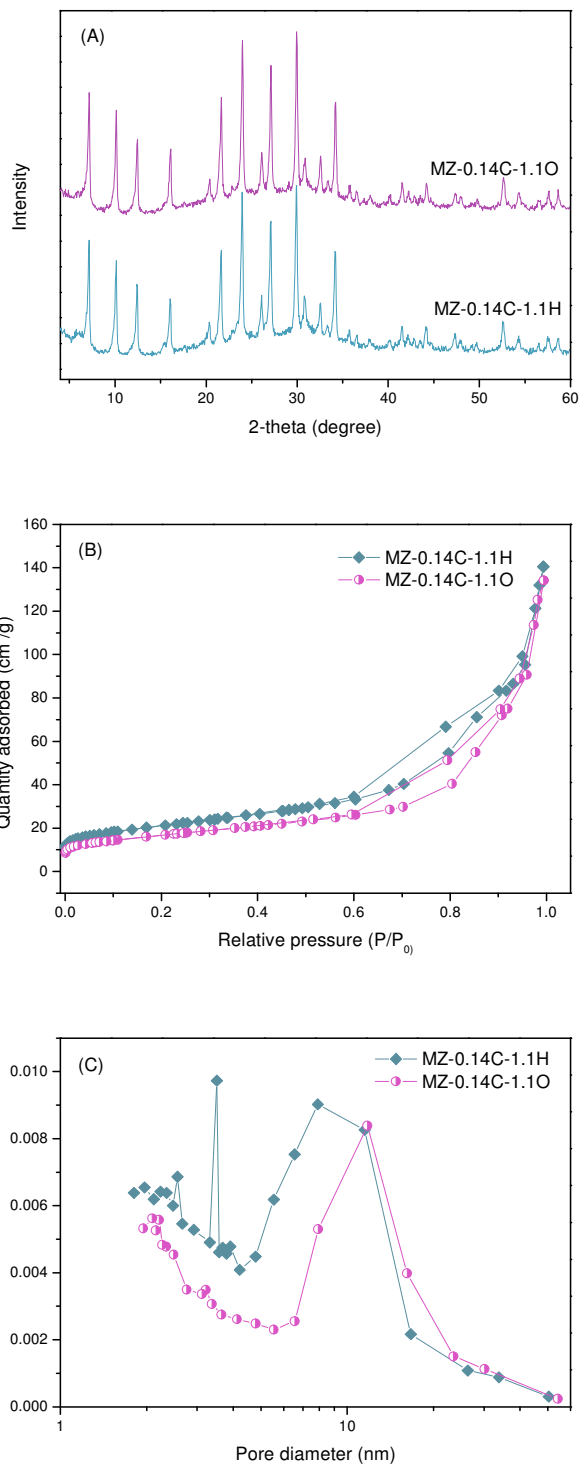


**Figure 4.9** PXRD patterns (A),  $N_2$  adsorption-desorption isotherms (B), and BJH pore size distribution (C) of the mesoporous Na-A zeolites synthesized with *n*-hexane (MZ-0.14C-1.1H) and *n*-octane (MZ-0.14C-1.1O).

4.9 and Table 4.3 show the results obtained from the XRD and N<sub>2</sub> adsorption-desorption at 77 K for the mesoporous Na-A zeolites synthesized by using *n*-hexane (MZ-0.14C-1.1H) and *n*-octane (MZ-0.14C-1.1O). The x-ray patterns indicate that the LTA framework structure was retained with changing the swelling agent (Figure 4.9A). The pore size distribution of MZ-0.14C-1.1H shows wide peaks centered at about 9.0 nm, while MZ-0.14C-1.1O shows a sharp peak centered at 11.7 nm (Figure 4.9C). Both samples contained mesopores larger than 7.9 nm which were obtained when only CTAB was used in the system (sample MZ-0.14C-0 in Figure 4.5). These results reveal that the molecules of the alkanes can be permeated into the core of CTAB micelles increasing their sizes. However, *n*-octane and *n*-dodecane show similar influence on the micelles size, as introducing either of them at 1.1: 0.14CTAB molar ratio into Na-A zeolite gel generated mesopores with diameter of 11.5 - 11.7 nm (discussed in detail in section 4.4 below).

### ***4.3.3 Influence of aging period on the mesopore size distribution***

As described in section 4.3.1, introducing the CTAB and *n*-dodecane into the gel was not effective in terms of forming the mesoporous Na-A zeolite without the room temperature aging. Therefore, it became crucial to investigate the effect of the aging period on the mesopore size distribution. Figure 4.10A shows the XRD patterns of MZ-0.14C-8.2D-14, MZ-0.14C-8.2D-17 and MZ-0.14C-8.2D-19 which were aged for 14, 17 and 19 days; respectively. The diffraction peaks of all patterns match the peaks that are identified as characteristics of LTA zeolite framework structure indicating that all samples are well crystalline Na-A zeolite<sup>140</sup>. However, the diffraction peaks recorded for MZ-0.14C-8.2D-14 show lower intensities than the peaks in the patterns of MZ-0.14C-8.2D-17 and MZ-0.14C-8.2D-19 suggesting a significant increase in the crystals size. The results obtained from N<sub>2</sub> adsorption-desorption analysis indicate that prolonging the aging period resulted in decrease in surface area (Table 4.3). The BET surface area measured for samples MZ-0.14C-8.2D-14, MZ-0.14C-8.2D-17 and MZ-0.14C-8.2D-19 were 76 m<sup>2</sup>.g<sup>-1</sup>, 41 and 28 m<sup>2</sup>.g<sup>-1</sup>; respectively. The isotherm of MZ-0.14C-8.2D-14 shown in Figure 4.10B is type IV with H3 hysteresis indicating that the sample is a mesoporous zeolite. However, the N<sub>2</sub> adsorption at high relative pressure (P/P<sub>0</sub> = 0.6 – 0.99) decreases gradually with increasing the aging period until almost a flattened isotherm type I which is typical of microporous material was obtained for the sample aged for 19 days (MZ-0.14C-8.2D-19).

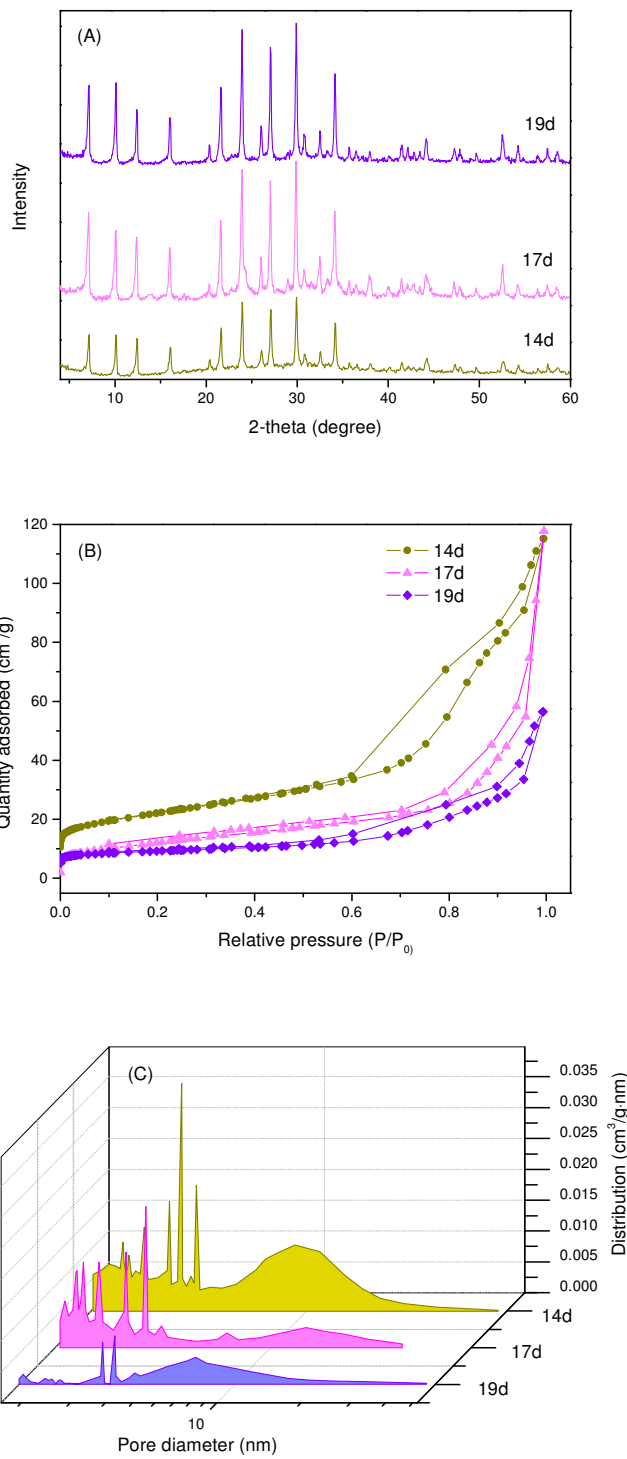


**Figure 4.10** PXRD patterns (A), N<sub>2</sub> adsorption-desorption isotherms (B), and BJH pore size distribution (C) of MZ-0.14C-8.2D-14, MZ-0.14C-8.2D-17 and MZ-0.14C-8.2D-19.

In Figure 4.10C, the pore size distribution of MZ-0.14C-8.2D-14 exhibits two scales of mesopores: small mesopores demonstrated by several peaks in the range 2 – 4 nm, and large scale mesopores represented by a broad peak extended between 5 and 15 nm but centered at 9.1 nm. Then with extending the aging period, a gradual decrease in the two types of the mesopores can be observed clearly in Figure 4.10C. The mesopores volume measured for MZ-0.14C-8.2D-14 and MZ-0.14C-8.2D-17 was  $0.17 \text{ cm}^3 \cdot \text{g}^{-1}$ , but it decreased dramatically to  $0.08 \text{ cm}^3 \cdot \text{g}^{-1}$  for MZ-0.14C-8.2D-19 (Table 4.3).

In summary, the results suggest that the LTA framework structure was retained in the synthesized samples with increasing the aging period, however, a local structural evolution probably occurred resulting in decrease in the mesoporous phase in the samples.

#### ***4.3.4 Influence of CTAB concentration on the mesopore size distribution***

The XRD pattern of the sample synthesized with low CTAB concentration (MZ-0.07C-8.2D) shows high intensity peaks that correspond to the LTA zeolite framework structure (Figure 4.11A). In contrast, the pattern of the sample synthesized with high CTAB ratio (MZ-0.21C-8.2D) shows a relatively high proportion of amorphous phase, suggesting partial transformation of the gel into LTA zeolite. However, extra peak at  $2\theta \sim 6^\circ$  appeared in the pattern indicating that another phase, most probably faujasite, was co-crystallizing with the Na-A zeolite<sup>140</sup>.

As described in section 4.3.3, sample MZ-0.14C-8.2D (MZ-0.14C-8.2D-14) is a mesoporous Na-A zeolite. The mesoporosity was retained with decreasing the CTAB ratio to 0.07 or increasing it to 0.21 (Figure 4.11B and C). The BET surface area and mesopores volume of MZ-0.14C-8.2D, MZ-0.07C-8.2D and MZ-0.21C-8.2D are  $76$ ,  $54$  and  $62 \text{ m}^2 \cdot \text{g}^{-1}$  and  $0.17$ ,  $0.19$  and  $0.16 \text{ cm}^3 \cdot \text{g}^{-1}$ ; respectively (Table 4.3). These results suggest that the highest mesopore pore volume was obtained with less CTAB concentration.

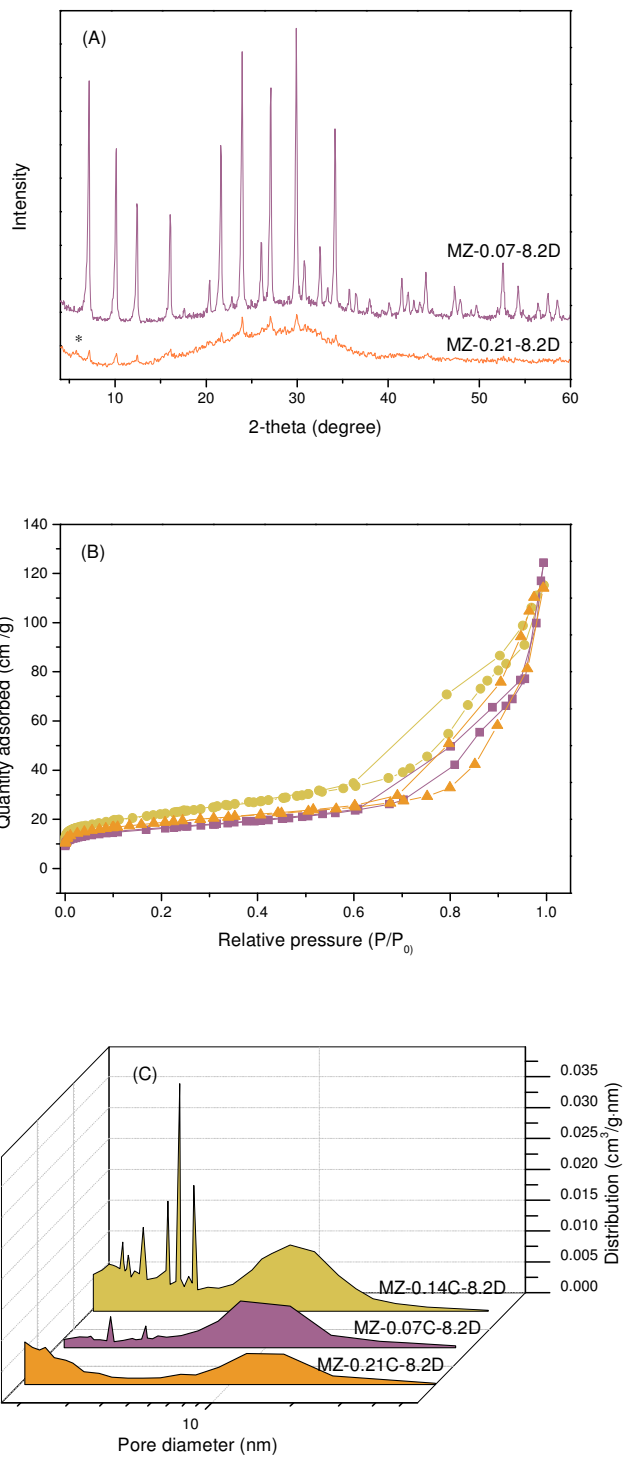


**Figure 4.11** PXRD patterns (A), N<sub>2</sub> adsorption-desorption isotherms (B), and BJH pore size distribution (C) of MZ-0.14C-8.2D, MZ-0.07C-8.2D and MZ-0.21C-8.2D

#### **4.3.5 Influence of the addition of two organic expanders to the zeolite / CTAB gel**

This section discusses the influence of incorporating an additional swelling agent to *n*-dodecane on the pore size distribution. The auxiliary swelling agent used was 1,3,5-timethylbenzene (TMB) which has been extensively used as a micellar expander to synthesize materials with large pores<sup>148</sup>.

The effect of the addition of TMB on the pore size distribution was investigated on samples with composition similar to sample MZ-0.14C.1.1D. Typically, the molar composition of the gel was 1.0Al<sub>2</sub>O<sub>3</sub>: 1.9SiO<sub>2</sub>: 3.2Na<sub>2</sub>O: 120H<sub>2</sub>O: 0.14CTAB: 1.1*n*-Dodecane: *y* TMB; where *y* was the amount in moles of TMB. The samples were named as MZ-0.14C-1.1D-*y*T, where T represents TMB. In addition to MZ-0.14C.1.1D, which was studied in detail in section 4.3.1, four other different 1.1D: *y*T molar ratios were investigated: 1.1:0.73, 1.1:1.1, 1.1:2.2 and 0:2.2. The synthesis method was exactly similar to the procedure described in the experimental section (section 4.2.2) which was followed to synthesize the other samples. In all experiment, the introduction of TMB was after the drop wise addition of *n*-dodecane and the crystallization at high temperature after the 14 days aging was for 6 to 8 h at 99°C. Samples details are listed in Table 4.5.

**Table 4.5 Experimental details of the samples synthesized to investigate the effects of incorporating two expander agents to zeolite/CTAB gel.**

Sample name	Al <sub>2</sub> O <sub>3</sub> : SiO <sub>2</sub> : Na <sub>2</sub> O: H <sub>2</sub> O (mole)	CTAB (mole)	<i>n</i> -dodecane (mole)	TMB (mole)	Ageing (days)
MZ-0.14C-1.1D-0.73T	1.0: 1.9: 3.2: 120	0.14	1.1	0.75	14
MZ-0.14C-1.1D-1.1T	1.0: 1.9: 3.2: 120	0.14	1.1	1.1	14
MZ-0.14C-1.1D-2.2T	1.0: 1.9: 3.2: 120	0.14	1.1	2.2	14
MZ-0.14C-2.2T	1.0: 1.9: 3.2: 120	0.14	—	2.2	14
MZ-0.14C-1.1D <sup>a</sup>	1.0: 1.9: 3.2: 120	0.14	1.1	—	14

<sup>a</sup> This sample has been characterized in section 4.3.1

The XRD patterns (Figure 4.12) indicate that all samples are well crystalline LTA zeolite. However, the crystallinity changes according to the concentration of TMB in the gel<sup>140</sup>. The comparison between the XRD patterns of MZ-0.14C-1.1D and MZ-0.14C-1.1D-0.73T suggests that introducing a small amount of TMB to the gel enhances the crystallinity of the product. This can be inferred from the disappearance of the amorphous phase, existing in the pattern of MZ-0.14C-1.1D (Figure 4.12), after the addition of TMB. The crystallinity increased further with increasing the molar ratio of TMB to *n*-dodecane to 1:1 (sample MZ-0.14C-1.1D-1.1T). However, the diffraction peaks of the x-ray pattern of sample MZ-0.14C-1.1D-2.2 show less intensity compared to MZ-0.14C-1.1D-1.1T suggesting that increasing the number of TMB moles to double the number of *n*-dodecane moles produces smaller crystals of Na-A zeolite. The optimum crystallinity was obtained when only TMB was included in the zeolite/CTAB gel as a micellar expansion agent (sample MZ-0.14C-2.2T).

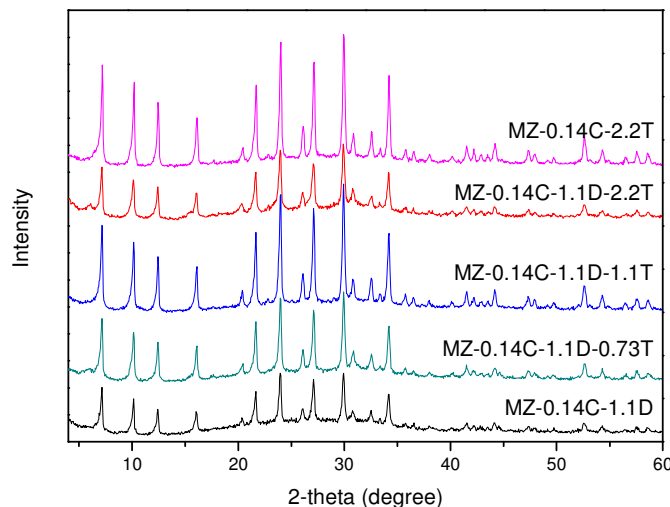


**Figure 4.12 XRD patterns of samples synthesized in presence of two micellar expanders; *n*-dodecane and TMB.**

The ideal method to investigate the effects of introducing two expanders to zeolite/CTAB gel is by comparing the N<sub>2</sub> adsorption-desorption measurements of the synthesized materials with MZ-0.14C-1.1D.

Figure 4.13 shows the isotherms obtained from the N<sub>2</sub> adsorption-desorption analysis at 77K with the corresponding BJH pore sized distribution (insets) of the samples synthesized with *n*-

dodecane: CTAB ratio at 1.1:0.73, 1.1:1.1, 1.1:2.2 and 1.1:0. The isotherms are type IV with H3 hysteresis suggesting that all the samples have mesoporous structures. At low relative pressure, the amount of  $N_2$  adsorbed was very small because the samples are NaA type zeolite<sup>142</sup>. The gradual increase in  $N_2$  uptake at relative pressure between 0.6 and 0.9 is attributed to the capillary condensation of  $N_2$  in the mesopores.

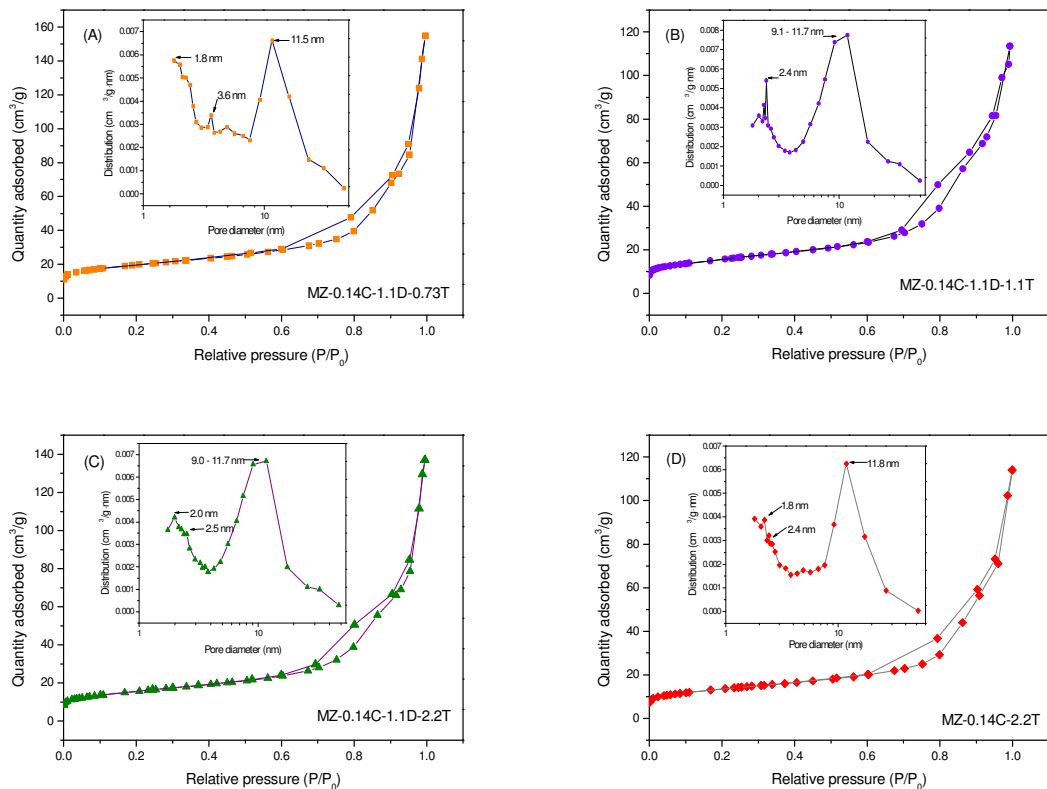


**Figure 4.13**  $N_2$  adsorption-desorption isotherms of MZ-0.14C-1.1D-0.73T (A), MZ-0.14C-1.1D-1.1T (B), MZ-0.14C-1.1D-2.2T (C) and MZ-0.14C-2.2T (D). The inset of each plot is the corresponding BJH pore size distributions measured from the adsorption branch.

The inclusion of a small amount of TMB as an additional expander to *n*-dodecane, sample MZ-0.14C-1.1D-0.73T, resulted in decreasing the BET surface and the mesopores volume. The BET surface area recorded for sample MZ-0.14C-1.1D-0.73T was  $66\text{ m}^2\cdot\text{g}^{-1}$  (Table 4.6), which is less than the BET surface area of sample MZ-0.14C-1.1D,  $87\text{ m}^2\cdot\text{g}^{-1}$  (Table 4.3). Furthermore, the mesopores volume was slightly less in the former ( $0.23\text{ cm}^3\cdot\text{g}^{-1}$ ) compared to the latter ( $0.25\text{ cm}^3\cdot\text{g}^{-1}$ ) (Table 4.3 and Table 4.6). The inclusion of a small amount of TMB has further effect on the pore size distribution at small scale region. The high intensity peaks at pore width 2.1, 2.2

and 2.5 nm in the BJH plot of MZ-0.14C-1.1D (Figure 4.5D-inset) disappeared and replaced by a small peak centered at 1.8 nm in the BJH plot of MZ-0.14C-1.1D-0.73T (Figure 4.13A-inset).

Further reduction in the values of BET surface area and mesopore volume was observed when the *n*-dodecane: TMB molar ratio was raised to 1: 1 in sample MZ-0.14C-1.1D-1.1T (Table 4.6). However, all the textural properties were retained with further raising the amount of TMB to double (sample MZ-0.14C-1.1D-2.2T). In other words, both samples MZ-0.14C-1.1D-1.1T and MZ-0.14C-1.1D-2.2T have exactly similar BET surface area, mesopore volume and pore size distribution at  $53 \text{ m}^2 \cdot \text{g}^{-1}$ ,  $0.17 \text{ cm}^3 \cdot \text{g}^{-1}$  and 2, 2.4, 9.0, 11.7 nm, respectively (Table 4.6 and Figure 4.13B,C).

**Table 4.6 Textural properties obtained from  $\text{N}_2$ -adsorption-desorption analysis of MZ-0.14C-1.1D-0.73T, MZ-0.14C-1.1D-1.1T, MZ-0.14C-1.1D-2.2T and MZ-0.14C-2.2T**

Sample	$S_{\text{BET}} (\text{m}^2 \cdot \text{g}^{-1})^a$	$V_{\text{meso}}^b (\text{cm}^3 \cdot \text{g}^{-1})$	$d_{\text{meso}}^c (\text{nm})$
MZ-0.14C-1.1D-0.73T	66	0.23	1.8, 3.6, 11.5
MZ-0.14C-1.1D-1.1T	53	0.17	2, 2.4, 9.1, 11.7
MZ-0.14C-1.1D-2.2T	53	0.17	2, 2.5, 9.0, 11.7
MZ-0.14C-2.2T	46	0.27	1.8, 2.4, 11.8

<sup>a</sup> Surface area obtained at relative pressure range of 0.05 – 0.3. <sup>b</sup> Mesopore volume was collected on pore size range between about 1.7 to 50 nm. <sup>c</sup> Mesopore size distribution was measured by BJH adsorption  $dV/dD$  pore volume.

In general, the results suggest that the incorporation of an auxiliary micelle expander resulted in decreasing the surface area and the mesopore volume, however, only slight change in the pore size distribution was observed. In other words, no additional swelling effect occurred after the addition of TMB. The explanation of these results cannot be attributed to saturation because the inclusion of higher *n*-dodecane concentration resulted in increasing the pore size to 13 nm in sample MZ-0.14C-2.75D (Table 4.3). Thus the reason is probably due to the electrostatic interactions of TMB molecules through the  $\pi$  electrons of their benzoic core with the positively charged heads of the surfactant<sup>88</sup>. Consequently, the molecules on the surface of the micelles act as a barrier preventing the incorporation of further TMB or *n*-dodecane molecules to the core of the micelles.

In contrast, the sole presence of TMB in zeolite/CTAB gel, sample MZ-0.14C-2.2T, showed a noticeable swelling effect. Table 4.6 shows that the BET surface area, mesopores volume and

the pores size distribution of MZ-.014C-2.2T are  $46 \text{ m}^2 \cdot \text{g}^{-1}$ ,  $0.17 \text{ cm}^3 \cdot \text{g}^{-1}$  and  $1.8, 2.4, 11.8 \text{ nm}$ , respectively. The optimum method to study the influence of TMB as a micelle expander is by comparing the  $\text{N}_2$  adsorption-desorption measurements of sample MZ-.014C-2.2T with sample MZ-0.14C-0. Figure 4.5B-inset and Figure 4.13D show that MZ-0.14C-0 has a broader pore size distribution compared to MZ-.014C-2.2T. The BJH distribution of the former is represented by a peak extended between 3.8 to 23 nm and centered at 7.9 nm, while the BJH distribution of the latter exhibits a narrower peak which extended between 7.5 to 23 nm and centered at 11.8 nm (Figure 4.5B-inset and Figure 4.13D). Generally, it can be deduced that the incorporation of the TMB molecules into the core of the CTAB micelles resulted in increasing the pore size especially in the large mesopore scale region, however, it resulted in decreasing the BET surface area and the mesopore volume significantly (Table 4.3 and Table 4.6).

It can be summarized that no additional swelling effect was observed accompanying the addition of auxiliary expander agent to the zeolite/CTAB/*n*-dodecane gel. In contrast, reduction in the values of BET surface area and mesopores volume was observed and also some changes in the pore size distribution. Using the TMB as a pore enlargement agent solely contributed to increase the size of the pores, especially in the large scale mesopores region.

#### ***4.3.6 The effect of calcination conditions on the pore size distribution***

The textural and porosity characteristics of the synthesized hierarchical zeolite are strictly linked to the conditions of removing the organic template molecules occluded within the pores. Different techniques have been described in the literature for template removal, such as calcination, and/or chemical extraction by using a solvent under reflux, microwave digestion, ultraviolet radiation<sup>67, 149, 150</sup>. In order to ensure obtaining the highest surface area and the real pore sized distribution a complete removal of the organic template from the pores is required

In this work, two different calcination methods were investigated: one-step air method and two-step nitrogen/air method. In the first method the samples were heated to  $550 \text{ }^\circ\text{C}$  using a ramp rate of  $2 \text{ }^\circ\text{C}/\text{min}$  in air flow for 5 h. In the two step calcination method, the samples were heated to  $550 \text{ }^\circ\text{C}$  at a ramp rate  $2 \text{ }^\circ\text{C}/\text{min}$  in  $\text{N}_2$  flow for 1 h followed by 4 h under air flow. Numbers 1 and 2 were included in the samples names as an indication of the type of the calcination method used, for example MZ-0.14C-1.1D-1 was calcined following one-step

method. The effect of the calcination methods on the pore size distribution and other textural properties were examined on three samples: MZ-0.14C-1.1D, MZ-0.14C-2.75D and MZ-0.14C-8.5D.

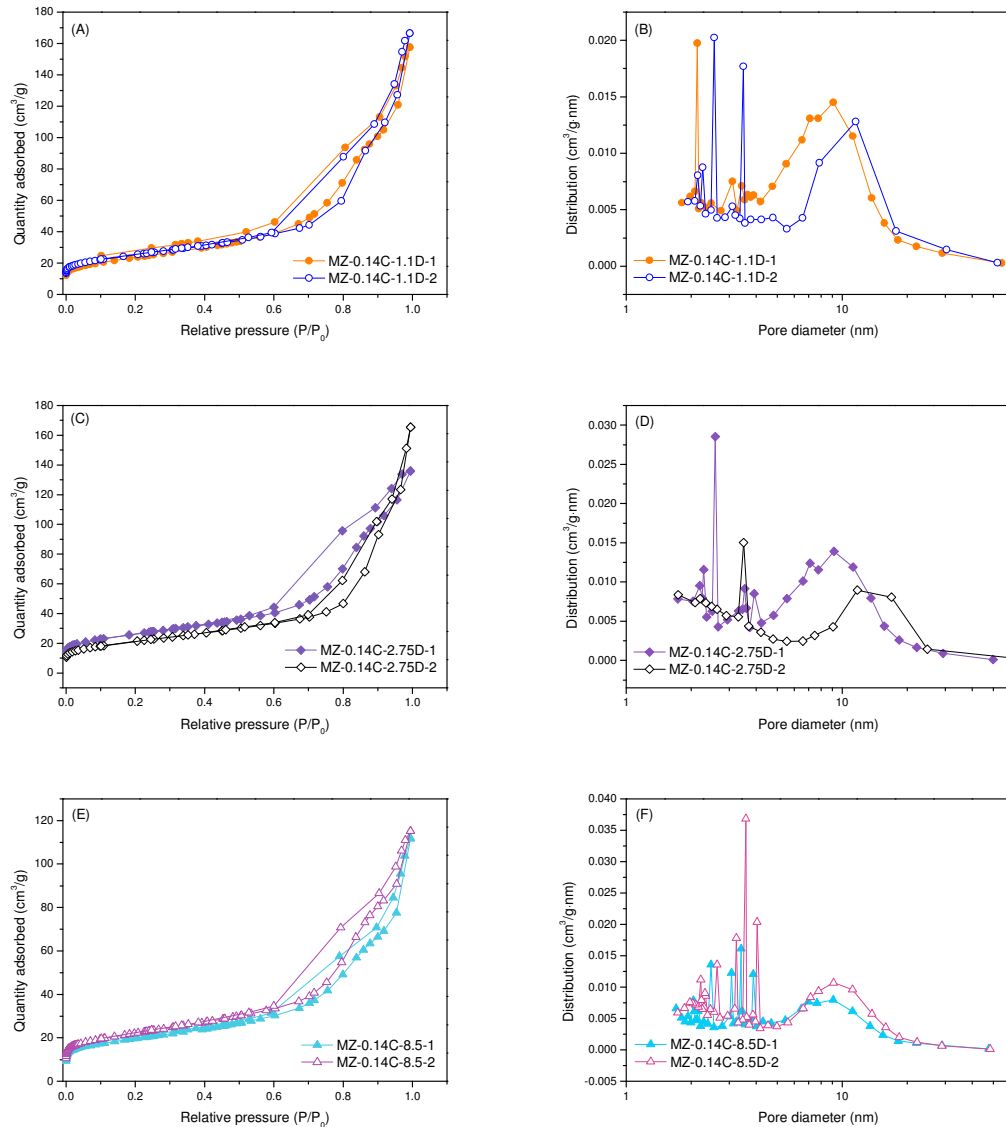


**Figure 4.14 N<sub>2</sub> adsorption-desorption isotherms (A, C and E) and BJH pore size distribution (B, D and F) of samples synthesized at two different calcinations conditions.**

The isotherms in Figure 4.14A, C and E indicate that the mesoporosity was retained in all samples after being subjected to either type of calcination methods. All samples show type IV isotherms with H3 hysteresis of mesoporous structures. However, Figure 4.14B, D and F and Table 4.7 suggest that the pore sizes distribution and surface area changed with changing the

calcination method. Samples MZ-0.14C-1.1D and MZ-0.14C-8.5D showed higher surface area with two-step calcination method, whereas the surface area of sample MZ-0.14C-2.75D was reduced. The reason probably is attributed to the appearance of relatively large pores (13.0 nm) after the two-step calcination.

The increase in the mesopore volume and the number of peaks in the small-scale mesopore region of all samples calcined in two-step method suggest that more organic molecules were removed from the pores (Figure 4.14 B, C and F and Table 4.7). Moreover, with two-step calcination method, the peak of the large scale mesopores of each sample shifted towards the right side and centered on higher pore width (Figure 4.14 B, C and F).

**Table 4.7 Textural and porosity characteristics of samples calcined at two different calcination methods.**

Sample	$S_{\text{BET}} (\text{m}^2 \cdot \text{g}^{-1})^a$	$V_{\text{meso}}^b (\text{cm}^3 \cdot \text{g}^{-1})$	$d_{\text{meso}}^c (\text{nm})$
MZ-0.14C-1.1D-1 <sup>d</sup>	83	0.24	2.1, 3.4, 9.1
MZ-0.14C-1.1D-2 <sup>e</sup>	87	0.25	2.1, 2.2, 2.5, 3.5, 11.5
MZ-0.14C-2.75D-1 <sup>d</sup>	90	0.20	2.2, 2.5, 3.3, 7.0, 9.1
MZ-0.14C-2.75D-2 <sup>e</sup>	75	0.25	3.5, 13.0
MZ-0.14C-8.5D-1 <sup>d</sup>	68	0.16	2, 2.5, 3.4, 9.0
MZ-0.14C-8.5D-2 <sup>e</sup>	76	0.17	2.2, 2.6, 3.2, ~ 9.1

<sup>a</sup> Surface area obtained at relative pressure range of 0.05 – 0.3. <sup>b</sup> Mesopore volume was collected on pore size range between about 1.7 to 50 nm. <sup>c</sup> Mesopore size distribution was measured by BJH adsorption  $dV/dD$  pore volume.<sup>d</sup> Samples calcined in air flow following one-step calcinations method. <sup>e</sup> Samples calcined in  $\text{N}_2$  and then air flow in two-step calcinations method.

Removing the organic template by combustion is a highly exothermic reaction which may increase the temperature of the sample and consequently causes shrinking or distorting the structure of the synthesized material. To reduce this potential shrinkage or damage, the samples were first heated in  $\text{N}_2$  flow allowing a great part of the organic species to be removed by an endothermic decomposition processes instead of combustion<sup>151, 152</sup>. During the second stage of heating in air flow, the remaining organic species inside the pores are burnt. Because the amount of the residual organic species is small, they do not cause a considerable increase in the temperature of the sample.

#### **4.3.7 Colloidal stability of synthesized mesoporous Na-A zeolite aqueous suspensions**

The colloidal stability of zeolite crystals is controlled by the balance between the attractive Van der Waals forces and the electrostatic repulsion<sup>153-156</sup>. The repulsive electrostatic force between the particles is determined by the charge of their surfaces which can be described by the zeta potential. The surface charge of zeolites particles is determined by the terminal  $\equiv\text{Si}-\text{OH}$  existing abundantly on their surfaces which could be protonated to  $\equiv\text{Si}-\text{OH}_2^+$  in low pH solutions or deprotonated to  $\equiv\text{Si}-\text{O}^-$  in high pH solutions<sup>153-155</sup>. However, for zeolites with framework containing Al, the bridge hydroxide groups  $\equiv\text{Si}-\text{OH}-\text{Al}\equiv$  are existed on their surface which can be easily deprotonted to  $\equiv\text{Si}-\text{O}^--\text{Al}\equiv$  in wide range of pH forming negatively charged zeolite<sup>155</sup>. Thus, the presence of more Al in the framework of zeolite results in a shift of the isoelectric point (IEP) of that zeolite to lower pH. The isoelectric point (IEP) is defined as the pH at which the zeta potential is zero<sup>153, 155, 156</sup>. At the isoelectric point the particles undergo a spontaneous aggregation driven by Van der Waals force.

The colloidal stability of the synthesized material was determined by measuring the zeta potential ( $\xi$ -potential) as a function of pH. The medium used was 0.01 M phosphate buffered saline (PBS) with pH 7.4 and contained NaCl 0.138 M and KCl 0.0027 M. The measurements were conducted on wide pH ranges which were obtained by adjusting the PBS pH by NaOH and HCl solutions.

Figure 4.15 shows the zeta potential as function of pH for calcined MZ-0.14C.014D and CZA. The zeta potential or the surface charge of both samples became more negative at high pH which is normal because the deprotonation of the hydroxyl groups increases. At low pH, the zeta potential of CZA surface decreased and reached to zero value around pH ~ 3.1 which represents the IEP. On the other hand, the zeta potentials of MZ-0.14C-0.14D show negative values throughout the entire pH range (Figure 4.15). Thus, the IEP for this sample, identified *via* extrapolating the data points at zeta potential  $\xi = 0$  mV, was at pH ~ 0<sup>154</sup>. This IEP shifting probably can be attributed to the higher surface area and larger pores of MZ-0.14C-0.14D compared to CZA. As described earlier (section 4.3.1) the particles in MZ-0.14C-0.14D contained large mesopores (2.5, 3.5 and 9 nm) (Table 4.3). In our system, the relatively large  $\text{HPO}_4^{2-}$  ions,  $\sim 4 - 5 \text{ \AA}$ <sup>157</sup>, can diffuse from the solution into the large pores of MZ-0.14C-0.14D

and reach to remote acidic sites inside the particles deprotonating them and hence charging them negatively<sup>154</sup>. Consequently, the neutralization of MZ-0.14C-0.14D can only be achieved by strongly acidic solutions. On the other hand, the zeta potential of CZA is related only to a couple layers from the external surface of the particles<sup>154, 158</sup>.

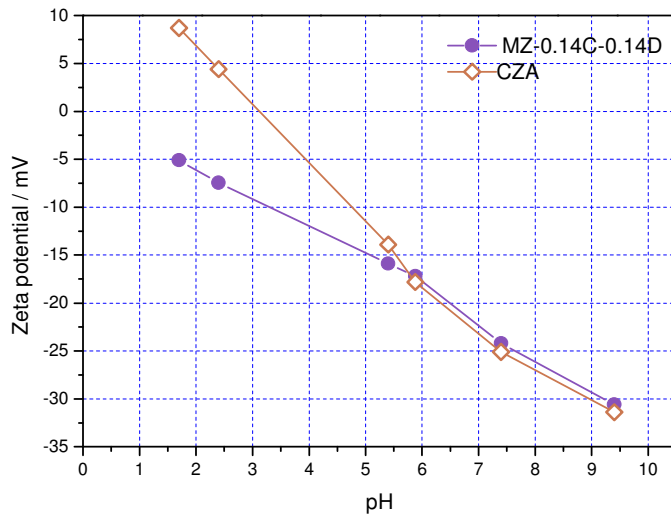


**Figure 4.15** Zeta potential as a function of pH of MZ-0.14C-0.14D and CZA.

#### 4.3.8 Ethylene adsorption-desorption measurements

Figure 4.16 shows the ethylene adsorption-desorption isotherms of mesoporous Na-A zeolite (sample MZ-0.14C0.14D) and conventional microporous Na-A zeolite (CZA) at 0 °C and pressure up to 850 kPa. It has been reported that ethylene molecules can be adsorbed on Na-A zeolite in spite of the discrepancy between the molecules size of the former (3.9 Å) and the pore sizes of the latter (3.5 Å)<sup>3</sup>. The driving force for this adsorption is the interaction energy that is determined by the  $\pi$  bond in the structure of ethylene molecules in addition to other physical properties, like high polarizability (3.5 Å<sup>3</sup>) and high quadrupole moment (0.48 Å<sup>3</sup>)<sup>3, 35, 42</sup>. In Figure 4.16, the isotherms show that at low pressure region (< 100 kPa), MZ-0.14C-0.14D adsorbed ethylene gas less than CZA. In contrast, at high pressure (850 kPa), the ethylene adsorption on MZ-0.14C-0.14D increased significantly to 4.32 mmol · g<sup>-1</sup> compared to 3.61 mmol · g<sup>-1</sup> on CZA. Even though the XRD patterns of both samples suggested that both materials have highly crystalline microporous LTA framework structure, the EDX-SEM analysis indicates

that the number of  $\text{Na}^+$  cations in MZ-0.14C-0.14D is about two-thirds the number of the cations in CZA. Normally ethylene adsorption on zeolite is driven by the strong interactions between the ethylene  $\pi$  bond and the electric field created by the cations of the hierarchical structure. Therefore the low ethylene adsorption on MZ-0.14C-0.14D at low pressure can be correlated to the low  $\text{Na}^+$  concentration (Table 4.4). On the other hand, the high adsorption capacity at high pressure is probably due to the high pore volume in MZ-0.14C-0.14D as measured by  $\text{N}_2$  adsorption-desorption analysis and also due to the presence of the mesopores which facilitate the transportation of the molecules to maximum number of active sites.

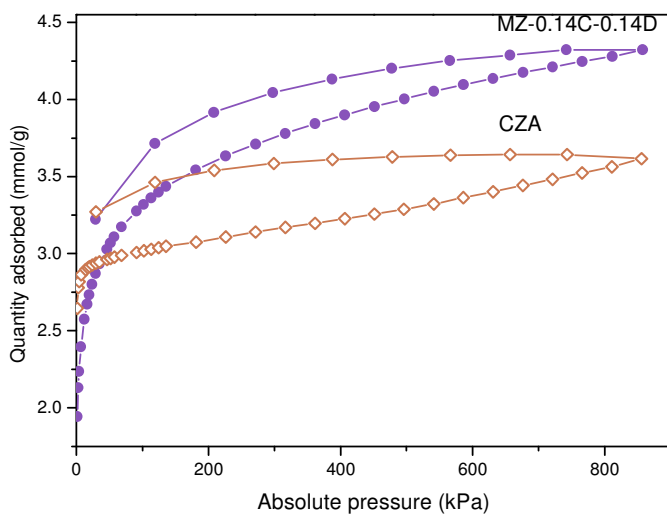


**Figure 4.16 Isotherms of ethylene gas adsorption on Mz-0.14C-0.14D and CZA at 0 °C and 850 kPa.**

#### **4.3.9 The hydrothermal stability of the synthesized micro-mesoporous NaA zeolite**

The hydrothermal stability of the mesoporous NaA zeolite named MZ-0.14C-0, which was synthesized by using CTAB as a template without introducing a micellar expansion agent, was assessed. Typically, 1 g of the MZ-0.14C-0 was added to 100 ml deionized water and then boiled under reflux for eight hours. Next, the sample was collected by filtration under vacuum and dried in oven at 70 °C. The XRD pattern of MZ-0.14C-0-HS, the hydrothermally tested sample, showed diffraction peaks with a considerably high intensities compared to MZ-0.14C-0 which

showed small and broad peaks indicating that the sample consisted of small sized crystals (Figure 4.17).

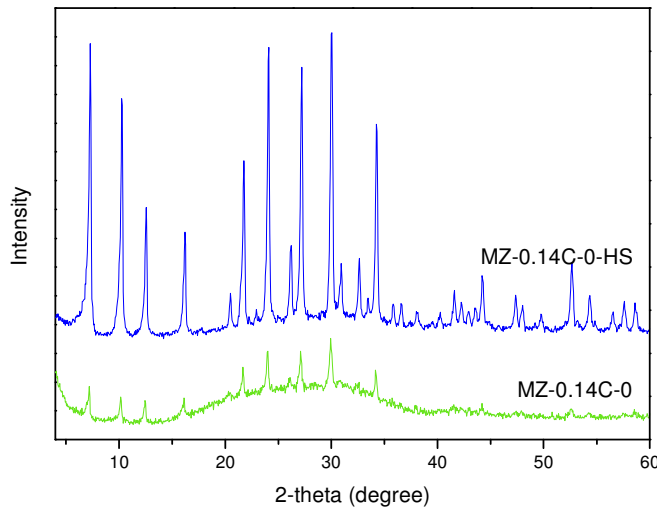


**Figure 4.17** XRD patterns of sample MZ-0.14C-0 and sample MZ-0.14C-0-HS.

The results of the detailed characterization of sample MZ-0.14C-0 in section 4.3.1 indicate that this sample consists of two types of particles, cubes and irregular spherical aggregates which consist of closely assembled crystallites (Figure 4.3A). The size of both types of particles lies in range between  $200 \pm 25$  and  $375 \pm 25$  nm. However, the majority of the particles are spherical aggregates and only few cubes were observed.

In contrast, the SEM images of the same sample after hydrothermal treatment (MZ-0.14C-0-HS) indicate that the sample comprises large cubic particles and small irregular aggregates (Figure 4.18A, B). The size of the cubes ranges from 400 to 550 nm, while the size of the spherical aggregates range between 200 and 250 nm. These results suggest that although, after the hydrothermal treatment the size of the aggregates was maintained, particles with a cubic morphology and larger size appeared.

These findings are in agreement with the XRD measurements indicating that the high intensity diffraction peaks are attributed to the large cubic crystals especially that they represent the major proportion of the particles.

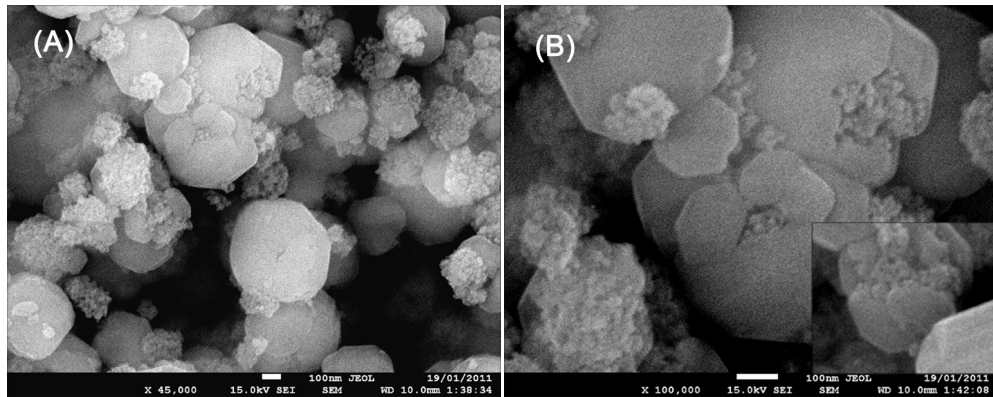


**Figure 4.18 Low and high magnification SEM images of sample MZ-0.14C-0-HS. The scale of images (A) and (B) is 100 nm.**

The isotherm of sample MZ-0.14C-0-HS shows a small  $N_2$  uptake at low relative pressure because the sample is NaA zeolite (Figure 4.10A). The  $N_2$  adsorption increased slightly till relative pressure 0.7 suggesting the presence of small mesopores with size close to micropore scale. Then at  $0.7 < P/P_0 < 0.99$ , the  $N_2$  uptake increased considerably indicating the existence of relatively large mesopores.

The pore size distribution curve of sample MZ-0.14C-0-HS showed two types of mesopores, 1.7 and 16 nm (Figure 4.19B). The comparison between the BJH distribution curves of the sample before and after the hydrothermal treatment clearly shows that some changes occurred in the porous structure of the synthesized material. Furthermore, the BET surface area and the mesopore volume decreased from  $89\text{ m}^2\cdot\text{g}^{-1}$  and  $0.27\text{ cm}^3\cdot\text{g}^{-1}$  before the hydrothermal treatment to  $75\text{ m}^2\cdot\text{g}^{-1}$  and  $0.21\text{ cm}^3\cdot\text{g}^{-1}$  after the hydrothermal treatment, respectively.

It is mentioned in section 4.3.1 that the mesoporosity in MZ-0.14C-0 is attributed to the interstitial voids between the aggregated crystallites in the spherical aggregates. Therefore, the increase in the number of the cubic particles on the expense of the spherical aggregates (as shown in the SEM images) is the reason behind decreasing the mesoporosity in sample MZ-0.14C-0-HS (Figure 4.19 A, B).

Moreover, a close observation of a cubic particle in the high magnification SEM image (Figure 4.18B and inset) reveals that the cubic particles are in origin spherical aggregates but they were converted into cubic morphology during the hydrothermal treatment.

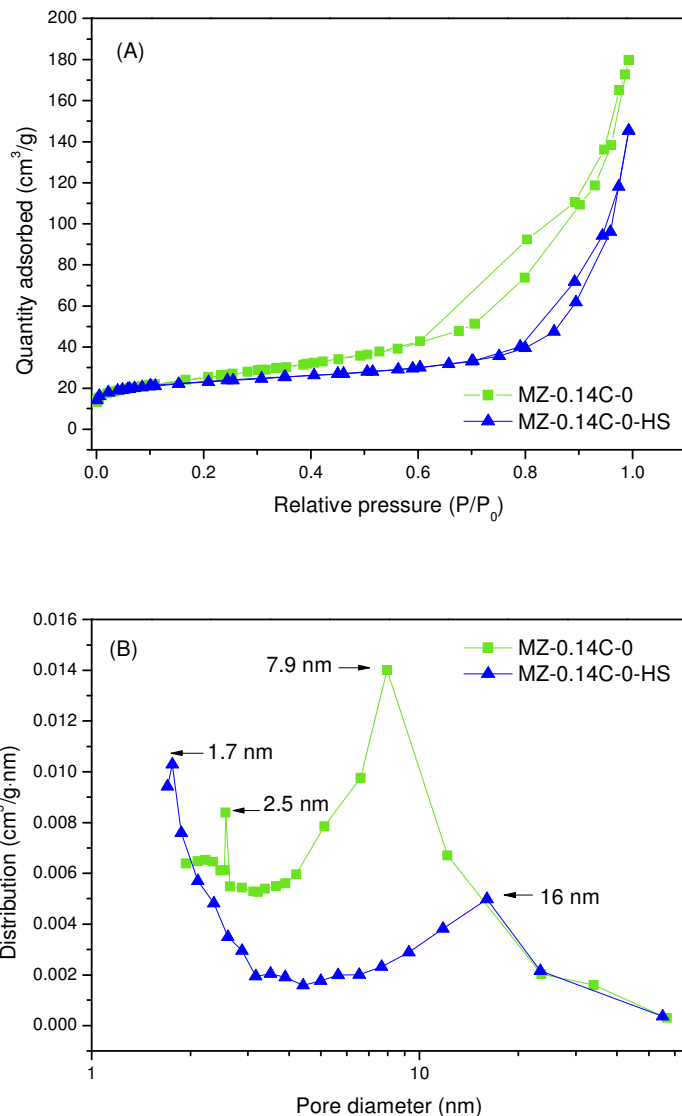


**Figure 4.19 N<sub>2</sub> adsorption-desorption isotherms (A) and BJH pore size distribution (B) of sample MZ-0.14C-0 and sample MZ-0.14C-0-HS.**

In summary, the framework structure of sample MZ-0.14C-0 was retained during the hydrothermal treatment, however, the textural and porous characteristics changed. The results reveal that the sample undergoes further crystallization during the hydrothermal treatment.

The above results show that MZ-0.14C-0 is a mesoporous Na-A zeolite synthesized by introducing a cationic surfactant, CTAB, into the reaction gel which then was aged at room

temperature for a sufficient period for zeolite seeds formation. The SEM, N<sub>2</sub> adsorption–desorption analysis and TEM images suggest that the aging of zeolite gel at room temperature worked cooperatively with CTAB molecules for generating the mesosized pores in the Na-A zeolite particles. Aging the gel without the inclusion of CTAB (sample ZA-st), or including CTAB molecules in zeolite gel without aging (sample ZA) generate Na-A zeolite with only micropores. In a previous study, mesoporous structures were synthesised by introducing swollen CTAB micelles into initially aged gel of type Y zeolite <sup>121</sup>. However, the product was not a pure mesoporous type Y zeolite, it was mesoporous composite of type Y zeolite and silica. Further, no mesoporous phase was obtained when only CTAB (without swelling agent) was introduced to the system. In our study, the results show that a pure mesoporous Na-A zeolite was prepared in presence of CTAB alone in the system. Furthermore, the results also show that the size of the mesopores was controlled by the addition of alkane molecules which act as swelling agent in the system.

The size of the aggregated crystallites was in range of 15 – 20 nm, therefore the Bragg diffractions could readily be observed by XRD. In such systems, the general mechanism is that the inorganic zeolite subunits are assembled with the organic aggregates (surfactant micelles) and the subsequent removal of these micelles produces pores which are mirror images of the micelles. Accordingly, pores with size equal to normal diameter of surfactant micelles (2 – 4 nm) were expected from the system wherein no swelling agent was involved. However, mesopores with size of ~ 7.9 nm were obtained in (MZ-0.14C-0). Ryoo *et al.*, owed such phenomenon to the condensation of the excess of surfactant molecules forming oligomers which might expand the surfactant micelles <sup>67</sup>.

The mesopore size distribution measured by N<sub>2</sub> adsorption-desorption isotherms showed that introducing *n*-dodecane with CTAB in the initial gel of Na-A zeolite increased the pores size. For example, 1: 1 molar ratio of *n*-dodecane: CTAB (sample MZ-0.14C-0.14D) enlarged the mesopore diameter from 7.9 (MZ-0.14C-0) to 9 nm (Figure 4.5 and Table 4.3). Further increasing the *n*-dodecane molar ratio to 1.1 and 2.75: 0.14 CTAB increased the pores diameter to 11.5 and 13 nm, respectively (Figure 4.5 and Table 4.3). Ulagappan *et al.* investigated swelling of CTAB micelles by alkanes in silica system at 1CTAB: 1 alkane molar ratio <sup>127</sup>. The *n*-dodecane in their system formed a core inside the micelles by one to one molecule interaction with the surfactant molecules adding their entire chain length to the micelle diameter <sup>127</sup>.

However, in our work the pore size expanded from 7.9 nm in the sample MZ-0.14C-0 to about 9.0 nm in sample MZ-0.14C-0.14D, which was less than the chain length of *n*-dodecane. These results indicate that *n*-dodecane behavior in our system is not in agreement with Ulagappan *et al.* mechanism. On the other hand, the results were more compatible with the “swelling effect” described by Kunieda *et al.* wherein they used *n*-decane to swell the micelles of polyoxyethylenedodecyl ether<sup>159</sup>. The “swelling effect” is the incorporation of alkane molecules in the inner core of the micelles expanding their volume<sup>130</sup>. The progressive increase in the pore size accompanied by raising the amount of *n*-dodecane in MZ-0.14C-1.1D and MZ-0.14C-2.75D (Table 4.3) is a further evidence for the “swelling effect” because when the number of *n*-dodecane molecules increases in the system they can profoundly penetrate and swell the core of the micelles. Especially at relatively low temperatures (room temperature in our system), as the less tightly aggregated and smaller associated number of the micelles result in smoother penetration for the *n*-dodecane molecules<sup>160</sup>.

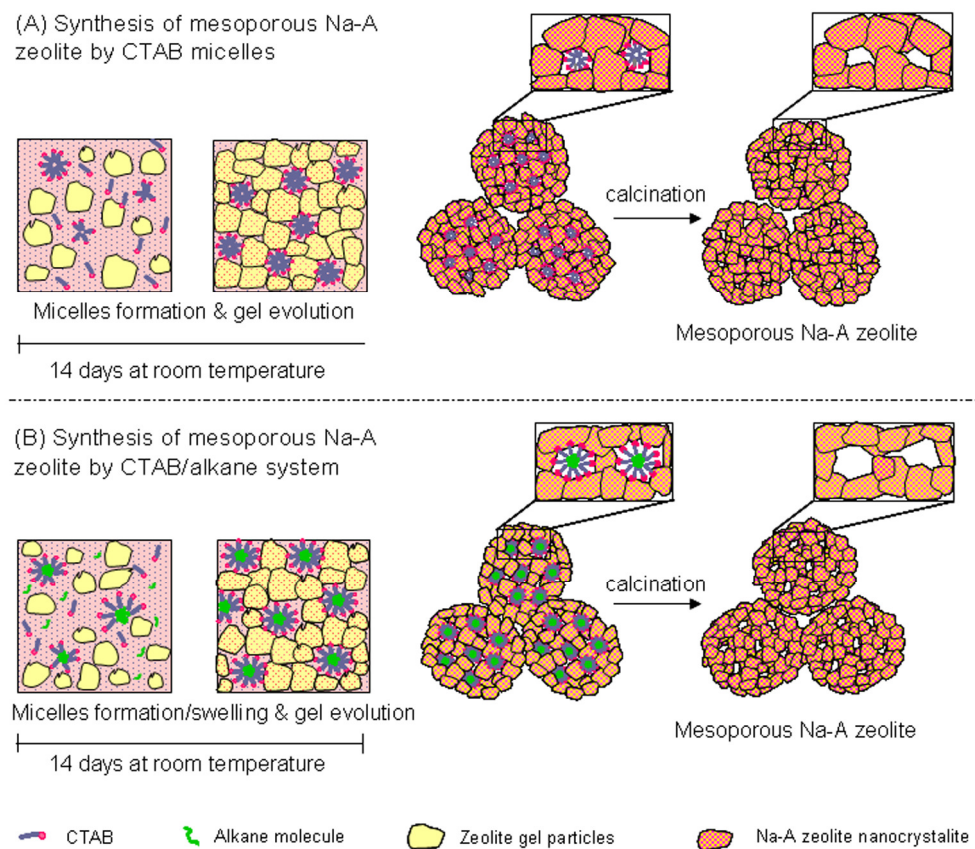
The solubilization of alkane molecules in the core of the micelles increases the packing parameter of the surfactant aggregations<sup>159</sup>. The packing parameter in surfactant – aqueous system is represented by:  $g = v_L / \alpha_S l$ , where  $v_L$  is the total volume of lipophilic tails of surfactant plus the organic additives,  $\alpha_S$  is the effective cross sectional area of the hydrophilic headgroups at the micelle-aqueous interface and  $l$  represents the kinetic length of hydrophobic chain of surfactant<sup>159, 161</sup>. Kunieda *et al.* defined “swelling” as the effect of oil to increase the volume of lipophilic part without expanding  $\alpha_S$ . This suggests that, in present work, the solubilization of *n*-dodecane molecules in the core of CTAB micelles increased  $v_L$  which in turn raised the packing parameter ( $g$ ) of the self organizing structures of surfactant molecules and made them more positive. Thus, increasing the charge density of the micelles accompanied with increasing their volume probably resulted in improving the affinity between the micelles and the aluminosilicate species<sup>159</sup>.

As Valtchev *et al.* investigated the synthesis of LTA and FAU zeolites at room temperature, tiny gel particles were formed directly after the mixing of the precursors<sup>16, 124-126</sup>. In our system, the TEM results show single lattice orientation in individual crystallites with the size of about 20 nm (Figure 4.6 images A-2, B-2, C-2 and D-2) which indicates that the nanocrystallites were generated from single amorphous particle domain. This suggests that tiny gel particles similar to those described by Valtchev *et al.* might be obtained after mixing the precursors in our system

which then evolved slowly and simultaneously with the micelles formation/swelling process. It is mentioned above that the penetration of the alkane molecules into the core of micelles increased their size and their positive charge which enhanced the assembly of the tiny miniature zeolite gel particles on the surface of these micelles. Afterwards, each of these gel particles was transformed into Na-A zeolite crystallites. The slow gel evolution and mass transformation facilitated the retention of the surfactant micelles within the aggregated crystallites. This speculated mechanism is demonstrated in the Scheme 1.

The presence of half cube-half aggregate particles (SEM images in Figure 4.3A-D) and also the high magnification SEM image of MZ-0.14C-0-HS (Figure 4.18B and inset) reveal that the system has probably undertaken a surface recrystallization route<sup>18, 141</sup>. Such growth mechanism normally takes place in system wherein aggregated gel particles are formed in the early stage of gel evolution. Thin islands of Na-A zeolite are formed on the surface of the aggregates which then might be joined together and self aligned according to their crystallographic orientation forming cubic crystals of LTA zeolite<sup>19</sup>.

Accordingly, a detailed study of the crystal growth of the synthesized micro-mesoporous zeolite has been undertaken and discussed in chapter 5 in order to understand the mechanism behind the formation of the mesoporous Na-A zeolite aggregates and hence the transformation of these aggregates into cubic crystals.



**Scheme 4.1 (A) Proposed mechanisms for the synthesis of mesoporous Na-A zeolite by using CTAB micelles at room temperature, (B) swelling the CTAB micelles by linear chain alkane molecules to enlarge the mesopores size in the produced Na-A zeolite**

## 4.4 Conclusion

In a one pot synthesis procedure, micro-mesoporous Na-A zeolites were successfully produced by the introduction of CTAB micelles to a slowly evolving zeolite system at room temperature. At the early stage of gel evolution, freshly formed miniature zeolite gel particles were assembled around the surface of the coexisting CTAB micelles forming aggregations of zeolite-CTAB. Aging the system for two weeks at room temperature induced slow mass transformation of the zeolite gel particles into nanocrystallites which then grew slowly retaining the CTAB micelles within the crystallization area. The CTAB micelles and the two week room temperature aging worked collaboratively forming the mesoporous Na-A zeolite. The introduction of CTAB micelles in the synthesis gel is not effective in term of generating the

mesopores without the aging at room temeprature and vice versa. The size of the mesopores was controlled by introducing different amounts/types of linear alkanes into the zeolite-CTAB system. The alkanes acted as swelling agents by permeating into the core of the micelles increasing their volume as well as their packing parameters which enhanced the density of their positive charge. Increasing the molar ratio of the swelling agent to CTAB produced larger mesopores. Furthermore, short hydrocarbon chain like *n*-hexane generated smaller pores than those obtained by long hydrocarbon chain like *n*-octane and *n*-dodecane.

Increasing the aging period for longer than two weeks resulted in a significant reduction in the surface area and the mesopore volume. Further, raising the CTAB concentration in the synthesis mixture resulted in inhibiting the crystallinity of Na-A zeolite. No additional swelling effect was observed with introducing an auxiliary micelle expander in addition to *n*-dedecane.

The calcination conditions showed considerable effects on the textural properties of the synthesized micro-mesoporous zeolite. The two-step N<sub>2</sub>/air calcination resulted in better removal of the template molecules from the pores and thus showed higher mesopore volume and wider pore sized distributions.

The IEP for the mesoporous Na-A zeolite was shifted to pH ~ 0 as compared to conventional microporous Na-A zeolite (pH ~ 3.1). Furthermore, our material showed higher pore volume compared to conventional Na-A zeolite which resulted in higher adsorption capacity for ethylene gas. Thus, our material offers potential applications in projects where ethylene recovery is involved, for example, from the purge gas stream in the polyethylene manufacturing plant.

# ***Chapter 5: Formation of LTA Zeolite Crystals with Multi-hollow Polycrystalline Core-shell Structure via Aggregation- recrystallization Route in the presence of Emulsion Droplets***

## **5.1 Introduction**

The results obtained in Chapter 4 indicated that micro-mesoporous Na-A zeolite can be synthesized at room temperature in the presence of CTAB molecules as a surfactant and a linear alkane as micelles expansion agent. The SEM and TEM characterization of the products implied that the zeolite system has undertaken a growth mechanism known as NARS: Nanoparticles - Aggregation – Surface recrystallization – Single crystal <sup>18</sup>. The fact that the synthesis of pure crystalline Na-A zeolite *via* aggregation-reverse crystallization route has not been reported yet was a motivation for us to conduct a detailed study on the growth of the crystals in our system.

Basically, there are two types of crystal growth mechanisms in zeolite systems. The first one is the traditional crystal growth which occurs via atom by atom addition to existing nuclei forming the morphology of polyhedron<sup>17,18 125</sup>. The second growth mechanism is a recent discovery which is called aggregation – reverse crystallization route. Such crystal growth mechanism normally takes place in systems where nanoparticle aggregations are formed in the early stage of the gel evolution<sup>18, 19, 162</sup>.

In our approach, the long time aging/reaction at room temperature induced slow formation and growth of zeolite crystals allowing us to track the entire sequence of crystallization events by investigating samples taken at different reaction periods.

In this chapter, we discuss the study conducted on a system containing high concentration *n*-dodecane in the zeolite gel/CTAB system. The volume fraction of *n*-dodecane was about 50 % of the whole volume of the mixture. Such large internal phase volume fraction transformed the

system to high internal phase emulsion, type oil/water<sup>163, 164</sup>. The *n*-dodecane (droplets) represents the internal phase (Oil), the zeolite gel is the external phase (water) and the CTAB is the emulsifier.

Section 2.6.5 in the literature review (chapter 2), presented studies in which emulsion droplets were involved in zeolite synthesis. In most of these studies, emulsion droplets were used to control the size and the shape of zeolite crystals. However, only a few studies concentrated on the direct synthesis of hierarchical zeolite with multi model pore size distribution by using emulsion droplets as a template.

In our system, we anticipate that the CTAB molecules will dissolve on the interface between the *n*-dodecane droplets and the zeolite gel, decreasing the surface tension of the droplets and charging them positively<sup>85</sup>. Subsequently, the positive droplets attract the negative aluminosilicate species in the synthesis gel. Under the moderate conditions at room temperature, the gel undergoes slow evolution and mass transformation into crystalline zeolite. Then the removal of the oil droplets and the organic CTAB molecules generates micro-mesoporous zeolite structures with hollows.

Hollow zeolite structures with mesoporous walls have attracted significant attention recently due to their promising application in controlled drug delivery, confined-space catalysis, large biomolecular separation systems, *etc*<sup>56, 165</sup>. Generally, three techniques have been used to synthesize spheres with hollow cores; namely, hard templating<sup>20, 22</sup>, soft templating<sup>56, 166</sup> and dual templating<sup>167-169</sup>. Recently, however, zeolite spheres/crystals with hollow cores were obtained from systems in which a surface to core crystallization mechanism was observed<sup>18, 165</sup>. For instance, hollow LTA and sodalite structures were synthesized by using three dimensional pore networks of crosslinked hydrogel polymers as reactors wherein *in situ* crystallization of the entrapped gel was performed<sup>162, 165</sup>. On the interface between the polymer network and the gel, zeolite nuclei are formed and grow rapidly forming oriented nanoparticle aggregations which consequently developed into hollow zeolite spheres/crystals by consuming the gel situated in the center of the aggregates<sup>165</sup>. However, the shells of these hollow structures are microporous, thus large molecules such as macromolecules cannot diffuse to the center. Hence, material with hollow cores and large-scale porous walls is highly desirable because they offer better mass transfer and less channel blockage<sup>167</sup>. Zhao *et al.* successfully synthesized MFI zeolite capsular

structures with hollow core and mesoporous shell<sup>57</sup>. Initially they created oil (TEOS) in water emulsion system followed by carefully controlling the TEOS hydrolysis temperature in the presence of TPAOH and CTAB as micro- and mesoporous templates, respectively. During the hydrothermal treatment at high temperature, the TEOS molecules diffuse outward through the zeolite seeds/CTAB layer that condensed along the oil (TEOS) / water interface leaving behind a hollow core surrounded with a mesoporous shell<sup>57</sup>. However, the average size of the mesopores in the shell of the hollow capsules is 3 nm which renders them impractical for applications where molecules with large molecular weight, like proteins, are involved. Therefore, the direct synthesis of hollow zeolite particles with fully crystalline mesoporous walls is still considered a challenge.

This chapter discusses systematic investigations of crystal formation and growth in zeolite/CTAB/*n*-dodecane system. Extensive observations were conducted on samples collected over different synthesis stages, *i.e.* directly after the addition of CTAB to the gel, after the introduction of *n*-dodecane, 48 h, 5, 6, 7, 8, 9, 12, and 14 days. The sample collected after 14 days aging was investigated before and after the high temperature crystallization. Furthermore, to explore the effects of prolonging the aging/reaction period to more than 14 days on the crystal growth, samples aged for 17, 19, and 44 days were also studied.

## 5.2 Experimental work

### 5.2.1 Materials

The chemicals used for this work were: sodium silicate solution (~ 26.5 % SiO<sub>2</sub>, ~ 10.6 % Na<sub>2</sub>O, Sigma Aldrich), sodium aluminate (50 – 56 % Al<sub>2</sub>O<sub>3</sub>, 40 – 45 % Na<sub>2</sub>O, Sigma Aldrich), sodium hydroxide ( $\geq$  99 %, Merck), cetyltrimethylammonium bromide (CTAB-Ajax Finechem) and *n*-dodecane (99 %, Merck). All chemicals were used without any further purification.

### 5.2.2 Synthesis

The initial gel of Na-A was prepared according to a method reported in the literature<sup>139</sup>. Typically, the synthesis commenced with dissolving 2 g sodium hydroxide in 37.6 g of deionised water. Then this alkaline solution was divided equally into two halves named (A) and

(B). To the first half (A), 3.9 g sodium aluminate was added and dissolved by vigorous stirring until a clear solution was obtained. 8.8 g of sodium silicate solution was added to the second half (B) and stirred for a few minutes. Then the two solutions (A) and (B) were mixed and stirred vigorously by using electronic overhead stirrer type Eurostar digital (manufactured by IKA-WERKE) at speed 540–580 rpm. The cationic emulsifier, cetyltrimethylammonium bromide (CTAB, 2 wt % of total synthesis mixture) was then added to the homogenized gel under continuous stirring for few minutes, followed by drop wise addition of 37.5 ml *n*-dodecane. It is well known that *n*-dodecane is hydrophobic; therefore its droplets trend to coalesce forming a separate layer from the zeolite synthesis mixture. However, the added CTAB molecules dissolve on the interface between the droplets and the synthesis mixture decreasing the surface tension of the droplets and hence stabilizing them. Also, the hydrophobic tails of CTAB molecules dissolve in *n*-dodecane droplets while the hydrophilic heads (positive amine group) dissolve in the synthesis solution around the droplets endowing them positive charge. Subsequently, the repulsive force between the positively charged droplets obstructs their coalescence and increases the emulsion stability. Accordingly, the zeolite system at this stage was transformed into a stable emulsion wherein the *n*-dodecane droplets represent the dispersed phase and the zeolite gel represents the continuous phase.

The gel obtained after the addition of CTAB was named CTAB/gel and the gel obtained after the *n*-dodecane introduction was named CTAB/Dod/gel.

The final homogenized and creamy emulsion was aged at room temperature for 14 days followed by elevated temperature crystallization at 95 °C for 5 h. During the room temperature aging, no phase separation was detected confirming the emulsion stability. Thereafter the product was collected by vacuum filtration and washed repeatedly with ethanol and water and finally dried at 90 °C overnight. The surfactant was removed by calcination at 550 °C with ramp rate 2 °C/min in N<sub>2</sub> flow for 1 h and then in air flow for 4 h. The collected product in this stage was denoted MZ-14d-cryst.

For comparison purposes, conventional Na-A zeolite was synthesized starting from the same initial gel composition which was then aged at room temperature for 14 days followed by hydrothermal crystallization at 95 °C for 5 h. The product was collected by filtration under

vacuum, washed frequently with water and finally dried at 90 °C overnight. The obtained zeolite was denoted as ZA-st in this work.

To investigate the mechanism of crystal growth and hollow formation in the produced particles, aliquots of synthesis mixture were taken at different periods of room temperature aging. These aliquots were denoted as MZ-*t*; where MZ represented the reactant mixture and *t* referred to the number of hours / days the sample was aged.

The effect of aging for longer than 14 days on the crystal size and morphology was also investigated. The synthesis conditions were exactly similar to the conditions used for sample MZ-14d-cryst. Three different aging periods were examined; 17, 19 and 44 days and the resultant products were named MZ-17d-cryst, MZ-19d-cryst and MZ-44d-cryst, respectively.

### 5.2.1 $\text{Ca}^{+2}$ ion-exchange

The resultant MZ-14d-cryst powder was ion exchanged into  $\text{Ca}^{+2}$  form using the following procedure: 1 g of MZ-14d-cryst was dispersed in 50 ml 1 M  $\text{CaCl}_2$  solution with magnetic stirring and under reflux at 60 °C for 12 h. The treatment was repeated four times. After each time the sample was collected by filtration and dried in an oven at 90 °C. The  $\text{Ca}^{+2}$  form sample was named MZ-14d-cryst- $\text{Ca}^{+2}$ .

## 5.3 Results and discussion

In this section, the identity and the characteristics of the prepared material are discussed followed by detailed investigation of the crystal growth mechanism. The wide angle x-ray pattern of sample MZ-14d-cryst (Figure 5.1) shows peaks that can be indexed onto the cubic unit cell of LTA zeolite framework structure when compared to standard crystal data published by International Zeolite Association <sup>140</sup>. The low angle XRD diffraction pattern in Figure 5.1-inset shows a single peak centered at  $2\theta = 0.8^\circ$  with  $d_{\text{spacing}} = 10.2 \text{ nm}$  indicating the presence of meso-sized pores in MZ-14d-cryst.

This mesoporosity was well confirmed by  $\text{N}_2$  adsorption-desorption measurements at (-196 °C) (Figure 5.2). The isotherm of sample MZ-14d-cryst is a typical type IV with steep increase in quantity of nitrogen adsorbed at relative pressure 0.6 to 0.99 caused by capillary condensation of

$\text{N}_2$  in the mesopores. The isotherm with H3 hysteresis and without level off at high relative pressure (close to unity) suggests that the product comprises of aggregated crystallites<sup>64, 143</sup>.

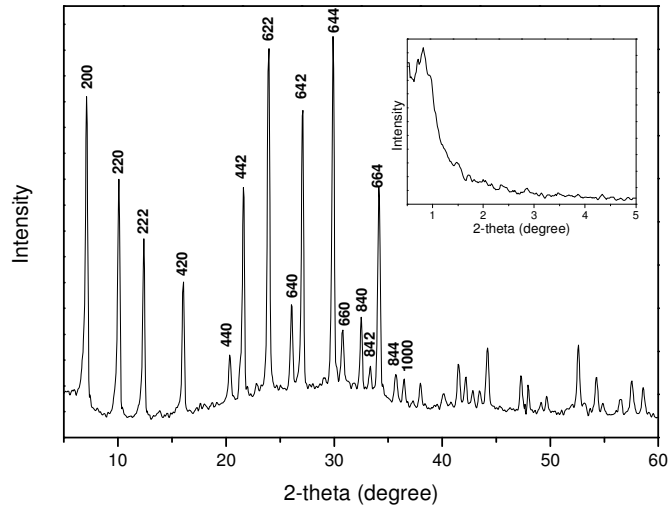


**Figure 5.1** Wide and small (inset) angle XRD patterns of MZ-14d-cryst. Indicated peaks can be linked to the literature<sup>140</sup>

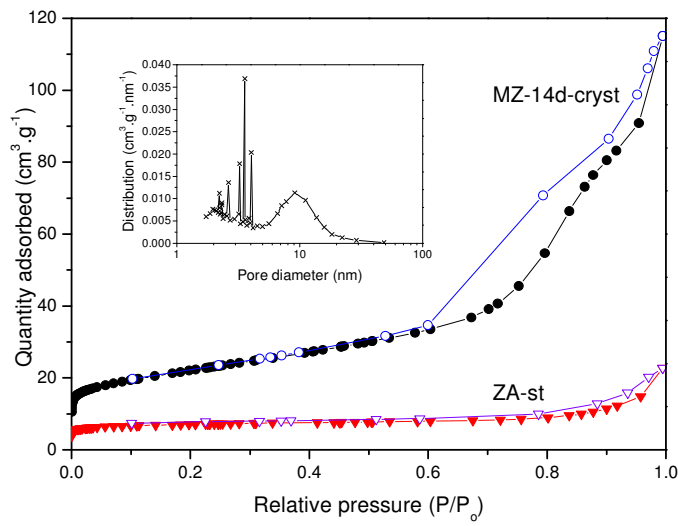


**Figure 5.2**  $\text{N}_2$  adsorption-desorption isotherms at (-196 °C) of MZ-14d-cryst and ZA-st. BJH mesopores size distribution obtained from the adsorption branch of sample MZ-14-cryst (inset).

In contrast, the isotherm of sample ZA-st show negligible N<sub>2</sub> adsorption – this small amount can be attributed to the presence of some mesoporosity as well as adsorption on the external crystal surface<sup>67</sup>. It is well known that the micropores in conventional Na-A zeolite are too small to be accessed by N<sub>2</sub> molecules due to pore blockage<sup>29, 142</sup>. The specific surface area and mesopore volume of sample MZ-14d-cryst are 76.06 m<sup>2</sup>·g<sup>-1</sup> and 0.17 cm<sup>3</sup>·g<sup>-1</sup>, respectively (Table 5.1).

The pore size distribution as obtained by BJH method using the adsorption branch shows two ranges of mesopores: small mesopores in the range of 2 – 4 nm and large mesopores represented by a broad peak centered at 9.1 nm (Figure 5.2-inset and Table 5.1). The large scale mesopores correspond in size to the *d*-spacing suggested by small angle XRD (10.2 nm).

Furthermore, the MZ-14d-cryst sample was converted into Ca<sup>+2</sup> form and named MZ-14d-cryst-Ca<sup>+2</sup>. The pore size distribution of MZ-14d-cryst-Ca<sup>+2</sup> was measured by N<sub>2</sub> adsorption-desorption analysis and compared to MZ-14d-cryst. The results indicate that the pore size distribution was retained after the ion exchange however the mesopore volume was slightly smaller (Figure 5.3A, B). The isotherm shows a steep uptake at  $P/P_o$  below 0.1 indicating microporous characteristics (Figure 5.3A). The size of the micropores using Horvath-Kawazoe method is 0.55 nm which is typical of the pore apertures of CaA zeolite crystal (Figure 5.3B-inset)<sup>170</sup>. At high relative pressure, between 0.4 and 0.99, the N<sub>2</sub> adsorption increased gradually forming type IV isotherm with H3 hysteresis which is indicative of capillary condensation of nitrogen in the mesopores (Figure 5.3A)<sup>143</sup>. The BET surface area of MZ-14-cryst-Ca<sup>+2</sup> was significantly higher than of MZ-14-cryst. The reason is that during the ion exchange process every Ca<sup>+2</sup> cation replaces two Na<sup>+</sup> cations which results in increasing the size of the unit cell aperture to ~5 Å and consequently increases the specific surface area<sup>3</sup>. The surface area and total pore volume at  $P/P_o$  0.99 are 380.6 m<sup>2</sup>·g<sup>-1</sup> and 0.31 cm<sup>3</sup>·g<sup>-1</sup>; respectively. The micropore volume as measured by t-plot is 0.16 cm<sup>3</sup>·g<sup>-1</sup> while the mesopores volume is 0.13 cm<sup>3</sup>·g<sup>-1</sup> (Table 5.1). The pore size distribution of MZ-14-cryst-Ca<sup>+2</sup> as obtained by BJH method using adsorption branch showed several peaks centered at 1.7, 2.1, 6.2 nm in addition to a broad peak extended between 7 to 11 nm but centered at 8.8 nm (Figure 5.3B). These results indicate that the pore size distribution observed in MZ-14-cryst was retained in MZ-14-cryst-Ca<sup>+2</sup>, however, the mesopore volume was slightly lower in the latter compared to the former.

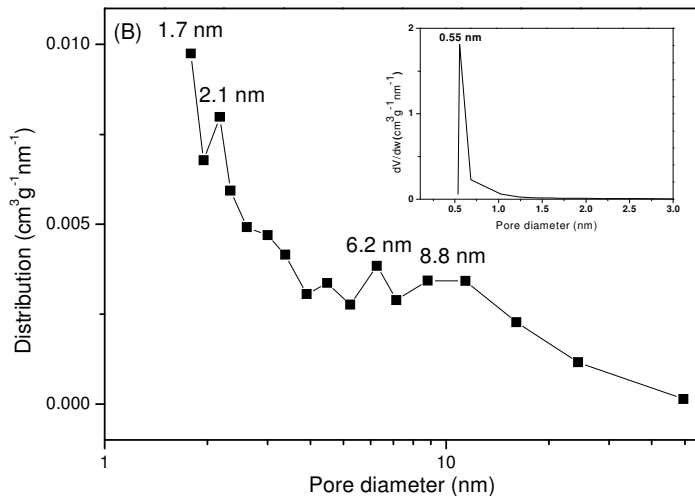
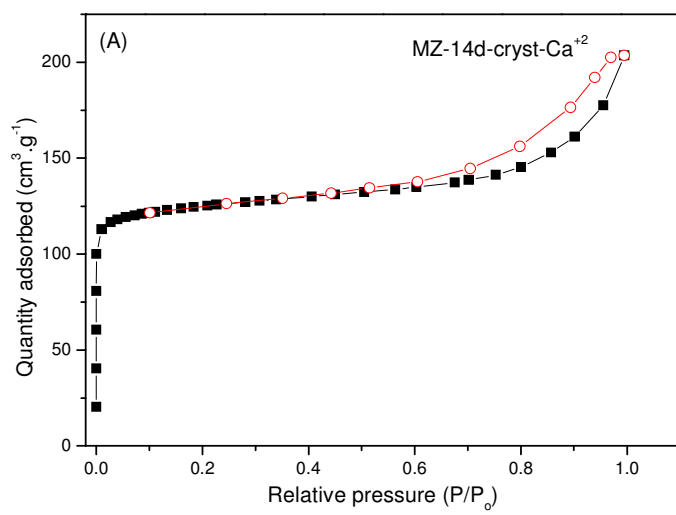


**Figure 5.3**  $\text{N}_2$  adsorption desorption isotherm at  $-196\text{ }^\circ\text{C}$  (A); (B) Pore size distribution obtained from BJH method using the adsorption branch of MZ-14d-cryst-Ca; inset- micropore size distribution calculated by Horvath-Kawazoe

The FTIR spectra for both, the ZA-st and MZ-14d-cryst, show four distinctive absorption bands at around 464, 556, 667 and  $1004\text{ cm}^{-1}$  (Figure 5.4). The absorption bands were assigned on the basis of previous studies<sup>146, 147</sup>. The band at  $556\text{ cm}^{-1}$  is attributed to the external vibration of double four-member rings which is the characteristic for zeolite A framework. The bands resolved at 667 and  $1004\text{ cm}^{-1}$  are assigned to the internal vibration of T-O (T = Si, Al) symmetric and asymmetric stretching, respectively. Finally, the band at  $464\text{ cm}^{-1}$  is assigned to

the T-O (T = Si, Al) bending. These observations compliment the XRD observation that both materials have zeolite A structure.

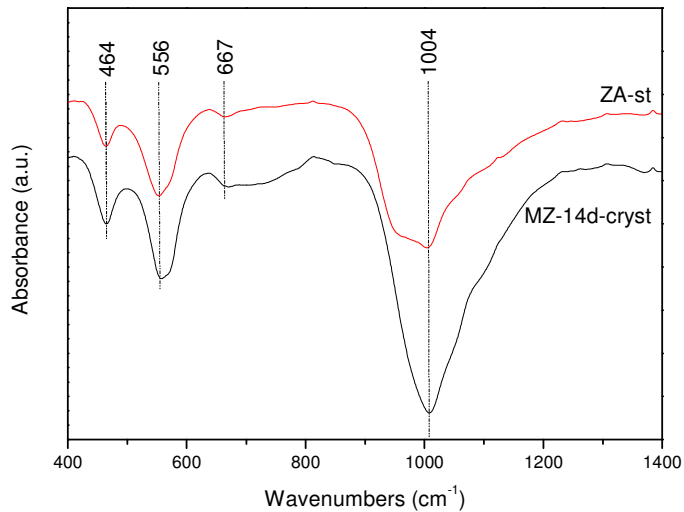


**Figure 5.4** FTIR spectra of MZ-14d-cryst and ZA-st

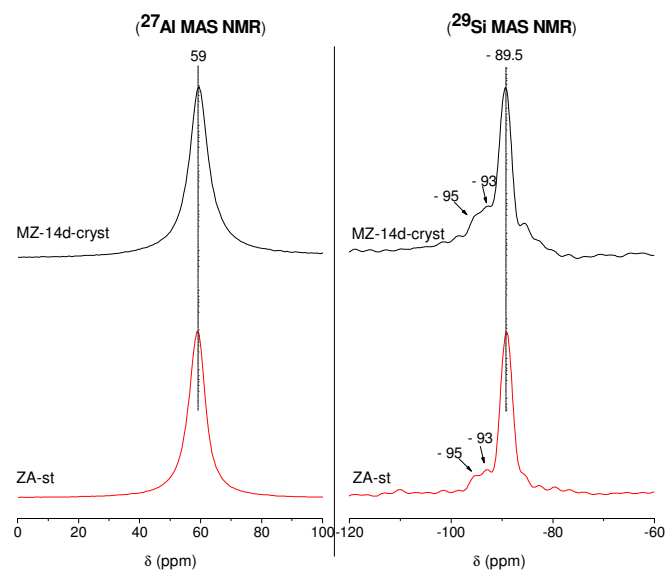


**Figure 5.5**  $^{27}\text{Al}$  MAS NMR (left) and  $^{29}\text{Si}$  MAS NMR (right) for ZA-st and MZ-14d-cryst.

The  $^{27}\text{Al}$  and  $^{29}\text{Si}$  NMR spectra of sample MZ-14d-cryst are in agreement with the spectra of ZA-st indicating the similarity in the structure of both materials (Figure 5.5). The  $^{27}\text{Al}$  spectra show a single narrow resonance signal centered at  $\delta = 59$  ppm which is assigned to tetrahedrally coordinated aluminum linked by oxygen bonds to silicon. The  $^{29}\text{Si}$  NMR spectra of ZA-st and MZ-14d-cryst show a sharp signal with chemical shift at  $\delta = -89.5$  ppm in addition to two shoulders at  $\delta = -93$  and  $-95$  ppm (Figure 5.5) which indicates that the framework structure of both materials consist mainly of  $\text{Si(OAl)}_4$  building units but with slight distortion in some sites in the lattice environment. The narrow peaks at chemical shift  $-89.5$  ppm in  $^{29}\text{Si}$  NMR and at  $59$  ppm in  $^{27}\text{Al}$  NMR spectra reveal that both materials are highly crystalline Na-A zeolite<sup>171-173</sup>.

The results obtained from XRD, FTIR and  $^{27}\text{Al}$  and  $^{29}\text{Si}$  NMR measurements indicate that both samples; namely, ZA-st and MZ-14d-cryst are Na-LTA type zeolite. Moreover, the low angle XRD and  $\text{N}_2$  adsorption-desorption analysis reveal that MZ-14d-cryst consists of a hierarchical pore structure, micro and mesopores.

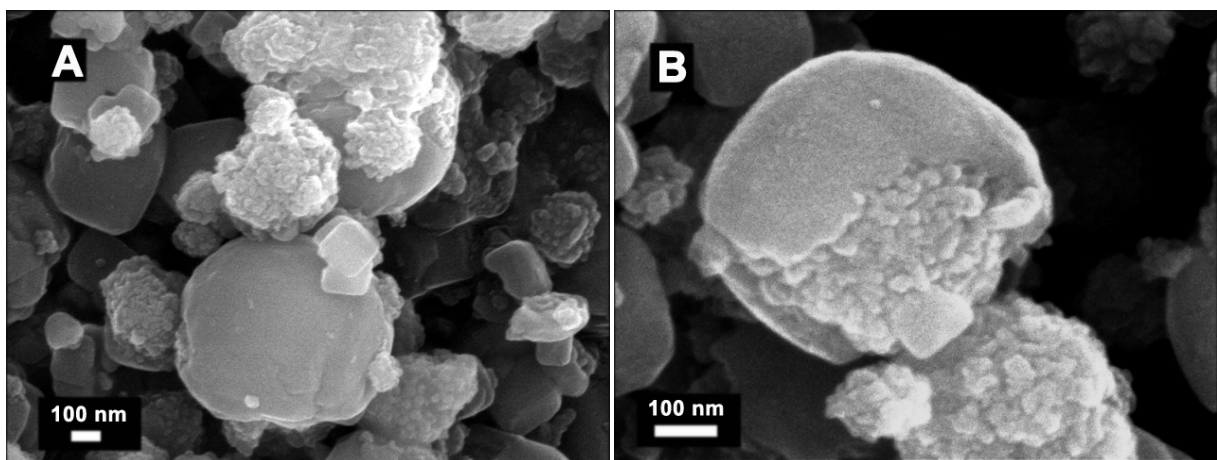


**Figure 5.6 SEM images of a group of particles (A) and focused on a single particle (B) of MZ-14d-cryst. The scale of images is 100 nm.**

The SEM results indicates that the sample MZ-14d-cryst mainly consists of two different types of particles; namely, rounded cubes with size range 300 to 570 nm and polycrystalline aggregates which show smaller size of range of 200 – 400 nm (Figure 5.6A). The diameter of the primary crystallites in the polycrystalline aggregates is 10 to 50 nm. Also, the image of a single particle in Figure 5.6B suggests that the cubic particles probably originally are polycrystalline aggregates which were recrystallized by building a cubic crystalline shell around them<sup>18</sup>.

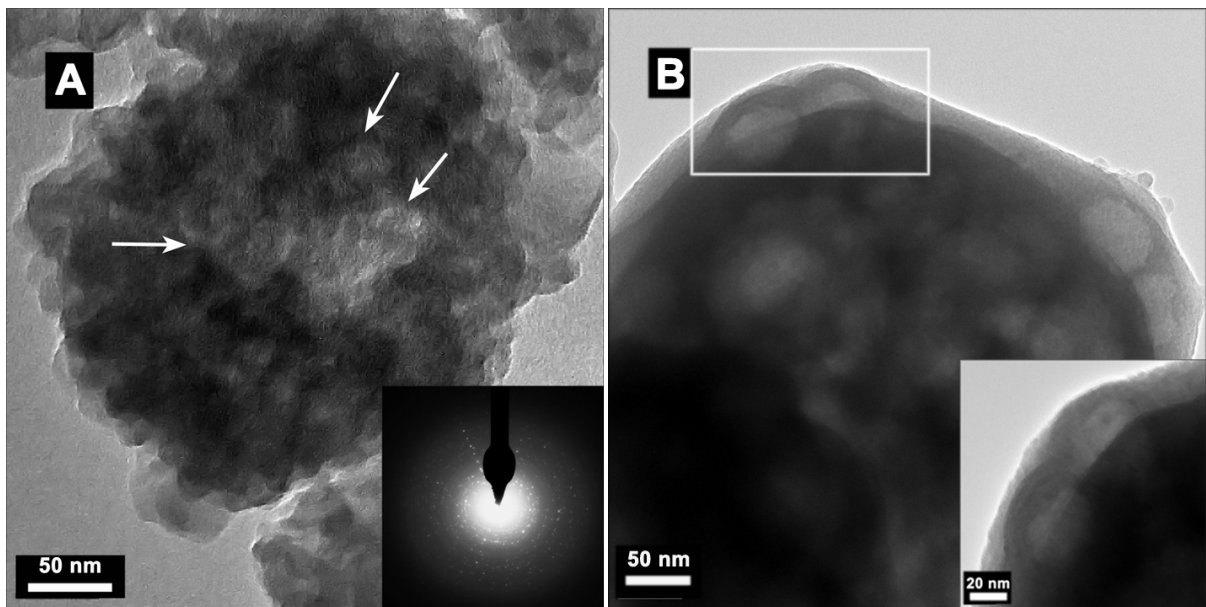


**Figure 5.7 TEM images of two different particles in the sample MZ-14d-cryst (A and B). The inset in image A shows the SAED pattern for the sample. The inset in image B shows the high magnification TEM image of the edge of the particle in (B) as marked by the rectangle.**

In agreement with the SEM results, TEM images show that MZ-14d-cryst consists of two types of particles; aggregates and cubes (Figure 5.7A, B). The aggregates are made of nanoparticles with size range of 15 – 50 nm aggregated around several hollows of size 50 – 140 nm (marked with white arrows in Figure 5.7A). A magnified image of an edge of a cubic particle reveals that the cubic shell is a thin layer surrounding aggregations of hollow structures (Figure 5.7B –inset). The size of the aggregates and the cubic particles are between 200 to 300 nm and 350 to 570 nm, respectively. The SAED pattern (Figure 5.7A -inset) of a group of particles in sample MZ-14-cryst shows polycrystalline rings and single crystal spots indicating that the sample contains polycrystalline particles and large single crystals.

The TEM and SEM results suggest that multi-hollow polycrystalline aggregates are probably formed in the early growth stage, which with increase in the crystallization time, undergo surface recrystallization by building a shell of LTA zeolite around them.

To understand the formation mechanism of the multi-hollow core-shell particles of Na-A zeolite, aliquots of the synthesis gel were taken at different periods of aging. These samples were washed, dried and calcined before being observed by means of TEM, Cryo-TEM, TGA, SEM, XRD, and ASAP 2020 (surface area).

### **5.3.1. First stage crystal growth: Formation of multi-hollow polycrystalline aggregates**

The first sample named CTAB/gel was taken directly after the addition of CTAB to the initial zeolite mixture. The TEM image of this sample shows non-uniform gel nanoparticles about 5 to 20 nm in size, which are aggregated forming large gel complexes (Figure 5.8A). On the other hand, the TEM image of sample CTAB/Dod/gel which was taken directly after introducing *n*-dodecane droplets into the CTAB/gel shows individual hollow gel particles about 20 – 45 nm in size (Figure 5.8B). The hollow diameter is between 15 – 33 nm and the shell thickness ranges between 3 to 5 nm. The image also shows tiny gel particles about 5 to 20 nm in size aggregated on the external surface of the hollow particles (marked with white arrows in Figure 5.8B).

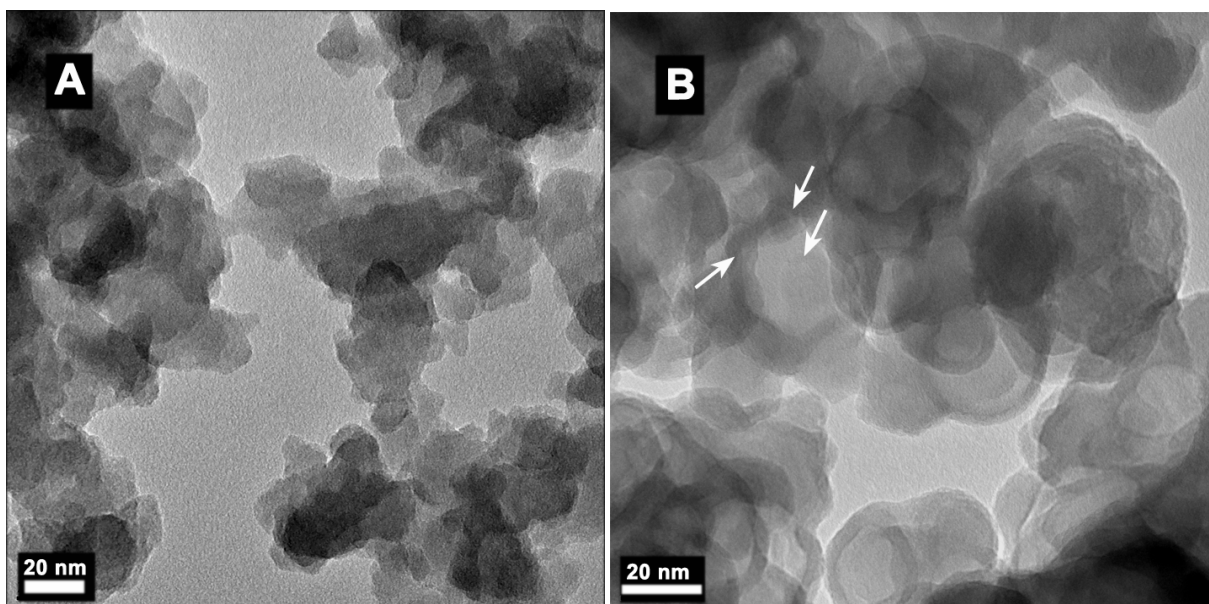


**Figure 5.8 TEM images for the aliquots taken from CTAB/gel (A) and CTAB/Dod/gel (B).**

In a complementary study, Cryo-TEM was used to measure the size distribution of freshly dispersed *n*-dodecane droplets. For this purpose, a fresh emulsion was prepared but by replacing the zeolite gel with water in order to avoid the dilution required for zeolite gel which might induce droplet coalescence. The conditions used in the preparation of CTAB/Dod/gel emulsion were retained with the preparation of fresh emulsion; such as, oil (*n*-dodecane): water ratio,

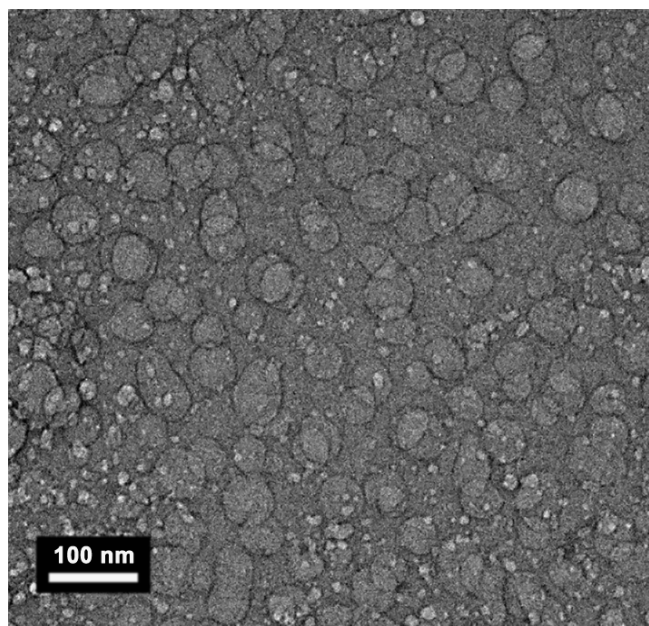


**Figure 5.9** Cryo-TEM image of a drop taken from the fresh emulsion

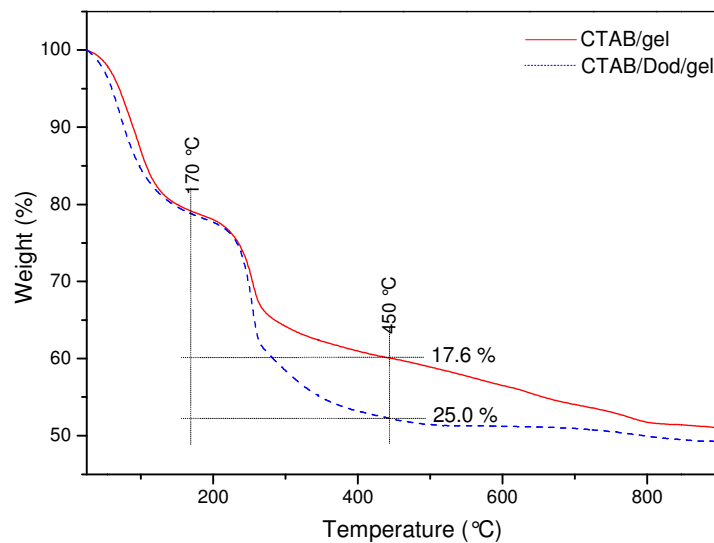


**Figure 5.10** Relative weight loss by TGA of as synthesized samples taken from CTAB/gel and CTAB/Dod/gel samples.

CTAB concentration and also the mixing conditions (speed and time). Immediately after stopping the mixer, a drop of the fresh emulsion was placed on carbon holly grid and tested by Cryo-TEM (Figure 5.9). The majority of the oil droplets show size range between 20 to 50 nm (Figure 5.9) corresponding the range of the hollow diameter observed by TEM (15 – 33 nm) (Figure 5.8B). However, some droplets with size larger than 50 and less than 150 nm were also observed.

The weight loss was also measured by thermogravimetric analyzer (TGA) on the as synthesized samples of CTAB/gel and CTAB/Dod/gel. In Figure 5.10, a 25 % weight loss was observed for CTAB/Dod/gel, due to decomposition of CTAB and *n*-dodecane between 170 to 450 °C, compared to 17.6% for CTAB/gel. This weigh loss difference can be attributed to the tiny oil droplets that might be embedded in the gel particles as observed by TEM (Figure 5.8B). Accordingly, the low contrast cores observed inside the gel particles in Figure 5.8B are probably replicates of oil droplets embedded within the gel while the dark contrast walls and the tiny aggregated particles can be attributed to aluminosilicate building units. The phase stability observed on the gel/emulsion for the entire aging period suggests that CTAB molecules were probably dissolved on the surface of the oil droplets stabilizing them as well as positively charging them (cationic ammonium group)<sup>85</sup>. Consequently, aggregation between the zeolite precursors and the positive *n*-dodecane droplets was enhanced.

The structure of the hollow gel particles was retained after 48 h aging (TEM image in Figure 5.11A) but the shell thickness increased from 5 to about 15 nm which is an indicative of more aluminosilicate species condensing on the external surface of the gel particles. Aggregation between the hollow gel particles can be observed after 6 days aging as shown in TEM results (Figure 5.11B). Also, this aggregation can be detected in the SEM image (Figure 5.12A) which shows 200 to 430 nm globular particles with a rough surface dispersed within the gel. These findings imply physical and structural rearrangements within the amorphous domain or probably a mass transformation into a crystalline phase has commenced<sup>124</sup>.

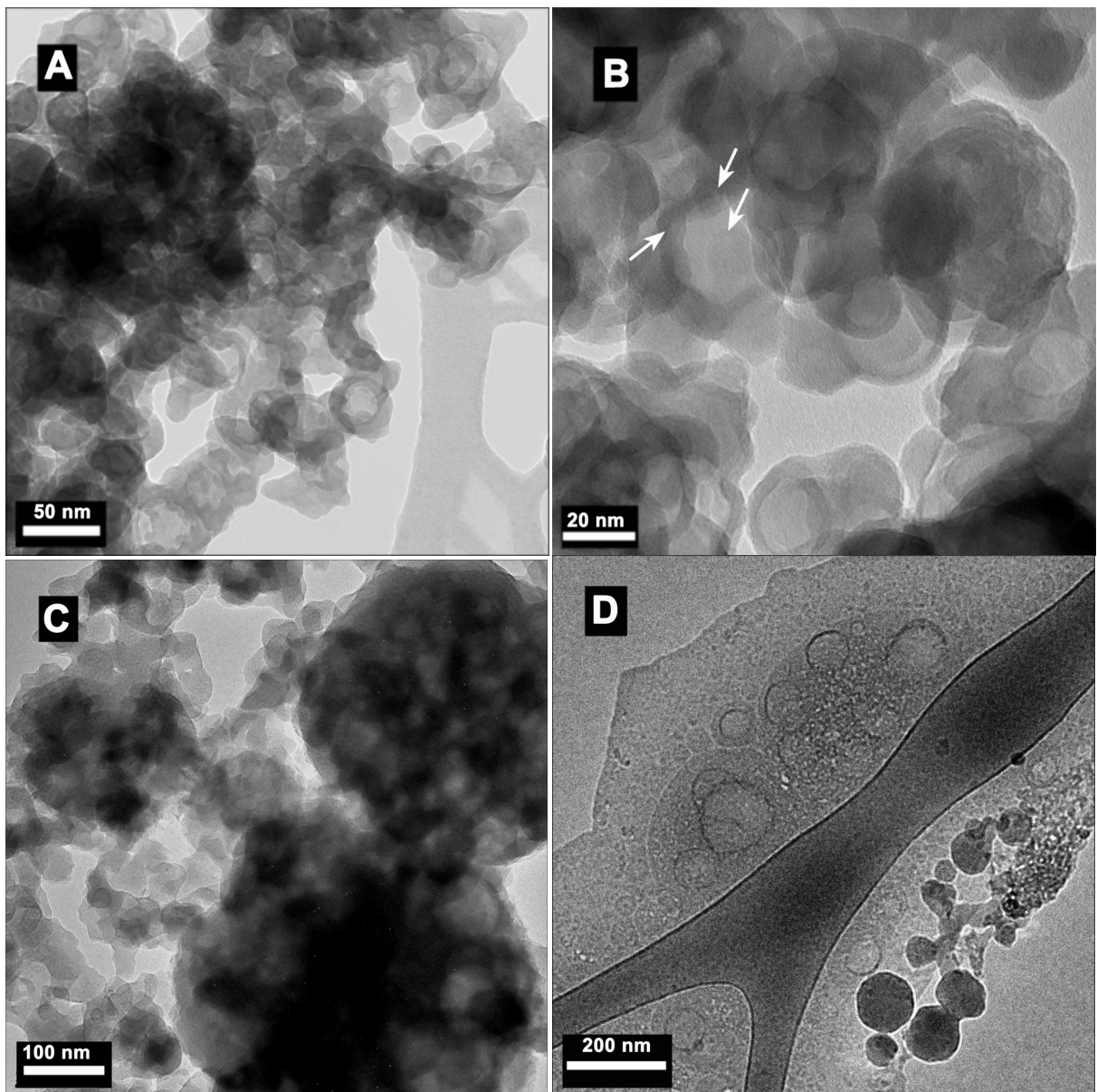


**Figure 5.11** TEM images for samples taken after 48 h (A), 6 days (B) and 9 days aging (C). Cryo-TEM image for the gel sample taken after 9 days aging (D).

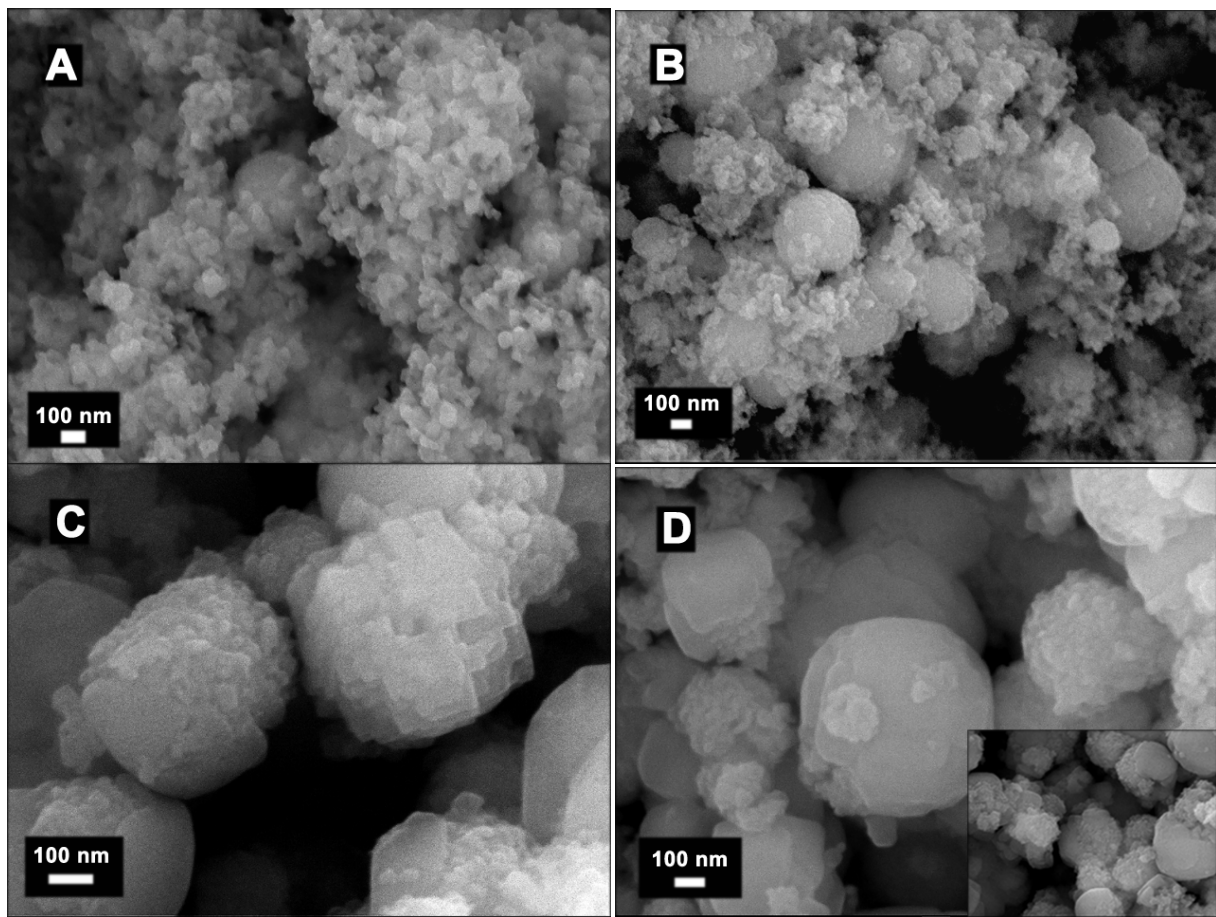


**Figure 5.12 SEM images for samples taken after 6d (A), 9 days (B) 12 days (C) and 14 days aging (D).**

However, the XRD patterns for the sample MZ-5d (Figure 5.13A) does not show any diffraction peaks, but only a broad peak ranging from  $15^\circ$  to  $40^\circ$   $2\theta$ . Nevertheless, the absence of Bragg diffractions does not necessarily mean the absence of a crystalline phase in the system, there are probably some crystals formed but XRD could not detect them either because they are embedded in the abundant amorphous gel or their size is very small<sup>174</sup> or because the amount of the crystalline phase is less than the detection limit (3 – 4 wt%) of the XRD technique<sup>124</sup>. The sample taken after 7 days aging shows diffraction peaks corresponding to LTA zeolite reported in literature<sup>140</sup>.

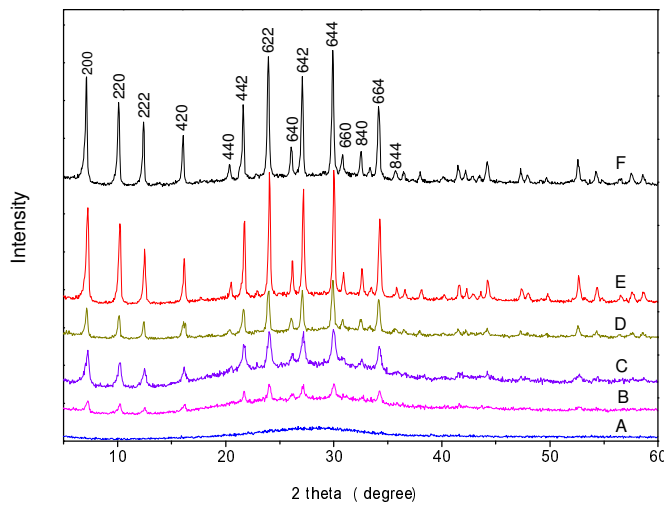


**Figure 5.13 Powder X-ray diffraction patterns of Na-A zeolite samples collected at different aging periods, 5 (A), 7 (B), 9 (C), 12 (D), 14 (E) days and also the pattern of the sample crystallized at elevated temperature after 14 days aging MZ-14d-crys (F). Indicated peaks can be linked to the literature<sup>140</sup>**

A substantial increase in the size and the number of the globular aggregates was observed in the SEM image after 9 days aging (Figure 5.12B). Also the TEM investigations for the same sample (Figure 5.11C) shows large particles with size range 350 to 430 nm that contain several hollows with diameter of 40 to 80 nm surrounded with aggregated nanoparticles. At the same stage a sample was taken from the gel/emulsion and examined by the Cryo-TEM (Figure 5.11D). Before the examination, the sample was diluted fivefold with water, shaken and immediately a drop was taken and placed on a carbon grid. The Cryo-TEM results show large particles with diameter of 360 to 480 nm holding oil droplets with diameter of 45 to 130 nm (Figure 5.11D), which are in agreement with TEM suggesting that the hollows are “casts” of the removed oil (*n*-dodecane) droplets.

The XRD pattern for the sample MZ-9d (Figure 5.13D) shows broad diffraction peaks with a “hump” in the mid range  $2\theta$  indicating that the material contains both nanosized LTA zeolite crystals and amorphous phase. Nevertheless, the XRD (Figure 5.13D) and the SEM (Figure 5.12C) investigations of MZ-12d shows that the amorphous phase disappears after 12d indicating the completion of mass transformation of the amorphous gel into crystalline phase.

A careful and close investigation of the SEM results of MZ-12d (Figure 5.12C) shows that the primary particles forming the aggregates became larger and more faceted compared to MZ-9d sample (Figure 5.12B). The above results suggest that the system most probably undergoes a nucleation/growth mechanism similar to the mechanism observed in the LTA zeolite formation at room temperature in a TMA-containing system<sup>125</sup>. The process can be summarized as follows, nuclei were probably formed inside the primary gel particles surrounding the droplets and then the viable nucleus grew by propagation consuming the gel phase surrounding them forming an LTA zeolite crystallite. During the growth of the crystallites, a mechanism of aggregation around the crystalline center was induced forming the globular aggregates<sup>124</sup>. After the crystallites formation was completed and the amorphous phase was exhausted in the period between 9 to 12 days; the system most likely entered the Ostwald ripening stage, in which the large particles grow at the expense of small particles<sup>18</sup>. Therefore, the size of crystallites composing the aggregates in MZ-12d is larger than in MZ-9d.

### ***5.3.2. Second stage of crystallization: Formation of multi-hollow polycrystalline core-shell particles***

The SEM investigation also shows that crystalline islands were developed on the surface of some of the polycrystalline aggregates (Figure 5.12C). By prolonging the aging period to 14 days (Figure 5.12D) these islands extended and merged forming a thin shell around the aggregates and then, more interestingly, oriented themselves forming the characteristic cubic shape of LTA zeolite (Figure 5.12D). The development of polycrystalline aggregates into single cubic crystals by surface recrystallization is directed under the force of minimizing surface free energy<sup>18, 162, 175</sup>.

The substantial increase in the intensity of the XRD diffractions of sample MZ-14d compared to MZ-12d (Figure 5.13D, E) suggests a rapid crystal growth which is, however, unlikely to occur at ambient conditions<sup>124</sup>. Therefore, it is more likely that the obtained single crystals of LTA type zeolite in fact are thin crystalline shell of LTA zeolite built around the hollow-polycrystalline aggregates which confirms the SEM results. However, in addition to single

crystals, the sample also contains polycrystalline aggregates which are free of or partially covered with crystalline shell (Figure 5.12D-inset).

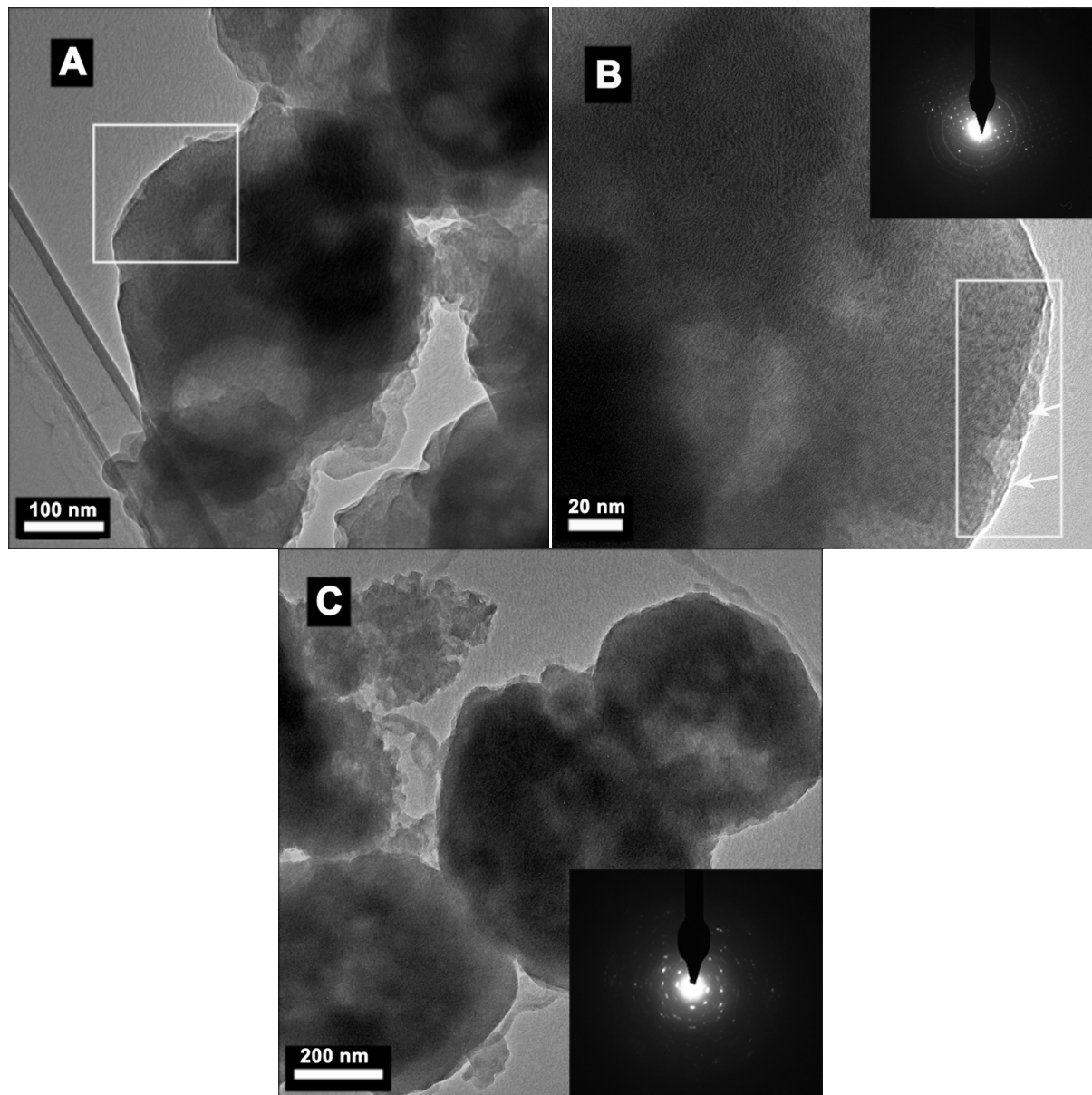


**Figure 5.14** Low and high magnification images of a particle from MZ-12d (A, B). Corresponding SAED pattern of the same particle (B-inset). TEM image of another group of particles from MZ-12d (C) with corresponding SAED pattern (C-inset).

The TEM images of MZ-12d (Figure 5.14A, C) show particles with hollow polycrystalline core. The magnified image of the area as marked by a white square in Figure 5.14A shows clearly the aggregated nanocrystallites covered with a thin shell (white arrows in Figure 5.14B). Also, the TEM measurements indicate that the size range of the hollows confined within the

polycrystalline core is 40 to 130 nm which is consistent with Cryo-TEM measurements (Figure 5.11D). The inset in Figure 5.14B is the corresponding SAED pattern which shows overlap of polycrystalline rings with single crystal diffraction spots. From the beam outward, three polycrystalline rings can be indexed to (622), (642) and (840) reflections in LTA zeolite structure, while the reflections of single crystal can be indexed to (200), (222), (440), (444) and (840). The SAED pattern of the particles presented in Figure 5.14C shows diffraction spots oriented in rings that can be indexed to (420), (622), and (820) planes in LTA zeolite structure (Figure 5.14C-inset). In other words, TEM and SAED investigations provide more evidence confirming that MZ-12d is LTA zeolite with two different morphologies *viz.* multi-hollow polycrystalline aggregates and single cubic crystals with multi-hollow-polycrystalline core.

It is well known that meso-sized voids among aggregated nanocrystallites can be considered as mesopores<sup>8, 54, 101, 121, 167</sup>. In a complementary study, N<sub>2</sub> adsorption-desorption analysis at 77K was conducted on samples taken after 6, 7, 8, 9, 12, 14 days aging to investigate the formation of the mesopores among the aggregated crystallites and to correlate this to the crystal growth mechanism. The isotherms of the samples aged for less than 9 days are type I which is typical of microporous materials (Figure 5.15A). The samples collected at day 12 and 14 show type IV isotherms with hysteresis loops at relative pressure higher than 0.4 indicating the presence of meso-sized pores (Figure 5.15C)<sup>176</sup>. The pore size distribution measured from the adsorption branch using the BJH method show that MZ-6d, MZ-7d, MZ-8d and MZ-9d mainly contained small mesopores at size range between 1.7 and 2.5 nm. However, very small peaks centered at higher pore width were also observed (Figure 5.15B and Table 5.1). The small mesopores are probably formed due to the presence of some small CTAB micelles (normal size 2 to 4 nm) within the amorphous gel. Thus, high specific surface area and high mesopore volume were measured in these samples (Table 5.1). The large mesopores are more pronounced in sample MZ-12d as demonstrated by two distinctive peaks centered at 6.4 and 9 nm in BJH pore size distribution in Figure 5.15D.

The SEM investigations indicated that only a few globular particles were presented in the sample collected after 7 days aging (Figure 5.12A), however, the number increased significantly after 9 days aging (Figure 5.12B). Thus, the appearance of small peaks in the large mesopore region of the BJH pore size distribution can be attributed to the voids among the aggregated gel nanoparticles in the globular particles.

The reduction in the specific surface area and the mesopore volume of the samples collected between day 7 and 9 is an indication that some gel evolution and aluminosilicate precursors reorganization has taken place.

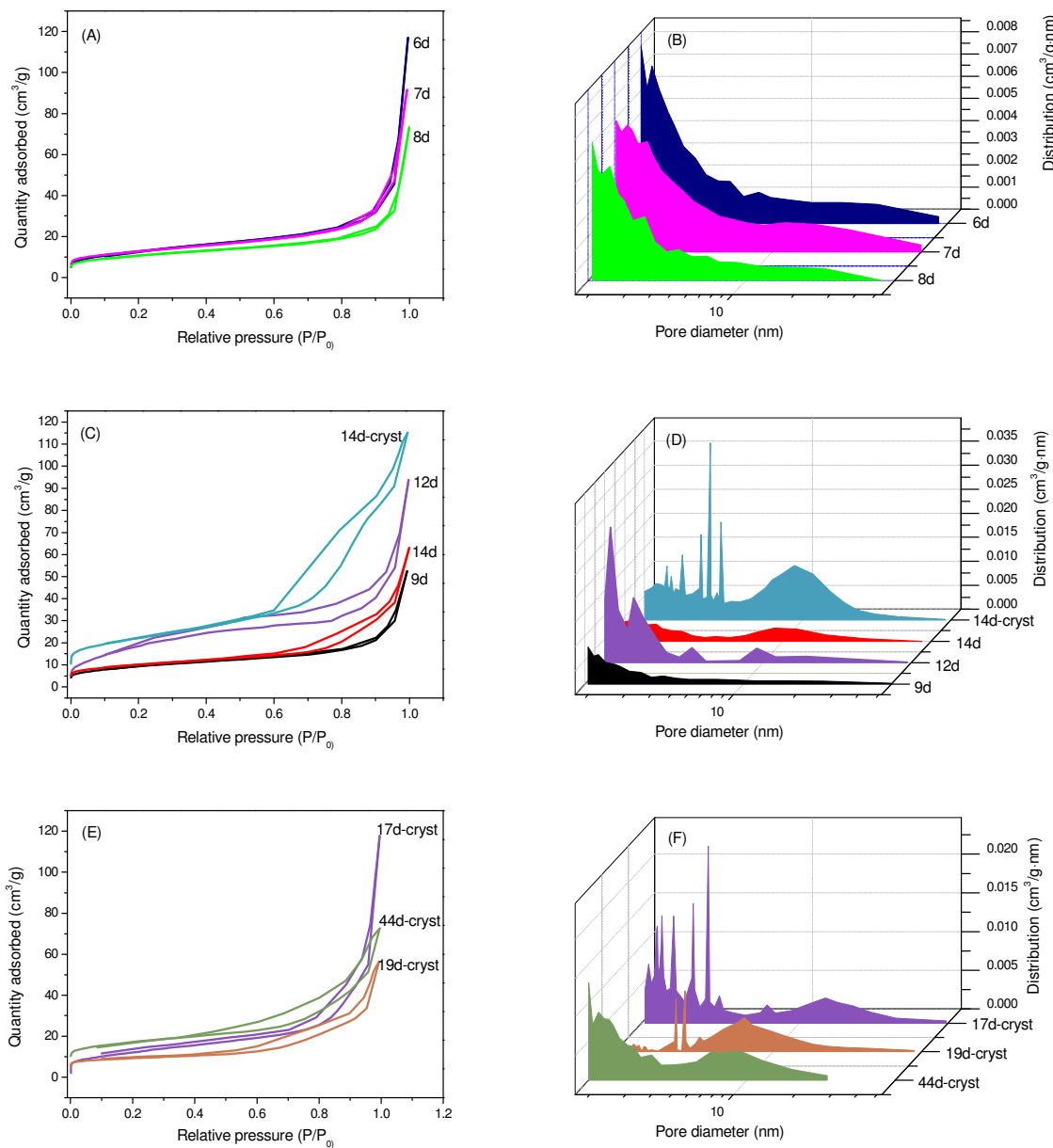


**Figure 5.15**  $\text{N}_2$  adsorption-desorption isotherms (A, C and E) and corresponding pore size distribution (B, D and F) of the samples aged for 6, 7, 8, 9, 12 and 14 days and of samples MZ-14d-cryst, MZ-17d-cryst, MZ-19d-cryst and MZ-44d-cryst.

**Table 5.1 Textural properties of reference Na-A zeolite (ZA-st), samples collected after various aging periods; 9, 12, 14 days and of MZ-14d-cryst-Ca<sup>+2</sup>**

Sample	$S_{\text{BET}}^a$ (m <sup>2</sup> .g <sup>-1</sup> )	$V_{\text{micro}}^b$ (cm <sup>3</sup> . g <sup>-1</sup> )	$V_{\text{meso}}^c$ (cm <sup>3</sup> .g <sup>-1</sup> )	$d_{\text{meso}}^d$ (nm)
ZA-st	22.43	-	0.028	-
MZ-6d	45.72	-	0.17	1.7, 1.9, 6.4
MZ-7d	43.68	-	0.13	1.7, 1.9, 2.5, 11.6
MZ-8d	37.2	-	0.1	1.7, 2.1, 3.2, 4.7
MZ-9d	32.92	-	0.07	1.8, 4.1, 6.4
MZ-12d	70.58	-	0.13	1.8, 2.7, 4.5, 9.3
MZ-14d	33.12	-	0.12	2, 2.5, 9.1
MZ-14d-cryst <sup>e</sup>	76.06	-	0.17	2.2 – 2.6, 3.5, 4, 9.1
MZ-17d-cryst <sup>f</sup>	42.5	-	0.17	~2.5, 3.5, 4, 6.9, 13.3
MZ-19d-cryst <sup>g</sup>	28.4	-	0.08	1.7, ~2.5, ~3.5, 4.3, 7.2
MZ-44d-cryst	56.9	-	0.1	1.7, ~2, ~3.4, 9.2
MZ-14d-cryst-Ca <sup>+2</sup>	380.6	0.16	0.13	1.7, 2.1, 6.2, 8.8

<sup>a</sup> Surface area obtained at relative pressure range of 0.05 – 0.3. <sup>b</sup> micropore volume as calculated by t-plot. <sup>c</sup> Mesopore volume was collected on pore size range between about 1.7 to 50nm. <sup>d</sup> Mesopore size distribution measured by BJH adsorption  $dV/dD$  pore volume. <sup>e</sup> This sample was named as MZ-0.14C-8.5D and MZ-0.14C-8.5D-14 in chapter 4. <sup>f</sup> This sample was named MZ-0.14C-8.5D-17 in chapter 4. <sup>g</sup> This sample was named MZ-0.14C-8.5D-19 in chapter 4.

After increasing the aging period to 14 days, the peak in the large scale mesopore region became broader ranging between 6.5 to 10.5 nm (Figure 5.15D). As the Na-A zeolite does not adsorb N<sub>2</sub> at 77K, the adsorption in this work was attributed to the mesopores which are represented by the voids between the aggregated crystallites. Thus, the appearance of large mesopores after 12 days which was enhanced after 14 days aging may be correlated to the size increase of the primary crystallites by Ostwald ripening within the polycrystalline aggregates, as was observed in SEM images in Figure 5.12C<sup>54</sup>.

In a complementary study, FTIR spectra were recorded for series of aliquots taken after different aging periods; 48 h and 6, 9 and 14 days (Figure 5.16). As described above, bands around 464, 556, 667 cm<sup>-1</sup> are the structure sensitive vibrations of LTA zeolite. These bands could not be observed in the spectrum of the sample taken after 48 h indicating the absence of LTA zeolite structure and suggesting that the sample is amorphous aluminosilicate gel<sup>124</sup>. Also, it was difficult to detect these bands clearly in the spectrum of the sample taken after 6 days aging in-spite of the small diffraction peaks observed in the XRD pattern of the same sample (Figure 5.13). However, with increasing the aging period to 9 and 14 days, the bands near 464, 556, 667 cm<sup>-1</sup> became sharper and can be distinguished easily indicating the presence of LTA zeolite structure. Further evidence of the gel evolution and zeolite formation is the gradual disappearance of the band observed near 850 cm<sup>-1</sup>. This band is attributed to Si–OH bending vibration; therefore, the simultaneous reduction of the intensity of this band with increasing the sharpness of LTA zeolite characteristics bands suggests increasing the number of atoms linked via oxygen to form LTA zeolite framework structure<sup>147</sup>.

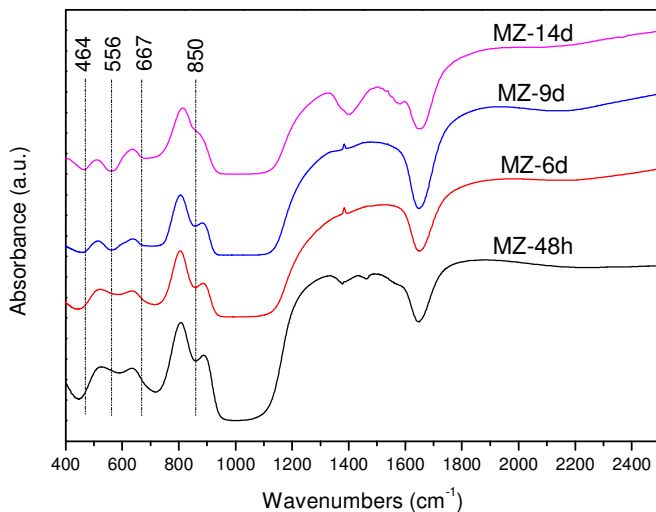


**Figure 5.16** FTIR spectra of series of samples taken after different aging periods; 48 h and 6, 9 and 14 days.

High temperature crystallization for the sample aged for 14 days does not show a noticeable increase in the intensity of the XRD peaks (Figure 5.13E, F) which suggests no increase in the size of the particles. However, the BET surface area and the mesopore volume were increased while retaining the size of the large scale mesopores (Figure 5.2, inset and Table 5.1). On the

other hand, the range of the small mesopores was retained over the period from 9 to 14 days and even after the high temperature crystallization, but the size distribution changed suggesting continuous local structural evolution.

Close observation by SEM of a particle in MZ-14d-cryst (Figure 5.6B) shows a shell thickness of about 50 nm which is more than that observed in either MZ-12d or MZ-14d. The increase in the shell thickness accompanied with maintaining the size of the particles (as inferred from XRD and SEM results) suggests a reverse crystallization mechanism from surface to core. In some zeolite systems, spherical aggregates of nanoparticles are formed in the early stage of crystal formation followed by surface recrystallization which is extended reversely to the core<sup>18, 19, 141</sup>. Such a route was observed in analcime zeolite system and called NARS (nanocrystallites-aggregation-surface recrystallization-single crystal)<sup>18</sup>. Until recently the only growth mechanism recognized for zeolites crystals was based on so called Bravais-Friedel-Donnay-Harker (BFDH) law and Hartman-Perdok theory<sup>18, 19, 141, 162</sup>. According to these theories, nuclei are formed and then grown slowly via atom by atom addition into layers resulting in monocrystalline zeolite<sup>125, 141</sup>.

### 5.3.3 Third stage of crystallization: Aging for longer than 14 days

This section discusses detailed investigations conducted by XRD, SEM and N<sub>2</sub> adsorption-desorption analysis on samples aged for 17, 19 and 44 days before being subjected to high temperature crystallization.

The XRD measurements shown in Figure 4.10A indicate that diffraction peaks of the sample aged for 17 days show higher intensities than the peaks of the pattern of sample MZ-14d-cryst. Accordingly, it can be inferred that the crystal growth continued till day 17. However, similar diffraction intensities can be observed for MZ-17d-cryst and MZ-19d-cryst (Figure 4.10A) suggesting that prolonging the aging period to 19 days does not have a noticeable influence on the crystal size.

These results reveal that the LTA framework structure was retained even after 19 day aging. In contrast, the XRD pattern of the sample collected after 44 days showed extra three peaks at 20.6.15°, 15.5° and 23.25° indicating the presence of a trace of impurity which probably was FAU zeolite (Figure 5.17) in addition to LTA. The long term aging resulted in formation of another

phase probably due to change in either the concentrations of the precursors or some of the precursors depleted after long reaction period. Hence, the dissolution and recrystallization of the small crystallites in presence of a different concentration milieu induced the formation of another framework structure.

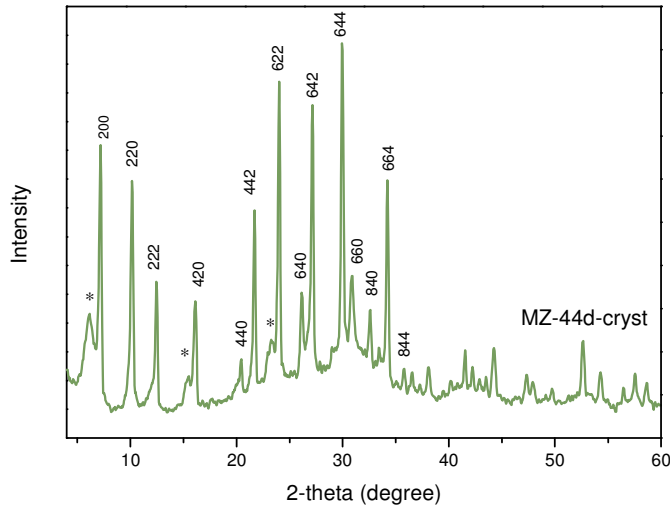


**Figure 5.17 XRD pattern of sample MZ-44d-cryst. The peaks marked with star correspond the FAU phase.**

In Figure 5.18 and Table 5.2, the SEM shows the effects of aging for longer than 14 days on the crystal size and morphology. Figure 5.18A, C and E clearly show that the number of the polycrystalline aggregates was reduced in sample MZ-17d-cryst and MZ-19d-cryst compared to MZ-14d-cryst. Alternatively, a substantial increase in the proportion of monocrystals with cubic or irregular (between spherical and cubic) morphologies can be observed. The high magnification SEM image of sample MZ-14d-cryst in Figure 5.18B shows that the aggregates were partially converted into cubic by building a shell on their surfaces. In contrast, Figure 5.18D and F suggest that the surface recrystallization continued and the crystalline islands on the surface of the polycrystalline aggregates fused together and oriented themselves forming single crystals with different morphologies and sizes.

The particle size distributions of samples MZ-14d-cryst, MZ-17d-cryst, MZ-19d-cryst and MZ-44d-cryst are listed in Table 5.2. Generally in all samples, the polycrystalline aggregates are smaller than the cubic morphology particles. This was expected because the cubes originally

were polycrystalline aggregates but they were covered with shell of a particular thickness which depends of the length of reaction/aging period.

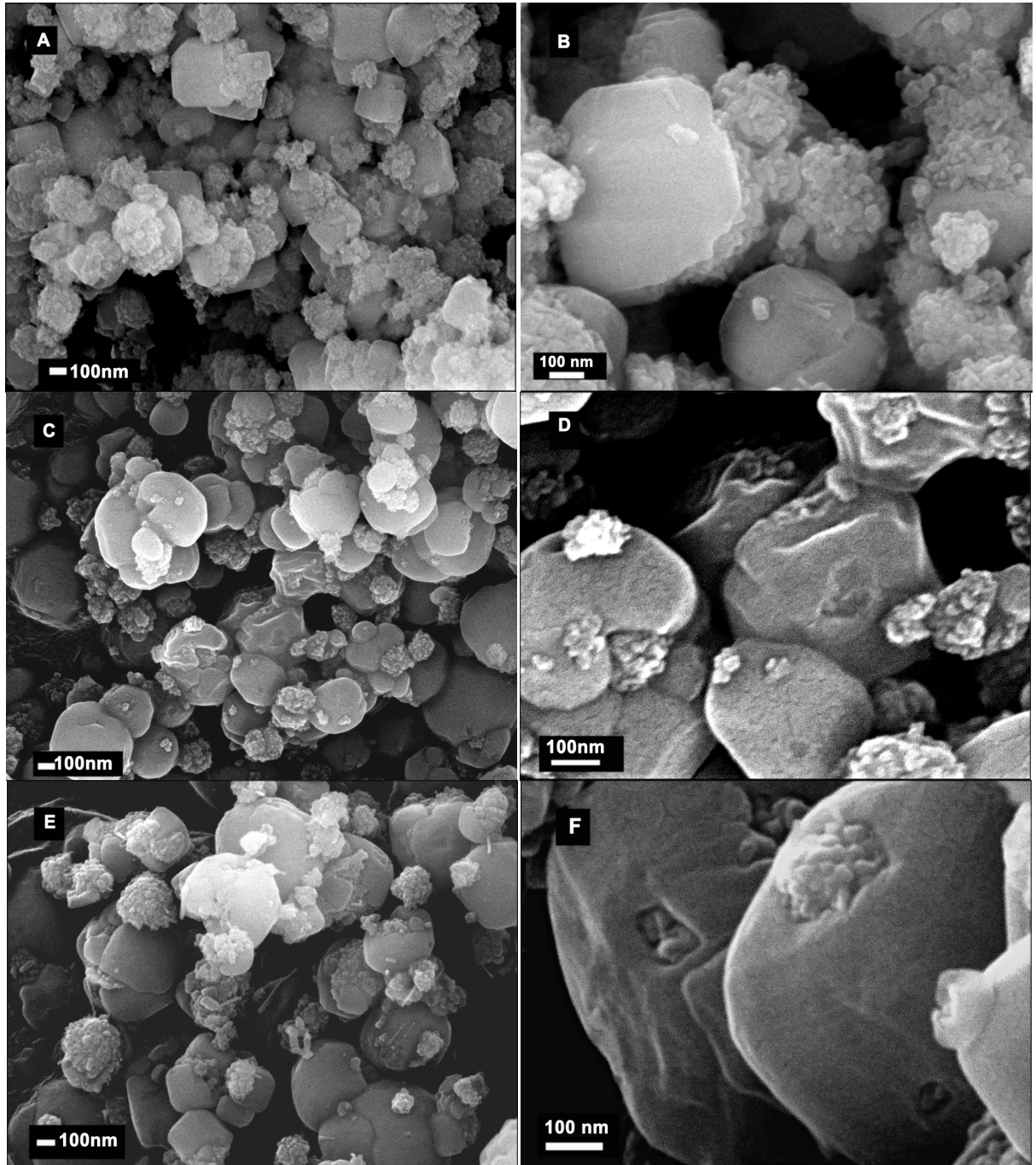


**Figure 5.18 SEM images of samples MZ-14d-cryst (A and B), MZ-17d-cryst (C and D) and MZ-19d-cryst (E and F).**

The size of the aggregates in sample MZ-14d-cryst ranges between 200 and 400 nm, whereas the size of the cubes was between 300 and 570 nm (Table 5.2). Cubes with larger scale were

observed in samples MZ-17d-cryst and MZ-19-cryst at 722 and 1000 nm, respectively. At the same time, the range of the size of the polycrystalline aggregates reduced to 150 – 350 nm in sample MZ-17d-cryst and to 100 – 350 nm in sample MZ-19d-cryst. The simultaneous increase in the size of the cubes and reduction in the size of the aggregates verify that the cubes were growing at the expense of the aggregates *via* Ostwald ripening process. In other words, the small aggregates dissolved providing aluminosilicate precursors which reorganized constructing another layer of the external surface of the cubic particles.

These results are in good agreement with the XRD measurements which indicated that the patterns of MZ-17d-cryst and M-19d-cryst showed diffraction peaks with higher intensities than the MZ-14d-cryst (Figure 4.10A).

**Table 5.2 Particle diameter as determined by SEM for samples aged for 14, 17, 19 and 44 days before being undertaken a high temperature crystallization.**

Sample name	Cubic crystals (nm)	Aggregates (nm)	Crystallites (nm)
MZ-14d-cryst	300 – 570	200 – 400	15 – 30
MZ-17d-cryst	300 – 722	150 – 350	13 – 33
MZ-19d-cryst	200 – 1000	100 – 350	15 – 30
MZ-44d-cryst	300 – 600	100 – 350	10 – 30

Figure 5.19A and B exhibit the SEM images of sample MZ-44d-cryst which was synthesized from gel aged for 44 days at room temperature before being subjected to high temperature crystallization. Careful and close observation of images 5.19A and B suggests that the small size polycrystalline aggregates with size around 100 nm were self assembled forming larger aggregate (inside the white rectangle in image 5.19B) and hence undertaken surface recrystallization growth route. Furthermore, the average size of the large single particles decreased to 600 nm which is smaller than the single crystals in sample MZ-17d-cryst and MZ-19-cryst (Table 5.2). These results imply that probably both types of particles, the polycrystalline aggregates and the single crystals, had undertaken dissolution recrystallization growth

mechanism<sup>17</sup>. The size of the primary crystallites in all samples was retained in the range 13 – 30 nm (Table 5.2).

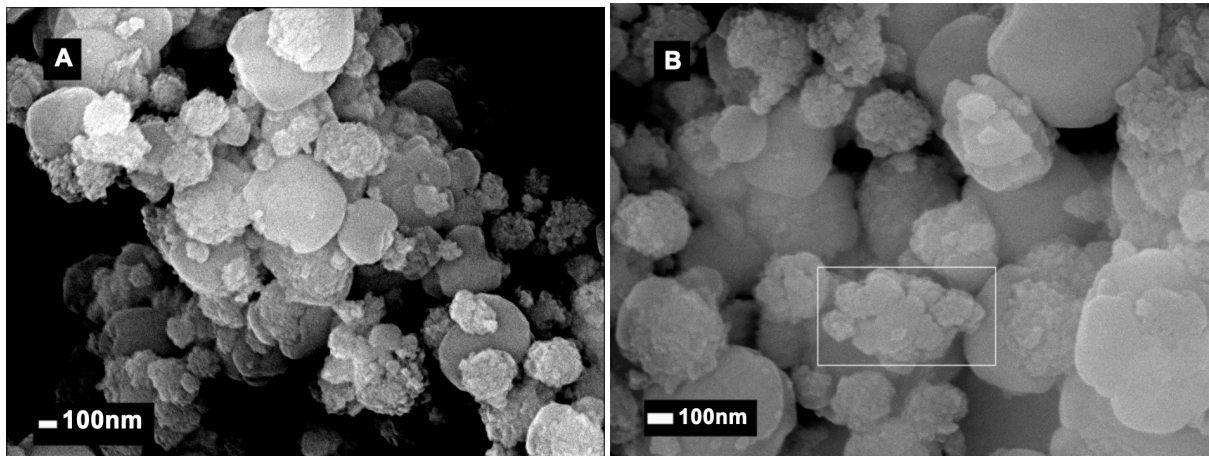


**Figure 5.19 SEM images of sample MZ-44d-cryst.**

The N<sub>2</sub> adsorption-desorption measurements indicate that increasing the aging period from 17 or 19 days resulted in decreasing the specific surface area and the mesopore size distribution. Table 5.1 shows that the BET surface area of MZ-14d-cryst was 76.06 m<sup>2</sup>·g<sup>-1</sup>, however, it reduced to 42.5 and 29.4 m<sup>2</sup>·g<sup>-1</sup> in samples MZ-17d-cryst and MZ-19d-cryst, respectively. The mesopore volume was retained with extending the aging period from 14 to 17 days, however, the pore size distribution shows significant changes in large scale mesopores (Table 5.1 and Figure 5.15E and F). A substantial reduction in the mesopores volume (0.08 cm<sup>3</sup>·g<sup>-1</sup>) and a significant difference were observed in the sample collected and crystallized after 19 days aging. The isotherms of samples MZ-17d-cryst and MZ-19d-cryst are type IV with H3 hysteresis suggesting that both samples are mesoporous LTA zeolites (Figure 5.15E).

These results are in good agreement with the findings obtained from the SEM and the XRD. As a result of prolonging the aging period, the transformation of the polycrystalline aggregates into single Na-A zeolite crystals enhanced and thus the XRD showed higher intensity and the N<sub>2</sub> adsorption decreased.

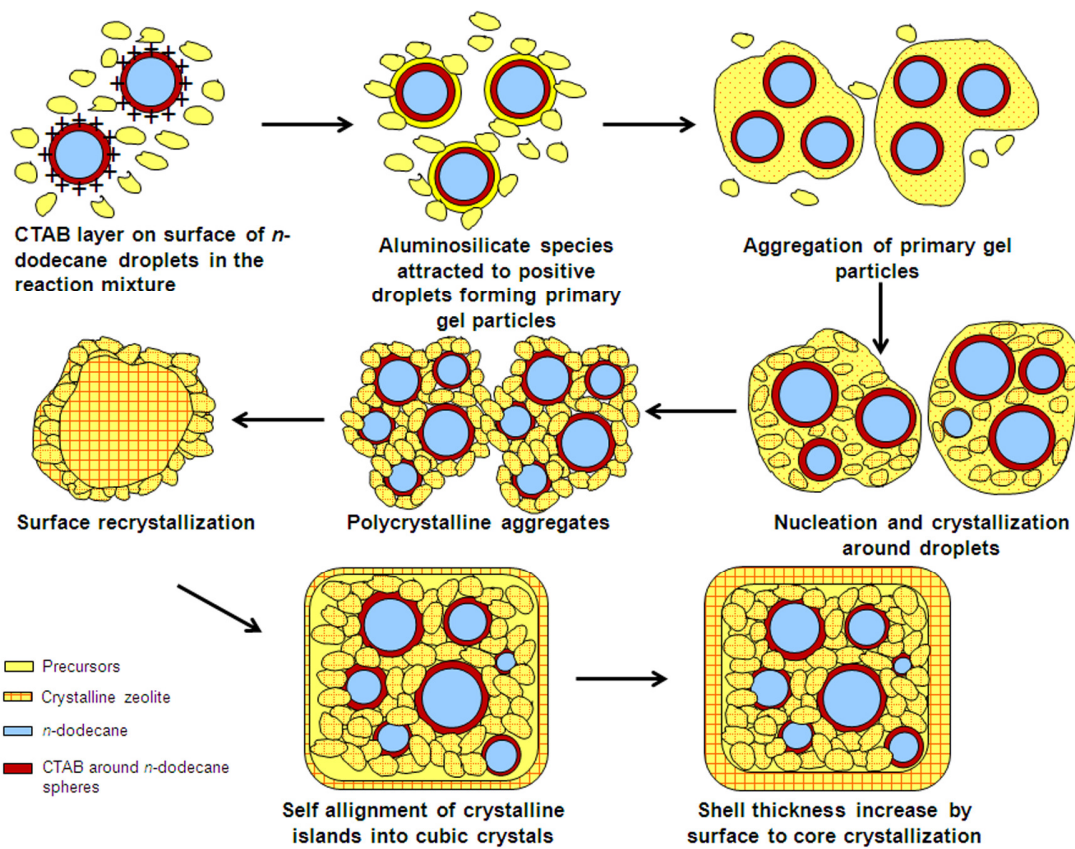
Further increase of the aging period to 44 days resulted in increase in the BET surface area to 56.9 m<sup>2</sup>·g<sup>-1</sup>, however, only a slight increase in the mesopores volume (at 0.1 cm<sup>3</sup>·g<sup>-1</sup>) was observed. The reason is probably the reduction in the size of the particles in general as observed by the SEM investigations.

### **5.3.4 Growth mechanism**

LTA zeolite has demonstrated an aggregation-recrystallization growth mechanism in the presence of chitosan biopolymer. Chitosan molecules aggregated with LTA zeolite precursors forming spherical aggregation which then were crystallized into single cubes with amorphous core<sup>162</sup>. Longer synthesis time resulted in reverse crystal growth but the zeolite phase transformed from LTA to sodalite <sup>19</sup>. In contrast, in our work the nanoparticles within the aggregates crystallized and grew forming polycrystalline aggregates prior to the surface recrystallization (as confirmed by XRD, SEM and TEM). We believe that probably the moderate crystallization conditions (room temperature) induced local crystallization and growth of each nanoparticle within the amorphous aggregates unlike the chitosan system where surface crystallization was faster than crystallite growth. Thus, the crystal growth mechanism in our system is probably more compatible with NARS route of core-shell and hollow icositetrahedra analcime zeolite <sup>18</sup>. However, the hollow formed in analcime crystals were due to reverse crystal growth while in our system were replicates of *n*-dodecane droplets as evidenced by the results obtained from TEM, Cryo-TEM and TGA. Thus, our work provides new insight into LTA zeolite crystallization by synthesizing monocrystalline cube-like Na-A zeolite shell with multi-hollow polycrystalline core.

In summary, the proposed crystal growth mechanism for the synthesis is shown in scheme 1 and can be described as follows: (1) Attraction of the aluminosilicate species and tiny building blocks to the surface of *n*-dodecane droplets directed by the positive ammonium groups on the surface of the droplets (primary nanoparticles) (2) Simultaneous nucleation-crystallization and aggregation forming secondary aggregates. (3) Completion of nanoparticle crystallization forming polycrystalline aggregates. (4) Increase in the size of the crystallites by Ostwald ripening process. (5) Surface recrystallization forming thin islands of Na-A zeolite on the surface of the polycrystalline aggregates. (6) In some particles, these islands might be joined together and self aligned according to their crystallographic orientation forming cubic crystals of LTA zeolite with polycrystalline core. (7) Prolonging the aging period to 14 days followed by subjecting the samples to high temperature crystallization induce surface to core crystallization which can be observed easily in the polycrystalline aggregates that are partially covered with the Na-A zeolite islands. The shell thickness increases by consumption of the nanocrystallites that attached to it by Ostwald ripening process. (8) Removing the CTAB layer and the *n*-dodecane

droplets by calcination leaves hollows which are replicas of the droplets inside the polycrystalline core.



**Scheme 5.1** Proposed mechanism for the synthesis of Na-A zeolite crystals with multi-hollow polycrystalline core.

## 5.4 Conclusion

We have demonstrated that Na-A zeolite crystals consisting of thin crystalline polyhedral shell and multi-hollow polycrystalline core can be synthesized by conducting a two step crystallization in the presence of emulsion droplets. The product also shows some particles which are multi-hollow polycrystalline aggregates that contain large mesopores attributed to voids among the aggregated crystallites. By systematic investigations of samples taken at different reaction stages, it is demonstrated that in presence of emulsion droplets, Na-A zeolite particles with multi-hollow polycrystalline core-shell structure can be grown according to an aggregation-recrystallization approach in contrast to the classic growth mechanism. The presence of positive *n*-dodecane droplets within the zeolite reaction mixture enhances the formation of nanoparticle aggregates at the early stage of gel evolution and organization. By conducting the crystallization at room temperature, the aggregated nanoparticles are crystallized locally forming polycrystalline aggregates which then undergo a reversed crystal growth. The crystallization takes place on the surface of the polycrystalline aggregates and extends inward. This work demonstrates two points; the synthesis of new kind of mesoporous Na-A with multi-hollow polycrystalline morphology and, for the first time, formation of LTA zeolite crystal *via* reverse crystallization route while retaining the identity of LTA zeolite.



# ***Chapter 6: Zeolite monoliths with channel structure mimicking a tree's vascular system: High effective diffusivity, low pressure drop and high adsorption capacity***

## **6.1 Introduction**

As described in section 2.8 (literature review), zeolite is powder and if placed directly in a packed bed reactor or adsorber will result in a large pressure drop. Conventionally, zeolite powder is mixed with a binder and shaped as pellets or beads a few millimeters in size which then are randomly packed in the adsorption column. The pressure drop in such processes is moderate but the mass transfer resistance through the macropores of the pellets / beads is very high. Numerous studies have been conducted to develop hierarchical structured adsorbents which show competitive or better adsorption characteristics than commercial beads<sup>40, 60-62, 71, 135</sup>. Monoliths, laminates and foams are examples of these structured adsorbents.

The structure of interest in this work is a monolith. Zeolite monoliths are either zeolite-substrate monoliths or self standing zeolite monoliths. The former can be prepared by depositing or growing zeolite as a layer or film on a non-removable substrate. The latter can be prepared by molding a paste of zeolite or zeolite with a binder into monolithic structures. Monoliths can be produced with different geometrical shapes and sizes, additionally; the number and the size of the channels in the monoliths are adjustable.

Even though the zeolite-substrate monoliths exhibited low pressure drop compared to beads, they show low adsorption capacity due to low zeolite loading per unit mass. Also, the difference between the thermal expansion coefficients of zeolite film and the substrate might cause the separation of the film from the substrate upon frequent heating for activation<sup>73, 133</sup>. Self standing monoliths have been studied in this work because they are more advantageous compared to

zeolite-substrate monoliths in term of offering higher adsorption capacity per unit weight of monolith.

In this chapter, self-standing zeolite monoliths with a unique network channeling structure, that mimics a tree's vascular system, have been synthesized. Furthermore, the primary building units of the walls of these monoliths are the micro-mesoporous LTA zeolite particles synthesized according to the procedure described in chapter 4. The main objective of this work is to fabricate hierarchical zeolite structures with adsorption characteristics competitive to commercial beads by following a practically applicable synthesis procedure that is suitable for large scale production.

The prepared monoliths have a cylindrical shape with dimensions of 1.4 cm diameter and 2.5 cm height. To maximize the adsorption properties, three different size ranges of channels are constructed in the body of the monolith; the large channels are interconnected to the medium and small channels and the medium channels are connected to small channels. Furthermore, the walls of these channels are built of mesoporous 5A zeolite particles as primary building units and silica as a permanent binder. We anticipate that the mesoporosity will enhance the diffusivity of guest molecules to remote active sites in 5A zeolite crystals and also reduce the influence of the micropores blockage by the binder. Two different cell densities are examined; 88 and 209 cpsi with wall thickness of 2.3 and 0.9 mm, respectively. It has been reported that 5A zeolite is one of the most efficient types of zeolites for CO<sub>2</sub> recovery<sup>177</sup>. Therefore, the prepared 5A zeolite monoliths are expected to show high CO<sub>2</sub> adsorption capacity and low pressure drop. Adsorption isotherms, pressure drop and CO<sub>2</sub> breakthrough data for both of 5A zeolite monoliths and beads were measured and compared. A breakthrough numerical simulation was conducted to describe and analyze the adsorption characteristics of CO<sub>2</sub> in the adsorption column packed with monoliths and beads.

## 6.2 Experimental section

### 6.2.1 Synthesis

#### 6.2.1.1 Synthesis of micro-mesoporous 4A zeolite

4A zeolite with hierarchical porosity was synthesized starting from initial gel with composition of 1.0Al<sub>2</sub>O<sub>3</sub>: 1.9SiO<sub>2</sub>: 3.2Na<sub>2</sub>O: 120H<sub>2</sub>O that was prepared following the previously reported procedure <sup>139</sup>. Typically, 2 g of sodium hydroxide ( $\geq$  99 %, Merck), was dissolved in 37.6 g of deionized water. Then one half of this alkaline solution was mixed with 3.9 g of sodium aluminate (50 – 56 % Al<sub>2</sub>O<sub>3</sub>, 40 – 45 % Na<sub>2</sub>O, Sigma Aldrich) under stirring until a clear solution was obtained. The other half of the alkaline solution was mixed with 8.7 g of sodium silicate (~ 26.5 % SiO<sub>2</sub>, ~ 10.6 % Na<sub>2</sub>O, Sigma Aldrich). The two solutions were then mixed and stirred vigorously by using electronic overhead stirrer type Eurostar digital (manufactured by IKA-WERKE) at speed 540–580 rpm. Next, 2.2 g of cetyltrimethylammonium bromide (CTAB-Ajax Finechem) was added to the obtained homogenous gel, also under continuous stirring, followed by drop wise addition of 1.38 ml of *n*-dodecane (99 %, Merck). The final homogenized gel with composition of 1.0Al<sub>2</sub>O<sub>3</sub>: 1.9SiO<sub>2</sub>: 3.2Na<sub>2</sub>O: 120H<sub>2</sub>O: 0.3CTAB: 0.3*n*-Dodecane was deposited in a sealed polypropylene bottle and aged at room temperature for two weeks. Finally the gel was heated in an oven at 99 °C for 4 h. The product was collected by filtration, washed repeatedly with ethanol and water and then dried at 70 °C overnight. The surfactant was removed by calcination at 550 °C using a ramp rate of 2 °C · min<sup>-1</sup> in N<sub>2</sub> flow for 1 h and then in air flow for 4 h. The produced material is denoted as ZANa in this chapter.

### 6.2.1.2 Ca<sup>+2</sup> ion-exchange

The resultant ZANa powder was ion exchanged into Ca form using the following procedure: 1 g of ZANa was dispersed in 50 ml 1 M CaCl<sub>2</sub> solution by stirring and under reflux at 60 °C for 12 h. The treatment was repeated five times. After each time the sample was collected by filtration and dried in oven at 90 °C. The ion exchanged sample was named ZACa in our work.

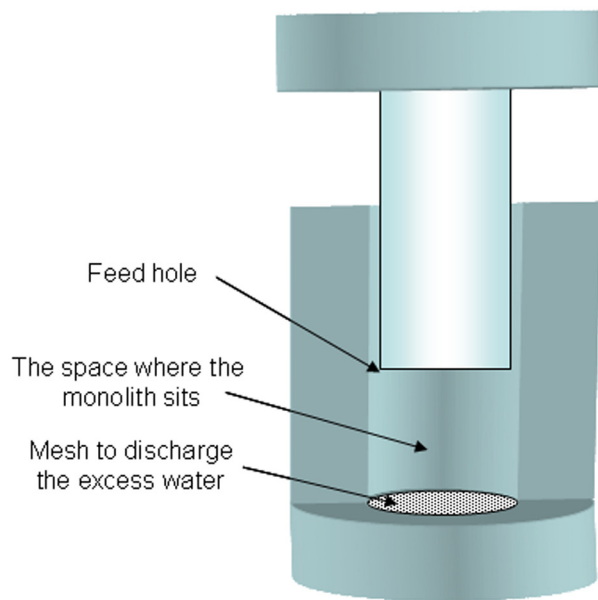
### 6.2.1.3 Preparation of hierarchical ZACa monoliths

In this work, ZACa zeolite monoliths were prepared following the reported procedure<sup>150, 178, 179</sup>. The first step was preparing a plasticized mixture which consisted of desired amounts of pre-prepared ZACa zeolite powder, silicon resin (233 Flake, 52 wt% silica, Dow Corning), methyl cellulose (Sigma-Aldrich) as a temporary binder or plasticizing organic binder, Poly(vinyl alcohol) (Sigma-Aldrich) as a co-binder and water. After calcination, 52 % of the added amount of silicon resin will remain in form of silica and act as a permanent binder in the fired monolith.

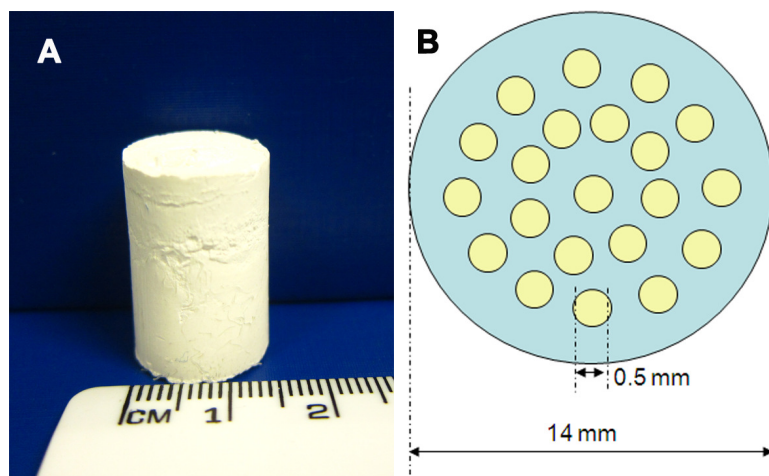
Therefore, the amount of silicon resin used in our experiments was calculated based on the concentration of the permanent binder required in the final monolith.

The monolith preparation started with grinding the silicon resin flakes manually by using a ceramic mortar and then a required amount of the grinded resin was mixed with the other dry components which all together then were blended for few minutes. Afterwards, a particular amount (Table 6.1) of plastic fibers with 0.16 mm diameter and 15 mm length (normally used for paper machine forming fabric, Huyck) was added to the dry mixture. This step was followed by adding a sufficient amount of water to prepare a plasticized mixture which was readily formable. For example, typically to prepare a monolith denoted M8 in Table 6.1 with final weight of 2.75 g as a fired monolith and consisted of 77.3 % zeolite A (ZACa) and 22.3 % silica; 2.13 g ZACa powder was blended together with 1.20 g of grinded silicon resin, 0.15 g methyl cellulose (5.45 wt % of fired monolith) and 0.04 g PVA (1.45 wt % of fired monolith). Then, 0.25 g (9.0 wt % of fired monolith) plastic fibers (0.16 mm Dia., 15 mm L) were mixed with powder mixture followed by adding 1.5 – 2 ml of deionised water (43 to 50 wt % of total powders). The next stage was shaping the monolith which was performed by using a homemade die with feedhole of 15 mm diameter (Scheme 6.1). The plasticized mixture was deposited into the feedhole of the die. In order to obtain a strong monolith, pressure up to 20 bar was applied to the mixture by using a press pelletizer (Pressmate XRF Scientific). Next, for better adsorption characteristics, parallel flow channels were created vertically through the monolith body by using a homemade channeling tool which contains variable number of pins (0.65 mm Dia., 30 mm L) mounted on a hard rubber base with diameter equal to the internal diameter of the die feedhole (15 mm). The pins were immersed in water for incipient wetness before being inserted into the die feedhole where the monolith sits. Then pressure was applied helping the pins to penetrate through the body of the monolith from the upper end to the lower end. Finally, the channeling tool was pulled back and the monolith was discharged from the die and directly placed in oven at 90 °C allowing methyl cellulose to quickly develop high gel strength and hence avoid skin cracking, which might occur if the green monoliths were left at room temperature <sup>179</sup>. After two days drying, the monoliths were calcined in a tubular furnace at 200 °C using a ramp rate of 1 °C / min in N<sub>2</sub> flow for 3 h followed by heating at 650 °C using a ramp rate of 1 °C/ min in air flow for 8 h. Four different monoliths were prepared by varying the following parameters: zeolite to silica ratio, plastic fiber concentration and the number of parallel channels. The concentrations of

methyl cellulose and poly vinyl alcohol were maintained in all the experiments. Table 6.1 shows the compositional and structural characteristics of the synthesized monoliths. Scheme 6.2A presents an overall picture of one of the synthesized monoliths.



**Scheme 6.1** Schematic diagram of the homemade die used to fabricate the monoliths



**Scheme 6.2** Overall picture of one of the synthesized monoliths (A) and schematic diagram of top view of a monolith with 21 parallel channels.

5A zeolite beads (UOP Co.) were used as a reference to evaluate the performance of the prepared monoliths. The binder concentration in UOP 5A beads is  $\sim$  18 wt %<sup>180</sup>. The morphology of the used 5A beads is irregular with dimensions range between 0.7 to 1.1 mm as estimated from the SEM results (Figure 6.5B and C).

**Table 6.1 Characteristics of the monoliths prepared in the experiments**

Sample	ZACa <sup>a</sup> wt %	SiO <sub>2</sub> <sup>a</sup> wt %	Plastic fiber <sup>b</sup> wt %	Parallel channels	Wall thickness <sup>c</sup> mm
M6	77.3	22.7	2.5	21	2.3
M7	77.3	22.7	9.0	21	2.3
M8	77.3	22.7	9.0	50	0.9
M9	92.0	8.0	9.0	50	0.9

<sup>a</sup> Weight percentage of zeolite and silica in the final fired monoliths.

<sup>b</sup> Weight percentage of plastic fiber calculated based on the desired weight of the final fired monoliths.

<sup>c</sup> Approximate values obtained by simple mathematic calculation (Scheme 6.2B).

## 6.2.2 Processing work

### 6.2.2.1 Adsorption isotherms

The adsorption isotherms of pure CO<sub>2</sub> and N<sub>2</sub> on the prepared monoliths and commercial 5A beads were measured using Micromeritics ASAP 2010. The samples were degassed at 350 °C for 15 h to about 10<sup>-5</sup> mmHg vacuum level before the analysis.

The dual-site Langmuir model was used to fit the adsorption isotherms of CO<sub>2</sub> and N<sub>2</sub>:

$$n_i = \frac{m_{1i}b_iP_i}{1 + b_iP_i} + \frac{m_{2i}d_iP_i}{1 + d_iP_i} \quad (1)$$

and

$$b_i = b_{\circ i} \exp\left(-\frac{Q_{li}}{RT}\right) ; \quad d_i = d_{\circ i} \exp\left(-\frac{Q_{2i}}{RT}\right) \quad (2)$$

Where  $n_i$  is the adsorbed amount of component  $I$  ( $\text{mol/kg}$ );  $m_{1i}$ ,  $m_{2i}$  are the maximum adsorbed amount of component  $I$  ( $\text{mol/kg}$ );  $P$  is gas pressure (kPa);  $b_i$ ,  $d_i$  are adsorption constants ( $1/\text{kPa}$ );  $T$  is temperature (K);  $R$  is ideal gas constant;  $Q$  is the heat of adsorption ( $\text{J} \cdot \text{mol}$ ).

### 6.2.2.2 Pressure drop

In pressure drop experiments, the same mass of monoliths or 5A beads listed in Table 6.5 were packed into the adsorption column (ID 15 mm x Length 120 mm). Pressure drop between the inlet and outlet of the column was measured under two different superficial velocities; 0.75 and  $1.24 \text{ m} \cdot \text{sec}^{-1}$ .

The pressure drop across the monoliths beds can be calculated using Hagen-Poiseuille equation:

$$\Delta P = \frac{8\mu L Q}{\pi r^4} \quad (3)$$

Where  $\Delta P$  is the pressure drop (Pas),  $\mu$  is the viscosity of the gas mixture (Pas · sec),  $L$  is the bed length (cm),  $Q$  represents the volumetric flow rate ( $\text{cm}^3 \cdot \text{sec}^{-1}$ ),  $r$  is the radius (cm) and  $\pi$  is the mathematical constant.

Pressure drop over 5A zeolite beads packed bed can be calculated using the Ergun equation:

$$\Delta P = \frac{150\mu v_o L_b}{\phi_s^2 D_p^2} \frac{(1-\varepsilon)^2}{\varepsilon^3} + \frac{1.75\rho v_o^2 L_b (1-\varepsilon)}{\phi_s D_p \varepsilon^3} \quad (4)$$

Where  $\Delta P$  is the pressure drop (Pas),  $L_b$  is the packed bed length (cm);  $v_o$  is the superficial velocity of the gas mixture ( $\text{cm} \cdot \text{sec}^{-1}$ ),  $\varepsilon$  is the void fraction of the bed;  $D_p$  is the average diameter of the beads (cm);  $\rho$  ( $\text{g} \cdot \text{cm}^{-3}$ ) and  $\mu$  (Pas · sec) are the density and the viscosity of the gas mixture.  $\Phi_b$  is the sphericity which was calculated using the dimensions of beads estimated from the SEM characterization.

### 6.2.2.3 CO<sub>2</sub> breakthrough measurements

The effective diffusivity of CO<sub>2</sub> in the synthesized monoliths was determined by conducting CO<sub>2</sub> breakthrough experiments. In every experiment, a series of monoliths (each with 14 mm OD and 20 – 25 mm H) were loaded into the adsorption column until the net weight of ZACa zeolite in the entire loaded monoliths ranged between 6.7 and 7.2 g (Table 6.5). The external surface (excluding upper and lower bases) of the monoliths was wrapped with Teflon tape to avoid gas bypass. Initial activation of the monoliths was conducted at 350 °C under N<sub>2</sub> flow for 10 h at heating ramp of 1 °C / min. Before each breakthrough experiment, pure N<sub>2</sub> gas was purged through the system loaded with the sample to remove any contaminants that might affect the results. A gas stream containing 15% CO<sub>2</sub> balanced with 85% N<sub>2</sub> was fed from the bottom of the column at a flowrate of 0.18 L · min<sup>-1</sup>, at 1.2bar and at room temperature. CO<sub>2</sub> concentration in an exhaust gas from the top of the column was measured by a CO<sub>2</sub> Analyzer (Servomex 1440) and experimental data was recorded in a computer by Advantech GeniDaq software. For comparison purposes, breakthrough experiment using 8.4 g of commercial 5A zeolite beads (average diameter of 0.9 mm) under similar run conditions was also conducted. The details of the monoliths and beads, *i.e.* size and weight, used for the breakthrough experiments are listed in Table 6.5. A blank experiment had also been conducted to eliminate the impact of tubing and valves of the system.

Numerical breakthrough simulation was used to estimate and analyze adsorption characteristics of the binary gases in an adsorbent bed packed with monoliths or beads. In this simulation, it was assumed that the feed gas was ideal and the axial dispersion was zero, the adsorption of components on adsorbents was a non-isothermal process, and the pressure at the exit of the bed was constant during whole breakthrough experiment.

The theory behind this model is based on conservation of mass, energy, momentum and constitutive relationships for kinetics and equilibrium. The mass balance can described as the following equation:

$$-D_{z_i} \frac{\partial^2 C_i}{\partial z^2} + \frac{\partial C_i}{\partial t} + \left( \frac{1 - \varepsilon_b}{\varepsilon_b} \right) \rho_{ads} \frac{\partial \bar{n}_i}{\partial t} = - \frac{\partial u C_i}{\partial z} \quad (5)$$

Where  $i$  represents the components 1 and 2;  $C_i$  is the concentration of component  $i$  (gmole · cm<sup>-3</sup>), that is,  $C_i = \frac{P_i}{RT}$ ;  $D_{Zi}$  is the axial dispersion coefficient (cm<sup>2</sup> · g<sup>-1</sup>);  $t$  is time (s);  $\varepsilon_b$  bed voidage (does not include voids in the adsorbent);  $z$  is the bed length (cm);  $\rho_{ads}$  is the adsorbent density ( $\rho_{ads} = \rho_{bed} / (1 - \varepsilon_b)$ ) (g · cm<sup>-3</sup>);  $n_i$  is loading of component  $i$  in the adsorbent (gmole · kg<sup>-1</sup>) and  $u$  is interstitial gas velocity ( $u = \text{superficial velocity}/\varepsilon_b$ ) (cm · s<sup>-1</sup>).

The energy balance was calculated from:

$$\rho_{bed} C_{ads} \frac{\partial T}{\partial t} - \rho_{bed} \sum_{i=1}^2 q_i \frac{\partial \bar{n}_i}{\partial t} - \rho_{bed} \dot{Q}_{gen} = -C_{gas} \frac{\partial (\hat{u} CT)}{\partial z} - \frac{4h_w}{D}(T - T_w) \quad (6)$$

Where  $\rho_{bed}$  is the bed density (g · cm<sup>-3</sup>);  $T$  is temperature (K),  $\bar{n}_i$  is the loading of component  $i$  in the adsorbent (gmole · kg<sup>-1</sup>),  $C$  (that is,  $\frac{P}{RT}$ ) is total gas concentration (gmole · cm<sup>-3</sup>),  $\hat{u}$  is the gas interstitial velocity,  $C_{ads}$  is the adsorbent heat capacity and  $C_{gas}$  the gas heat capacity,  $h_w$  the heat transfer coefficient from the bed to the wall and  $T_w$  the wall temperature.

The pressure drop with the adsorption bed can be described with equations (3) and (4).

To determine the rate of adsorption, the Linear Driving Force based on solid diffusion was used:

$$\frac{\partial \bar{n}_i}{\partial t} = k_i (\bar{n}_i^* - \bar{n}_i) \quad (7)$$

$$\text{For monolith bed } k_i = D_{ei} * k \quad (8)$$

Where  $k$  for a monolith was determined by Patton *et al*<sup>181</sup> based on the channel density (cpsi) and wall thickness.

$$\text{For packed bed } k_i = \frac{15D_{ei}}{R_p^2} \quad (9)$$

Where  $R_p$  is the average diameter of beads (cm). The only unknown parameter was therefore the effective diffusivity for component  $i$  ( $D_{ei}$ ) which was determined by fitting the simulated breakthrough curve to the experimental values. The parameter  $D_{ei}$  therefore is intrinsic to the diffusion of in the zeolite monolith walls or the beads, respectively and is in turn related to the pore network within these structures.

## 6.3 Results and discussion

### 6.3.1 Micro-mesoporous primary building units

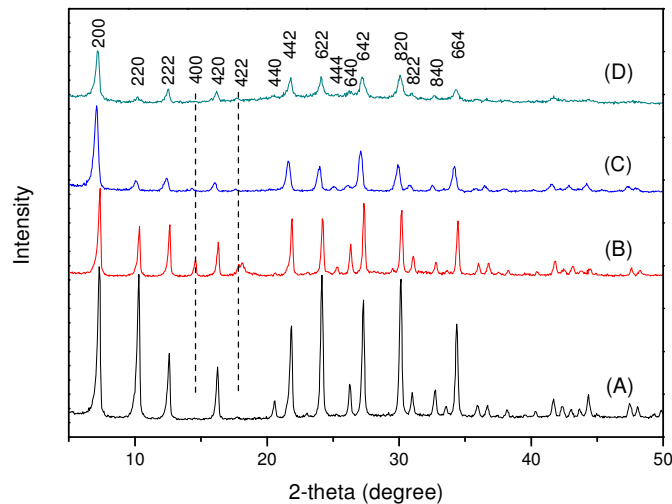


**Figure 6.1 XRD patterns of the ZANa (A), ZACa powder (B), 5A zeolite beads (C) and M8 monolith after being crushed to powder (D).**

The XRD pattern of the material named ZANa, synthesized in the first section of the experiments, indicates that the material is a highly crystalline NaA zeolite when compared to the standard data of LTA zeolite published by International Zeolite Association (Figure 6.1A)<sup>140</sup>. After the ion exchange process, the ZACa sample shows that the diffraction peaks of LTA framework structure were retained (Figure 6.1B). However, most of the peaks show lower intensities than in ZANa, probably due to prolonged heating and stirring during the ion exchanging process which might change the size of the particles. Also Figure 6.1B shows that

the peaks at  $2\theta \sim 14.5$  and  $17.5$ , matching the (400) and (422) planes in LTA zeolite structure, are more pronounced in ZACa than in ZANa. Such behavior is well known in the literature for 5A zeolite<sup>182</sup>.

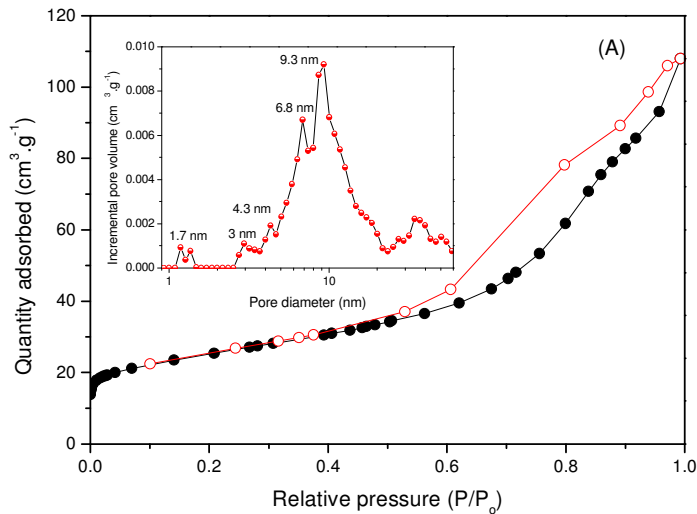


**Figure 6.2**  $\text{N}_2$  adsorption-desorption isotherm for ZANa zeolite at  $-196$   $^\circ\text{C}$  (A) and pore size distribution (inset).

It is a well known characteristic of NaA zeolite that it cannot adsorb  $\text{N}_2$  at  $(-196$   $^\circ\text{C})$  because of the  $\text{Na}^+$  cations which occupy positions near the micropore apertures minimizing their size and hence prohibiting the  $\text{N}_2$  molecules diffusion<sup>29, 142</sup>. ZANa should thus be an ideal reference to investigate the presence of mesopores in the structure of the prepared material.

The isotherm of ZANa in Figure 6.2A shows a steep increase in  $\text{N}_2$  adsorption at low relative pressure  $P/P_o$  between 0.0 and 0.3 exhibiting type I isotherm which is normally observed for microporous materials. However, the micropores in our material are not accessible to  $\text{N}_2$  molecules at the analysis temperature, thus type I isotherm suggests the presence of small mesopores with size close to micropore range<sup>143</sup>. At high relative pressure, in the range between 0.4 to 0.99,  $\text{N}_2$  adsorption increases significantly displaying type IV isotherm with H3 hysteresis due to capillary condensation of  $\text{N}_2$  gas within the mesopores<sup>64, 143</sup>. The absence of the plateau at  $P/P_o$  close to 1.0 suggests that ZANa particles consists of aggregated crystallites<sup>143</sup>. In Figure 6.2 inset, broad pore size distributions can be observed with several small peaks at 1.7, 3, 4.3 nm and two dominant narrow peaks centered at pore diameter 6.8 and 9.3 nm.

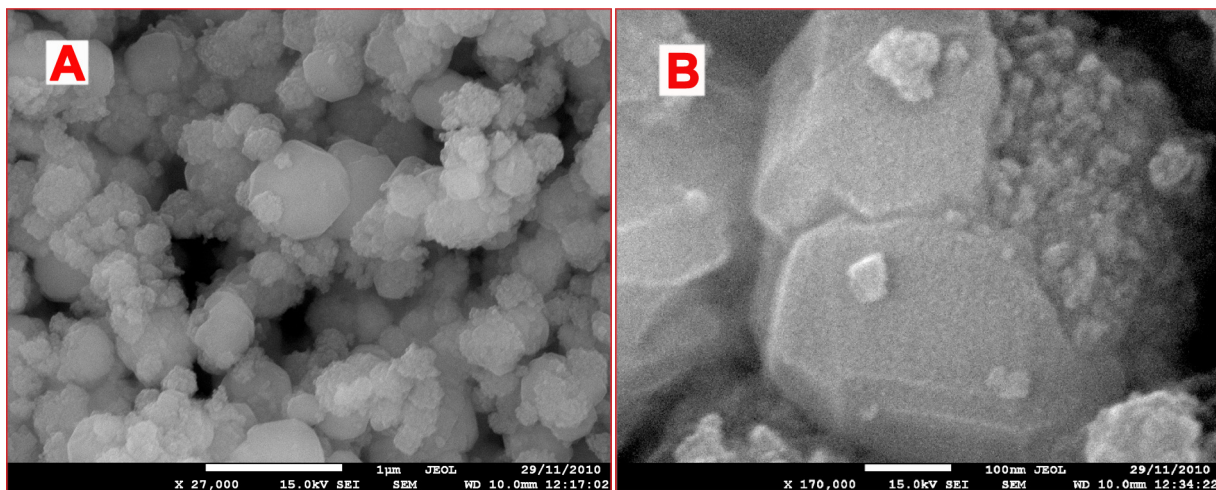


**Figure 6.3 SEM images of a group of particles (A) and a single particle (B) of ZANa zeolite.**

The SEM observation of a group of particles of ZANa zeolite (Figure 6.3A) shows the presence of two types of particles, aggregates and cubes. Figure 6.3B indicates that the aggregates had undertaken surface recrystallization. In other words the crystal growth in this system was according to NARS (nanocrystallites-aggregation-surface recrystallization-single crystal) mechanism similar to what observed for the samples synthesized following the same procedure but with different initial gels compositions in chapters 4 and 5<sup>18</sup>.

The aforementioned findings indicate that the synthesized ZANa is a well crystalline 4A zeolite with bimodal pore size distribution, micropores and mesopores. The consistency between the XRD patterns of the prepared ZANa and LTA reveals the presence of micropores in ZANa structure. The mesopores are demonstrated by the interstitial voids among the aggregated crystallites which were formed due to the presence of CTAB micelles and *n*-dodecane molecules in synthesis mixture.

### **6.3.2 Physical Characterization of monoliths**

The standard descriptions of the silicon resin used in our experiments indicated that it contains 52 wt % silica. This amount of silica was expected to remain as a binder for zeolite particles after the removal of all the other organic components by calcination<sup>150, 178, 179</sup>. To verify that, TG analysis was conducted on pure silicon resin to calculate the weight loss percentage between 25 to 900 °C.

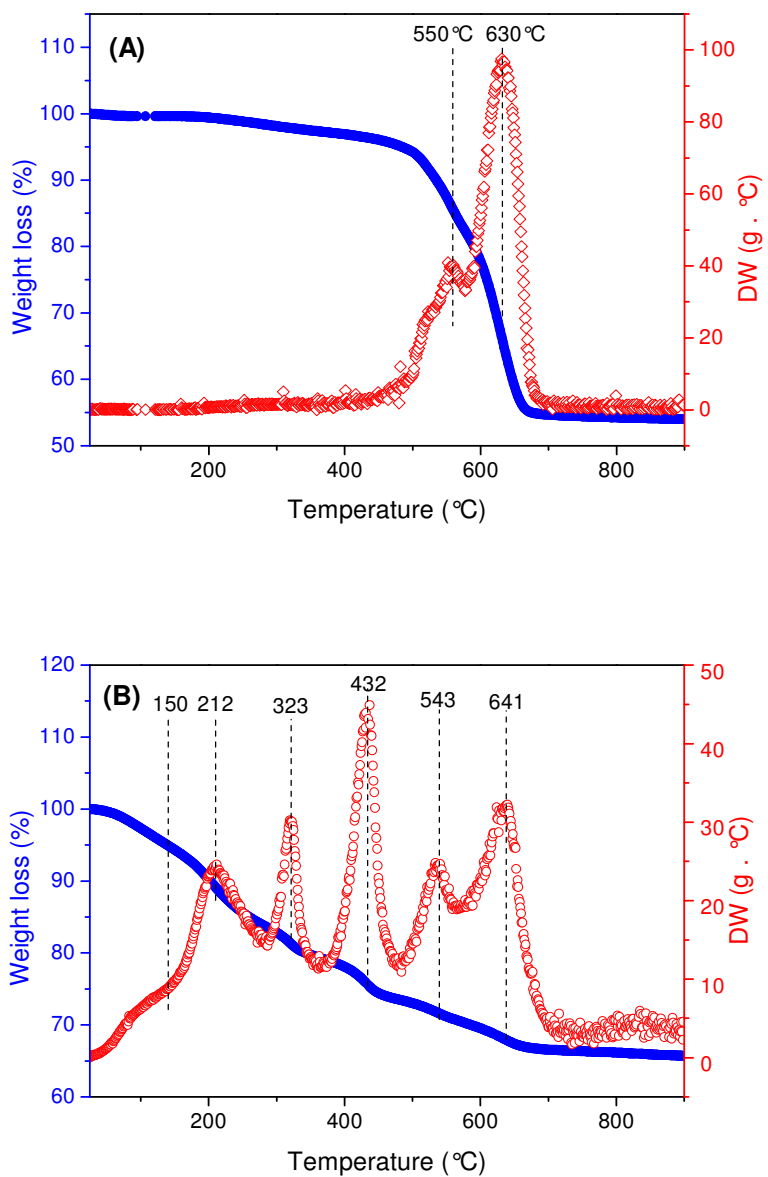


**Figure 6.4 Thermogravimetry and differential thermogravimetry curves of pure resin (A) and as synthesized M8 monolith (B).**

Figure 6.4A indicates that the organics integrated into the resin composition were completely decomposed at less than 650 °C; particularly at 550 and 630 °C. The TGA results show total weight loss about 54 wt% which is close to what was expected (48 wt %). Thus, in this work we

assumed that after calcinations, 52 wt % of the added resin will remain in form of silica and act as a permanent binder in the fired monolith.

The TGA results for as synthesized monolith named M8 show six weight loss steps between 25 and 900°C with total weight loss of 34.29 % (Figure 6.4B). The weight loss at and below 150 °C corresponds to water desorption. The other weight loss steps appearing between 150 and 700 °C might be associated with the decomposition of the organic additives in M8 composition. By simple calculations, for M8 monolith, the weight fraction of the components excluding water that was expected to decompose *via* calcination was about 26.9 wt %. This fraction is consistent with the weight loss (26.8 wt %) measured by TG analysis between 150 and 650 °C. Accordingly, the M8 monoliths obtained after firing/calcination represent the remaining fired solids (73.1 wt % of the composition mixture) which consisted of 77.3 wt % (2.13 g) ZACa as primary building units and 22.7 wt % (~ 0.62 g) silica as a permanent binder.

The XRD patterns of M8 monolith (crushed into powder), commercial 5A beads and ZACa (Figure 6.1C and D) are compatible with the pattern of LTA framework structure published by International Zeolite Association<sup>140</sup>. However, both M8 and 5A beads show lower intensities peaks than pure ZACa, probably due to the presence of the binder. Furthermore, the fraction of the binder in M8 monolith is about 22.7 wt % which is higher than in commercial 5A beads (18 wt %), therefore, XRD pattern of the former shows lower intensity peaks than the latter.

The SEM image in Figure 6.4A is of a small fragment taken from the monolith named M8. The image shows large-scale channels with diameter of 450 – 550 µm distributed on the surface of the monolith and separated by walls with 500 to 1000 µm of thickness. These parallel channels most likely represent the channels formed by the pins (650 µm D) of the channeling tool. However, the difference in the diameter of the pins compared to their mirror channels is attributed to the shrinkage that might have occurred during the drying and calcination.

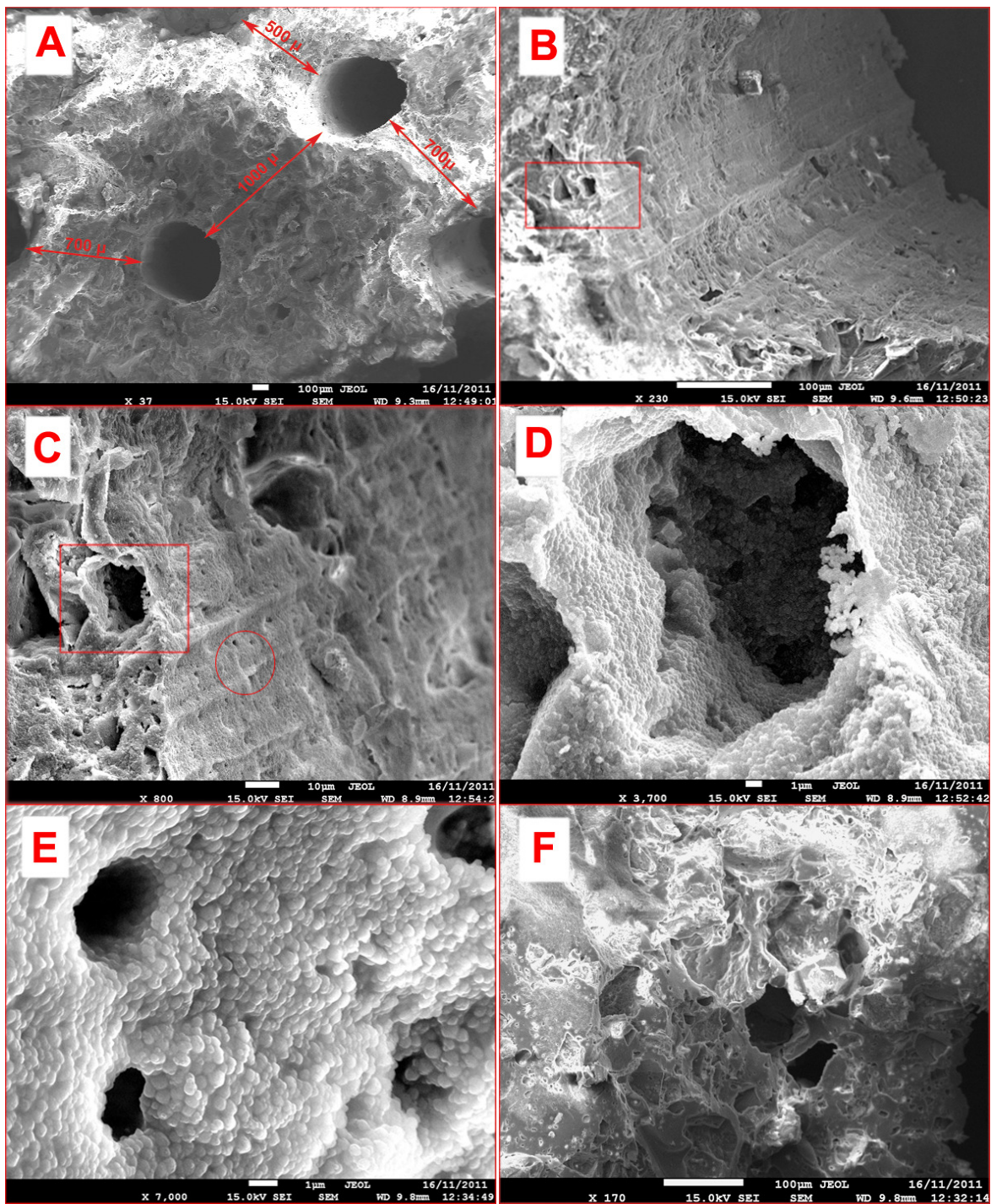


**Figure 6.5** SEM images of a top view of a fragment taken from M8 monolith (A), image of a parallel channel cross sectioned along its length (B), high magnification image of the area marked with a rectangle in image B (C), high magnification image for the area marked with a square in image C (D), high magnification image for the area marked with a circle in image C (E), SEM image of another area on the surface of M8 monolith (F).

Figure 6.4B and 4C show the low and high magnification images of the interior surface of a parallel channel which was cross sectioned along its length. Channels with two different scales can be observed on the interior surface of the parallel channels; namely medium-scale channels with diameter of few tens of micrometers (surrounded with a square in Figure 6.5C) and small-scale channels with diameter of few micrometers (surrounded with a circle in Figure 6.5C). Furthermore, the medium-scale channels appear to be randomly distributed on the external surface of the monolith (Figure 6.5F). The diameter of the medium-scale channels ranges from 20 to 85  $\mu\text{m}$  and most probably they were formed due to firing the plastic fiber (diameter 165  $\mu\text{m}$ ) by calcination.

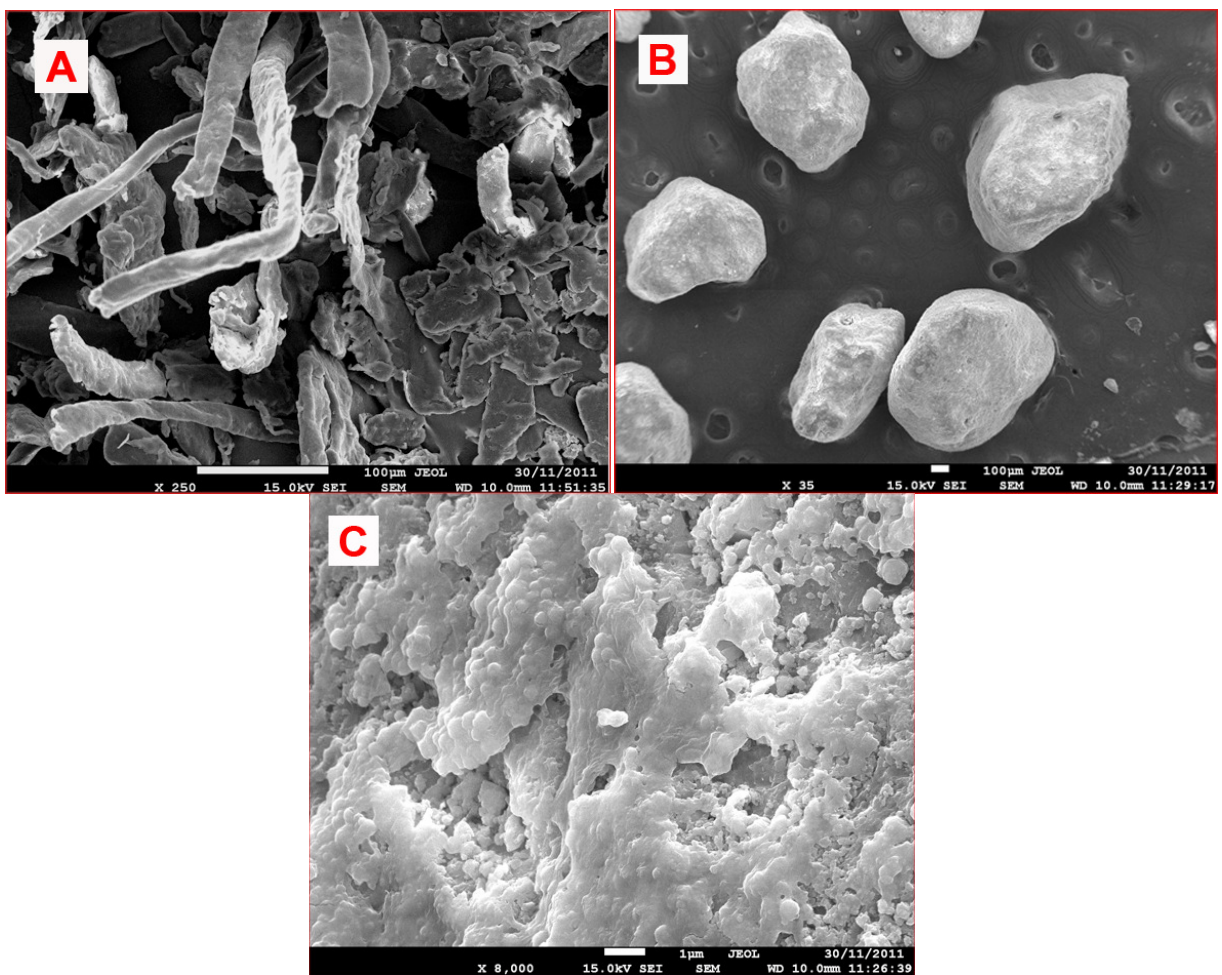


**Figure 6.6 SEM images of methyl cellulose fiber (A), 5A commercial beads (B) and high magnification image of the surface of 5A beads (C).**

Figure 6.5C and E indicate that the size of the small-scale channels ranges between 1 and 9  $\mu\text{m}$  and they are dispersed abundantly on the surface of the monolith including the interior walls

of the parallel channels. The formation of the small-scale channels can be attributed to the decomposition, *via* calcination, of methyl cellulose fibers that were used as temporary organic binder within the mixture of precursors of the monolith. This is confirmed by SEM image in Figure 6.6A which indicates that methyl cellulose fibers are flattened stripes with flat oval cross sectional diameter of  $6.5 \mu\text{m}$  and large diameter range between  $20$  to  $40 \mu\text{m}$ . Similarly to large-scale channels, the sizes of the medium and small-scale channels were smaller than the size of the parent fibers due to the shrinkage due to drying and calcination.

The commercial 5A beads that were used in this work have irregular shape with diameter ranging between  $0.7$  to  $1.1 \text{ mm}$  (Figure 6.6B). The high magnification image of the surface of the beads indicates that the only paths the beads offer for the gas molecules to reach to the micropores are the interstices between the packed crystals and binder.

The surface area and pore size distribution of M8, M9 and 5A beads were measured by  $\text{N}_2$  adsorption-desorption at  $-196^\circ \text{ C}$ . The isotherms of the three samples show steep uptakes at  $P/P_o$  below  $0.1$  indicating the microporous characteristics (Figure 6.7A). The size of the micropores in all samples using Horvath-Kawazoe method is  $0.48 \text{ nm}$  which is the typical size of the entrances of CaA zeolite crystal (Table 6.2) <sup>180</sup>.  $\text{N}_2$  adsorption at M8 and M9 increased gradually until reaching a plateau at  $P/P_o$  between  $0.4$  and  $0.5$  which is an indicative of capillary condensation of nitrogen in mesopores (Figure 6.7A). Both samples show isotherms which can be considered as combination of types IV and I. Such type of isotherm may be observed in case of materials that contain several types of pores and with materials that show broad mesopore size distribution

143 .

Figure 6.7B shows the mesopore size distribution calculated using DFT theory. Two main peaks can be observed in both samples; the first peak centered at  $1.7 \text{ nm}$  and the second peak extended between  $2$  and  $6 \text{ nm}$  but centered at  $3.4 \text{ nm}$  (Figure 6.7B). These pores are most likely the same meso-sized pores observed in ZANA (Figure 6.2-inset), however, their size is smaller in M8 and M9 monoliths. Table 6.2 shows that the mesopore volume was retained after the ion exchange process. The difference in the mesopore size distribution may be attributed to long duration of heating and stirring during the ion exchange.

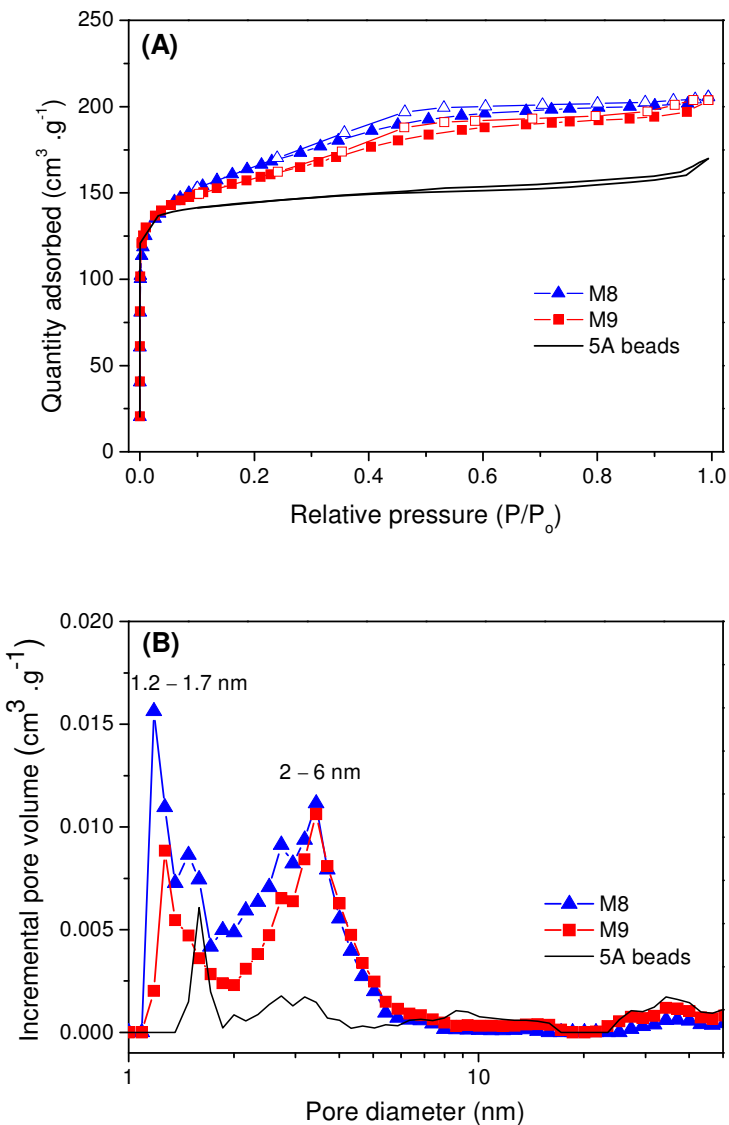


**Figure 6.7**  $\text{N}_2$  adsorption-desorption isotherms (A) and the corresponding pore size distribution (B) of M8 and M9 monoliths and 5A beads.

In Figure 6.7A, the isotherm of 5A zeolite beads is type I with a very narrow hysteresis which is typical of microporous materials or mesoporous materials with pore size close to micropore range<sup>143</sup>.

Table 6.2 shows that there is only a small difference in micropore volume of the three samples; M8, M9 and 5A beads at  $0.13$ ,  $0.15$  and  $0.19 \text{ cm}^3 \cdot \text{g}^{-1}$ , respectively. However, M8 and M9 show significant mesopore volume at  $0.18$  and  $0.16 \text{ cm}^3 \cdot \text{g}^{-1}$ , whereas no mesoporosity was

observed in 5A beads. M8 and M9 show higher BET surface area compared to 5A beads, which is expected, due to the presence of the mesopores. However, M9 monolith has lower surface area ( $500 \text{ m}^2 \cdot \text{g}^{-1}$ ) than M8 ( $528 \text{ m}^2 \cdot \text{g}^{-1}$ ) in spite of higher zeolite content in the former. The reason may be that M9 is less packed than M8 due to less binder concentration resulting in creation of more channels in macro scale, which are beyond the detection limit of the instrument.

**Table 6.2 Pore structural properties as measured by  $\text{N}_2$  adsorption-desorption analysis at (-196 °C)**

Sample	$S_{\text{BET}}^a$ ( $\text{m}^2 \cdot \text{g}^{-1}$ )	$V_{\text{micro}}^b$ ( $\text{cm}^3 \cdot \text{g}^{-1}$ )	$V_{\text{meso}}^c$ ( $\text{cm}^3 \cdot \text{g}^{-1}$ )	$d_{\text{micro}}^d$ (nm)	$d_{\text{meso}}^e$ (nm)
ZANa	85 <sup>f</sup>	0.009	0.16	-	1.7, 3, 4.3, 6.8, 9.3
M8	528	0.13	0.18	0.48	1.2, 1.5, 2.7, 3.4
M9	500	0.15	0.16	0.48	1.2, 2.7, 3.4
5A beads	436	0.19	0.07	0.48	1.6

<sup>a</sup> Surface area obtained at relative pressure range of 0.05 – 0.3. <sup>b</sup> micropore volume as calculated by t-plot. <sup>c</sup> mesopore volume determined by subtracting the micropore volume from the total pore volume calculated at a relative pressure of 0.99. <sup>d</sup> micropore diameter was measured using Horvath-Kawazoe method. <sup>e</sup> mesopore size distribution was calculated using Density functional theory. <sup>f</sup>  $S_{\text{BET}}$  in this sample is almost equal to the surface area of mesopores because  $\text{N}_2$  gas molecules cannot diffuse the micropores of 4A zeolite at -196 °C.

In addition to  $\text{N}_2$  adsorption-desorption analysis, mercury porosimetry is another technique used to determine the pore size distribution of the prepared monoliths. As shown in Figure 6.8, all the three types of monoliths show multimodal pore size distribution by exhibiting peaks centered at 0.003, 0.14, 3.6, 9, 85 and 600  $\mu\text{m}$ . The small pores of 0.003  $\mu\text{m}$  (3 nm) represent the mesopores associated with the structure of the primary building units (Figure 6.7B and Table 6.2).

The second peak centered at 0.14  $\mu\text{m}$  (140 nm) is attributed to interstitial voids among the primary building units (ZACa particles) of the walls of the monoliths. The intensity of this peak in M9 monolith is higher than in M7 and M8 which, indicates that the former contained more interstitial voids (Figure 6.8). This was probably a consequence of less binder concentration in M9 which results in the formation of loose aggregates. Further supporting the reason proposed above for the lower surface area measured for M9 compared to M8 monolith.

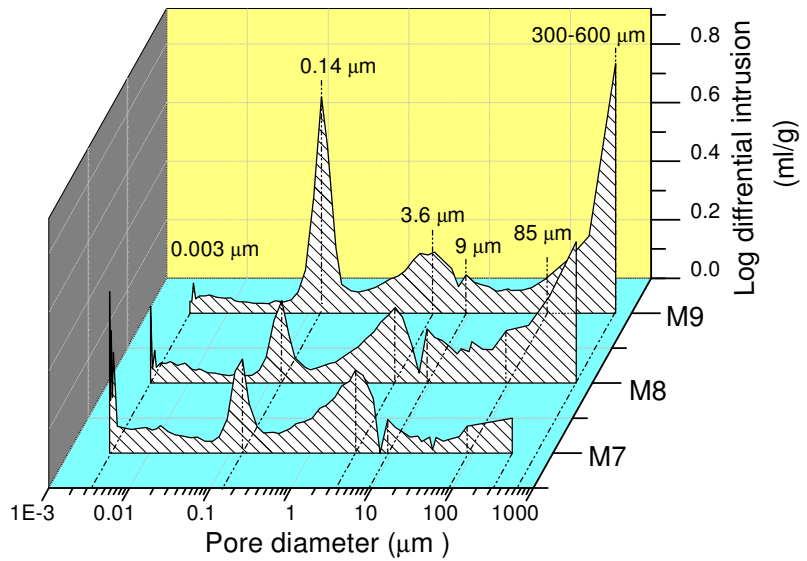


**Figure 6.8 Pore size distribution of M7, M8 and M9 as determined by mercury (Hg) porosimetry.**

The pore size distribution determined by mercury porosimetry was around 3.6 and 9  $\mu\text{m}$ , which is in agreement with the small-scale channels observed by SEM, that were attributed to the decomposition of methyl cellulose fibers. The composition of the initial gel of the three samples: M7, M8 and M9, contained equal amounts of methyl cellulose fibers, therefore the peaks showed nearly identical intensities. The shoulders at 85  $\mu\text{m}$  in the pore size distributions of all the three samples can be attributed to the decomposed plastic fibers. The last peak, centered at about 600  $\mu\text{m}$ , corresponds to the volume of mercury intruded in the parallel channels (500  $\mu\text{m}$  as measured by SEM). However, the intensities of this peak cannot provide an accurate indication for the pore volume because the segments of samples used in the analyses did not necessarily contain similar number or volume of parallel channels.

### 6.3.3 Adsorption isotherms

Figure 6.9 shows the  $\text{CO}_2$  and  $\text{N}_2$  adsorption isotherms of M8, M9 and 5A beads at different temperatures. It can be observed that, at all temperatures, the amount of  $\text{CO}_2$  adsorbed by M9 was about 1.2 to 1.3 times higher than the amount adsorbed on M8. This is in consistent with the ratio of zeolite amount in M9 to zeolite amount in M8 which equals to  $\sim 1.2$  (92.0 wt %: 77.3 wt %, Table 6.1). It is well known that  $\text{CO}_2$  adsorption on zeolite is driven by the electric field

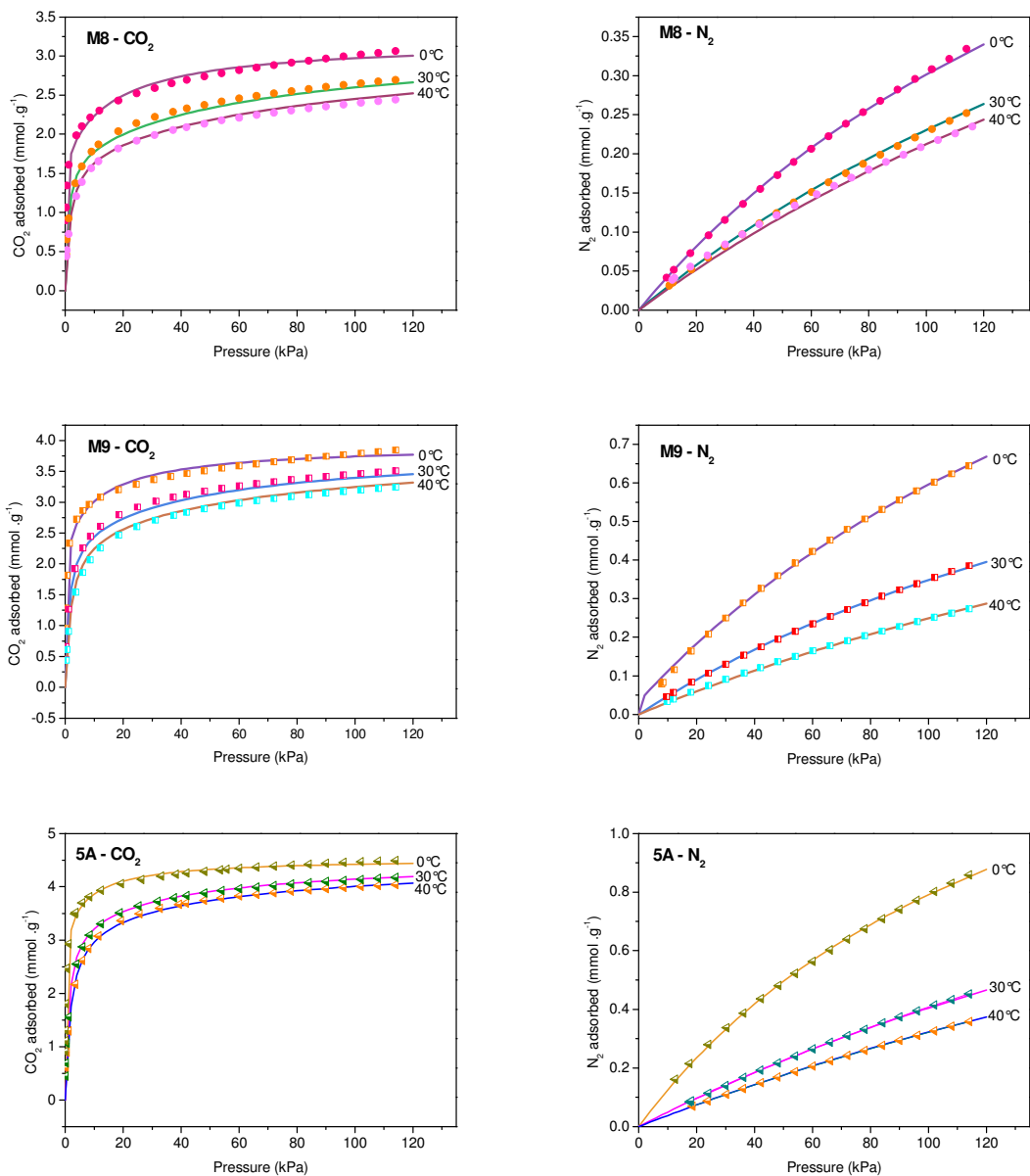


**Figure 6.9**  $\text{CO}_2$  and  $\text{N}_2$  isotherms at 0, 30 and 40°C of M8 M9 and 5A beads. The experimental data are labeled by symbols and the simulation data are labeled by solid lines.

generated by the charge balancing cations inside the pores<sup>60</sup>. Accordingly, the adsorption capability of the prepared monoliths to  $\text{CO}_2$  is proportional to the weight fraction of zeolite incorporated in their composition. Furthermore, at partial pressure of 1.2 bar, the  $\text{CO}_2$  adsorption capacity of 5A beads was about 1.46 and 1.26 times higher than the adsorption capacities of M8 and M9, respectively. This was expected, because the equilibrium adsorption mainly occurs in micropores and the micropore volume of 5A beads, as measured by  $\text{N}_2$  adsorption analysis at (-

196 °C), was about 1.45 and 1.26 times the micropore volume of M8 and M9 monoliths; respectively (Table 6.2). For all samples, dual-site Langmuir adsorption isotherms (solid line curves in Figure 6.9) were fitted to the experimental CO<sub>2</sub> and N<sub>2</sub> adsorption data (curves labeled with symbols in Figure 6.9) and the fitted parameters are given in Table 6.3.

**Table 6.3 Dual-site Langmuir isotherm parameters for CO<sub>2</sub> and N<sub>2</sub>**

Samples	$m_1$ (mol·Kg <sup>-1</sup> )	$m_2$ (mol·Kg <sup>-1</sup> )	$b_0$ (kPa <sup>-1</sup> )	$Q_1$ (J·mol)	$d_0$ (kPa <sup>-1</sup> )	$Q_2$ (J·mol)
<b>CO<sub>2</sub></b>						
M8	1.7421	1.4526	1.25E-07	40051.0	9.74E-08	30126.8
M9	1.4455	2.4876	1.28E-07	29940.6	4.17E-07	36505.1
5A beads	1.2274	3.3083	4.39E-08	33363.5	3.11E-07	37418.5
<b>N<sub>2</sub></b>						
M8	0.9397	0	1.08E-04	8.57E+03	1.00E+00	100
M9	1.4574	0	2.86E-06	1.76E+04	1.00E+00	100
5A beads	1.9485	0	4.25E-07	2.20E+04	1.00E+00	100

### 6.3.4 Processing work

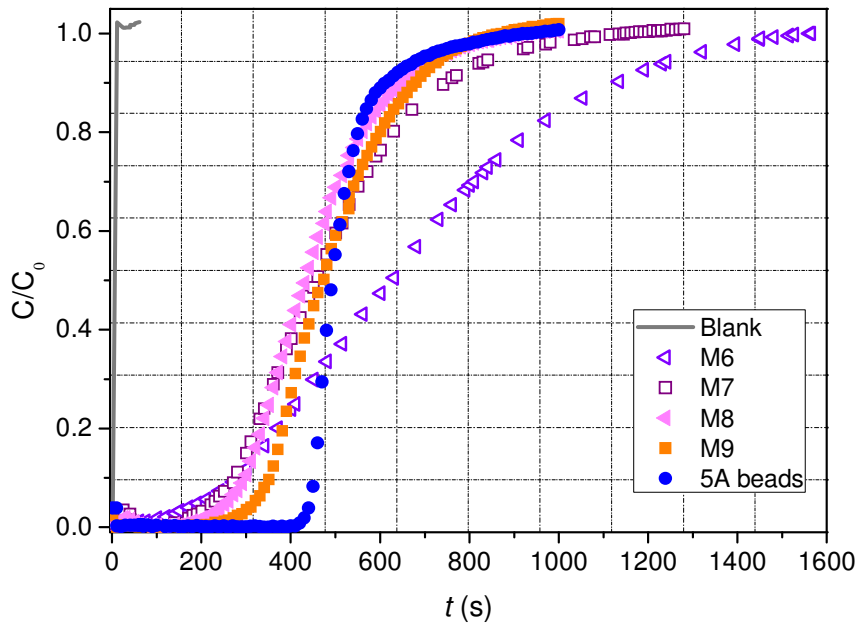
#### 6.3.4.1 Breakthrough profiles

Figure 6.10 shows the CO<sub>2</sub> breakthrough curves of M6, M7, M8, M9, 5A beads and empty bed (blank experiment) at volume flow rate of 0.18 L · min<sup>-1</sup>. The breakthrough curve recorded for the blank system is very sharp, which indicates that all the dispersion observed in the following breakthrough measurements can be attributed to mass transfer resistance and to velocities distribution in the channels of the samples.

M6 monolith shows a very broad CO<sub>2</sub> breakthrough curve with width of 1079 s (Figure 6.10 and Table 6.5). Breakthrough width is defined here as the difference between the time to reach 5 % and 95% of final concentration <sup>70, 183</sup>. On the other hand, the CO<sub>2</sub> breakthrough of M7 monolith shows a sharper increase in CO<sub>2</sub> uptake forming profile with a width of 621 s. The monolith characteristics as shown in Table 6.1 indicate that both monoliths, M6 and M7, are identical in terms of the number of parallel channels, wall thickness, composition (zeolite: silica

ratio) and small scale channel concentration (methyl cellulose fiber mirror). However, the concentration of the plastic fiber in the precursor mixtures of M6 and M7 monoliths was different, 2.5 wt % in former and 9.0 wt % in the latter. Consequently, the number of the medium-scale channels, the mirror of the plastic fiber (20 to 85  $\mu$ ), was higher in M7 than in M6 which probably resulted in less mass transfer resistance and better gas distribution.

The CO<sub>2</sub> breakthrough front of M8 monolith was sharper with a narrower width (470 s) compared to M7 monolith (Figure 6.10 and Table 6.5). The structural and compositional characteristics of M7 and M8 were similar, however the number of the parallel channels in the former was 21 (88 cpsi) while in latter was 50 (209 cpsi) (Table 6.1). The increase of the cell density in the prepared monoliths resulted in decrease in the wall thickness (Table 6.1) and consequently enhanced the flow distribution and led to reduction of the mass transfer resistance.



**Figure 6.10** CO<sub>2</sub> breakthrough curves determined experimentally at 0.18 L·min<sup>-1</sup> of Blank, M6, M7, M8, M9 and 5A beads

**Table 6.4 Samples characteristics for breakthrough and pressure drop experiments**

Sample	Weight of monolith (g)	Net weight of loaded zeolite (g)	Bed length (mm)
M6	10.0	7.7	75
M7	9.3	7.2	75
M8	8.7	6.7	72
M9	7.9	7.2	65
5A beads	8.4	6.9	63

The time to reach 50 % of final concentration is correlated to zeolite loading and hence to the adsorption capacity of the monoliths. M6, M7 and M8 monoliths reached to 50% of the final concentration after 631, 461 and 440 seconds, respectively. This sequence is in agreement with the order of zeolite amounts loaded for the breakthrough experiments (M6 > M7 > M8); more zeolite amounts resulted in longer time to reach 50% of final concentration, Table 6.5.

Table 6.1 shows that M9 monolith contained channels similar to M8 but the concentration of silica in the former was 8% and in the latter was 22.3%. The breakthrough front of M9 was steeper with narrower width (410 s) than the breakthrough curve of M8 (Figure 6.10 and Table 6.5). The large interparticle voids that possibly formed due to less binder concentration in M9, as described in section 6.3.2, probably enhanced the flow of the adsorptive molecules throughout the adsorbent.

Table 6.5 shows that the time to reach 50 % of final concentration measured for M9 was 471s which was 1.07 times higher than the time measured for M8 (440 s). This can be attributed to higher zeolite loading in M9 experiment which is also 1.07 times higher than the zeolite loading in M8 experiment (Table 6.4).

The CO<sub>2</sub> breakthrough experiment performed on a packed bed of 8.4 g of 5A beads showed a steep curve with width of 250 s (Figure 6.10 and Table 6.5). The characteristics of the breakthrough front of beads packed bed indicate that it required longer time to reach 5 % of final concentration than M8 and M9 monoliths, while it reached to 95 % of final concentration after 700 s which was closer to the time recorded for M8 and M9 (731 s).

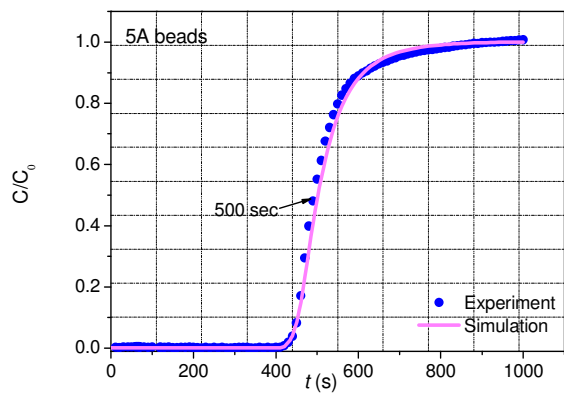
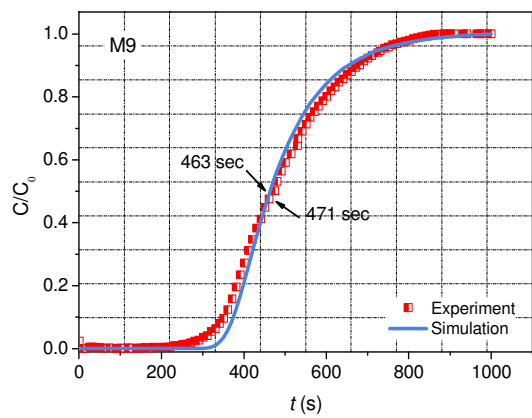
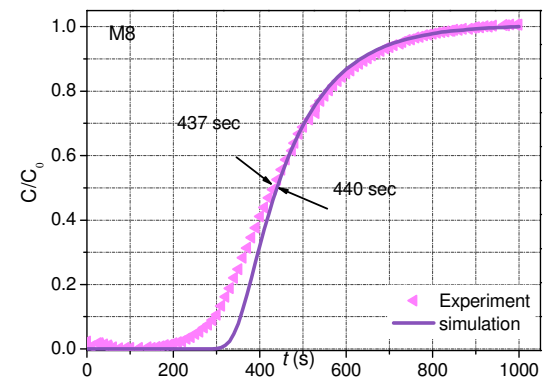


**Figure 6.11** The experimental (symbols) and simulation (solid lines)  $\text{CO}_2$  breakthrough profiles of samples M8, M9 and 5A beads at  $0.18 \text{ L} \cdot \text{min}^{-1}$ . Black arrow on each plot highlights the corresponding time to reach 50 % of final concentration.

Figure 6.11 shows the experimental (symbols) and fitted (lines)  $\text{CO}_2$  breakthrough curves of M8, M9 and 5A beads. The effective diffusivities of both samples were obtained by simulating

the experimental data and the results indicate that the diffusivity of CO<sub>2</sub> molecules in M8 and M9 was about six times faster than in 5A beads, at  $9.0 \times 10^{-6}$  for the former and  $1.5 \times 10^{-6}$  for the latter (Table 6.5). M8 and M9 monoliths were considered as ideal references for comparison with 5A beads because the wall thickness of these samples is equal to diameter of 5A beads (0.9 mm).

**Table 6.5 Summary of CO<sub>2</sub> adsorption properties extracted from breakthrough curves.**

Sample	Time to reach 5% of final concentration (s)	Time to reach 50% of final concentration (s)	Time to reach 95% of final concentration (s)	Break-through width (s)	De (cm <sup>2</sup> ·s <sup>-1</sup> )
M6	201	631	1280	1079	n.a.
M7	230	461	851	621	n.a.
M8	261	440	731	470	$9 \times 10^{-6}$
M9	321	471	731	410	$9 \times 10^{-6}$
5A beads	450	500	250	700	$1.5 \times 10^{-6}$

The value of the effective diffusivity includes the diffusivity of gas molecules in the interstices in the body of the adsorbent (monolith or beads) plus the diffusivity in zeolite crystals themselves <sup>183, 184</sup>. In 5A beads, gas molecules diffuse through two routes: (1) The micropores in the framework structure of 5A zeolite, (2) The interstitial voids between the zeolite crystals and the binder. Our monoliths, on the other hand, contained a network of interconnected channels and pores; namely, parallel channels (500  $\mu$ m), medium scale channels (20 – 85  $\mu$ m), small scale channels (9 – 1  $\mu$ m) and finally the meso and micro-sized pores in the structure of the zeolite particles. Through this channel / pore network, gas molecules were capable of rapidly reaching the remote active sites in the monoliths.

The diffusion of the gas molecules within our monoliths occurred simultaneously through four different routes namely: (1) parallel channels – meso and micropores of the primary building units of the walls of the parallel channels; (2) parallel channels - medium scale channels - small scale channels – meso and micropores of the walls building units; (3) parallel channels -

small scale channels – meso and micropores of the walls; (4) parallel channels - medium scale channels – meso and micropores of the walls.

#### 6.3.4.2 Pressure drop

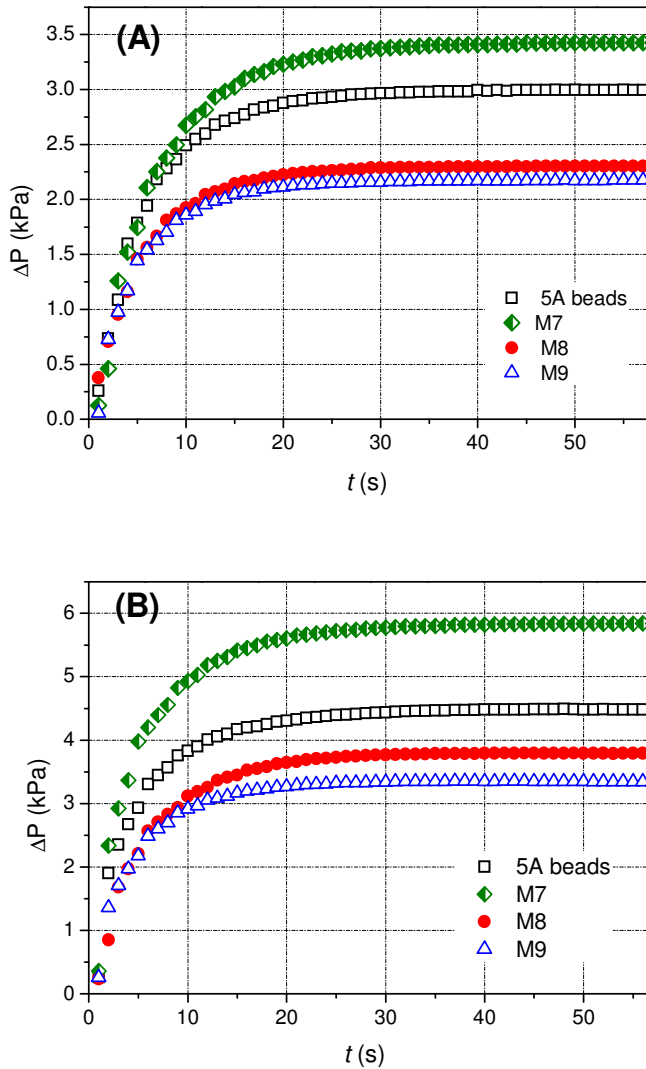


**Figure 6.12 The experimental results of the pressure drop across beds of monoliths or 5A beads measured at gas flow at two different superficial velocities; 0.71 (A) or 1.24 (B)  $\text{m} \cdot \text{sec}^{-1}$ .**

Figure 6.12A and B show the experimental results of pressure drop across packed beds of M7, M8 and M9 monoliths and 5A beads measured at two different superficial velocities, 0.75 and  $1.24 \text{ m} \cdot \text{sec}^{-1}$ .

The pressure drop per unit length was calculated by dividing the experimental results over the length of the corresponding bed. At superficial velocity  $0.7 \text{ m} \cdot \text{sec}^{-1}$ , the pressure drop per unit length recorded for beads packed bed was 1.3 times higher than the M8 or M9 monolith bed, and it increased to 1.4 times at  $1.2 \text{ m} \cdot \text{sec}^{-1}$  superficial velocity (Table 6.6). The pressure drop increases consistently with increasing the gas velocity due to increase in friction.

The results reveal that a column loaded with M7 monolith shows higher pressure drop per unit length than the beds of M8 or M9 monoliths. Since M8 and M9 monoliths contain higher cell density (209 cpsi) than M7 monolith (88 cpsi), we anticipate that the parallel channels plus the medium and small channels offer efficient and rapid mass transport for the adsorptive molecules throughout the monolith body and as a consequence the pressure drop reduced.

Table 6.6 shows that M8 and M9 which have similar channeling structures but different silica ratios exhibit similar pressure drop per unit length. This observation suggests that the influence of the additional interstices voids, which might be formed in M9 monolith due to less closely packed particles, on the pressure drop is negligible.

**Table 6.6 Summary of pressure drop measurements obtained experimentally ( $\Delta P_{\text{exp}}$ ) and theoretically ( $\Delta P_{\text{equ}}$ ) at two different superficial velocities of gas flow across monoliths and packed beds.**

sample	$0.7 \text{ m} \cdot \text{sec}^{-1}$			$1.2 \text{ m} \cdot \text{sec}^{-1}$		
	$\Delta P_{\text{exp}}$	$\Delta P_{\text{per unit length}}^a$	$\Delta P_{\text{equ}}^b$	$\Delta P_{\text{exp}}$	$\Delta P_{\text{per unit length}}^a$	$\Delta P_{\text{equ}}^b$
M7	3.4	0.4	3.4	5.8	0.7	5.7
M8	2.3	0.3	2.3	3.7	0.5	3.7
M9	2.1	0.3	2.1	3.3	0.5	3.5
5A beads	2.9	0.4	2.5	4.4	0.7	4.6

<sup>a</sup>Calculated by dividing the experimental results ( $\Delta P_{\text{exp}}$ ) over the length of the corresponding bed (Table 6.4).

<sup>b</sup>Calculated using equation (3) for monolith beds and equation (4) for beads packed bed.

Hagen-Poiseuille and Ergun equations were used to calculate the pressure drop across beds of the monoliths and the beads, respectively. For monoliths beds, the mathematical constant for Hagen-Poiseuille equation was estimated using the  $\Delta P_{\text{exp}}$  measurements at  $0.7 \text{ m} \cdot \text{sec}^{-1}$  superficial velocity. Similarly, for packed bed, the voidage value for Ergun equations was estimated using the  $\Delta P_{\text{exp}}$  measurements at  $0.7 \text{ m} \cdot \text{sec}^{-1}$  superficial velocity. The values obtained

from the mathematical modeling ( $\Delta P_{\text{equ}}$ ) are in good agreement with the experimental measurements ( $\Delta P_{\text{exp}}$ ) (Table 6.6) which indicates that a reliable prediction for large scale beds can be obtained.

In summary, the role of the number of the parallel channels (cell density) in the reduction of mass transfer resistance and the enhancement of diffusivity was demonstrated by the sharper breakthrough trend and lower pressure drop of M8 and M9 monoliths compared to M7 monolith. Also, the influence of plastic fiber concentration or in other words, the medium scale size channels was demonstrated by a significant reduction in the breakthrough width of M7 compared to M6. Future work is required to investigate the effects of the small size channels and the mesopores on the diffusivity and pressure drop.

## 6.4 Conclusion

Zeolite monolith with channeling structure mimicking a tree's vascular system was prepared. In other words, the body of the monoliths consisted of large parallel channels interconnected to medium and small scale channels. The medium and small scale channels are abundantly distributed throughout the walls of the monoliths for even gas distribution. Further, the primary building units used to construct the walls of the monoliths are mesoporous 5A zeolite particles which offer 3.4 nm interstitial paths for the gas molecules to reach to the micropores. Monoliths with two different cell densities, 88 and 209 cpsi, were prepared. The performance of the prepared monoliths was evaluated on CO<sub>2</sub> adsorption and compared with 5A beads. It was found that increasing the cell density (number of parallel channels) and raising the concentration of medium scale channels resulted in reducing the width of CO<sub>2</sub> breakthrough curves significantly. The experimental CO<sub>2</sub> breakthrough data were simulated and the results indicate that the diffusivity of CO<sub>2</sub> molecules in the prepared monoliths is six times faster than the diffusivity in 5A beads. The high diffusivity is attributed to network channeling system that allowed the gas molecules to move throughout the monoliths walls readily. Even though 5A beads have diameter equals to the wall thickness of the monolith, they only offer small interstitial voids between the zeolite crystals and the binder. The pressure drop across 5A beads packed bed was 1.3 times higher than the pressure drop across beds of the prepared monoliths. The pressure drop measurements obtained experimentally were in agreement with the values obtained by using mathematical modeling. In summary, our results indicate that the prepared monoliths are

competitive alternatives to traditional 5A beads to be used in gas separation by adsorption processes because they show high diffusivity, low pressure drop and comparable adsorption capacity.

# **Chapter 7: Conclusion and recommendations for future work**

## **7.1 Conclusion**

In a one-pot synthesis procedure, micro-mesoporous Na-A zeolites were successfully produced by the introduction of CTAB micelles to a slowly evolving zeolite system at room temperature. At the early stage of gel evolution, freshly formed miniature zeolite gel particles were assembled around the surface of the coexisting CTAB micelles forming aggregations of zeolite-CTAB. Aging the system for two weeks at room temperature induced slow mass transformation of the zeolite gel particles into nanocrystallites, which then grew slowly retaining the CTAB micelles within the crystallization domain. The CTAB micelles and the two week room temperature aging worked collaboratively forming the mesoporous Na-A zeolite. The introduction of CTAB micelles in the synthesis gel is not effective in terms of generating the mesopores without the aging at room temperature and vice-versa. The size of the mesopores was controlled by introducing different amounts/types of linear alkanes (swelling agents) into the zeolite-CTAB system. Increasing the molar ratio of the swelling agent to CTAB produced larger mesopores. Furthermore, short hydrocarbon chains like *n*-hexane generated smaller pores than those obtained by long hydrocarbon chains like *n*-octane and *n*-dodecane. The alkanes acted as swelling agents by permeating into the core of the micelles increasing their volume as well as their packing parameters, which enhanced the density of their positive charge. Increasing the aging period for longer than two weeks resulted in a significant reduction in the surface area and the mesopore volume. Further, raising the CTAB concentration in the synthesis mixture resulted in inhibiting the crystallinity of Na-A zeolite. The IEP (Iso-Electric Point) for the mesoporous Na-A zeolite was shifted to pH ~ 0 as compared to conventional microporous Na-A zeolite (pH ~ 3.1). Furthermore, our material shows higher pore volume compared to conventional Na-A zeolite, which resulted in higher adsorption capacity for ethylene gas. Thus, our material offers potential applications in projects where ethylene recovery is involved, for example, from the purge gas stream in the polyethylene manufacturing plant.

Furthermore, the formation and growth mechanism of the zeolite crystals in the gel/CTAB/*n*-dodecane system were studied in detail. The ratio of *n*-dodecane: CTAB was raised until the

system reached the emulsion stage. The *n*-dodecane droplets stabilized by the CTAB molecules represent the dispersed phase and the zeolite gel is the continuous phase of the emulsion. The results demonstrated that produced Na-A zeolite crystals consisted of thin crystalline polyhedral shell and multi-hollow polycrystalline core. The product also shows some particles which are multi-hollow polycrystalline aggregates that contain large mesopores attributed to voids between the aggregated crystallites. By systematic investigations of samples taken at different reaction stages, it is demonstrated that Na-A zeolite particles with multi-hollow polycrystalline core-shell structure can be grown according to an aggregation-recrystallization approach in contrast to the classic growth mechanism. The presence of positive *n*-dodecane droplets within the zeolite reaction mixture enhances the formation of nanoparticle aggregates at the early stage of gel evolution and organization. By conducting the crystallization at room temperature, the aggregated nanoparticles are crystallized locally forming polycrystalline aggregates which then undergo a reversed crystal growth. The crystallization takes place on the surface of the polycrystalline aggregates and extends inwards. This part of our work demonstrates two points; the synthesis of a new kind of mesoporous Na-A with multi-hollow polycrystalline morphology and also demonstrate, for the first time, formation of LTA zeolite crystal *via* reverse crystallization route while retaining the identity of LTA zeolite.

The synthesized micro-mesoporous Na-A zeolite particles were ion exchanged to Ca-A zeolite particles and then used as primary building units to fabricate self standing zeolite monoliths with channeling structure that mimics a tree's vascular system. In other words, the body of the monoliths consisted of large parallel channels interconnected to medium and small scale channels. The medium and small scale channels are abundantly distributed throughout the walls of the monoliths for even flow gas distribution. Additionally, the walls of all these channels were constructed of micro-mesoporous Ca-A zeolite particles, which offer 3.4 nm interstitial paths for the gas molecules to reach to the micropores. Monoliths with two different cell densities, 88 and 209 cpsi, were prepared. The performance of the prepared monoliths was evaluated on CO<sub>2</sub> adsorption and compared with 5A beads. It was found that increasing the cell density (number of parallel channels) and raising the concentration of medium scale channels resulted in reducing the width of breakthrough curves significantly. The experimental CO<sub>2</sub> breakthrough data were simulated and the results indicate that the diffusivity of CO<sub>2</sub> molecules in the prepared monoliths is six times faster than the diffusivity in 5A beads. The high diffusivity

is attributed to the network channeling system that allows the gas molecules to move throughout the monoliths walls readily. On the other hand, the 5A beads have diameter equal to the wall thickness of the monolith, but they only offer small interstitial voids between the zeolite crystals and the binder. The pressure drop across 5A beads packed bed was 1.3 times higher than the pressure drop across beds of the prepared monoliths. The pressure drop measurements obtained experimentally were in agreement with the values obtained by using mathematical modeling. In summary, our results indicate that the prepared monoliths are competitive alternatives to traditional 5A beads to be used in gas separation by adsorption processes because they show high diffusivity, low pressure drop and comparable adsorption capacity.

## 7.2 Recommendations for future work

- The first part of this work presented a novel route to synthesize micro-mesoporous zeolite particles. This route is low crystallization and growth rate at room temperature in the presence of cetyltrimethylammonium bromide –CTAB.
- 1. In addition to the parameters that have been studied in this work, it would be interesting to investigate the effect of the length of the hydrophobic portion of the surfactant molecules on the size of the mesopores. Surfactants with shorter or longer alkyl group can be used; such as dodecyltrimethylammonium bromide ( $C_{12}TABr$ ), tetradecyltrimethylammonium bromide ( $C_{14}TABr$ ), or octadecyltrimethylammonium bromide ( $C_{18}TABr$ ).
- 2. It is recommended to investigate the possibility of synthesizing other types of zeolites such as zeolite X and Y following the same route. The influence of the introduction of a straight alkane as swelling agent to the system on the pore size distribution can also be studied. Furthermore, controlling the size of the mesopores by changing the length of the hydrocarbon or the concentration of the swelling agent.
- The second part of this work included using the pre-synthesized micro-mesoporous zeolite particles as primary building units to fabricate hierarchical monolithic structures with innovative channeling design that mimics a tree's vascular system. The fabricated monoliths showed diffusivity six times higher than the diffusivity of the commercial beads. This work included a studying of the effects of the number of

the large parallel channels and the concentration of the medium scale channels on the diffusivity and the pressure drop. Additional work can be accomplished for better understanding and results:

1. It is recommended to investigate the role of introducing building units with micro and mesopores rather than only micropores on the diffusivity enhancement and pressure drop reduction. Also, the effect of the concentration of the small size channels or in other words the methyl cellulose concentration on the processing characteristics of the monolith.
2. Investigating the possibility of fabricating monoliths with thinner wall thickness which can be accomplished by increasing the number of the parallel channels. The binder concentration is probably required to be increased for more stable walls. The influence of thinner walls and higher cell density on the effective diffusivity can be studied.

## **References**

1. Dyer, A., An Introduction To Zeolite Molecular Sieves. John Wiley and Sons: New York, 1988.
2. L. B. McCusker; Baerlocher, C., Introduction To Zeolite Science and Practice. Elsevier: Amsterdam, 2007.
3. Breck, D. W., Zeolite molecular sieves: structure, chemistry, and use. John Wiley and Sons: New York, 1974.
4. Tosheva, L.; Valtchev, V.; Sterte, J., Silicalite-1 containing microspheres prepared using shape-directing macro-templates. *Microporous and Mesoporous Materials* 2000, 35-36, 621-629.
5. Jacobsen, C. J. H.; Madsen, C.; Houzvicka, J.; Schmidt, I.; Carlsson, A., Mesoporous Zeolite Single Crystals. *Journal of the American Chemical Society* 2000, 122, (29), 7116-7117.
6. Schmidt, I.; Madsen, C.; Jacobsen, C. J. H., Confined Space Synthesis. A Novel Route to Nanosized Zeolites. *Inorganic Chemistry* 2000, 39, (11), 2279-2283.
7. Egeblad, K.; Christensen, C. H.; Kustova, M.; Christensen, C. H., Templating Mesoporous Zeolites. *Chemistry of Materials* 2007, 20, (3), 946-960.
8. Tao, Y.; Kanoh, H.; Kaneko, K., Synthesis of mesoporous zeolite a by resorcinol-formaldehyde aerogel templating. *Langmuir* 2005, 21, (2), 504-507.
9. Tao, Y.; Kanoh, H.; Kaneko, K., ZSM-5 monolith of uniform mesoporous channels. *Journal of the American Chemical Society* 2003, 125, (20), 6044-6045.
10. Nishiyama, N.; Ueyama, K.; Matsukata, M., A defect-free mordenite membrane synthesized by vapour-phase transport method. *Journal of the Chemical Society, Chemical Communications* 1995, (19), 1967-1968.
11. Takahashi, R.; Sato, S.; Sodesawa, T.; Nishino, H.; Yachi, A., Synthesis of monolithic zeolites with macropores. *Journal of the Ceramic Society of Japan* 2006, 114, (1329), 421-424.

12. Jifang Cheng, S. P., Bin Yue, Linping Qian, Chunxia He, Yan Zhou and Heyong He, Synthesis and characterization of hollow zeolite microspheres with a mesoporous shell by O/W/O emulsion and vapor-phase transport method. *Microporous and Mesoporous Materials* 2008, 115, (3), pp. 383-388.
13. Zhao, D.; Huo, Q.; Feng, J.; Chmelka, B. F.; Stucky, G. D., Nonionic triblock and star diblock copolymer and oligomeric surfactant syntheses of highly ordered, hydrothermally stable, mesoporous silica structures. *Journal of the American Chemical Society* 1998, 120, (24), 6024-6036.
14. Zhao, D.; Feng, J.; Huo, Q.; Melosh, N.; Fredrickson, G. H.; Chmelka, B. F.; Stucky, G. D., Triblock copolymer syntheses of mesoporous silica with periodic 50 to 300 angstrom pores. *Science* 1998, 279, (5350), 548-552.
15. Ottaviani, M. F.; Moscatelli, A.; Desplantier-Giscard, D.; Di Renzo, F.; Kooyman, P. J.; Alonso, B.; Galarneau, A., Synthesis of Micelle-Templated Silicas from Cetyltrimethylammonium Bromide/1,3,5-Trimethylbenzene Micelles. *The Journal of Physical Chemistry B* 2004, 108, (32), 12123-12129.
16. Valtchev, V. P.; Tosheva, L.; Bozhilov, K. N., Synthesis of Zeolite Nanocrystals at Room Temperature. *Langmuir* 2005, 21, (23), 10724-10729.
17. Cundy, C. S.; Cox, P. A., The hydrothermal synthesis of zeolites: Precursors, intermediates and reaction mechanism. *Microporous and Mesoporous Materials* 2005, 82, (1-2), 1-78.
18. Chen, X.; Qiao, M.; Xie, S.; Fan, K.; Zhou, W.; He, Y., Self-construction of core-shell and hollow zeolite analcime Icositetrahedra: A reversed crystal growth process via oriented aggregation of nanocrystallites and recrystallization from surface to core. *Journal of the American Chemical Society* 2007, 129, (43), 13305-13312.
19. Greer, H.; Wheatley, P. S.; Ashbrook, S. E.; Morris, R. E.; Zhou, W., Early Stage Reversed Crystal Growth of Zeolite A and Its Phase Transformation to Sodalite. *Journal of the American Chemical Society* 2009, 131, (49), 17986-17992.
20. Valtchev, V.; Mintova, S., Layer-by-layer preparation of zeolite coatings of nanosized crystals. *Microporous and Mesoporous Materials* 2001, 43, (1), 41-49.

21. Lee, Y. J.; Lee, J. S.; Park, Y. S.; Yoon, K. B., Synthesis of large monolithic zeolite foams with variable macropore architectures. *Advanced Materials* 2001, 13, (16), 1259-1263.
22. Wang, X. D.; Tang, Y.; Wang, Y. J.; Gao, Z.; Yang, W. L.; Fu, S. K., Fabrication of hollow zeolite spheres. *Chemical Communications* 2000, (21), 2161-2162.
23. Dong, A.; Wang, Y.; Tang, Y.; Ren, N.; Zhang, Y.; Yue, Y.; Gao, Z., Zeolitic tissue through wood cell templating. *Advanced Materials* 2002, 14, (12), 926-929.
24. Grande, C. A.; Cavenati, S.; Barcia, P.; Hammer, J.; Fritz, H. G.; Rodrigues, A. E., Adsorption of propane and propylene in zeolite 4A honeycomb monolith. *Chemical Engineering Science* 2006, 61, (10), 3053-3063.
25. Yang, R. T., Zeolites and Molecular Sieves. In Adsorbents: Fundamentals and Applications. John Wiley & Sons, Inc.: New York, 2003; pp 157-190.
26. Ch. Baerlocher; W. M. Meier; Olson, D. H., Atlas of Zeolite Framework Types. 5<sup>th</sup> ed.; Elsevier: Amsterdam, 2001.
27. Wells, S. A.; Sartbaeva, A.; Gatta, G. D., Flexibility windows and phase transitions of ordered and disordered ANA framework zeolites. *Europhysics Letters* 2011, 94, (5), 56001.
28. Jaramillo, E.; Chandross, M., Adsorption of Small Molecules in LTA Zeolites. 1. NH<sub>3</sub>, CO<sub>2</sub>, and H<sub>2</sub>O in Zeolite 4A. *The Journal of Physical Chemistry B* 2004, 108, (52), 20155-20159.
29. Breck, D. W.; Eversole, W. G.; Milton, R. M.; Reed, T. B.; Thomas, T. L., Crystalline zeolites. I. The properties of a new synthetic zeolite, type A. *Journal of the American Chemical Society* 1956, 78, (23), 5963-5971.
30. Reed, T. B.; Breck, D. W., Crystalline zeolites. II. Crystal structure of synthetic zeolite, type A. *Journal of the American Chemical Society* 1956, 78, (23), 5972-5977.
31. Nakano, T.; Matsumoto, J.; Cong Duan, T.; Watanabe, I.; Suzuki, T.; Kawamata, T.; Amato, A.; Pratt, F. L.; Nozue, Y., Fast muon spin relaxation in ferromagnetism of potassium clusters in zeolite A. *Physica B: Condensed Matter* 2009, 404, (5-7), 630-633.

32. Porcher, F.; Dusausoy, Y.; Souhassou, M.; Lecomte, C., Epitaxial growth of zeolite X on zeolite A and twinning in zeolite A: Structural and topological analysis. *Mineralogical Magazine* 2000, 64, (1), 1-8.
33. Langmi, H. W.; Walton, A.; Al-Mamouri, M. M.; Johnson, S. R.; Book, D.; Speight, J. D.; Edwards, P. P.; Gameson, I.; Anderson, P. A.; Harris, I. R., Hydrogen adsorption in zeolites A, X, Y and RHO. *Journal of Alloys and Compounds* 2003, 356-357, (0), 710-715.
34. Granato, M. A.; Vlugt, T. J. H.; Rodrigues, A. E. In Molecular simulation of propane-propylene binary adsorption equilibrium in zeolite 4a. *AICHE Annual Meeting, Conference Proceedings* 2006; 2006.
35. Romero-Peláez, A.; Aguilar-Armenta, G., Adsorption Kinetics and Equilibria of Carbon Dioxide, Ethylene, and Ethane on 4A(CECA). *Zeolite. Journal of Chemical & Engineering Data* 2010, 55, (9), 3625-3630.
36. Christensen, C. H.; Johannsen, K.; Schmidt, I., Catalytic Benzene Alkylation over Mesoporous Zeolite Single Crystals: Improving Activity and Selectivity with a New Family of Porous Materials. *Journal of the American Chemical Society* 2003, 125, (44), 13370-13371.
37. Vijaikumar, S.; Subramanian, T.; Pitchumani, K., Zeolite encapsulated nanocrystalline CuO: A redox catalyst for the oxidation of secondary alcohols. *Journal of Nanomaterials* 2008, 2008, (1).
38. Weitkamp, J., Zeolites and catalysis. *Solid State Ionics* 2000, 131, (1-2), 175-188.
39. Xu, F.; Wang, Y.; Wang, X.; Zhang, Y.; Tang, Y.; Yang, P., A Novel Hierarchical Nanozeolite Composite as Sorbent for Protein Separation in Immobilized Metal-Ion Affinity Chromatography. *Advanced Materials* 2003, 15, (20), 1751-1753.
40. Mosca, A.; Hedlund, J.; Ridha, F. N.; Webley, P., Optimization of synthesis procedures for structured PSA adsorbents. *Adsorption* 2008, 14, (4-5), 687-693.
41. R. P. Townsend; Coker, E. N., Ion exchange in zeolites. Elsevier: Amsterdam, 2001; Vol. 137.

42. Harper, R. J.; Stifel, G. R.; Anderson, R. B., Adsorption of gases on 4A synthetic zeolite. *Canadian Journal of Chemistry* 1969, 47, (24), 4661-4670.
43. Romero-Perez, A.; Aguilar-Armenta, G., Adsorption Kinetics and Equilibria of Carbon Dioxide, Ethylene, and Ethane on 4A(CECA) Zeolite. *Journal of Chemical & Engineering Data* 2010, 55, (9), 3625-3630.
44. Miano, F., Adsorption of hydrocarbon vapour mixtures onto zeolite 5A. *Colloids and Surfaces A: Physicochemical and Engineering Aspects* 1996, 110, (1), 95-104.
45. Li, G.; Xiao, P.; Webley, P.; Zhang, J.; Singh, R.; Marshall, M., Capture of CO<sub>2</sub> from high humidity flue gas by vacuum swing adsorption with zeolite 13X. *Adsorption* 2008, 14, (2), 415-422.
46. Silva, J. A. C.; Rodrigues, A. r. E., Sorption and Diffusion of n-Pentane in Pellets of 5A Zeolite. *Industrial & Engineering Chemistry Research* 1997, 36, (2), 493-500.
47. Bezus, A. G.; Kiselev, A. V.; Du, P. Q., The influence of size, charge and concentration of exchange cations on the adsorption of ethane and ethylene by zeolites. *Journal of Colloid And Interface Science* 1972, 40, (2), 223-232.
48. Chue, K. T.; Kim, J. N.; Yoo, Y. J.; Cho, S. H.; Yang, R. T., Comparison of Activated Carbon and Zeolite 13X for CO<sub>2</sub> Recovery from Flue Gas by Pressure Swing Adsorption. *Industrial & Engineering Chemistry Research* 1995, 34, (2), 591-598.
49. Singh, R. K.; Webley, P., Adsorption of N<sub>2</sub>, O<sub>2</sub> and Ar in Potassium Chabazite. *Adsorption* 2005, 11, (0), 173-177.
50. Cheng, X.-w.; Wang, J.; Guo, J.; He, H.-y.; Long, Y.-c., FER zeolite crystallized in THF-Na<sub>2</sub>O-SiO<sub>2</sub>-Al<sub>2</sub>O<sub>3</sub>-H<sub>2</sub>O reactant system containing catalytic amount of organic additives. *Microporous and Mesoporous Materials* 2009, 119, (1-3), 60-67.
51. Christensen, C. H.; Johannsen, K.; Schmidt, I.; Christensen, C. H., Catalytic Benzene Alkylation over Mesoporous Zeolite Single Crystals: Improving Activity and Selectivity with a New Family of Porous Materials. *Journal of the American Chemical Society* 2003, 125, (44), 13370-13371.

52. Zhu, H.; Liu, Z.; Kong, D.; Wang, Y.; Xie, Z., Synthesis and Catalytic Performances of Mesoporous Zeolites Templated by Polyvinyl Butyral Gel as the Mesopore Directing Agent. *The Journal of Physical Chemistry C* 2008, 112, (44), 17257-17264.
53. Cho, K.; Ryoo, R.; Asahina, S.; Xiao, C.; Klingstedt, M.; Umemura, A.; Anderson, M. W.; Terasaki, O., Mesopore generation by organosilane surfactant during LTA zeolite crystallization, investigated by high-resolution SEM and Monte Carlo simulation. *Solid State Sciences* 2011, 13, (4), 750-758.
54. Choi, M.; Cho, H. S.; Srivastava, R.; Venkatesan, C.; Choi, D. H.; Ryoo, R., Amphiphilic organosilane-directed synthesis of crystalline zeolite with tunable mesoporosity. *nature materials* 2006, 5, (9), 718-723.
55. Choi, M.; Srivastava, R.; Ryoo, R., Organosilane surfactant-directed synthesis of mesoporous aluminophosphates constructed with crystalline microporous frameworks. *Chemical Communications* 2006, (42), 4380-4382.
56. Li, Y.; Shi, J.; Hua, Z.; Chen, H.; Ruan, M.; Yan, D., Hollow spheres of mesoporous aluminosilicate with a three-dimensional pore network and extraordinarily high hydrothermal stability. *Nano Letters* 2003, 3, (5), 609-612.
57. Zhao, J.; Hua, Z.; Liu, Z.; Li, Y.; Guo, L.; Bu, W.; Cui, X.; Ruan, M.; Chen, H.; Shi, J., Direct fabrication of mesoporous zeolite with a hollow capsular structure. *Chemical Communications* 2009, (48), 7578-7580.
58. Zhao, J.; Zhou, J.; Chen, Y.; He, Q.; Ruan, M.; Guo, L.; Shi, J.; Chen, H., Fabrication of mesoporous zeolite microspheres by a one-pot dual-functional templating approach. *Journal of Materials Chemistry* 2009, 19, (41), 7614-7616.
59. Herrmann, C.; Haas, J.; Fetting, F., Effect of the crystal size on the activity of ZSM-5 catalysts in various reactions. *Applied Catalysis* 1987, 35, (2), 299-310.
60. Mosca, A.; Hedlund, J.; Webley, P. A.; Grahn, M.; Rezaei, F., Structured zeolite NaX coatings on ceramic cordierite monolith supports for PSA applications. *Microporous and Mesoporous Materials* 2010, 130, (1-3), 38-48.
61. Rezaei, F.; Webley, P., Structured adsorbents in gas separation processes. *Separation and Purification Technology* 2010, 70, (3), 243-256.

62. Rezaei, F.; Webley, P., Optimum structured adsorbents for gas separation processes. *Chemical Engineering Science* 2009, 64, (24), 5182-5191.
63. Shams, K.; Mirmohammadi, S. J., Preparation of 5A zeolite monolith granular extrudates using kaolin: Investigation of the effect of binder on sieving/adsorption properties using a mixture of linear and branched paraffin hydrocarbons. *Microporous and Mesoporous Materials* 2007, 106, (1-3), 268-277.
64. Huang, Y.; Wang, K.; Dong, D.; Li, D.; Hill, M. R.; Hill, A. J.; Wang, H., Synthesis of hierarchical porous zeolite NaY particles with controllable particle sizes. *Microporous and Mesoporous Materials* 2010, 127, (3), 167-175.
65. Wang, H.; Holmberg, B. A.; Yan, Y., Synthesis of Template-Free Zeolite Nanocrystals by Using in Situ Thermoreversible Polymer Hydrogels. *Journal of the American Chemical Society* 2003, 125, (33), 9928-9929.
66. Everett, D. H., *Pure Appl. Chem.* 1972, 31, 585.
67. Cho, K.; Cho, H. S.; De Menorval, L. C.; Ryoo, R., Generation of mesoporosity in LTA zeolites by organosilane surfactant for rapid molecular transport in catalytic application. *Chemistry of Materials* 2009, 21, (23), 5664-5673.
68. Van Donk, S.; Janssen, A. H.; Bitter, J. H.; de Jong, K. P., Generation, Characterization, and Impact of Mesopores in Zeolite Catalysts. *Catalysis Reviews* 2003, 45, (2), 297-319.
69. Jacobsen, C. J. H.; Madsen, C.; Houzvicka, J.; Schmidt, I.; Carlsson, A., Mesoporous zeolite single crystals [2]. *Journal of the American Chemical Society* 2000, 122, (29), 7116-7117.
70. Mosca, A.; Hedlund, J.; Webley, P. A.; Grahn, M.; Rezaei, F., Structured zeolite NaX coatings on ceramic cordierite monolith supports for PSA applications. *Microporous and Mesoporous Materials* 130, (1-3), 38-48.
71. Li, G.; Singh, R.; Li, D.; Zhao, C.; Liu, L.; Webley, P. A., Synthesis of biomorphic zeolite honeycomb monoliths with 16 000 cells per square inch. *Journal of Materials Chemistry* 2009, 19, (44).
72. Mintova, S.; Bein, T., Microporous films prepared by spin-coating stable colloidal suspensions of zeolites. *Advanced Materials* 2001, 13, (24), 1880-1883.

73. Lee, Y.-J.; Yoon, K. B., Effect of composition of polyurethane foam template on the morphology of silicalite foam. *Microporous and Mesoporous Materials* 2006, 88, (1-3), 176-186.
74. Walsh, D.; Kulak, A.; Aoki, K.; Ikoma, T.; Tanaka, J.; Mann, S., Preparation of higher-order zeolite materials by using dextran templating. *Angewandte Chemie - International Edition* 2004, 43, (48), 6691-6695.
75. Valtchev, V., Silicalite-1 hollow spheres and bodies with a regular system of macrocavities. *Chemistry of Materials* 2002, 14, (10), 4371-4377.
76. Yoon, K. B.; Lee, Y. J.; Park, Y. S.; Lee, J. S. Method of the preparation of macroporous foam comprising zeolite or zeotype material. *US patent No. 6777364B2* 2004.
77. Dong, A.; Wang, Y.; Tang, Y.; Zhang, Y.; Ren, N.; Gao, Z., Mechanically stable zeolite monoliths with three-dimensional ordered macropores by the transformation of mesoporous silica spheres. *Advanced Materials* 2002, 14, (20), 1506-1510.
78. Wang, Y.; Caruso, F., Macroporous zeolitic membrane bioreactors. *Advanced Functional Materials* 2004, 14, (10), 1012-1018.
79. Wang, Y.; Tang, Y.; Dong, A.; Wang, X.; Ren, N.; Shan, W.; Gao, Z., Self-Supporting Porous Zeolite Membranes with Sponge-like Architecture and Zeolitic Microtubes. *Advanced Materials* 2002, 14, (13-14), 994-997.
80. Zhang, B.; Davis, S. A.; Mann, S., Starch gel templating of spongelike macroporous silicalite monoliths and mesoporous films. *Chemistry of Materials* 2002, 14, (3), 1369-1375.
81. Wang, L.; Yin, C.; Shan, Z.; Liu, S.; Du, Y.; Xiao, F. S., Bread-template synthesis of hierarchical mesoporous ZSM-5 zeolite with hydrothermally stable mesoporosity. *Colloids and Surfaces A: Physicochemical and Engineering Aspects* 2009, 340, (1-3), 126-130.
82. Holmes, S. M.; Markert, C.; Plaisted, R. J.; Forrest, J. O.; Agger, J. R.; Anderson, M. W.; Cundy, C. S.; Dwyer, J., A novel method for the growth of silicalite membranes on stainless steel supports. *Chemistry of Materials* 1999, 11, (11), 3329-3332.

83. Huang, L.; Wang, Z.; Sun, J.; Miao, L.; Li, Q.; Yan, Y.; Zhao, D., Fabrication of ordered porous structures by self-assembly of zeolite nanocrystals [5]. *Journal of the American Chemical Society* 2000, 122, (14), 3530-3531.
84. Lee, Y. J.; Yoon, K. B., Effect of composition of polyurethane foam template on the morphology of silicalite foam. *Microporous and Mesoporous Materials* 2006, 88, (1-3), 176-186.
85. Hans-Jürgen Butt, K. G., Michael Kappl, Surfactants, Micelles, Emulsions, and Foams in Physics and Chemistry of Interfaces. In Wiley-VCH GmbH & Co. KGaA: Weinheim, The Federal Republic of Germany, 2003.
86. Raimondi, M. E., Invited article Liquid crystal templating of porous materials. *Liquid Crystals* 1999, 26, (3), 305-339.
87. Kresge, C. T.; Leonowicz, M. E.; Roth, W. J.; Vartuli, J. C.; Beck, J. S., Ordered mesoporous molecular sieves synthesized by a liquid-crystal template mechanism. *Nature* 1992, 359, (6397), 710-712.
88. Blin, J. L.; Su, B. L., Tailoring pore size of ordered mesoporous silicas using one or two organic auxiliaries as expanders. *Langmuir* 2002, 18, (13), 5303-5308.
89. Christiansen, S. C.; Zhao, D.; Janicke, M. T.; Landry, C. C.; Stucky, G. D.; Chmelka, B. F., Molecularly Ordered Inorganic Frameworks in Layered Silicate Surfactant Mesophases. *Journal of the American Chemical Society* 2001, 123, (19), 4519-4529.
90. Hedin, N.; Graf, R.; Christiansen, S. C.; Gervais, C.; Hayward, R. C.; Eckert, J.; Chmelka, B. F., Structure of a Surfactant-Templated Silicate Framework in the Absence of 3D Crystallinity. *Journal of the American Chemical Society* 2004, 126, (30), 9425-9432.
91. Beck, J. S.; Vartuli, J. C.; Roth, W. J.; Leonowicz, M. E.; Kresge, C. T.; Schmitt, K. D.; Chu, C. T. W.; Olson, D. H.; Sheppard, E. W., A new family of mesoporous molecular sieves prepared with liquid crystal templates. *Journal of the American Chemical Society* 1992, 114, (27), 10834-10843.
92. Beck, J. S.; Vartuli, J. C.; Kennedy, G. J.; Kresge, C. T.; Roth, W. J.; Schramm, S. E., Molecular Or Supramolecular Templating: Defining The Role of Surfactant Chemistry In

- the Formation of M41S and Zeolitic Molecular Sieves. In *Studies in Surface Science and Catalysis*, 1995; Vol. 98, pp 15-16.
93. Beck, J. S.; Vartuli, J. C.; Roth, W. J.; Leonowicz, M. E.; Kresge, C. T.; Schmitt, K. D.; Chu, C. T. W.; Olson, D. H.; Sheppard, E. W.; McCullen, S. B.; Higgins, J. B.; Schlenker, J. L., A new family of mesoporous molecular sieves prepared with liquid crystal templates. *Journal of the American Chemical Society* 1992, 114, (27), 10834-10843.
  94. Zhao, D.; Feng, J.; Huo, Q.; Melosh, N.; Fredrickson, G. H.; Chmelka, B. F.; Stucky, G. D., Triblock Copolymer Syntheses of Mesoporous Silica with Periodic 50 to 300 Angstrom Pores. *Science* 1998, 279, (5350), 548-552.
  95. Chen, D.; Li, Z.; Yu, C.; Shi, Y.; Zhang, Z.; Tu, B.; Zhao, D., Nonionic block copolymer and anionic mixed surfactants directed synthesis of highly ordered mesoporous silica with bicontinuous cubic structure. *Chemistry of Materials* 2005, 17, (12), 3228-3234.
  96. Han, Y.; Li, N.; Zhao, L.; Li, D.; Xu, X.; Wu, S.; Di, Y.; Li, C.; Zou, Y.; Yu, Y.; Xiao, F. S., Understanding of the high hydrothermal stability of the mesoporous materials prepared by the assembly of triblock copolymer with preformed zeolite precursors in acidic media. *Journal of Physical Chemistry B* 2003, 107, (31), 7551-7556.
  97. Santacruz, I.; Nieto, M. I.; Moreno, R.; Faraldo, M.; Sastre, E., A novel method to prepare zeolites with hierarchical porosity. *Advanced Engineering Materials* 2005, 7, (9), 858-861.
  98. Liu, Y.; Xu, J.; Jin, L.; Fang, Y.; Hu, H., Synthesis and modification of zeolite NaA adsorbents for separation of hydrogen and methane. *ASIA-PACIFIC JOURNAL OF CHEMICAL ENGINEERING* 2009, 4, 666-671.
  99. Holland, B. T.; Abrams, L.; Stein, A., Dual templating of macroporous silicates with zeolitic microporous frameworks. *Journal of the American Chemical Society* 1999, 121, (17), 4308-4309.
  100. Sen, T.; Tiddy, G. J. T.; Casci, J. L.; Anderson, M. W., One-pot synthesis of hierarchically ordered porous-silica materials with three orders of length scale. *Angewandte Chemie - International Edition* 2003, 42, (38), 4649-4653.

101. Hua, J.; Han, Y., One-step preparation of zeolite silicalite-1 microspheres with adjustable macroporosity. *Chemistry of Materials* 2009, 21, (12), 2344-2348.
102. Yang, H.; Liu, Q.; Liu, Z.; Gao, H.; Xie, Z., Controllable synthesis of aluminosilica monoliths with hierarchical pore structure and their catalytic performance. *Microporous and Mesoporous Materials* 2010, 127, (3), 213-218.
103. Huang, Y.; Dong, D.; Yao, J.; He, L.; Ho, J.; Kong, C.; Hill, A. J.; Wang, H., In Situ Crystallization of Macroporous Monoliths with Hollow NaP Zeolite Structure. *Chemistry of Materials* 2010, 22, (18), 5271-5278.
104. Imhof, A.; Pine, D. J., Uniform macroporous ceramics and plastics by emulsion templating. *Advanced Materials* 1998, 10, (9), 697-700.
105. Imhof, A.; Pine, D. J., Ordered macroporous materials by emulsion templating. *Nature* 1997, 389, (6654), 948-951.
106. Manoharan, V. N.; Imhof, A.; Thorne, J. D.; Pine, D. J., Photonic crystals from emulsion templates. *Advanced Materials* 2001, 13, (6), 447-450.
107. Bibette, J., Depletion interactions and fractionated crystallization for polydisperse emulsion purification. *Journal of Colloid And Interface Science* 1991, 147, (2), 474-478.
108. Yi, G. R.; Yang, S. M., Microstructures of porous silica prepared in aqueous and nonaqueous emulsion templates. *Chemistry of Materials* 1999, 11, (9), 2322-2325.
109. Sun, J.; Ma, D.; Zhang, H.; Bao, X.; Weinberg, G.; Su, D., Macro-mesoporous silicas complex and the carbon replica. *Microporous and Mesoporous Materials* 2007, 100, (1-3), 356-360.
110. Das, A.; Das, N.; Naskar, M. K.; Kundu, D.; Chatterjee, M.; Maiti, H. S., Influence of process parameters on the formation of Silicalite-1 zeolite particles. *Ceramics International* 2009, 35, (5), 1799-1806.
111. Carr, C. S.; Shantz, D. F., Synthesis of high aspect ratio low-silica zeolite L rods in oil/water/surfactant mixtures. *Chemistry of Materials* 2005, 17, (24), 6192-6197.
112. Lee, S.; Shantz, D. F., Zeolite growth in nonionic microemulsions: Synthesis of hierarchically structured zeolite particles. *Chemistry of Materials* 2005, 17, (2), 409-417.

113. Carn, F.; Colin, A.; Achard, M. F.; Deleuze, H.; Sellier, E.; Birot, M.; Backov, R., Inorganic monoliths hierarchically textured via concentrated direct emulsion and micellar templates. *Journal of Materials Chemistry* 2004, 14, (9), 1370-1376.
114. Yuan, Z. Y.; Su, B. L., Insights into hierarchically meso-macroporous structured materials. *Journal of Materials Chemistry* 2006, 16, (7), 663-677.
115. Cheng, J.; Pei, S.; Yue, B.; Qian, L.; He, C.; Zhou, Y.; He, H., Synthesis and characterization of hollow zeolite microspheres with a mesoporous shell by O/W/O emulsion and vapor-phase transport method. *Microporous and Mesoporous Materials* 2008, 115, (3), 383-388.
116. Shan, W.; Zhang, Y.; Wang, Y.; Xia, J.; Tang, Y., Synthesis of meso-/macroporous zeolite (Fe,Al)-ZSM-5 microspheres from diatomite. *Chemistry Letters* 2004, 33, (3), 270-271.
117. Anderson, M. W.; Holmes, S. M.; Hanif, N.; Cundy, C. S., Hierarchical pore structures through diatom zeolitization. *Angewandte Chemie - International Edition* 2000, 39, (15), 2707-2710.
118. Groen, J. C.; Zhu, W.; Brouwer, S.; Huynink, S. J.; Kapteijn, F.; Moulijn, J. A.; Perez-Ramirez, J., Direct Demonstration of Enhanced Diffusion in Mesoporous ZSM-5 Zeolite Obtained via Controlled Desilication. *Journal of the American Chemical Society* 2006, 129, (2), 355-360.
119. Huo, Q.; Margolese, D. I.; Ciesla, U.; Demuth, D. G.; Feng, P.; Gier, T. E.; Sieger, P.; Firouzi, A.; Chmelka, B. F., Organization of Organic Molecules with Inorganic Molecular Species into Nanocomposite Biphase Arrays. *Chemistry of Materials* 1994, 6, (8), 1176-1191.
120. Liu, Y.; Zhang, W.; Pinnavaia, T. J., Steam-Stable Aluminosilicate Mesostructures Assembled from Zeolite Type Y Seeds. *Journal of the American Chemical Society* 2000, 122, (36), 8791-8792.
121. Gu, F. N.; Wei, F.; Yang, J. Y.; Lin, N.; Lin, W. G.; Wang, Y.; Zhu, J. H., New Strategy to Synthesis of Hierarchical Mesoporous Zeolites. *Chemistry of Materials* 2010, 22, (8), 2442-2450.

122. Karlsson, A.; Stocker, M.; Schmidt, R., Composites of micro- and mesoporous materials: Simultaneous syntheses of MFI/MCM-41 like phases by a mixed template approach. *Microporous and Mesoporous Materials* 1999, 27, (2-3), 181-192.
123. Chen, X.; Huang, L.; Li, Q., Hydrothermal transformation and characterization of porous silica templated by surfactants. *Journal of Physical Chemistry B* 1997, 101, (42), 8460-8467.
124. Valtchev, V. P.; Bozhilov, K. N., Transmission Electron Microscopy Study of the Formation of FAU-Type Zeolite at Room Temperature. *The Journal of Physical Chemistry B* 2004, 108, (40), 15587-15598.
125. Mintova, S.; Olson, N. H.; Valtchev, V.; Bein, T., Mechanism of zeolite a nanocrystal growth from colloids at room temperature. *Science* 1999, 283, (5404), 958-960.
126. Valtchev, V. P.; Bozhilov, K. N., Evidences for zeolite nucleation at the solid-liquid interface of gel cavities. *Journal of the American Chemical Society* 2005, 127, (46), 16171-16177.
127. Ulagappan, N.; Rao, C. N. R., Evidence for supramolecular organization of alkane and surfactant molecules in the process of forming mesoporous silica. *Chemical Communications* 1996, (24), 2759-2760.
128. Kunieda, H.; Ozawa, K.; Huang, K.-L., Effect of Oil on the Surfactant Molecular Curvatures in Liquid Crystals. *The Journal of Physical Chemistry B* 1998, 102, (5), 831-838.
129. Ruggles, J. L.; Gilbert, E. P.; Holt, S. A.; Reynolds, P. A.; White, J. W., Expanded mesoporous silicate films grown at the air-water interface by addition of hydrocarbons. *Langmuir* 2003, 19, (3), 793-800.
130. Blin, J. L.; Otjacques, C.; Herrier, G.; Su, B. L., Pore size engineering of mesoporous silicas using decane as expander. *Langmuir* 2000, 16, (9), 4229-4236.
131. Li, Y. Y.; Perera, S. P.; Crittenden, B. D., Zeolite Monoliths for Air Separation: Part 2: Oxygen Enrichment, Pressure Drop and Pressurization. *Chemical Engineering Research and Design* 1998, 76, (8), 931-941.

132. Zhang, J.; Singh, R.; Webley, P. A., Alkali and alkaline-earth cation exchanged chabazite zeolites for adsorption based CO<sub>2</sub> capture. *Microporous and Mesoporous Materials* 2008, 111, (1-3), 478-487.
133. Rezaei, F.; Mosca, A.; Webley, P.; Hedlund, J.; Xiao, P., Comparison of traditional and structured adsorbents for co<sub>2</sub> separation by vacuum-swing adsorption. *Industrial and Engineering Chemistry Research* 2010, 49, (10), 4832-4841.
134. Ivanova, S.; Louis, B.; Madani, B.; Tessonniere, J. P.; Ledoux, M. J.; Pham-Huu, C., ZSM-5 Coatings on Beta-SiC Monoliths:A Possible New Structured Catalyst for the Methanol-to-Olefins Process. *The Journal of Physical Chemistry C* 2007, 111, (11), 4368-4374.
135. Rezaei, F.; Mosca, A.; Webley, P.; Hedlund, J.; Xiao, P., Comparison of traditional and structured adsorbents for CO<sub>2</sub> separation by vacuum-swing adsorption. *Industrial and Engineering Chemistry Research* 2010, 49, (10), 4832-4841.
136. Sachse, A.; Galarneau, A.; Di Renzo, F.; Fajula, F.; Coq, B., Synthesis of zeolite monoliths for flow continuous processes. the case of sodalite as a basic catalyst. *Chemistry of Materials* 2010, 22, (14), 4123-4125.
137. Tong, Y.; Zhao, T.; Li, F.; Wang, Y., Synthesis of Monolithic Zeolite Beta with Hierarchical Porosity Using Carbon as a Transitional Template. *Chemistry of Materials* 2006, 18, (18), 4218-4220.
138. Mori, H.; Aotani, K.; Sano, N.; Tamon, H., Synthesis of a hierarchically micro-macroporous structured zeolite monolith by ice-templating. *Journal of Materials Chemistry* 2011, 21, (15), 5677-5681.
139. Thompson, R.W.; Franklin, K.C.; in: Robson, H.; Lillerud, K.P. (Eds.), *Verified Synthesis of Zeolitic Materials*; Elsevier Science: Amsterdam, 2001; pp. 153-157, 179-181.
140. Gramlich, V.; Meier, M.; in: Treacy, M.M.J.;J.B. (Eds.), *Collection of Simulated XRD Powder Patterns for Zeolites*; Elsevier: Amsterdam, 2001, p. 215.
141. Zhou, W., Reversed Crystal Growth: Implications for Crystal Engineering. *Advanced Materials*, (2010), 22: , 3086-3092. .

142. Gora, L., Study of the crystallization of zeolite NaA by quasi-elastic light-scattering spectroscopy and electron microscopy. *Zeolites* 1997, 18, (2-3), 115-118.
143. Kruk, M.; Jaroniec, M., Gas adsorption characterization of ordered organic-inorganic nanocomposite materials. *Chemistry of Materials* 2001, 13, (10), 3169-3183.
144. Melchior, M. T.; Vaughan, D. E. W.; Jarman, R. H.; Jacobson, A. J., The characterization of Si-Al ordering in A-type zeolite (ZK4) by  $^{29}\text{Si}$  NMR. *Nature* 1982, 298, (5873), 455-456.
145. Lippmaa, E.; Maegi, M.; Samoson, A.; Tarmak, M.; Engelhardt, G., Investigation of the structure of zeolites by solid-state high-resolution silicon-29 NMR spectroscopy. *Journal of the American Chemical Society* 1981, 103, (17), 4992-4996.
146. Aronne, A.; Esposito, S.; Ferone, C.; Pansini, M.; Pernice, P., FTIR study of the thermal transformation of barium-exchanged zeolite A to celsian. *Journal of Materials Chemistry* 2002, 12, (10), 3039-3045.
147. Flanigen Edith, M.; Khatami, H.; Szymanski Herman, A., Infrared Structural Studies of Zeolite Frameworks. In Molecular Sieve Zeolites-I, *Journal of American Chemical society* 1974, 101, pp 201-229.
148. Beck, J. S. Method for synthesizing mesoporous crystalline materials. *US patent No. 5057296*, 1991.
149. Benamor, T.; Michelin, L.; Lebeau, B. n. d.; Marichal, C., Flash induction calcination: A powerful tool for total template removal and fine tuning of the hydrophobic/hydrophilic balance in SBA-15 type silica mesoporous materials. *Microporous and Mesoporous Materials* 2012, 147, (1), 334-342.
150. Beeckman, J. W. U. S.; Sweeten, G. R. U. S.; Chester, A. W. U. S.; McWilliams, J. P. U. S.; Mazzone, D. N. U. S. Structured bodies with siliceous binder. *US patent No. 7902103B2*, 2011.
151. Serrano, D. P.; Garcia, R. A.; Linares, M.; Gil, B., Influence of the calcination treatment on the catalytic properties of hierarchical ZSM-5. *Catalysis Today* 2012, 179, (1), 91-101.

152. Ernst, S.; Kokotailo, G. T.; Weitkamp, J., Zeolite ZSM-20: synthesis and characterization through XRD, SEM and thermal analysis. *Zeolites* 1987, 7, (3), 180-182.
153. Larlus, O.; Mintova, S.; Bein, T., Environmental syntheses of nanosized zeolites with high yield and monomodal particle size distribution. *Microporous and Mesoporous Materials* 2006, 96, (1-3), 405-412.
154. Mäurer, T.; Kraushaar-Czarnetzki, B., Effect of Electrolyte Addition on the Colloidal Stability of Aqueous Zeolite Sols. *Helvetica Chimica Acta* 2001, 84, (9), 2550-2556.
155. Yang, W.; Wang, X.; Tang, Y.; Wang, Y.; Ke, C.; Fu, S., Layer-By-Layer Assembly of Nanozeolite Based on Polymeric Microsphere: Zelite Coated Sphere and Hollow Zeolite Sphere. *Journal of Macromolecular Science, Part A* 2002, 39, (6), 509-526.
156. Maurer, T.; Muller, S. P.; Kraushaar-Czarnetzki, B., Aggregation and peptization behavior of zeolite crystals in sols and suspensions. *Industrial and Engineering Chemistry Research* 2001, 40, (12), 2573-2579.
157. Montastruc, L.; Azzaro-Pantel, C.; Biscans, B.; Cabassud, M.; Domenech, S., A thermochemical approach for calcium phosphate precipitation modeling in a pellet reactor. *Chemical Engineering Journal* 2003, 94, (1), 41-50.
158. Thomassen, L. C. J.; Napierska, D.; Dinsdale, D.; Lievens, N.; Jammaer, J.; Lison, D.; Kirschhock, C. E. A.; Hoet, P. H.; Martens, J. A., Investigation of the cytotoxicity of nanozeolites A and Y. *Nanotoxicology* 2012, 6, (5), 472-485.
159. Kunieda, H.; Ozawa, K.; Huang, K. L., Effect of oil on the surfactant molecular curvatures in liquid crystals. *Journal of Physical Chemistry B* 1998, 102, (5), 831-838.
160. Fan, J.; Yu, C.; Lei, J.; Zhang, Q.; Li, T.; Tu, B.; Zhou, W.; Zhao, D., Low-temperature strategy to synthesize highly ordered mesoporous silicas with very large pores. *Journal of the American Chemical Society* 2005, 127, (31), 10794-10795.
161. Wan, Y.; Zhao, D., On the controllable soft-templating approach to mesoporous silicates. *Chemical Reviews* 2007, 107, (7), 2821-2860.
162. Yao, J.; Li, D.; Zhang, X.; Kong, C. H.; Yue, W.; Zhou, W.; Wang, H., Cubes of zeolite A with an amorphous core. *Angewandte Chemie - International Edition* 2008, 47, (44), 8397-8399.

163. Binks, B. P., Macroporous silica from solid-stabilized emulsion templates. *Advanced Materials* 2002, 14, (24), 1824-1827.
164. Zhang, H.; Hardy, G. C.; Khimyak, Y. Z.; Rosseinsky, M. J.; Cooper, A. I., Synthesis of Hierarchically Porous Silica and Metal Oxide Beads Using Emulsion-Templated Polymer Scaffolds. *Chemistry of Materials* 2004, 16, (22), 4245-4256.
165. Han, L.; Yao, J.; Li, D.; Ho, J.; Zhang, X.; Kong, C.-H.; Zong, Z.-M.; Wei, X.-Y.; Wang, H., Hollow zeolite structures formed by crystallization in crosslinked polyacrylamide hydrogels. *Journal of Materials Chemistry* 2008, 18, (28), 3337-3341.
166. Lin, H.-P.; Mou, C.-Y.; Liu, S.-B.; Tang, C.-Y., Hollow spheres of MCM-41 aluminosilicate with pinholes. *Chemical Communications* 2001, (19), 1970-1971.
167. Wu, X.; Tian, Y.; Cui, Y.; Wei, L.; Wang, Q.; Chen, Y., Raspberry-like silica hollow spheres: Hierarchical structures by dual latex - Surfactant templating route. *Journal of Physical Chemistry C* 2007, 111, (27), 9704-9708.
168. Li, W.; Sha, X.; Dong, W.; Wang, Z., Synthesis of stable hollow silica microspheres with mesoporous shell in nonionic W/O emulsion. *Chemical Communications* 2002, (20), 2434-2435.
169. Fujiwara, M.; Shiokawa, K.; Sakakura, I.; Nakahara, Y., Preparation of Hierarchical Architectures of Silica Particles with Hollow Structure and Nanoparticle Shells: A Material for the High Reflectivity of UV and Visible Light. *Langmuir* 2010, 26, (9), 6561-6567.
170. E. Jaramillo; M. Chandross, Adsorption of small molecules in LTA zeolites. 1. NH<sub>3</sub>, CO<sub>2</sub>, and H<sub>2</sub>O in zeolite 4A. *Journal of Physical Chemistry B* 2004, 108, (52), 20155-20159.
171. Engelhardt, G.; in: van Bekkum, H.; Flanigen, E. M.; Jacobs, P.A.; Jason, J.C. (Eds.); Solid state NMR spectroscopy applied to zeolites. In Studies in Surface Science and Catalysis, Elsevier: Amsterdam, 2001, Vol. 137, pp 387-418.
172. Shi, J.; Anderson, M. W.; Carr, S. W., Direct observation of zeolite a synthesis by in situ solid-state NMR. *Chemistry of Materials* 1996, 8, (2), 369-375.

173. Smaihi, M.; Barida, O.; Valtchev, V., Investigation of the Crystallization Stages of LTA-Type Zeolite by Complementary Characterization Techniques. *European Journal of Inorganic Chemistry* 2003, (24), 4370-4377.
174. Serrano, D. P.; Van Grieken, R., Heterogenous events in the crystallization of zeolites. *Journal of Materials Chemistry* 2001, 11, (10), 2391-2407.
175. Zhou, W., Reversed crystal growth: Implications for crystal engineering. *Advanced Materials* 2010, 22, (28), 3086-3092.
176. Gregg, S. J.; Sing, K. S. W.; Adsorption surface area and porosity. 2nd ed. ed.; Academic Press: New York, 1982, p. 111.
177. Wang, Y.; LeVan, M. D., Adsorption equilibrium of carbon dioxide and water vapor on zeolites 5a and 13X and silica gel: Pure components. *Journal of Chemical and Engineering Data* 2009, 54, (10), 2839-2844.
178. Shy-Hsein Wu, Molecular sieve structures using aqueous emulsions. US:Corning Incorporated 1996.
179. Shy-Hsein Wu, K. E. Z., Method of making small pore hydrophilic molecular sieve bodies. *US patent No. 5492883*, 2001.
180. Chudasama, C. D.; Sebastian, J.; Jasra, R. V., Pore-size engineering of zeolite A for the size/shape selective molecular separation. *Industrial and Engineering Chemistry Research* 2005, 44, (6), 1780-1786.
181. Patton, A.; Crittenden, B. D.; Perera, S. P., Use of the linear driving force approximation to guide the design of monolithic adsorbents. *Chemical Engineering Research and Design* 2004, 82, (8), 999-1009.
182. Kyotani, T., Grazing incidence X-ray diffraction analysis of zeolite NaA membranes on porous alumina tubes. *Analytical Sciences* 2006, 22, (7), 961-964.
183. Valdes-Soles, T.; Linders, M. J. G.; Kapteijn, F.; Marban, G.; Fuertes, A. B., Adsorption and breakthrough performance of carbon-coated ceramic monoliths at low concentration of n-butane. *Chemical Engineering Science* 2004, 59, (13), 2791-2800.
184. Sargent, R.W.; Whitford, C. J.; Diffusion of Carbon Dioxide in Type 5A Molecular Sieve. American Chemical Society: Washington, 1971.

## ***Appendix-Relevant Publications***





## Direct synthesis of hierarchical LTA zeolite *via* a low crystallization and growth rate technique in presence of cetyltrimethylammonium bromide

Fatin Hasan <sup>a</sup>, Ranjeet Singh <sup>a</sup>, Gang Li <sup>b</sup>, Dongyuan Zhao <sup>a</sup>, Paul A. Webley <sup>b,\*</sup>

<sup>a</sup> Department of Chemical Engineering, Monash University, Clayton, Victoria 3800, Australia

<sup>b</sup> Department of Chemical and Biomolecular Engineering, Melbourne School of Engineering, The University of Melbourne, Victoria 3010, Australia

### ARTICLE INFO

#### Article history:

Received 20 February 2012

Accepted 11 May 2012

Available online 23 May 2012

#### Keywords:

Hierarchical zeolites

Slow crystallization and growth rate

Micelle expansion

Polycrystalline aggregates

Ethylene gas adsorption

### ABSTRACT

Slow crystallization and growth rate at room temperature in the presence of surfactant micelles is a new strategy used to synthesize hierarchical Na–A zeolites. The observed structure of the hierarchical materials was consistent with a two stage growth mechanism. During the early stage of the gel evolution, miniature zeolite gel particles were formed and assembled around surfactant (cetyltrimethylammonium bromide – CTAB) micelles. In a second stage, the slow mass transformation into crystalline phase and the low growth rate of the formed crystallites retained the CTAB micelles within the crystallization domain. After the removal of CTAB templates, the products showed large mesopores which were attributed to the interstitial voids between the aggregated zeolite nanocrystallites. The size of the mesopores can be further expanded by using linear hydrocarbons as swelling agents. The influences of the added amount of the hydrocarbons and the length of the hydrocarbon chains on the mesopore size were examined. The effects of the aging period and CTAB concentration in the synthesis mixture on the pore size distribution were also investigated. The colloidal suspension of the synthesized zeolite showed negative zeta potential throughout the entire range of pH. The mesoporous Na–A zeolite synthesized in this work showed higher ethylene adsorption capacity as compared to the conventional microporous Na–A zeolite. XRD, DLS, SEM, N<sub>2</sub> adsorption–desorption at 77 K, TEM, <sup>29</sup>Si NMR and FTIR techniques were used to characterize the hierarchical Na–A zeolite.

© 2012 Elsevier Inc. All rights reserved.

## 1. Introduction

Zeolites are crystalline aluminosilicates with unique features associated with the regular, microscopic interconnected pores and windows which provide access to some molecules in the mixture while excluding others. Therefore, zeolites have wide range of applications as adsorbents and catalysts especially in the oil and petrochemical industry. The small size of their pores (<1.3 nm) is also unfortunately a hindrance since those molecules which have access to the pore space must diffuse through these windows and cages to the active adsorption/reaction sites. Therefore, to overcome this diffusion limitation, various techniques have been investigated to synthesize zeolites with large pores [1–6]. Such zeolites are attractive since they retain the adsorption and reaction properties while improving their transportation properties. One of these techniques is soft templating which is based on a cooperative assembly between ordered organic surfactant aggregates and inorganic species generating organic–inorganic composites. Subsequent removal of

the surfactant aggregates produces ordered mesoporous materials. Highly ordered mesoporous silicate materials with controllable pores could be obtained simply by direct addition of surfactant molecules into the synthesis mixture [1,7,8]. However, no mesoporous zeolite has been obtained by following the same procedure, probably due to the weak interactions between the surfactant and large aluminosilicate building block species which results in exclusion of the surfactant micelles during the crystallization and growth of zeolites. Recently, however, Choi et al. have synthesized MFI and LTA zeolites containing micro- and mesopores in one phase by direct addition of amphiphilic organosilane surfactant into the synthesis mixture [9]. In addition to quaternary ammonium and alkyl chain groups, which are the characteristic of common surfactants, the molecule contains a methoxysilyl moiety. This hydrolysable moiety has the ability to interact strongly through covalent bonds with aluminosilicate species in the growing crystals [9,10].

In another strategy, pre-prepared surfactant solution was added to pre-formed zeolite nanoclusters and followed by hydrothermal treatment. The zeolite seeds were assembled on the pre-formed micelle aggregates producing well-ordered mesoporous structures built of zeolite nanoclusters [11]. However, no long range atomic order of crystalline zeolites was detected in the XRD pattern. This is probably due to the relatively small size of the assembled zeolite

\* Corresponding author. Address: Department of Chemical and Biomolecular Engineering, Room 3.21A, Melbourne School of Engineering, The University of Melbourne, Victoria 3010, Australia. Fax: +61 3 83444153.

E-mail address: paul.webley@unimelb.edu.au (P.A. Webley).

seeds, less than XRD detection limit. On the other hand, larger zeolite seeds cannot be assembled under the direction of the surfactant due to the weak charge density or the relatively small size of the micelles (2–4 nm).

Many studies have investigated the influence of the synthesis temperature on the interaction between the silicate species and surfactant molecules [12–14]. Beck et al. obtained mesoporous silica MCM-41 at 100 °C by using aggregates of alkyltrimethylammonium bromide molecules as templates [13]. Increasing the reaction temperature to 150 °C enhanced the MCM-41 crystallinity, but at 200 °C only an amorphous material was obtained. They reported that at low temperatures, the formation of ordered aggregates of surfactant molecules is favorable while at high temperatures the preformed micelles were decomposed and thus the surfactant molecules acted as single molecule structure-directing agents [13]. Furthermore, Chen et al. described that in the silicate – cetyltrimethylammonium bromide (CTAB) system, the structure of the produced MCM-41 transformed from hexagonal to lamellar and then to microporous MFI framework by increasing the reaction temperature from room temperature to 150 °C and then to 165 °C, respectively [12].

These findings suggest that a possible approach to produce hierarchical zeolite is low temperature crystallization of zeolites in the presence of surfactant micelles. Several successful attempts were published in which microporous zeolite-type materials were crystallized at room temperature [15–18]. The methodology of our approach is underpinned by points: (1) simultaneous formation of zeolite seeds and surfactant micelles in one pot, (2) low growth rate of zeolite seeds at ambient conditions, (3) increasing and controlling the size of the micelles by using different amounts and types of linear alkanes. Under such moderate conditions and a slowly developing system, we anticipate the swollen micelles will be retained and not expelled from the crystallization domain.

In the present work therefore, we have successfully synthesized Na-A zeolite with large mesopores (~7.9 nm) by direct addition of commercially available surfactant (CTAB) into the synthesis mixture. The slow formation and growth of zeolite seeds in presence of CTAB micelles by aging the gel at room temperature was the key factor for retaining these micelles in the crystallization domain. Conducting the experiments without the aging step resulted in microporous Na-A zeolite. Furthermore, the size of the mesopores could be controlled by using alkanes with different hydrocarbon chain length as swelling agents viz *n*-dodecane, *n*-octane, and *n*-hexane. These alkanes were used in engineering the pore size of the mesoporous silica [19–23]. However, their swelling tendency was guided by the system conditions; therefore, they showed different behaviors in different silica systems [19,22]. The influence of the following parameters on tailoring the size of the mesopores was investigated; namely, the concentration of the swelling agent, the length of the alkane chain of the swelling agent, the aging period and the concentration of CTAB in the synthesis gel. The colloidal stability of the synthesized mesoporous particles was examined and compared with conventional Na-A zeolite. The stability of zeolite suspensions is crucial for potential utility in colloidal chemistry and for obtaining optimum catalytic properties [24]. Furthermore, the enhancement of the adsorption capacity of the synthesized micro-mesoporous Na-A zeolite was demonstrated by conducting ethylene gas adsorption experiments.

## 2. Experimental work

### 2.1. Synthesis

The initial gel of Na-A zeolite was prepared according to the procedure reported in the literature [25]. A typical synthesis proce-

dure started with dissolving 2 g of sodium hydroxide in 37.6 g of deionized water. Then one half of this alkaline solution was mixed with 3.9 g of sodium aluminate under stirring until a clear solution was obtained. The other half of the alkaline solution was mixed with 8.7 g of sodium silicate. The two solutions were mixed and stirred vigorously by a mechanical stirrer until the produced gel was homogenized. Then 1.04 g of the cationic surfactant CTAB was added to the initial gel under stirring. The molar composition of the final gel was 1.0Al<sub>2</sub>O<sub>3</sub>:1.9SiO<sub>2</sub>:3.2Na<sub>2</sub>O:120H<sub>2</sub>O:0.14CTAB. After that, a calculated amount of the swelling agent (i.e. *n*-dodecane, or *n*-octane, or *n*-hexane) was added drop by drop under stirring which continued for few minutes before the resultant homogenized gel was stored in a sealed polypropylene bottle and aged at room temperature for 2 weeks. Finally the gel was heated in an oven at 99 °C for 4 h. The product was collected by filtration, washed repeatedly with ethanol and water and then dried at 70 °C overnight. The surfactant was removed by calcination at 550 °C using a ramp rate of 2 °C min<sup>-1</sup> in N<sub>2</sub> flow for 1 h and then in air flow for 4 h.

The final samples were denoted as MZ-0.14C-xD, where MZ represented the initial gel of the reactants, 0.14C indicated the molar ratio of CTAB, and *x* was the molar ratio of *n*-dodecane (D). For investigating the influence of the hydrocarbon chain length on the pore size distribution; *n*-octane and *n*-hexane were used rather than *n*-dodecane and the samples were denoted as MZ-0.14C-1.1O and MZ-0.14C-1.1H, respectively.

Zeolite gel with composition of MZ-0.14C-1.1D was prepared and crystallized directly at 99 °C for 4 h without aging at room temperature. The aim of this experiment was to investigate whether mesoporous Na-A zeolite would be formed by only introducing CTAB and *n*-dodecane into the reaction mixture without room temperature aging. This sample was named ZA.

Furthermore, to investigate whether aging the Na-A zeolite gel without the inclusion of CTAB and *n*-dodecane would form the mesopores; conventional gel was prepared and aged at room temperature for 2 weeks prior being crystallized at 99 °C for 4 h. The product was collected by filtration under vacuum, washed frequently with water and dried at 70 °C overnight. The obtained zeolite was denoted as ZA-st in this work.

Beside the 14 days aging, two more aging periods were studied viz; 17 and 19 days. For this purpose, gel with molar composition 1.0Al<sub>2</sub>O<sub>3</sub>:1.9SiO<sub>2</sub>:3.2Na<sub>2</sub>O:120H<sub>2</sub>O:0.14CTAB:8.5*n*-dodecane was used. The samples were named MZ-0.14C-8.2D-*t*, where *t* represented the number of days the gel was aged.

The influence of CTAB concentration on the pore size distribution was also investigated. The gel used for this purpose was 1.0Al<sub>2</sub>O<sub>3</sub>:1.9SiO<sub>2</sub>:3.2Na<sub>2</sub>O:120H<sub>2</sub>O:*y*CTAB:8.5*n*-dodecane, where *y* was 0.07, 0.14 and 0.21. The samples were named MZ-0.07-8.2D, MZ-0.14C-8.2D and MZ-0.21C-8.2D.

For comparison purposes, conventional Na-A zeolite was prepared typically according to the procedure reported in the literature [25]. The prepared sample was named CZA in this work.

All prepared samples with their gels compositions are listed in Table S1 (supporting information).

### 2.2. Characterization

The crystallinity of the synthesized samples was characterized by powder X-ray diffraction (PXRD) type Phillips PW1140/90 using CuK $\alpha$  radiation at 2 $\theta$  from 4 to 60 ° in steps of 0.05° and a scan rate of 1 ° min<sup>-1</sup>. The morphology of the products was investigated at 15 kV, using a JEOL 7001F FEG scanning electron microscope (SEM). The sample was crushed and sprinkled on carbon tape mounted on a metal stub and coated with 1 nm layer of platinum metal. The energy dispersive X-ray spectrometer (EDXS) attached to the SEM equipment was used to conduct elemental analysis of

the samples. The final concentration for each element was obtained by taking the average of number of measurements at different spots. N<sub>2</sub> adsorption–desorption isotherms were measured at 77 K by a Micromeritics ASAP 2020 gas adsorption analyzer. All samples were degassed at 350 °C for 15 h under vacuum before analysis. The BET surface area was calculated using the adsorption data collected over a relative pressure ( $P/P_0$ ) range of 0.05–0.3. The pore volume was taken at  $P/P_0 = 0.992$ . The mesopore diameter distribution was measured by the Barrett–Joyner–Halenda (BJH) algorithm using the adsorption branch. The detailed features of the produced particles were investigated by transmission electron microscopy (TEM) type CM20 at accelerating voltage of 200 kV. The sample was finely crushed, dispersed in ethanol and sonicated for 10 min; then a drop of this suspension was dispersed on a Cu grid coated with a thin layer of carbon. The particle size, particle size distribution (PSD) and zeta potential were performed on Zetasizer Nano ZS (Malvern Instrument). The colloidal stability of the synthesized material was determined by measuring the zeta potential ( $\zeta$ -potential) as a function of pH. The media used was 0.01 M phosphate buffered saline (PBS) with pH 7.4 and contained NaCl (0.138 M) and KCl (0.0027 M). The measurements were conducted on wide pH ranges which were obtained by adjusting the PBS pH by NaOH and HCl solutions. The Fourier transform infrared (FTIR) spectra were recorded on a Perkin Elmer 100 FT-IR spectrometer in 1400–400 cm<sup>−1</sup> with a resolution of 4 cm<sup>−1</sup> using KBr pellets. The <sup>29</sup>Si solid state nuclear magnetic resonance (NMR) spectra were performed at room temperature on Bruker Avance 300 spectrometer equipped with a 4 mm magic angle spinning (MAS) probe at spinning speeds of 10–14 kHz with resonance frequency of 59.6 MHz for <sup>29</sup>Si. The spectra were collected in single pulse mode with 10 s recycle delay and 3  $\mu$ s excitation pulse. Chemical shifts are referred to tetra methyl silane (TMS) as a standard. The ethylene gas adsorption desorption isotherms were measured at 0 °C and at pressure up to 850 kPa by a Micromeritics ASAP 2050 Xtended Pressure Sorption analyzer.

### 3. Results and discussion

#### 3.1. Influence of direct addition of CTAB with different concentrations of swelling agent

**Fig. 1** shows the wide angle XRD patterns of Na-A zeolites synthesized with CTAB and different molar ratios of *n*-dodecane ( $x = 0, 0.14, 1.1, 2.75$ ) as a swelling agent. All the samples exhibited diffraction peaks characteristic of well-crystallized LTA zeolite and match the standard crystal data published by International Zeolite Association of the face-centered cubic (fcc) unit cell with  $a = 24.61 \text{ \AA}$  [26]. The sample prepared without swelling agent (MZ-0.14C-0) showed broad diffraction peaks indicating the small size of the crystalline particles. The pattern also shows a relatively high proportion of amorphous phase, suggesting partial transformation of the gel into zeolite. **Fig. 1** indicates that the addition of *n*-dodecane with equal molar ratio to CTAB in the sample MZ-0.14C-0.14D enhanced the crystallinity of the produced Na-A zeolite. However, the crystallinity decreased gradually with increasing the *n*-dodecane concentration as shown in XRD patterns for the samples MZ-0.14C-1.1D and MZ-0.14C-2.75D.

The mean particle diameter and particle size distribution (PSD) curves obtained from the dynamic light scattering (DLS) technique for the synthesized zeolites are included in **Table S2** and **Fig. S1 (supporting information)**. The average diameter of the particles increases with increase in the ratio of *n*-dodecane in the composition of the synthesis gel of the prepared materials. The average particle diameter of MZ-0.14C-0, MZ-0.14C-0.14D, MZ-0.14C-1.1D and MZ-0.14C-2.75D were 492, 511, 520 and 595 nm; respectively. On the

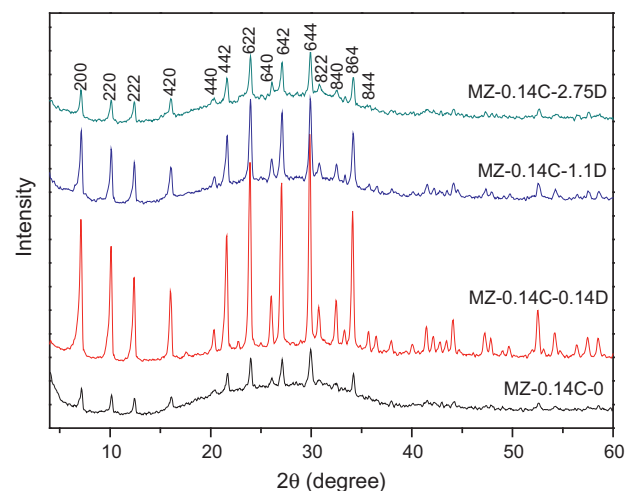


**Fig. 1.** PXRD patterns of Na-A zeolites synthesized with different molar ratios of *n*-dodecane as micellar swelling agent.

other hand, the sample named ZA-st, synthesized from conventional gel of LTA zeolite that was aged for 14 days at room temperature before being crystallized at high temperature, shows an average particle diameter of 569 nm (**Table S2**). The DLS measurements show high polydispersity index (PDI) in the range 0.25–0.3 suggesting a multimodal particle size distribution. This can also be deduced from the PSD curve of each sample (**Fig. S1**) which shows a broad peak extending from ~200 to ~1000 nm.

**Fig. 2A–D** and inset show the SEM images of the zeolites samples synthesized using only CTAB or CTAB with various amounts of *n*-dodecane in the synthesis composition. These images show some particles with cubic morphology and others which consist of closely aggregated nanoparticles forming irregular spherical aggregates. In general these spherical aggregates exhibit smaller size compared to the particles with cubic habit, except for the samples MZ-0.14C-0 and MZ-0.14C-2.75D, where both types of particles lie in a similar size range, which is between  $200 \pm 25$  and  $375 \pm 25$  nm for the former and between  $300 \pm 25$  and  $600 \pm 50$  nm for the latter. Also the SEM results for these two samples show that the major proportion of the particles are spherical aggregations with few cube-like particles. For MZ-0.14C-0.14D and MZ-0.14C-1.1D, the aggregates size ranges from  $125 \pm 25$  to  $250 \pm 25$  nm and the size of the cube-like particles ranges from 200 to about 570 nm. Generally the nanoparticles within the aggregates are about 15–20 nm in size except for a few of size 40–50 nm. In general, the average particle diameter obtained from the DLS for every sample, except MZ-0.14C-0, lie within the range of the particle size distribution determined by the SEM (**Table S2 in supporting information**). The SEM investigation (**Fig. 2B–D**) also shows that crystalline islands were developed on the surface of some of the polycrystalline aggregates suggesting that surface recrystallization had probably taken place [27,28].

The SEM image of ZA-st shows that the sample consists of cubic crystals in the size range from 250 to 850 nm (**Fig. 2E**). On the other hand, cubic crystals with size around 3–6  $\mu\text{m}$  can be observed in the SEM images of samples ZA (**Fig. 2F**) and CZA (**Fig. S2 in supporting information**). The small size of Na-A zeolite crystals in ZA-st compared to ZA and CZA is attributed to the room temperature aging, as the role of room temperature aging in enhancing the number of the nuclei and thus reducing the crystals size has been reported [29,30]. According to SEM images, the nanoparticle aggregates were absent in the samples named ZA, ZA-st and CZA.

The XRD and SEM findings indicate that aging the synthesis mixture without introducing CTAB and *n*-dodecane produces cubes of zeolite Na-A with submicron size (sample ZA-st). Further, the

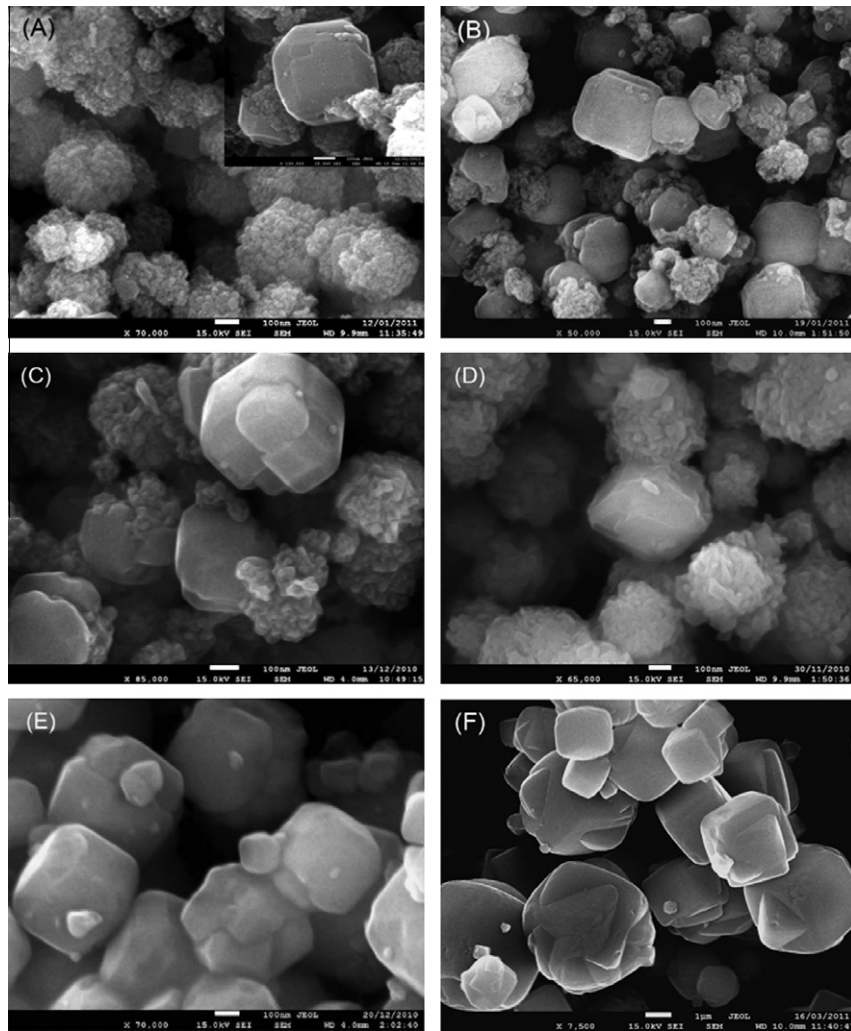


**Fig. 2.** SEM images of MZ-0.14C-0 (A and inset), MZ-0.14C-0.14D (B), MZ-0.14C-1.1D (C) and MZ-0.14C-2.75D (D). Images E and F are of ZA-st and ZA, respectively. The scale of images A–E and insets is 100 nm, while that of image F is 1 μm.

Na-A zeolite synthesized from a mixture including CTAB and *n*-dodecane and then crystallized directly without aging contains cubes of micron-scale size (ZA). The absence of the nanoparticle aggregates in ZA-st and ZA suggests that both factors, aging and CTAB and *n*-dodecane addition, induced the formation of the nanoparticle aggregates of Na-A zeolite.

It is well known that conventional Na-A zeolite does not adsorb N<sub>2</sub> at 77 K due to pore blockage by Na<sup>+</sup> cations in the unit cell structure. These Na<sup>+</sup> cations occupy positions close to the pore apertures reducing their size from 4.4 Å to less than 3.1 Å and thus prohibiting the admission of nitrogen molecules (kinetic radius ~3.4 Å) into the super-cages [30,31]. This is confirmed in our work as shown in Fig. 3A in which the adsorption–desorption isotherms of ZA-st shows very little adsorption which can be attributed to adsorption of the N<sub>2</sub> molecules on the external surface of the crystals. In contrast, the isotherms of Na-A zeolites synthesized from gels that contained a constant amount of CTAB but varying amount of *n*-dodecane; MZ-0.14C-0, MZ-0.14C-0.14D, MZ-0.14C-1.1D and MZ-0.14C-2.75D, show a steep increase in the adsorption amount over the relative pressure range between 0.6 and 0.99 which is attributed to capillary condensation of N<sub>2</sub> within the mesopores (Fig. 3B–E). The isotherms for these samples are of type IV with H3 hysteresis, without a plateau at high relative pressure (close to unity) which suggests that the products are com-

prised of aggregated crystallites [32,33]. The highest mesopore volume recorded was 0.27 cm<sup>3</sup> g<sup>-1</sup> (Table 1) which was obtained when only CTAB was introduced into the reaction gel (sample MZ-0.14C-0) and when CTAB: *n*-dodecane molar ratio is 1:1 (sample MZ-0.14C-0.14D). The mesopore volume decreased slightly to about 0.25 cm<sup>3</sup> g<sup>-1</sup> with increasing the *n*-dodecane molar ratio to 1.1 and 2.75. Table 1 and the insets in Fig. 3B–E show two mesopore size distributions; small mesopores in the range 1.9–3.5 nm and large mesopores in the range 7.9–13 nm. The influence of *n*-dodecane molar ratios is more pronounced in the large mesopore domain, as BJH pore size distribution show narrow peaks centered on 7.9, 9.0, 11.5 and 13.0 nm for samples with 0, 0.14, 1.1 and 2.75 *n*-dodecane molar ratios, respectively. In general, a progressive increase in the mesopore size could be detected with increasing the amount of *n*-dodecane in the synthesis gel. In contrast, no N<sub>2</sub> adsorption was measured on ZA which was synthesized from the gel contained 0.14C:1.1D molar ratio and crystallized directly without aging at room temperature. The results obtained from N<sub>2</sub> adsorption–desorption analysis is in agreement with the SEM, and reveal that the presence of CTAB micelles in the synthesis gel is not effective in terms of forming the mesoporous Na-A zeolite without the aging at room temperature and vice versa.

Fig. 4A-1 and the inset display TEM images of MZ-0.14C-0 at high and low magnification, respectively; which exhibits relative

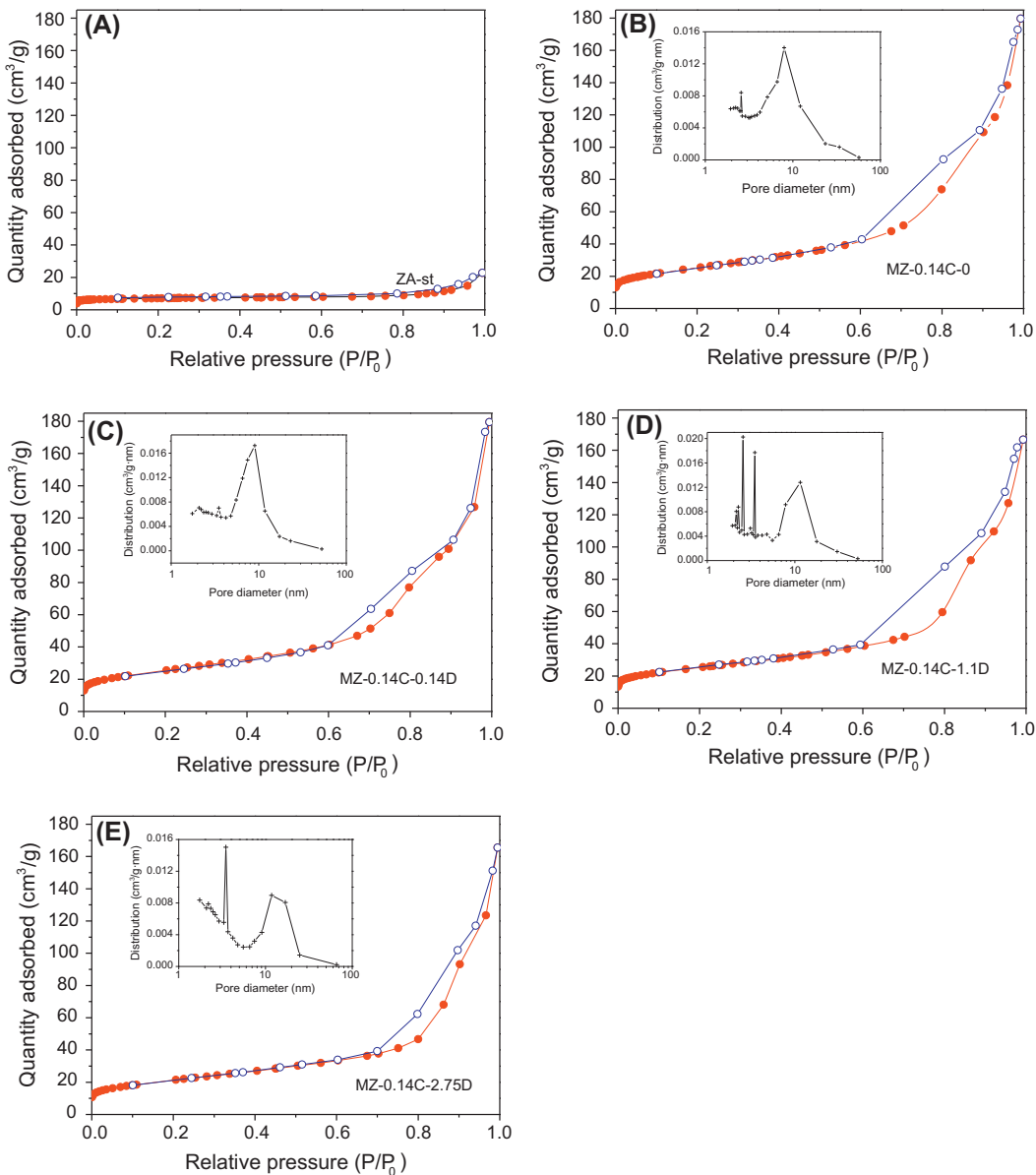


**Fig. 3.**  $N_2$  adsorption-desorption isotherms at 77 K of ZA-st (A), MZ-0.14C-0 (B), MZ-0.14C-0.14D (C), MZ-0.14C-1.1D (D) and MZ-0.14C-2.75D (E). The inset with each plot is the corresponding BJH mesopore size distribution obtained from the adsorption branch.

uniform nanoparticles with size of 15–25 nm (marked with black arrows in A-1) agglomerated to form spherical aggregates with average overall size around 300 nm. The images also show the mesopores which are represented by the interstitial voids (marked with white arrows in A-1) between the aggregated nanoparticles. On the other hand, the TEM investigations of the samples MZ-0.14C-0.14D, MZ-0.14C-1.1D and MZ-0.14C-2.75D show the three types of particles; single cubic particles, spherical aggregates and also show some particles which are “half cube” “half aggregate” (Fig. 4 images B-1, C-1 and D-1). In agreement with the SEM results, the TEM images indicate that the spherical aggregates comprise of 15–20 nm sized particles that are closely compacted confining mesoscopic voids which represent the mesopores. The SAED patterns shown in the insets in the images (Fig. 4B-1 and D-1) confirm the crystallinity observed by the XRD patterns for MZ-0.14C-0.14D and MZ-0.14C-2.75D.

The TEM findings support the XRD, SEM and  $N_2$ -adsorption-desorption analysis indicating that the products are mesoporous

materials with two types of particles, cubes and nanoparticle aggregates. Further, the mesoporosity is represented by the voids confined between the compacted nanoparticles in the aggregates. However, all the above results do not provide direct evidence of whether the aggregated nanoparticles are pure zeolite A or another mesoporous phase was formed. Therefore, the lattice fringes of 15–20 nm crystallites within the nanoparticle aggregates were observed by high magnification TEM. Fig. 4A-2, B-2, C-2 and D-2 show the lattice fringes resolved on the nanoparticles of samples MZ-0.14C-0, MZ-0.14C-0.14D, MZ-0.14C-1.1D and MZ-0.14C-2.75D, respectively. These images show single oriented lattice fringes, indicating that these nanoparticles are zeolite A crystallites, which started forming from a single nucleus in one isolated amorphous gel particle [17]. The lattice fringes in images 4A-2, B-2, C-2 and D-2 correspond to  $d$ -spacing 8.5, 8.1, 12.0, and 3.7 Å which match well with the (220), (220), (200) and (622) planes in LTA zeolite structure; respectively. These results reveal that the nanoparticles within the mesoporous aggregates are Na-A zeolite crystallites.

**Table 1**

Textural properties for the samples synthesized in the work.

Sample	$S_{\text{BET}}$ ( $\text{m}^2 \text{ g}^{-1}$ ) <sup>a</sup>	$V_{\text{meso}}$ ( $\text{cm}^3 \text{ g}^{-1}$ ) <sup>b</sup>	$d_{\text{meso}}$ (nm) <sup>c</sup>
MZ-0.14C-0	89	0.27	2.5, 7.9
MZ-0.14C-0.14D	89	0.27	2.0, 3.5, 9.0
MZ-0.14C-1.1D	87	0.25	2.5, 3.5, 11.5
MZ-0.14C-2.75D	75	0.25	3.5, 13.0
MZ-0.14C-1.1H	73	0.21	2.5, 3.5, ~9.0
MZ-0.14C-1.1O	58	0.20	2.0, 11.7
MZ-0.14C-8.5D-14 <sup>d</sup>	76	0.17	2–4, ~9.1
MZ-0.14C-8.5D-17	41	0.17	2–4, 6.9, 13
MZ-0.14C-8.5D-19	28	0.08	3.3, 4.3, 7.2
MZ-0.07C-8.5D	54	0.19	2.7, 3.7, 9.5
MZ-0.21C-8.5D	62	0.16	1.8, 2.1, 13.4
CZA	–	–	–
ZA-st	22	–	–

<sup>a</sup> Surface area obtained at relative pressure range of 0.05–0.3.

<sup>b</sup> Mesopore volume was collected on pore size range between about 1.7 and 50 nm.

<sup>c</sup> Mesopore size distribution was measured by BJH adsorption  $dV/dD$  pore volume.

<sup>d</sup> This sample (MZ-0.14C-8.5D-14) was also named as MZ-0.14C-8.5D in the text.

To further confirm that the produced mesoporous material is a pure phase of LTA zeolite,  $^{29}\text{Si}$  NMR spectra were obtained. In Fig. 5, the  $^{29}\text{Si}$  NMR spectrum of ZA-st shows a single resonance signal centered at  $\delta = -89.2$  ppm which is assigned to Si (4Al). Also a low intensity shoulder appeared at  $\delta = -94.5$  ppm which is attributed to coexistence of Si (3Al). These results indicate that the sample contains a less ordered region in which  $\text{SiO}_4$  tetrahedra are linked to three Al and one Si. This behavior is consistent with studies conducted by Lippmaa et al. and Melchior et al. on zeolite A [34,35]. The  $^{29}\text{Si}$  NMR spectra for the MZ-0.14C-0 and MZ-0.14C-1.1D samples indicate the existence of different environment in the lattice of the synthesized mesoporous Na-A zeolites (Fig. 5). The spectrum of the sample MZ-0.14C-0 synthesized with only CTAB is broad and shows extra resonances at  $\delta = -83.3$  and  $-86.9$  ppm in addition to the Si(4Al) peak which is also shifted down to  $-88.8$  ppm rather than  $-89.5$  ppm. On the other hand, the sample MZ-0.14C-1.1D shows sharp resonance at  $\delta = -89.0$  ppm and also a wide region which extends from  $\delta = -78$  to  $-86$  ppm, but with very low intensity. The same resonances were observed by Greene et al. in  $^{29}\text{Si}$  NMR spectra of zeolite A and they attributed them to lower polymerized Si species [27]. These results show the absence of any other phase rather than a pure LTA type zeolite in the synthesised samples.

Furthermore, SEM-EDX was used to measure the concentration of Si, Al, Na and O on the surface of the nanoparticle aggregates in sample MZ-0.14C-0.14D and also the concentration of these elements on the surface of cubic particles in the same sample (Table 2). The results show consistency in the concentration of all elements in both types of particles suggesting that both the cubic particles and the nanoparticles are comprised of the same material.

A complementary IR study was performed on standard microporous Na-A zeolite (ZA-st) and mesoporous Na-A zeolites synthesized in the presence of CTAB only as well as CTAB with various amounts of *n*-dodecane. The absorption bands were assigned on the basis of previous studies [36,37]. All IR spectra show bands at around 464, 560, 670, and 1000  $\text{cm}^{-1}$  (Fig. 6). The absorption bands centred at 1000 and 670  $\text{cm}^{-1}$  are assigned to the internal vibration of Al-O and Si-O asymmetric and symmetric stretching, respectively [36,37]. The corresponding internal bending of Al-O and Si-O bonds is represented by the bands centered at 464  $\text{cm}^{-1}$ . Moreover, the characteristic of Na-A zeolite structure is represented by the absorption band at 560  $\text{cm}^{-1}$  which is attrib-

uted to the external vibration of the tetrahedron of the secondary building units (4DR).

The results obtained from high magnification TEM,  $^{29}\text{Si}$  NMR, SEM-EDX and FTIR reveal that the produced mesoporous material consists of one phase which is a pure Na-A zeolite with Si/Al ratio = 1.1. The results also show that concentrations of the elements (Al, Si O and Na) in the cubic particles are exactly similar to the concentrations of the elements in the nanoparticles within the aggregates (Table 2). However, the number of  $\text{Na}^+$  cations in the structure of MZ-0.14C-0.14D is less than in CZA. The reason is probably the early involvement of CTAB molecules in zeolite gel which then was aged to evolve slowly, some of the  $\text{Na}^+$  cations were probably superseded by the cationic ammonium group from the CTAB molecules. Then during calcination, ammonium groups were decomposed totally leaving Na-A zeolite crystals with less number of  $\text{Na}^+$  cations.

### 3.2. Influence of chain length of the swelling agent on the mesopore size distribution

Other alkanes with different hydrocarbon chain length were introduced into the Na-A zeolite – CTAB system to examine the influence of the chain length on the micelle expansion. Fig. 7 and Table 1 show the results obtained from the XRD and  $\text{N}_2$  adsorption–desorption at 77 K for the mesoporous Na-A zeolites synthesized by using *n*-hexane (MZ-0.14C-1.1H) and *n*-octane (MZ-0.14C-1.1O). The X-ray patterns indicate that the LTA framework structure was retained with changing the swelling agent (Fig. 7A). The pore size distribution of MZ-0.14C-1.1H shows wide peaks centered at about 9.0 nm, while MZ-0.14C-1.1O shows a sharp peak centered at 11.7 nm (Fig. 7C). Both samples contained mesopores larger than 7.9 nm which were obtained when only CTAB was used in the system (sample MZ-0.14C-0 in Fig. 3). These results reveal that the molecules of the alkanes can be permeated into the core of CTAB micelles increasing their sizes. However, *n*-octane and *n*-dodecane show similar influence on the micelle size, as introducing either of them at 1.1:0.14CTAB molar ratio into Na-A zeolite gel generated mesopores with diameter of 11.5–11.7 nm (discussed in more detail in Section 3.7).

### 3.3. Influence of aging period on the mesopore size distribution

As described in Section 3.1, introducing the CTAB and *n*-dodecane into the gel was not effective in terms of forming the mesoporous Na-A zeolite without the room temperature aging. Therefore, it became crucial to investigate the effect of the aging period on the mesopore size distribution. Fig. 8A shows the XRD patterns of MZ-0.14C-8.2D-14, MZ-0.14C-8.2D-17 and MZ-0.14C-8.2D-19 which were aged for 14, 17 and 19 days; respectively. The diffraction peaks of all patterns match the peaks that are identified as characteristics of LTA zeolite framework structure indicating that all samples are well crystalline Na-A zeolite [26]. However, the diffraction peaks recorded for MZ-0.14C-8.2D-14 show lower intensities than the peaks in the patterns of MZ-0.14C-8.2D-17 and MZ-0.14C-8.2D-19 suggesting a significant increase in the crystal size.

The results obtained from  $\text{N}_2$  adsorption–desorption analysis indicate that prolonging the aging period resulted in decreasing the surface area (Table 1). The BET surface area measured for samples MZ-0.14C-8.2D-14, MZ-0.14C-8.2D-17 and MZ-0.14C-8.2D-19 were  $76 \text{ m}^2 \text{ g}^{-1}$ ,  $41 \text{ m}^2 \text{ g}^{-1}$  and  $28 \text{ m}^2 \text{ g}^{-1}$ ; respectively. The isotherm of MZ-0.14C-8.2D-14 shown in Fig. 8B is type IV with H3 hysteresis indicating that the sample is a mesoporous zeolite. However, the  $\text{N}_2$  adsorption at high relative pressure ( $P/P_0 = 0.6$ –0.99) decreases gradually with increasing the aging

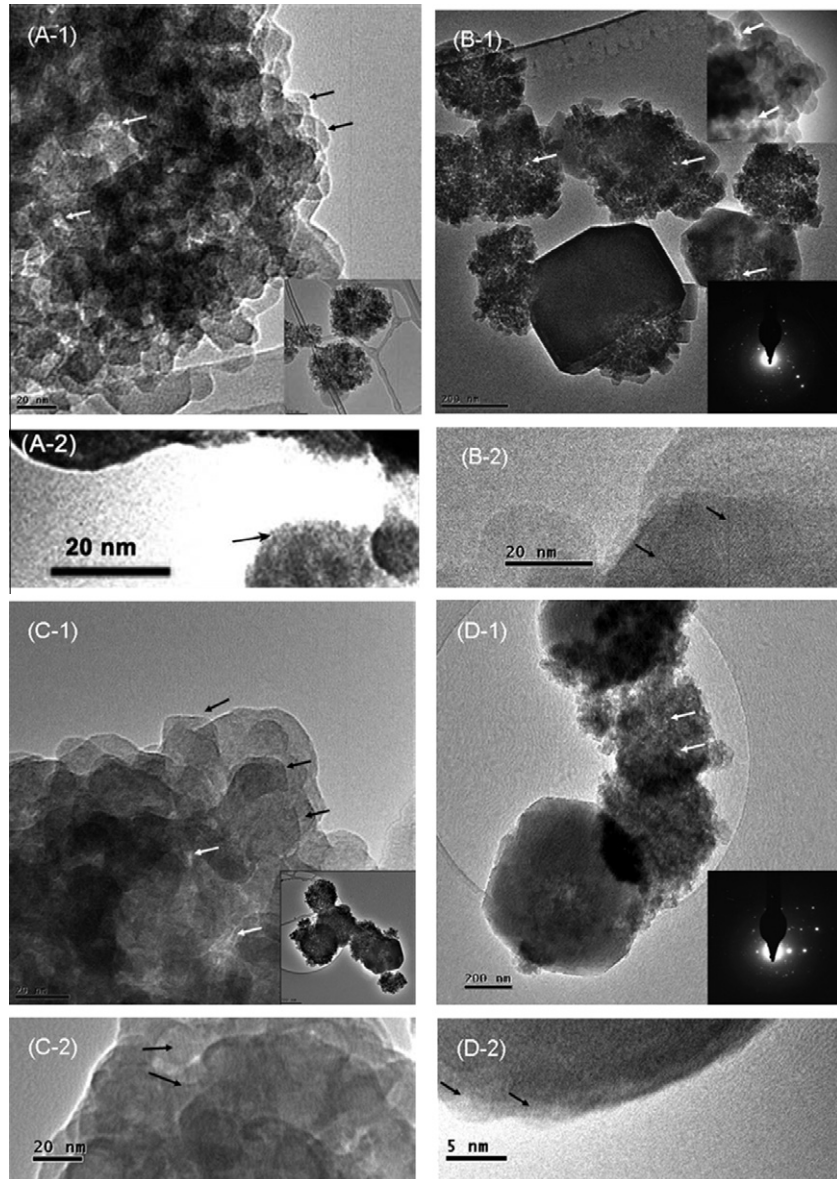


**Fig. 4.** High and low magnification images of MZ-0.14C-0 (A-1, A-2), MZ-0.14C-0.14D (B-1, B-2), MZ-0.14C-1.1D (C-1, C-2) and MZ-0.14C-2.75D (D-1, D-2). The insets on the bottom right corner in images B-1 and D-1 are the corresponding SAED patterns. The white arrows in images A-1, B-1, C-1 and D-1 mark the intracrystalline mesopores. The black arrows A-2, B-2, C-2 and D-2 show the lattice fringes.

period until almost a flattened isotherm type I which is typical of microporous material was obtained for the sample aged for 19 days (MZ-0.14C-8.2D-19). In Fig. 8C, the pore size distribution of MZ-0.14C-8.2D-14 exhibits two scales of mesopores; small mesopores demonstrated by several peaks appeared in the range 2–4 nm, and large scale mesopores represented by a broad peak extended between 5 and 15 nm but centered at 9.1 nm. Then with extending the aging period, a gradual decrease in two types of the mesopores can be observed clearly in Fig. 8C. The mesopore volume measured for MZ-0.14C-8.2D-14 and MZ-0.14C-8.2D-17 was  $0.17 \text{ cm}^3 \text{ g}^{-1}$ , but it decreased dramatically to  $0.08 \text{ cm}^3 \text{ g}^{-1}$  for MZ-0.14C-8.2D-19 (Table 1).

In summary, the results suggest that the LTA framework structure was retained in the synthesized samples with increasing the aging period; however a local structural evolution was probably occurring resulting in a decrease in the mesoporous phase in the samples.

### 3.4. Influence of CTAB concentration on the mesopore size distribution

The XRD pattern of the sample synthesized with low CTAB concentration (MZ-0.07C-8.2D) shows high intensity peaks that correspond to the LTA zeolite framework structure (Fig. 9A). In contrast, the pattern of the sample synthesized with high CTAB ratio (MZ-0.21C-8.2D) shows a relatively high proportion of amorphous phase, suggesting partial transformation of the gel into LTA zeolite. However, an extra peak at  $2\theta \sim 6^\circ$  appeared in the pattern indicating that another phase, most probably faujasite, was forming with the Na-A zeolite [26].

As described in Section 3.3, sample MZ-0.14C-8.2D (MZ-0.14C-8.2D-14) is a mesoporous Na-A zeolite. The mesoporosity was retained with decreasing the CTAB ratio to 0.07 or increasing it to 0.21 (Fig. 9B and C). The BET surface area and mesopores volume of MZ-0.14C-8.2D, MZ-0.07C-8.2D and MZ-0.21C-8.2D are 76, 54 and  $62 \text{ m}^2 \text{ g}^{-1}$  and  $0.17$ ,  $0.19$  and  $0.16 \text{ cm}^3 \text{ g}^{-1}$ ; respectively

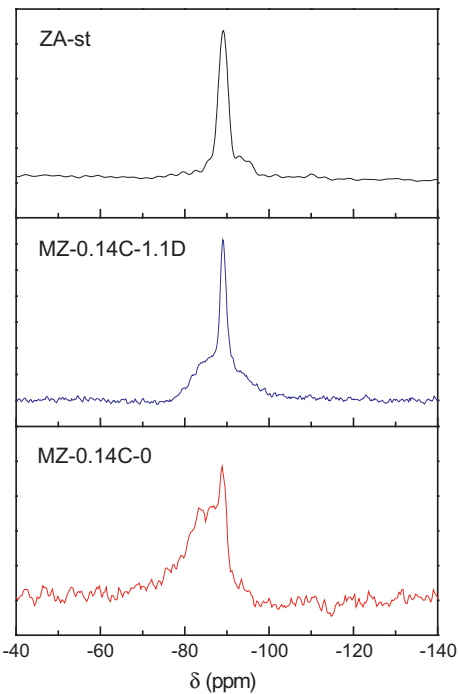


**Fig. 5.** 29Si NMR spectra of the samples; ZA-st, MZ-0.14C-1.1D and MZ-0.14C-0.

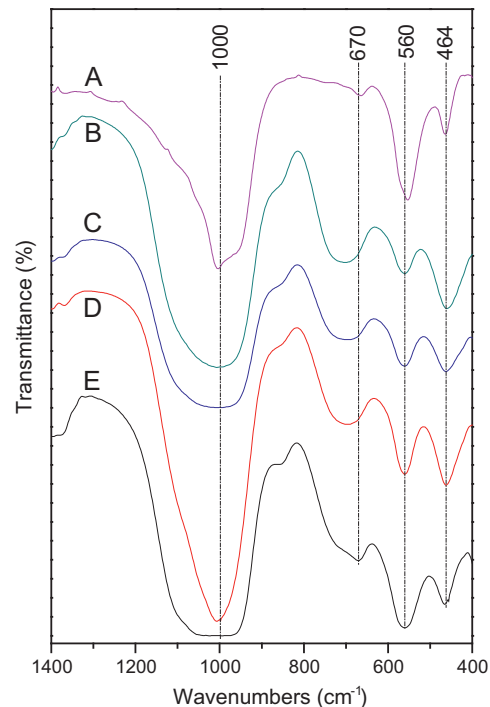


**Fig. 6.** FTIR spectra of ZA-st (A), MZ-0.14C-0 (B), MZ-0.14C-0.14D (C), MZ-0.14C-1.1D (D) and MZ-0.14C-2.75D (E).

**Table 2**

The elemental analyses of samples MZ-0.14C-0.14D and conventional zeolite A (CZA).

Sample	Si% mole	Al% mole	Na% mole	O% mole
MZ-0.14C-0.14D (nanoparticle aggregates)	16.52	14.97	8.66	59.84
MZ-0.14C-0.14D (cubes)	16.70	14.80	8.57	59.91
CZA	14.86	13.60	13.67	57.51

(Table 1). These results suggest that the highest mesopore pore volume was obtained with lower CTAB concentration.

### 3.5. Colloidal stability of synthesized mesoporous Na-A zeolite aqueous suspensions

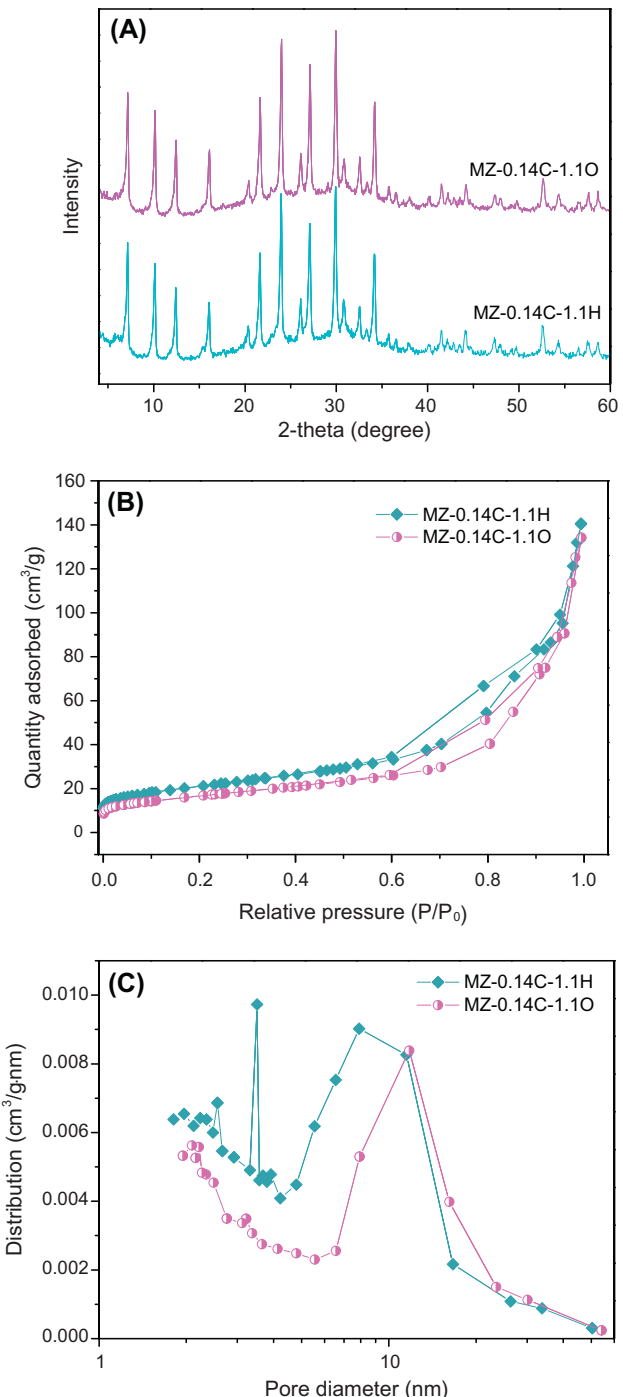
The colloidal stability of zeolite crystals is controlled by the balance between the Van der Waals and the repulsive electrostatic forces [24,38–40]. The electrostatic repulsion between the particles is determined by the charge of their surfaces which can be described by the zeta potential. The surface charge of zeolites with aluminosilicate framework results from the deprotonation of silanol groups (Si-OH) which are abundantly distributed on their surfaces [24,38,39]. For example, the surface of LTA zeolite consists of (T-O)<sub>3</sub> Si-OH Al(-O-Si)<sub>3</sub> which can be easily deprotonated forming (T-O)<sub>3</sub> Si-O<sup>-</sup> Al(-O-Si)<sub>3</sub> over a wide range of pH making the zeolite surface negatively charged [39]. Thus, zeta potential of the zeolite surface at a given pH is determined by the number of the hydroxyl groups on the surface. At a particular pH, all the acidic sites on zeolite surface are neutralized making the zeta potential zero and in consequence the particles undergo a spontaneous aggregation driven by Van der Waals forces; this occurs at the isolectric point (IEP) [38–40].

Fig. 10 shows the zeta potential as function of pH for MZ-0.14C, 014D and CZA. The zeta potential of both samples became more negative at high pH which is expected because the deprotonation of the hydroxyl groups increases. At low pH, the zeta potential of CZA surface decreased and reached zero around

pH ~ 3.1 which represents the IEP. On the other hand, the zeta potentials of MZ-0.14C-0.14D show negative values throughout the entire pH range (Fig. 10). Thus, the IEP for this sample, identified via extrapolating the data points at zeta potential  $\zeta = 0$  mV, was at pH ~ 0 [24]. This IEP shifting probably can be attributed to the higher surface area and larger pores of MZ-0.14C-0.14D compared to CZA. As described earlier (Section 3.1) the particles in MZ-0.14C-0.14D contained large mesopores (2.5, 3.5 and 9 nm) (Table 1). In our system, the relatively large HPO<sub>4</sub><sup>2-</sup> ions, ~4–5 Å [41], can diffuse from the solution into the large pores of MZ-0.14C-0.14D and reach remote acidic sites inside the particles deprotonating them and hence charging them negatively [24]. Consequently, the neutralization of MZ-0.14C-0.14D can only be achieved by strongly acidic solutions. On the other hand, the zeta potential of CZA is related only to a few layers from the external surface of the particles [24,42].

### 3.6. Ethylene adsorption–desorption measurements

Fig. 11 shows the ethylene adsorption–desorption isotherms of mesoporous Na-A zeolite (sample MZ-0.14C-0.14D) and conventional microporous Na-A zeolite (CZA) at 0 °C and pressure up to 850 kPa. It has been reported that ethylene molecules can be adsorbed on Na-A zeolite in spite of the discrepancy between the molecules size of the former (3.9 Å) and the pore sizes of the latter (3.5 Å) [43]. The driving force for this adsorption is the interaction energy that is determined by the  $\pi$  bond in the structure of ethylene molecules in addition to other physical properties; like high polarizability (3.5 Å<sup>3</sup>) and high quadrupole moment (0.48 Å<sup>3</sup>) [43–45]. In Fig. 11, the isotherms show that at low pressure region (<100 kPa), MZ-0.14C-0.14D adsorbed ethylene gas less than CZA. In contrast, at high pressure (850 kPa), the ethylene adsorption on MZ-0.14C-0.14D increased significantly to 4.32 mmol g<sup>-1</sup> compared to 3.61 mmol g<sup>-1</sup> on CZA. Even though the XRD patterns of both samples suggested that both materials have highly crystalline microporous LTA framework structure, the EDX-SEM analysis



**Fig. 7.** PXRD patterns (A), N<sub>2</sub> adsorption–desorption isotherms (B), and BJH pore size distribution (C) of the mesoporous Na-A zeolites synthesized with *n*-hexane (MZ-0.14C-1.1H) and *n*-octane (MZ-0.14C-1.1O).

indicates that the number of Na<sup>+</sup> cations in MZ-0.14C-0.14D is about two thirds the number of the cations in CZA. Normally ethylene adsorption on zeolite is driven by the strong interactions between the ethylene  $\pi$  bond and the electric field created by the cations of the micropore structure. Therefore the low ethylene adsorption on MZ-0.14C-0.14D at low pressure can be correlated to the low Na<sup>+</sup> concentration. On the other hand, the high adsorption capacity at high pressure is probably due to the high pore volume in MZ-0.14C-0.14D as measured by N<sub>2</sub> adsorption–desorption analysis and also due to the presence of the mesopores which facilitate the transportation of the molecules to maximum number of active sites.

### 3.7. Discussion

The above results show that MZ-0.14C-0 is a mesoporous Na-A zeolite synthesised by introducing a cationic surfactant, CTAB, into the reaction gel which then was aged at room temperature for a sufficient period for zeolite seeds formation. The SEM, N<sub>2</sub> adsorption–desorption analysis and TEM images suggest that the aging of zeolite gel at room temperature worked cooperatively with CTAB molecules for generating the mesosized pores in the Na-A

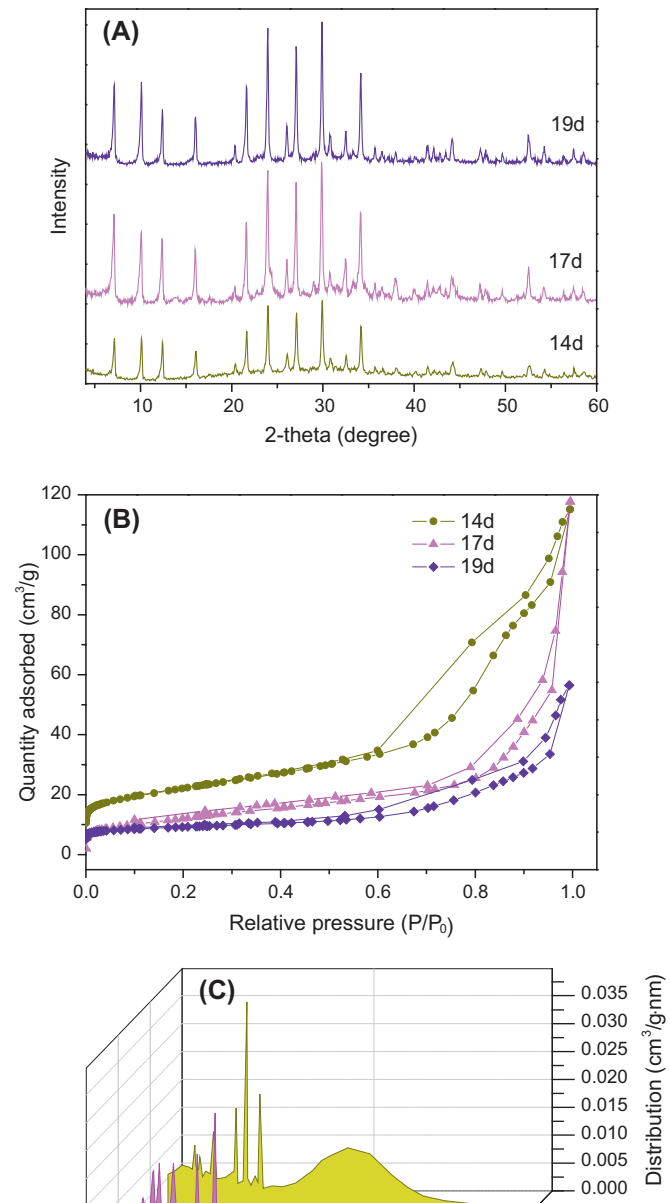


**Fig. 8.** PXRD patterns (A), N<sub>2</sub> adsorption–desorption isotherms (B), and BJH pore size distribution (C) of MZ-0.14C-8.2D-14, MZ-0.14C-8.2D-17 and MZ-0.14C-8.2D-19.

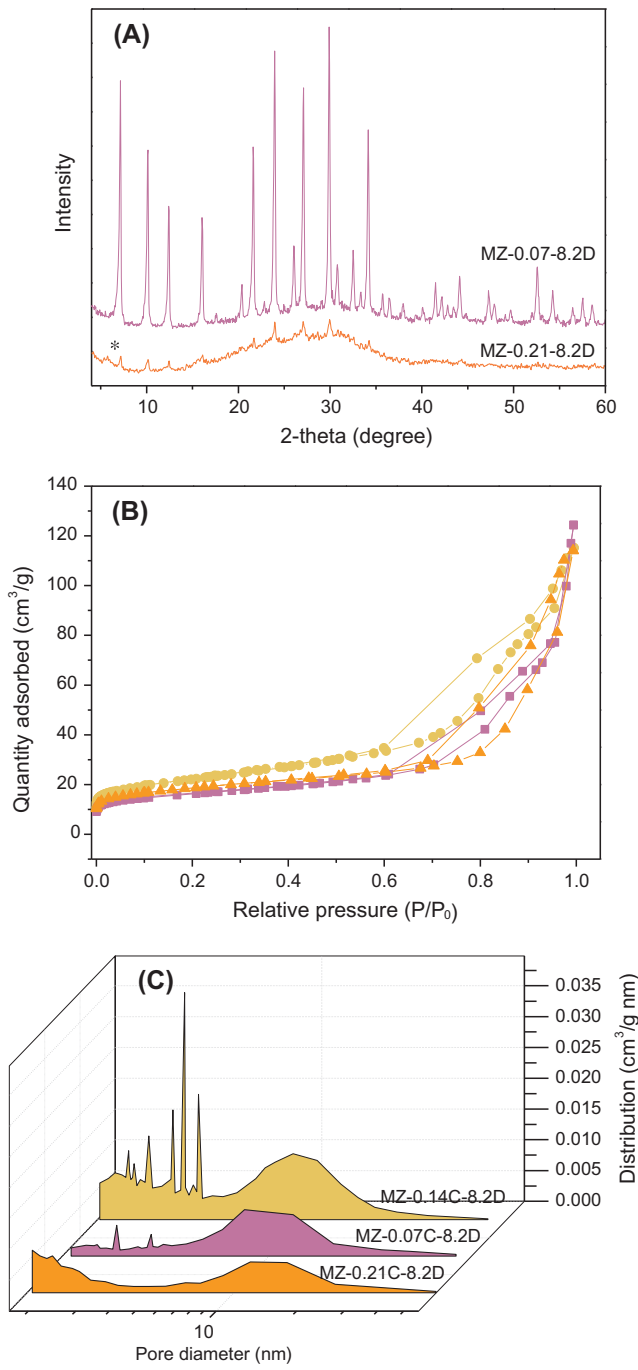


**Fig. 9.** PXRD patterns (A), N<sub>2</sub> adsorption–desorption isotherms (B), and BJH pore size distribution (C) of MZ-0.14C-8.2D, MZ-0.07C-8.2D and MZ-0.21C-8.2D.

zeolite particles. Since aging the gel without the inclusion of CTAB (sample ZA-st), or including CTAB molecules in zeolite gel without aging (sample ZA) generate Na-A zeolite with only micropores. In a previous study, mesoporous structures were synthesised by introducing swollen CTAB micelles into initially aged gel of type Y zeolite [46]. However, the product was not a pure mesoporous type Y zeolite; it was mesoporous composite of type Y zeolite and silica. Further, no mesoporous phase was obtained when only CTAB (without swelling agent) was introduced to the system. In our study, the results show that a pure mesoporous Na-A zeolite was prepared in presence of CTAB alone in the system. Furthermore, the results also show that the size of the meopores was controlled by the addition of alkane molecules which act as swelling agent in the system.

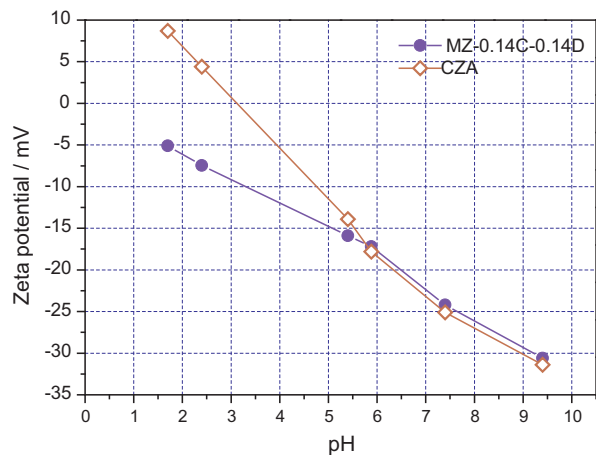


**Fig. 10.** Zeta potential as a function of pH of MZ-0.14C-0.14D and CZA.

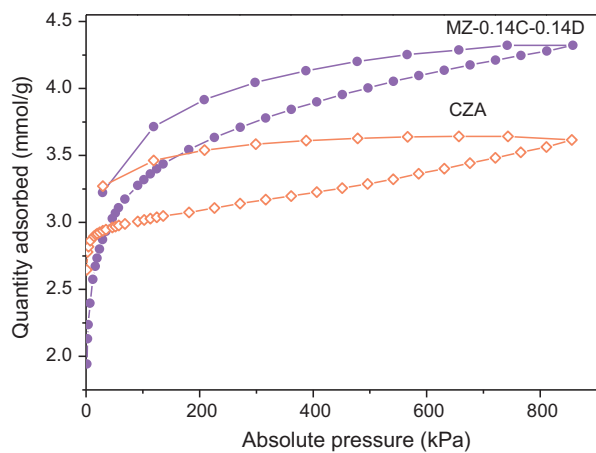


**Fig. 11.** Isotherms of ethylene gas adsorption on Mz-0.14C-0.14D and CZA at 0 °C and 850 kPa.

The size of the aggregated crystallites was in range of 15–20 nm, therefore the Bragg diffractions could readily be observed by XRD. In such systems, the general mechanism is that the inorganic zeolite subunits are assembled with the organic aggregations (surfactant micelles) and the subsequent removal of these micelles produces pores which are mirror images of the micelles. Accordingly, pores with size equal to normal diameter of surfactant micelles (2–4 nm) were expected from the system wherein no swelling agent was involved. However, mesopores with size of ~7.9 nm were obtained in (MZ-0.14C-0). Ryoo et al., owed such phenomenon to the condensation of the excess of surfactant molecules forming oligomers which might expand the surfactant micelles [10].

The mesopore size distribution measured by N<sub>2</sub> adsorption–desorption isotherms showed that introducing *n*-dodecane with CTAB in the initial gel of Na-A zeolite increased the pores size. For example, 1:1 M ratio of *n*-dodecane: CTAB (sample MZ-0.14C-0.14D) enlarged the mesopore diameter from 7.9 (MZ-0.14C-0) to 9 nm (Fig. 3 and Table 1). Further increasing the *n*-dodecane molar ratio to 1.1 and 2.75:0.14 CTAB increased the pores diameter to 11.5 and 13 nm, respectively (Fig. 3 and Table 1). Ulagappan et al. investigated swelling of CTAB micelles by alkanes in silica system at 1CTAB:1 alkane molar ratio [19]. The *n*-dodecane in their system formed a core inside the micelles by one to one molecule interaction with the surfactant molecules adding their entire chain length to the micelle diameter [19]. However,

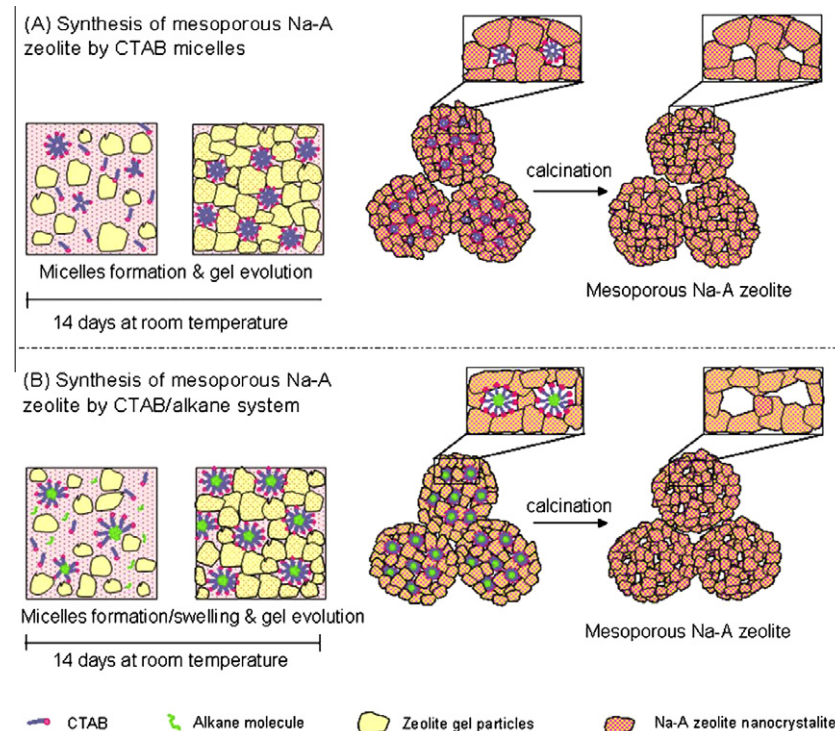


**Fig. 12.** (A) Proposed mechanisms for the synthesis of mesoporous Na-A zeolite by using CTAB micelles at room temperature, (B) swelling the CTAB micelles by linear chain alkane molecules to enlarge the mesopores size in the produced Na-A zeolite.

in our work the pore size expanded from 7.9 nm in the sample MZ-0.14C-0 to about 9.0 nm in sample MZ-0.14C-0.14D, which was less than the chain length of *n*-dodecane. These results indicate that *n*-dodecane behavior in our system is not in agreement with Ulagappan et al. mechanism. On the other hand, the results were more compatible with the “swelling effect” described by Kunieda et al. wherein they used *n*-decane to swell the micelles of polyoxyethylenedodecyl ether [20]. The “swelling effect” is the incorporation of alkane molecules in the inner core of the micelles expanding their volume [21]. The progressive increase in the pore size accompanied by raising the amount of *n*-dodecane in MZ-0.14C-1.1D and MZ-0.14C-2.75D (Table 1) is a further evidence for the “swelling effect” because when the number of *n*-dodecane molecules increases in the system they can profoundly penetrate and swell the core of the micelles. Especially at relatively low temperatures (room temperature in our system); as the less tightly aggregated and smaller associated number of the micelles result in smoother penetration for the *n*-dodecane molecules [47].

The solubilization of alkane molecules in the core of the micelles increases the packing parameter of the surfactant aggregations [20]. The packing parameter in surfactant – aqueous system is represented by:  $g = v_L/\alpha_S l$ , where  $v_L$  is the total volume of lipophilic tails of surfactant plus the organic additives,  $\alpha_S$  is the effective cross sectional area of the hydrophilic headgroups at the micelle-aqueous interface and  $l$  represents the kinetic length of hydrophobic chain of surfactant [20,48]. Kunieda et al. defined “swelling” as the effect of oil to increase the volume of lipophilic part without expanding  $\alpha_S$ . This suggests that, in present work, the solubilization of *n*-dodecane molecules in the core of CTAB micelles increased  $v_L$  which in turn raised the packing parameter ( $g$ ) of the self organizing structures of surfactant molecules and made them more positive. Thus, increasing the charge density of the micelles accompanied with increasing their volume probably resulted in improving the affinity between the micelles and the aluminosilicate species [20].

As Valtchev et al. investigated the synthesis of LTA and FAU zeolites at room temperature, tiny gel particles were formed directly after the mixing of the precursors [15–18]. In our system, the TEM results show single lattice orientation in individual crystallites with the size of about 20 nm (Fig. 4; images A-2, B-2, C-2 and D-2) which indicates that the nanocrystallites were generated from single amorphous particle domain. This suggests that tiny gel particles similar to those described by Valtchev et al. might be obtained after mixing the precursors in our system which then evolved slowly and simultaneously with the micelles formation/swelling process. It is mentioned above that the penetration of the alkane molecules into the core of micelles increased their size and their positive charge which enhanced the assembly of the tiny miniature zeolite gel particles on the surface of these micelles. Afterwards, each of these gel particles was transformed into Na-A zeolite crystallites. The slow gel evolution and mass transformation facilitated the retention of the surfactant micelles within the aggregated crystallites. This speculated mechanism is demonstrated in Fig. 12. The presence of half cube-half aggregate particles (SEM images in Fig. 2A–D) reveals that the system has probably undertaken a surface recrystallization route [28,49]. Such growth mechanism normally takes place in system wherein aggregated gel particles are formed in the early stage of gel evolution. Thin islands of Na-A zeolite are formed on the surface of the aggregates which then might be joined together and self aligned according to their crystallographic orientation forming cubic crystals of LTA zeolite [27]. Meanwhile, elaborated study is being conducted in our lab to understand a detailed growth mechanism and mesopores formation in such systems.

#### 4. Conclusion

In a one pot synthesis procedure, micro-mesoporous Na-A zeolites were successfully produced by the introduction of CTAB

micelles to a slowly evolving zeolite system at room temperature. At the early stage of gel evolution, freshly formed miniature zeolite gel particles were assembled around the surface of the coexisting CTAB micelles forming aggregations of zeolite-CTAB. Aging the system for 2 weeks at room temperature induced slow mass transformation of the zeolite gel particles into nanocrystallites which then grew slowly retaining the CTAB micelles within the crystallization area. The CTAB micelles and the 2 week room temperature aging worked collaboratively forming the mesoporous Na-A zeolite. The introduction of CTAB micelles in the synthesis gel is not effective in terms of generating the mesopores without the aging at room temperature and vice versa. The size of the mesopores was controlled by introducing different amounts/types of linear alkanes into the zeolite-CTAB system. Increasing the molar ratio of the swelling agent to CTAB produced larger mesopores. Furthermore, short hydrocarbon chain like *n*-hexane generated smaller pores than those obtained by long hydrocarbon chain like *n*-octane and *n*-dodecane. The alkanes acted as swelling agents by permeating into the core of the micelles increasing their volume as well as their packing parameters which enhanced the density of their positive charge. Increasing the aging period for longer than 2 weeks resulted in a significant reduction in the surface area and the mesopore volume. Further, raising the CTAB concentration in the synthesis mixture resulted in inhibiting the crystallinity of Na-A zeolite. The IEP for the mesoporous Na-A zeolite was shifted to pH close to zero as compared to conventional microporous Na-A zeolite (pH ~ 3.1). Furthermore, our material shows higher pore volume compared to conventional Na-A zeolite which resulted in higher adsorption capacity for ethylene gas. Thus, our material offers potential applications in projects where ethylene recovery is involved, for example, from the purge gas stream in the polyethylene manufacturing plant.

## Acknowledgments

The authors thank the Australian Research Council (ARC) for the financial support for conducting this work. The authors also appreciate Monash Centre for Electron Microscopy (MCEM) for continuous support and access to TEM and SEM facilities.

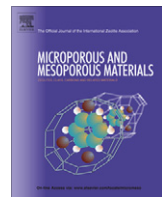
## Appendix A. Supplementary material

(1) Detailed information about the chemicals used in this work. (2) List of samples synthesized in the experiments and their gel compositions. (3) Particle size distribution (PDS) curves obtained from DLS for MZ-0.14C-0 (A), MZ-0.14C-0.14D (B), MZ-0.14C-1.1D (C), MZ-0.14C-2.75D (D) and ZA-st (E). (4) SEM image of CZA sample.

Supplementary data associated with this article can be found, in the online version, at <http://dx.doi.org/10.1016/j.jcis.2012.05.027>.

## References

- [1] D. Zhao, Q. Huo, J. Feng, B.F. Chmelka, G.D. Stucky, *J. Am. Chem. Soc.* 120 (1998) 6024.
- [2] D. Chen, Z. Li, C. Yu, Y. Shi, Z. Zhang, B. Tu, D. Zhao, *Chem. Mater.* 17 (2005) 3228.
- [3] K.B. Yoon, Y.J. Lee, Y.S. Park, J.S. Lee, US Patent No. 6777364 B2, 2004.
- [4] Y.J. Lee, K.B. Yoon, *Microporous Mesoporous Mater.* 88 (2006) 176.
- [5] J. Hua, Y. Han, *Chem. Mater.* 21 (2009) 2344.
- [6] B.T. Holland, L. Abrams, A. Stein, *J. Am. Chem. Soc.* 121 (1999) 4308.
- [7] D. Zhao, J. Feng, Q. Huo, N. Melosh, G.H. Fredrickson, B.F. Chmelka, G.D. Stucky, *Science* 279 (1998) 548.
- [8] M.F. Ottaviani, A. Moscatelli, D. Desplantier-Giscard, F. Di Renzo, P.J. Kooyman, B. Alonso, A. Galarneau, *J. Phys. Chem. B* 108 (2004) 12123.
- [9] M. Choi, H.S. Cho, R. Srivastava, C. Venkatesan, D.H. Choi, R. Ryoo, *Nat. Mater.* 5 (2006) 718.
- [10] K. Cho, H.S. Cho, L.C. De Menorval, R. Ryoo, *Chem. Mater.* 21 (2009) 5664.
- [11] Y. Liu, W. Zhang, T.J. Pinnavaia, *J. Am. Chem. Soc.* 122 (2000) 8791.
- [12] X. Chen, L. Huang, Q. Li, *J. Phys. Chem. B* 101 (1997) 8460.
- [13] J.S. Beck, J.C. Vartuli, G.J. Kennedy, C.T. Kresge, W.J. Roth, S.E. Schramm, in: H.G. Karge, J. Weitkamp (Eds.), *Studies in Surface Science and Catalysis*, vol. 98, Elsevier, Germany, 1995, p. 15.
- [14] A. Karlsson, M. Stocker, R. Schmidt, *Microporous Mesoporous Mater.* 27 (1999) 181.
- [15] V.P. Valtchev, L. Tosheva, K.N. Bozhilov, *Langmuir* 21 (2005) 10724.
- [16] V.P. Valtchev, K.N. Bozhilov, *J. Phys. Chem. B* 108 (2004) 15587.
- [17] S. Mintova, N.H. Olson, V. Valtchev, T. Bein, *Science* 283 (1999) 958.
- [18] V.P. Valtchev, K.N. Bozhilov, *J. Am. Chem. Soc.* 127 (2005) 16171.
- [19] N. Ulagappan, C.N.R. Rao, *Chem. Commun.* (1996) 2759.
- [20] H. Kunieda, K. Ozawa, K.L. Huang, *J. Phys. Chem. B* 102 (1998) 831.
- [21] J.L. Blin, C. Otjacques, G. Herrier, B.L. Su, *Langmuir* 16 (2000) 4229.
- [22] J.L. Blin, B.L. Su, *Langmuir* 18 (2002) 5303.
- [23] J.L. Ruggles, E.P. Gilbert, S.A. Holt, P.A. Reynolds, J.W. White, *Langmuir* 19 (2003) 793.
- [24] T. Mäurer, B. Kraushaar-Czarnetzki, *Helv. Chim. Acta* 84 (2001) 2550.
- [25] R.W. Thompson, K.C. Franklin, in: H. Robson, K.P. Lillerud (Eds.), *Verified Synthesis of Zeolitic Materials*, Elsevier, Amsterdam, 2001, p. 179.
- [26] V. Gramlich, W.M. Meier, in: M.M.J. Treacy, J.B. Higgins (Eds.), *Collection of Simulated XRD Powder Patterns for Zeolites*, Elsevier, Amsterdam, 2001, p. 215.
- [27] H. Greer, P.S. Wheatley, S.E. Ashbrook, R.E. Morris, W. Zhou, *J. Am. Chem. Soc.* 131 (2009) 17986.
- [28] W. Zhou, *Adv. Mater.* 22 (2010) 3086.
- [29] C.S. Cundy, P.A. Cox, *Microporous Mesoporous Mater.* 82 (2005) 1.
- [30] L. Gora, *Zeolites* 18 (1997) 115.
- [31] D.W. Breck, W.G. Eversole, R.M. Milton, T.B. Reed, T.L. Thomas, *J. Am. Chem. Soc.* 78 (1956) 5963.
- [32] M. Kruk, M. Jaroniec, *Chem. Mater.* 13 (2001) 3169.
- [33] Y. Huang, K. Wang, D. Dong, D. Li, M.R. Hill, A.J. Hill, H. Wang, *Microporous Mesoporous Mater.* 127 (2010) 167.
- [34] M.T. Melchior, D.E.W. Vaughan, R.H. Jarman, A.J. Jacobson, *Nature* 298 (1982) 455.
- [35] E. Lippmaa, M. Maegi, A. Samoson, M. Tarmak, G. Engelhardt, *J. Am. Chem. Soc.* 103 (1981) 4992.
- [36] A. Aronne, S. Esposito, C. Ferone, M. Pansini, P. Pernice, *J. Mater. Chem.* 12 (2002) 3039.
- [37] E.M. Flanigen, H. Khatami, H. Szymanski, *Molecular Sieve Zeolites-I*, Adv. Chem. Ser., vol. 101, American Chemical Society, Washington DC, 1971, p. 201.
- [38] O. Larlus, S. Mintova, T. Bein, *Microporous Mesoporous Mater.* 96 (2006) 405.
- [39] W. Yang, X. Wang, Y. Tang, Y. Wang, C. Ke, S. Fu, *J. Macromol. Sci. Part A* 39 (2002) 509.
- [40] T. Mäurer, S.P. Muller, B. Kraushaar-Czarnetzki, *Ind. Eng. Chem. Res.* 40 (2001) 2573.
- [41] L. Montastruc, C. Azzaro-Pantel, B. Biscans, M. Cabassud, S. Domenech, *Chem. Eng. J.* 94 (2003) 41.
- [42] L.C.J. Thomassen, D. Napierska, D. Dinsdale, N. Lievens, J. Jammaer, D. Lison, C.E.A. Kirschhock, P.H. Hoet, J.A. Martens, *Nanotoxicology* 5 (2011) 1.
- [43] D.W. Breck, *Zeolite Molecular Sieves: Structure, Chemistry, and Use*, John Wiley and Sons, New York, 1974.
- [44] A. Romero-Pérez, G. Aguilar-Armenta, *J. Chem. Eng. Data* 55 (2010) 3625.
- [45] R.J. Harper, G.R. Stifel, R.B. Anderson, *Can. J. Chem.* 47 (1969) 4661.
- [46] F.N. Gu, F. Wei, J.Y. Yang, N. Lin, W.G. Lin, Y. Wang, J.H. Zhu, *Chem. Mater.* 22 (2010) 2442.
- [47] J. Fan, C. Yu, J. Lei, Q. Zhang, T. Li, B. Tu, W. Zhou, D. Zhao, *J. Am. Chem. Soc.* 127 (2005) 10794.
- [48] Y. Wan, D. Zhao, *Chem. Rev.* 107 (2007) 2821.
- [49] X. Chen, M. Qiao, S. Xie, K. Fan, W. Zhou, Y. He, *J. Am. Chem. Soc.* 129 (2007) 13305.



## Formation of LTA zeolite crystals with multi-hollow polycrystalline core–shell structure *via* aggregation–recrystallization route in presence of emulsion droplets

Fatin Hasan<sup>a</sup>, Ranjeet Singh<sup>a</sup>, Paul A. Webley<sup>b,\*</sup>

<sup>a</sup>Department of Chemical Engineering, Monash University, Clayton, Victoria 3800, Australia

<sup>b</sup>Department of Chemical and Biomolecular Engineering, Melbourne School of Engineering, The University of Melbourne, Victoria 3010, Australia

### ARTICLE INFO

#### Article history:

Received 29 February 2012

Received in revised form 1 May 2012

Accepted 2 May 2012

Available online 14 May 2012

#### Keywords:

Slow crystallization rate

Emulsion droplets

Multi-hollow polycrystalline aggregates

Reversed crystal growth

### ABSTRACT

Na-A zeolite crystals consisting of thin crystalline polyhedral shell and multi-hollow polycrystalline core were formed for the first time following reverse crystallization mechanism. These extraordinary crystals were formed *via* two step crystallization from a system which included *n*-dodecane droplets stabilised with cetyltrimethylammonium bromide. A systematic investigation of the crystal growth over different crystallization stages indicates that at the first stage of crystal growth aggregates of nanocrystallites are formed which then undergo surface to core crystallization. At the start, *n*-dodecane droplets surrounded by a thin layer of cetyltrimethylammonium bromide enhance the formation of aggregates of amorphous nanoparticle which later transform into polycrystalline aggregates by local crystallization of each nanoparticle into a crystallite. Crystallized islands are built on the surface of the polycrystalline aggregates which are then extended and merged resulting in typical cubic morphology of LTA zeolite. Surface recrystallization continues towards the core *via* Oswald ripening process increasing the thickness of the shell. During the entire growth process, the *n*-dodecane droplets are retained inside the polycrystalline aggregates, probably due to slow crystallization rate at room temperature. The removal of the *n*-dodecane droplets and cetyl trimethylammonium bromide molecules results in Na-A zeolite particles with core–shell structure. The shell is highly crystalline Na-A zeolite and the core comprises of multi-hollow polycrystalline aggregates. The product shows mesoporosity with large size distribution attributed to polycrystalline aggregates that are free of the crystallized shell. Characterization of the samples was performed using transmission electron microscopy, scanning electron microscopy, cryogenic temperature transmission electron microscopy, X-ray diffraction, thermogravimetric analyzer, solid state NMR, FTIR, and N<sub>2</sub> adsorption–desorption analysis.

© 2012 Elsevier Inc. All rights reserved.

### 1. Introduction

Hollow zeolite structures with mesoporous walls have attracted significant attention recently due to their promising application in controlled drug delivery, confined-space catalysis, large biomolecular separation systems, etc. [1,2]. Generally, three techniques have been used to synthesize spheres with hollow cores; namely, hard templating [3,4], soft templating [1,5] and dual templating [6–8]. Recently, however, zeolite spheres/crystals with hollow cores were obtained from systems in which a surface to core crystallization mechanism was observed [2,9]. For instance, hollow LTA and sodalite structures were synthesized by using three

dimensional pore networks of crosslinked hydrogel polymers as reactors wherein *in situ* crystallization of the entrapped gel was performed [2,10]. On the interface between the polymer network and the gel, zeolite nuclei are formed and grow rapidly forming oriented nanoparticle aggregations which are consequently developed into hollow zeolite spheres/crystals by consuming the gel situated in the center of the aggregates [2]. However, the shells of these hollow structures are microporous; thus large molecules such as macromolecules cannot diffuse to the center. Hence, material with hollow cores and large-scale porous walls is highly desirable because they offer better mass transfer and less channel blockage [6]. Zhao et al. successfully synthesized MFI zeolite capsular structures with hollow core and mesoporous shell [11]. Initially they created an oil (TEOS) in water emulsion system followed by carefully controlling the TEOS hydrolysis temperature in the presence of TPAOH and CTAB as micro- and mesopores templates, respectively. During the hydrothermal treatment at high

\* Corresponding author. Address: Department of Chemical and Biomolecular Engineering, Room 3.21A, Melbourne School of Engineering, The University of Melbourne, Victoria 3010, Australia. Tel.: +61 3 90357873; fax: +61 3 83444153.

E-mail addresses: [fatin.hasan@monash.edu.au](mailto:fatin.hasan@monash.edu.au) (F. Hasan), [ranjeet.singh@monash.edu.au](mailto:ranjeet.singh@monash.edu.au) (R. Singh), [paul.webley@unimelb.edu.au](mailto:paul.webley@unimelb.edu.au) (P.A. Webley).

temperature, the TEOS molecules diffuse outward through the zeolite seeds/CTAB layer that condensed along the oil (TEOS)/water interface leaving behind a hollow core surrounded with a mesoporous shell [11]. However, the average size of the mesopores in the shell of the hollow capsules is 3 nm which renders them impractical for applications where molecules with large molecular weight, like proteins, are involved. Therefore, the direct synthesis of hollow zeolite particles with fully crystalline mesoporous walls is still considered a challenge.

Herein, we report for the first time the synthesis of Na-A zeolite particles with multi-hollow core–shell structure *via* a reversed growth mechanism in an emulsion/gel system. The strategy in this work is based on slow *in situ* crystallization of Na-A zeolite system at room temperature in the presence of *n*-dodecane droplets and cetyltrimethylammonium bromide molecules. The product exhibits large mesopore size distribution which is attributed to voids between the aggregated crystallites in the multi-hollow-polycrystalline aggregates. The slow crystallization kinetics allowed a detailed investigation of all the stages of the formation of Na-A zeolite particles with multi-hollow and polycrystalline core. To illustrate our approach, LTA zeolite was selected because it is important for a wide range of applications such as ion exchange, adsorption and medical purposes and also because highly crystalline LTA zeolite can be obtained at room temperature crystallization within a relatively short period of time [12–14].

## 2. Experimental work

### 2.1. Materials

The chemicals used for this work were: sodium silicate solution (~26.5% SiO<sub>2</sub> and ~10.6% Na<sub>2</sub>O, Sigma Aldrich), sodium aluminate (50–56% Al<sub>2</sub>O<sub>3</sub> and 40–45% Na<sub>2</sub>O, Sigma Aldrich), sodium hydroxide (>99%, Merck), cetyltrimethylammonium bromide (CTAB-Ajax Finechem) and *n*-dodecane (99%, Merck). All chemicals were used without any further purification.

### 2.2. Synthesis

The initial gel of Na-A was prepared according to a method reported in the literature [15]. Typically, the synthesis commenced with dissolving 2 g sodium hydroxide in 37.6 g of de-ionised water. Then this alkaline solution was divided equally into two halves named as (A) and (B). To the first half (A), 3.9 g sodium aluminate was added and dissolved by vigorous stirring until a clear solution was obtained. 8.8 g of sodium silicate solution was added to the second half (B) and stirred for a few minutes. Then the two solutions (A) and (B) were mixed and stirred vigorously by using electronic overhead stirrer type Eurostar digital (manufactured by IKA-WERKE) at speed 540–580 rpm. The cationic emulsifier, cetyltrimethylammonium bromide (CTAB, 2 wt.% of total synthesis mixture) was then added to the homogenized gel under continuous stirring for few minutes, followed by drop wise addition of 37.5 ml *n*-dodecane. The gel obtained after the addition of CTAB was named CTAB/gel and the gel obtained after the *n*-dodecane introduction was named CTAB/Dod/gel. At this stage the system was transformed into an emulsion wherein the *n*-dodecane droplets represent the dispersed phase and the zeolite gel represents the continuous phase of the emulsion. CTAB molecules act as an emulsifier and occupy the interface between the droplets and the continuous phase increasing the emulsion stability.

The final homogenized and creamy emulsion was aged at room temperature for 14 days followed by elevated temperature crystallization at 95 °C for 5 h. During the room temperature aging, no phase separation was detected confirming the emulsion stability.

Thereafter the product was collected by vacuum filtration and washed repeatedly with ethanol and water and finally dried at 90 °C overnight. The surfactant was removed by calcination at 600 °C with ramp rate 2 °C/min in air flow for 6 h. The collected product in this stage was denoted MZ-14d-cryst.

For comparison purposes, conventional Na-A zeolite was synthesized starting from the same initial gel composition which was then aged at room temperature for 14 days followed by hydrothermal crystallization at 95 °C for 5 h. The product was collected by filtration under vacuum, washed frequently with water and finally dried at 90 °C overnight. The obtained zeolite was denoted as ZA-st in this work.

To investigate the mechanism of crystal growth and hollow formation in the produced particles, aliquots of synthesis mixture were taken at different periods of room temperature aging. These aliquots were denoted as MZ-*t*; where MZ represented the reactants mixture and *t* referred to the number of hours/days the sample was aged.

### 2.3. Characterization

Powder X-ray diffraction (PXRD, Phillips PW1140/90) with Cu K $\alpha$  radiation was used to examine the crystallinity of samples in 2θ range 5–60° in steps of 0.05° and a scan rate of 1° min<sup>-1</sup>. The low angle diffraction pattern was obtained on Scintag PAD V diffractometer with carbon monochromator. The particles size and morphology were investigated by scanning electron microscope (SEM, JEOL 7001F FEG) at 15 kV. The sample was crushed and sprinkled on carbon tape mounted on a metal stub and coated with 1 nm layer of platinum metal. N<sub>2</sub> adsorption–desorption isotherms were measured at (−196 °C) by a Micromeritics ASAP 2020 gas adsorption analyzer. All samples were degassed at 350 °C for 15 h under vacuum before analysis. The BET surface area was calculated using the adsorption data collected over a relative pressure ( $P/P_0$ ) range of 0.05–0.3. The pore volume was measured at  $P/P_0 = 0.99$  and the BJH mesopore size distribution was measured using the adsorption branch. Transmission electron microscope (TEM, CM20) at 200 kV accelerating voltage was used to investigate the detailed features of the produced particles. The sample was finely crushed, then dispersed in ethanol and sonicated for 10 min. Thereafter a drop of this suspension was dispersed on a Cu grid coated with a thin layer of carbon. The FTIR spectra were recorded on a Perkin Elmer 100 FT-IR spectrometer in range 1400–400 cm<sup>-1</sup> with a resolution of 4 cm<sup>-1</sup> using KBr pellets. The <sup>29</sup>Si and <sup>27</sup>Al solid state nuclear magnetic resonance (MAS-NMR) spectra were performed at room temperature on a Bruker Avance 300 spectrometer equipped with a 4 mm magic angle spinning (MAS) probe at spinning speeds of 10–14 kHz with resonance frequency of 59.6 MHz for <sup>29</sup>Si and 78.2 MHz for <sup>27</sup>Al. The spectra were collected in single pulse mode with 10 s recycle delay and 3 μs excitation pulse. The standards used for chemical shifts referring are tetramethyl silane (TMS) for <sup>29</sup>Si and aluminum nitrate solution for <sup>27</sup>Al. Thermogravimetric analysis (TGA) was conducted on Mettler Toledo TGA/SDTA851 in air flow of 20 ml min<sup>-1</sup> and at heating rate of 10 °C min<sup>-1</sup> to 900 °C.

The emulsion features and the droplet size were characterized by using cryogenic temperature transmission electron microscope (Cryo-TEM, Tecnai F30-FEI) equipped with an anti-contaminator and cold stage that allows imaging of quick frozen samples. The samples for the Cryo-TEM analyses were prepared by plunge freezing. Briefly, a drop of the emulsion was placed on Holey carbon film supported by a copper TEM grid. The drop was blotted gently with filter paper from both sides of the grids to remove the excess liquid and form a thin film of sample spanning the holes of the support film. The sample was vitrified by plunging in liquid ethane. The vitrified specimens were transferred and loaded into the TEM

cryo-holder under liquid nitrogen at ( $-196^{\circ}\text{C}$ ). The temperature of the specimens was maintained under ( $-170^{\circ}\text{C}$ ) throughout the TEM examination which was operated at 300 kV. All characterizations were carried out on calcined samples unless noted otherwise.

### 3. Results and discussion

The wide range X-ray pattern of sample MZ-14d-cryst (Fig. 1) shows peaks that can be indexed onto the cubic unit cell of LTA zeolite framework structure as compared to standard crystal data published by International Zeolite Association [16]. The low angle XRD diffraction pattern in Fig. 1-inset shows a single peak centered at  $2\theta = 0.8^{\circ}$  with  $d_{\text{spacing}}$  10.2 nm indicating the presence of meso-sized pores in MZ-14d-cryst. This mesoporosity was well confirmed by  $\text{N}_2$  adsorption–desorption measurements at ( $-196^{\circ}\text{C}$ ) (Fig. 2). The isotherm of sample MZ-14d-cryst is a typical IV type with steep increase in quantity of nitrogen adsorbed at relative pressure 0.6–0.99 which is caused by capillary condensation of  $\text{N}_2$  in the mesopores. The IV isotherm with H3 hysteresis and without level off at high relative pressure (close unity) suggests that the product comprises of aggregated crystallites [17,18].

In contrast, the isotherm of sample ZA-st shows negligible  $\text{N}_2$  adsorption which can be attributed to the presence of some mesoporosity [19]. It is well known that the micropores in conventional Na-A zeolite are too small to be accessed by  $\text{N}_2$  molecules due to pore blockages [20,21]. The specific surface area and mesopore volume of sample MZ-14d-cryst are  $76.06 \text{ m}^2 \text{ g}^{-1}$  and  $0.17 \text{ cm}^3 \text{ g}^{-1}$ , respectively (Table S1). The pore size distribution as obtained by BJH method using the adsorption branch shows two ranges of mesopores: small mesopores in range of 2–4 nm and large mesopores represented by broad peak centered at 9.1 nm (Fig. 2-inset and Table S1). The large scale mesopores correspond in size to the  $d$ -spacing suggested by small angle XRD (10.2 nm).

Further, the MZ-14d-cryst sample was converted into  $\text{Ca}^{+2}$  form and named MZ-14d-cryst- $\text{Ca}^{+2}$  (see the Supporting information). The pore size distribution of MZ-14d-cryst- $\text{Ca}^{+2}$  was measured by  $\text{N}_2$  adsorption–desorption analysis and compared to MZ-14d-cryst. The results indicate that the pore size distribution was retained after the ion exchange; however the mesopore volume was slightly smaller (see Fig. S4A, B in the Supporting information). The results obtained have been described in detail in the Supporting information.

The FTIR spectra for both the ZA-st and MZ-14d-cryst show four distinctive absorption bands at around 464, 556, 667 and  $1004 \text{ cm}^{-1}$  (see Fig. S1 in the Supporting information). The absorp-

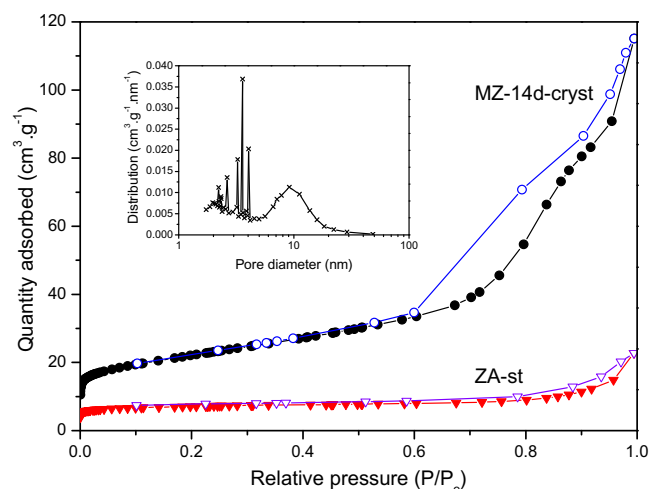


**Fig. 2.**  $\text{N}_2$  adsorption–desorption isotherms at ( $-196^{\circ}\text{C}$ ) of MZ-14d-cryst and ZA-st. BJH mesopores size distribution obtained from the adsorption branch of sample MZ-14d-cryst (inset).

tion bands were assigned on the basis of previous studies [22,23]. The band at  $556 \text{ cm}^{-1}$  is attributed to the external vibration of double four-member rings which is the characteristic for zeolite A framework. The bands resolved at 667 and  $1004 \text{ cm}^{-1}$  are assigned to the internal vibration of T–O (T = Si and Al) symmetric and asymmetric stretching, respectively. Finally, the band at  $464 \text{ cm}^{-1}$  is related to the T–O (T = Si and Al) bending. These observations complement the XRD observation that both materials have zeolite A structure.

The  $^{27}\text{Al}$  and  $^{29}\text{Si}$  NMR spectra of sample MZ-14d-cryst show agreement with the spectra of ZA-st indicating the similarity in the structure of both materials (see Fig. S2 in the Supporting information). The  $^{27}\text{Al}$  spectra show a single narrow resonance signal centered at  $\delta = 59 \text{ ppm}$  which is assigned to tetrahedrally coordinated aluminum linked by oxygen bonds to silicon. The  $^{29}\text{Si}$  NMR spectra of ZA-st and MZ-14d-cryst show a sharp signal with chemical shift at  $\delta = -89.5 \text{ ppm}$  in addition to two shoulders at  $\delta = -93$  and  $-95 \text{ ppm}$  (see Fig. S2 in the Supporting information) which indicates that the framework structure of both materials consist mainly of  $\text{Si(OAl)}_4$  building units but with slight distortion in some sites in the lattice environment. The narrow peaks at chemical shift  $-89.5 \text{ ppm}$  in  $^{29}\text{Si}$  NMR and at  $59 \text{ ppm}$  in  $^{27}\text{Al}$  NMR spectra reveal that both materials are highly crystalline Na-A zeolite [24–26].

The results obtained from XRD, FTIR and  $^{27}\text{Al}$  and  $^{29}\text{Si}$  NMR measurements indicate that both samples; namely, ZA-st and MZ-14d-cryst are Na-LTA type zeolite. Moreover, the low angle XRD and  $\text{N}_2$  adsorption–desorption analysis reveal that MZ-14d-cryst consists of a hierarchical pore structure, micro and mesopores.

The SEM results indicate that the sample MZ-14d-cryst mainly consists of two different types of particles; namely, rounded cubes with size range 300–750 nm and polycrystalline aggregates which show smaller size of range of 200–400 nm (Fig. 3A). The diameter of the primary crystallites in the polycrystalline aggregates is 10–50 nm. Also, the image of a single particle in Fig. 3B suggests that the cubic particles probably originally are polycrystalline aggregates which were recrystallized by building a cubic crystalline shell around them [9].

In agreement with the SEM results, TEM images show that MZ-14d-cryst consists of two types of particles; aggregates and cubes (Fig. 4A and B). The aggregates are formed of nanoparticles with size range of 15–50 nm aggregated around several hollows of size 50–140 nm (marked with white arrows in Fig. 4A). A magnified im-

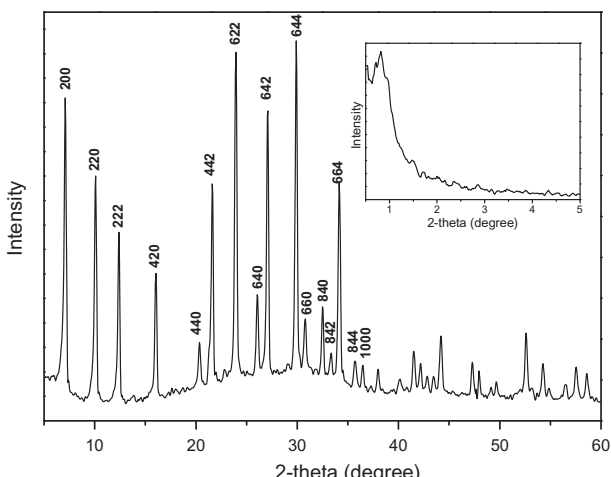


**Fig. 1.** Wide and small (inset) angle XRD patterns of MZ-14d-cryst. Indicated peaks can be linked to the literature [16].

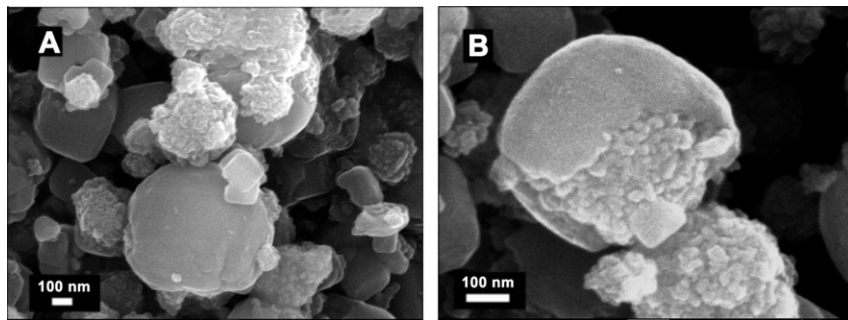


**Fig. 3.** SEM images of a group of particles (A) and focused on a single particle (B) of MZ-14d-cryst. The scale of images is 100 nm.

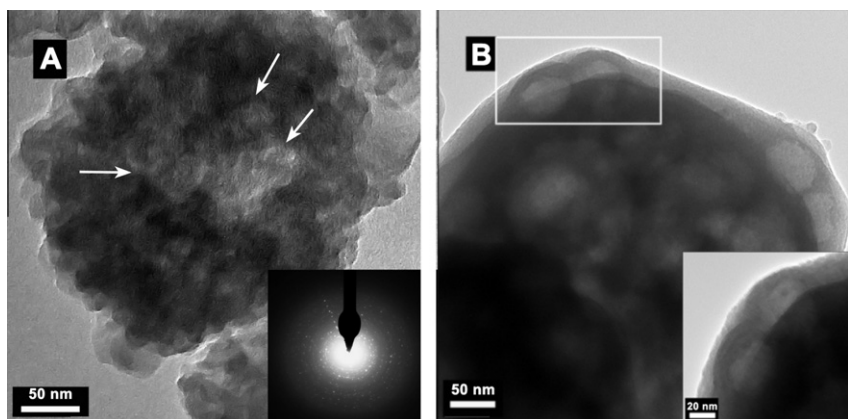


**Fig. 4.** TEM images of two different particles in the sample MZ-14d-cryst (A and B). The inset in image A shows the SAED pattern for the sample. The inset in image B shows the high magnification TEM image of the edge of the particle in (B) as marked by the rectangle.

age of an edge of a cubic particle reveals that the cubic shell is a thin layer surrounding aggregations of hollow structures (Fig. 4B-inset). The size of the aggregates and the cubic particles are between 200–300 nm and 350–570 nm, respectively. The SAED pattern (Fig. 4A-inset) of a group of particles in sample MZ-14-cryst shows polycrystalline rings and single crystal spots indicating that the sample contains polycrystalline particles and large single crystals.

The TEM and SEM results suggest that multi-hollow polycrystalline aggregates are probably formed in the early growth stage which, with increase in the crystallization time, undergoes surface recrystallization by building a shell of LTA zeolite around them.

To reveal the formation mechanism of the multi-hollow core-shell particles of Na-A zeolite, aliquots of the synthesis gel were taken at different periods of aging. These samples were washed, dried and calcined before being observed by means of TEM, Cryo-TEM, TGA, SEM, XRD, and ASAP 2020 (surface area).

### 3.1. First stage crystal growth: Formation of multi-hollow polycrystalline aggregates

The first sample named CTAB/gel was taken directly after the addition of CTAB to the initial zeolite mixture. The TEM image of this sample shows non-uniform gel nanoparticles about 5–20 nm in size, which are aggregated forming large gel complexes (Fig. 5A). On the other hand, the TEM image of sample CTAB/Dod/gel which was taken directly after introducing *n*-dodecane droplets into the CTAB/gel shows individual hollow gel particles about 20–45 nm in size (Fig. 5B). The hollow diameter is between 15 and 33 nm and the shell thickness ranges between 3 and 5 nm. The image also shows tiny gel particles about 5–20 nm in size are

aggregated on the external surface of the hollow particles (marked with white arrows in Fig. 5B).

In a complementary study, Cryo-TEM was used to measure the size distribution of freshly dispersed *n*-dodecane droplets. For this purpose, a fresh emulsion was prepared but by replacing the zeolite gel with water in order to avoid the dilution required for zeolite gel which might induce droplet coalescence. The conditions used in the preparation of CTAB/Dod/gel emulsion were retained with the preparation of fresh emulsion; such as, oil (*n*-dodecane):water ratio, CTAB concentration and also the mixing conditions (speed and time). Immediately after stopping the mixer, a drop of the fresh emulsion was placed on carbon holey grid and tested by Cryo-TEM (Fig. 6). The majority of the oil droplets show size range between 20 and 50 nm (Fig. 6) corresponding the range of the hollow diameter observed by TEM (15–33 nm) (Fig. 5B). However, some droplets with size larger than 50 and less than 150 nm were also observed.

The weight loss was also measured by thermogravimetric analyzer (TGA) on the as synthesized samples of CTAB/gel and CTAB/Dod/gel. In Fig. 7, a 25% weight loss was observed for CTAB/Dod/gel, due to decomposition of CTAB and *n*-dodecane between 170 and 450 °C, compared to 17.6% for CTAB/gel. This weigh loss difference can be attributed to the tiny oil droplets that might be embedded in the gel particles as observed by TEM (Fig. 5B). Accordingly, the low contrast cores observed inside the gel particles in Fig. 5B are probably replicates of oil droplets embedded within the gel while the dark contrast walls and the tiny aggregated particles can be attributed to aluminosilicate building units. The phase stability observed on the gel/emulsion for the entire aging period suggests that CTAB molecules were probably dissolved on the surface of the oil droplets stabilizing them as well

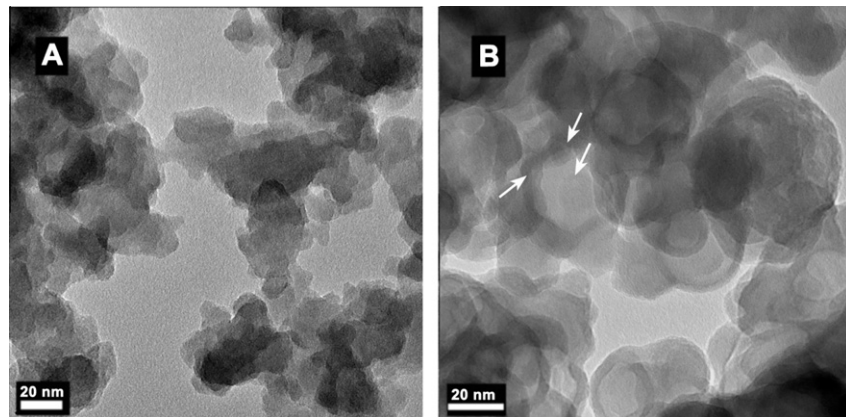


**Fig. 5.** TEM images for the aliquots taken from CTAB/gel (A) and CTAB/Dod/gel (B).

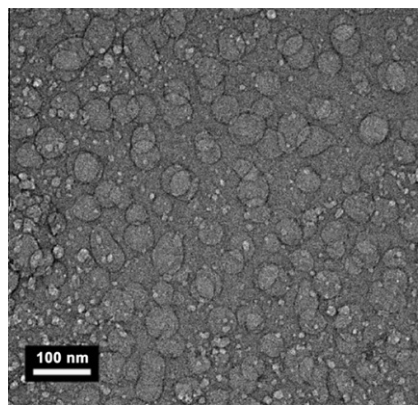


**Fig. 6.** Cryo-TEM image of a drop taken from the fresh emulsion.

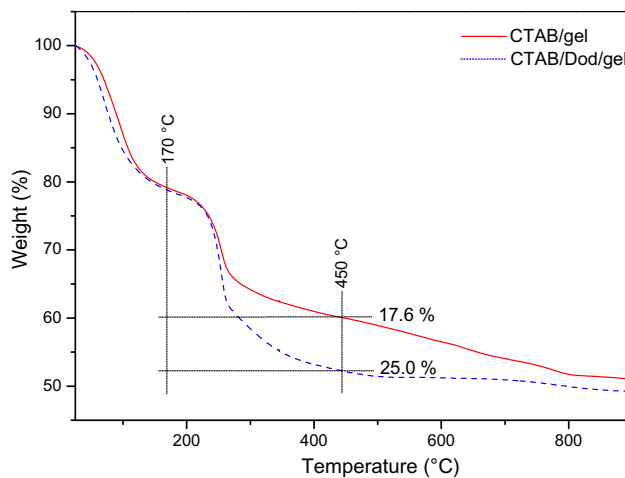


**Fig. 7.** Relative weight loss by TGA of as synthesized samples taken from CTAB/gel and CTAB/Dod/gel samples.

as positively charging them (cationic ammonium group) [27]. Consequently, aggregation between the zeolite precursors and the positive *n*-dodecane droplets was enhanced.

The structure of the hollow gel particles was retained after 48 h aging (TEM image in Fig. 8A) but the shell thickness increased to about 5–15 nm which is an indicative of more aluminosilicate species condensing on the external surface of the gel particles. Aggregation between the hollow gel particles can be observed after

6 days aging as shown in TEM results (Fig. 8B). Also, this aggregation can be detected in the SEM image (Fig. 9A) which shows 200–430 nm globular particles with a rough surface dispersed within the gel. These findings imply physical and structural rearrangements within the amorphous domain or probably a mass transformation into a crystalline phase had commenced [28].

However, the XRD patterns for the sample MZ-5d (Fig. 10A) does not show any diffractions peaks, but only a broad peak ranging from 15° to 40°,  $2\theta$ . Nevertheless, the absence of Bragg diffractions does not necessarily mean the absence of a crystalline phase in the system; there are probably some crystals formed but XRD could not detect them either because they are embedded in the abundant amorphous gel or their size is very small [29] or because the amount of the crystalline phase is less than the detection limit (3–4 wt.%) of the XRD technique [28]. The sample taken after 7 days aging shows diffraction peaks corresponding to LTA zeolite in literature references [16].

A substantial increase in the size and the number of the globular aggregates was observed in the SEM image after 9 days aging (Fig. 9B). Also the TEM investigations for the same sample (Fig. 8C) show large particles with size range 350–430 nm that contain several hollows with diameter of 40–80 nm surrounded with aggregated nanoparticles. At the same stage a sample was taken from the gel/emulsion and examined by the Cryo-TEM (Fig. 8D). Before the examination, the sample was diluted fivefold with water, shaken and immediately a drop was taken and placed on a carbon grid. The Cryo-TEM results show large particles with diameter of 360–480 nm holding oil droplets with diameter of 45–130 nm (Fig. 8D), which are in agreement with TEM suggesting that the hollows are “casts” of the removed oil (*n*-dodecane) droplets.

The XRD pattern for the sample MZ-9d (Fig. 10D) shows broad diffraction peaks with a “hump” in the mid range  $2\theta$  indicating that the material contains both nanosized LTA zeolite crystals and amorphous phase. Nevertheless, the XRD (Fig. 10D) and the SEM (Fig. 9C) investigations of MZ-12d show that the amorphous phase disappears after 12 days indicating the completion of mass transformation of the amorphous gel into crystalline phase.

A careful and close investigation of the SEM results of MZ-12d (Fig. 9C) shows that the primary particles forming the aggregates became larger and more faceted compared to MZ-9d sample (Fig. 9B). The above results suggest that the system most probably undergoes a nucleation/growth mechanism similar to the mechanism observed in the LTA zeolite formation at room temperature in a TMA-containing system [14]. In summary the process is as follows, nuclei were probably formed inside the primary gel particles surrounding the droplets and then the viable nucleus grew by

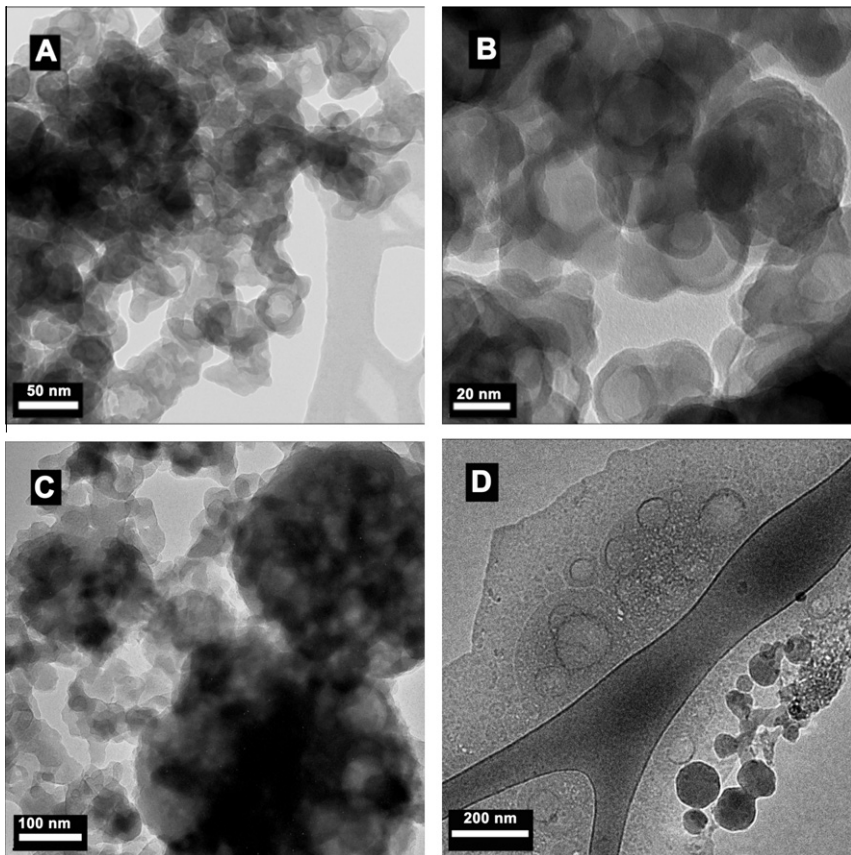


**Fig. 8.** TEM images for samples taken after 48 h (A), 6 days (B) and 9 days aging (C). Cryo-TEM image for the gel sample taken after 9 days aging (D).

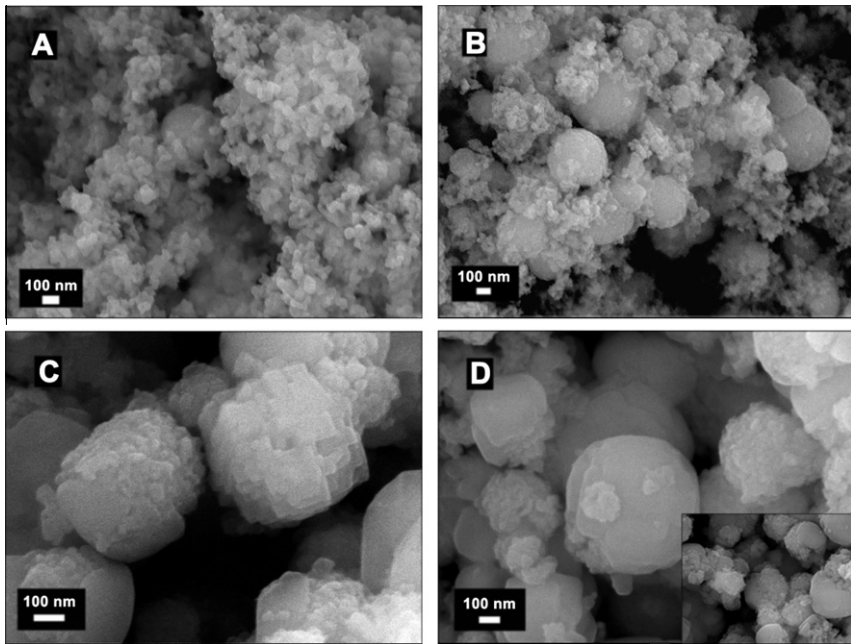


**Fig. 9.** SEM images for samples taken after 6 days (A), 9 days (B) 12 days (C) and 14 days aging (D).

propagation consuming the gel phase surrounding them forming an LTA zeolite crystallite. During the growth of the crystallites, a mechanism of aggregation around the crystalline center was induced forming the globular aggregates [28]. After the crystallites formation was completed and the amorphous phase was ex-

hausted in the period between 9 and 12 days; the system most likely entered the Ostwald ripening stage, in which the large particles grow at the expense of small particles [9]. Therefore, the size of crystallites composing the aggregates in MZ-12d is larger than in MZ-9d.

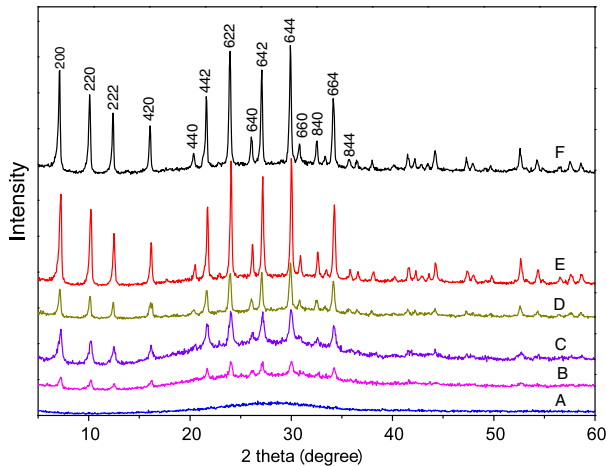


**Fig. 10.** Powder X-ray diffraction patterns of Na-A zeolite samples collected at different aging periods, 5 days (A), 7 days (B), 9 days (C), 12 days (D), 14 days (E) and also the pattern of the sample crystallized at elevated temperature after 14 days aging MZ-14d-crys (F). Indicated peaks can be linked to the literature [16].

### 3.2. Second stage of crystallization: Formation of multi-hollow polycrystalline core-shell particles

The SEM investigation also shows that crystalline islands were developed on the surface of some of the polycrystalline aggregates (Fig. 9C). By prolonging the aging period to 14 days (Fig. 9D) these islands were extended and merged forming a thin shell around the aggregates and then, more interestingly, oriented themselves

forming the characteristic cubic shape of LTA zeolite (Fig. 9D). The development of polycrystalline aggregates into single cubic crystals by surface recrystallization is directed under the force of minimizing surface free energy [9,10,30].

The substantial increase in the intensity of the XRD diffractions of sample MZ-14d compared to MZ-12d (Fig. 10D and E) suggests a rapid crystal growth which is however unlikely to occur at ambient conditions [28]. Therefore, it is more likely that the obtained single crystals of LTA type zeolite in fact are thin crystalline shell of LTA zeolite built around the hollow-polycrystalline aggregates which confirms the SEM results. However, in addition to single crystals, the sample also contains polycrystalline aggregates which are free of or partially covered with crystalline shell (Fig. 9D-inset).

The TEM images of MZ-12d (Fig. 11A and C) show particles with hollow polycrystalline core. The magnified image of the area as marked by a white square in Fig. 11A shows clearly the aggregated nanocrystallites covered with a thin shell (white arrows in Fig. 11B). Also, the TEM measurements indicate that the size range of the hollows confined within the polycrystalline core is 40–130 nm which is consistent with Cryo-TEM measurements (Fig. 8D). The inset in Fig. 11B is the corresponding SAED pattern which shows overlap of polycrystalline rings with single crystal diffraction spots. From the beam outward, the three polycrystalline rings can be indexed to (622), (642) and (840) reflections in LTA zeolite structure, while the reflections of single crystal can be indexed to (200), (222), (440), (444) and (840). The SAED pattern of the particles presented in Fig. 11C shows diffraction spots oriented in rings that can be indexed to (420), (622), and (820) planes in LTA zeolite structure (Fig. 11C-inset). In other words, TEM and SAED investigations provide more evidence confirming that MZ-12d is LTA zeolite with two different morphologies viz.

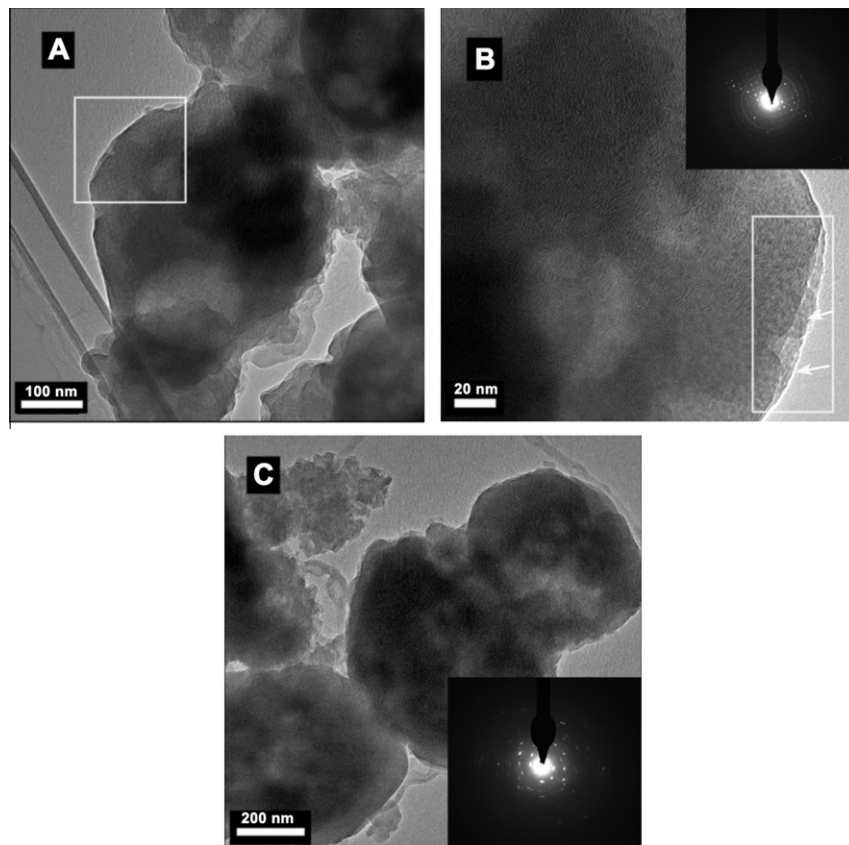


**Fig. 11.** Low and high magnification images of a particle from MZ-12d (A and B). Corresponding SAED pattern of the same particle (B-inset). TEM image of another group of particles from MZ-12d (C) with corresponding SAED pattern (C-inset).

multi-hollow polycrystalline aggregates and single cubic crystals with multi-hollow-polycrystalline core.

It is well known that meso-sized voids among aggregated nanocrystallites can be considered as mesopores [6,31–34]. In a complementary study, N<sub>2</sub> adsorption–desorption analysis at (−196 °C) was conducted on the samples MZ-9d, MZ-12d and MZ-14d to investigate the formation of the mesopores among the aggregated crystallites and to correlate this to the crystal growth mechanism. All the samples show type IV isotherms with hysteresis loops at relative pressure higher than 0.4 indicating the presence of meso-sized pores (see Fig. S3A in the Supporting information) [35]. The pore size distribution measured from the adsorption branch using the BJH method shows that after 9 days aging only small size mesopores ranging between 1.8 and 4 nm were formed (see Fig. S3B and Table S1 in the Supporting information). However, in addition to the small mesopores, MZ-12d shows a new generation of pores represented by a small peak centered at 9 nm (see Fig. S3B in the Supporting information) which became broader ranging between 6.5 and 10.5 nm with increasing the aging period to 14 days.

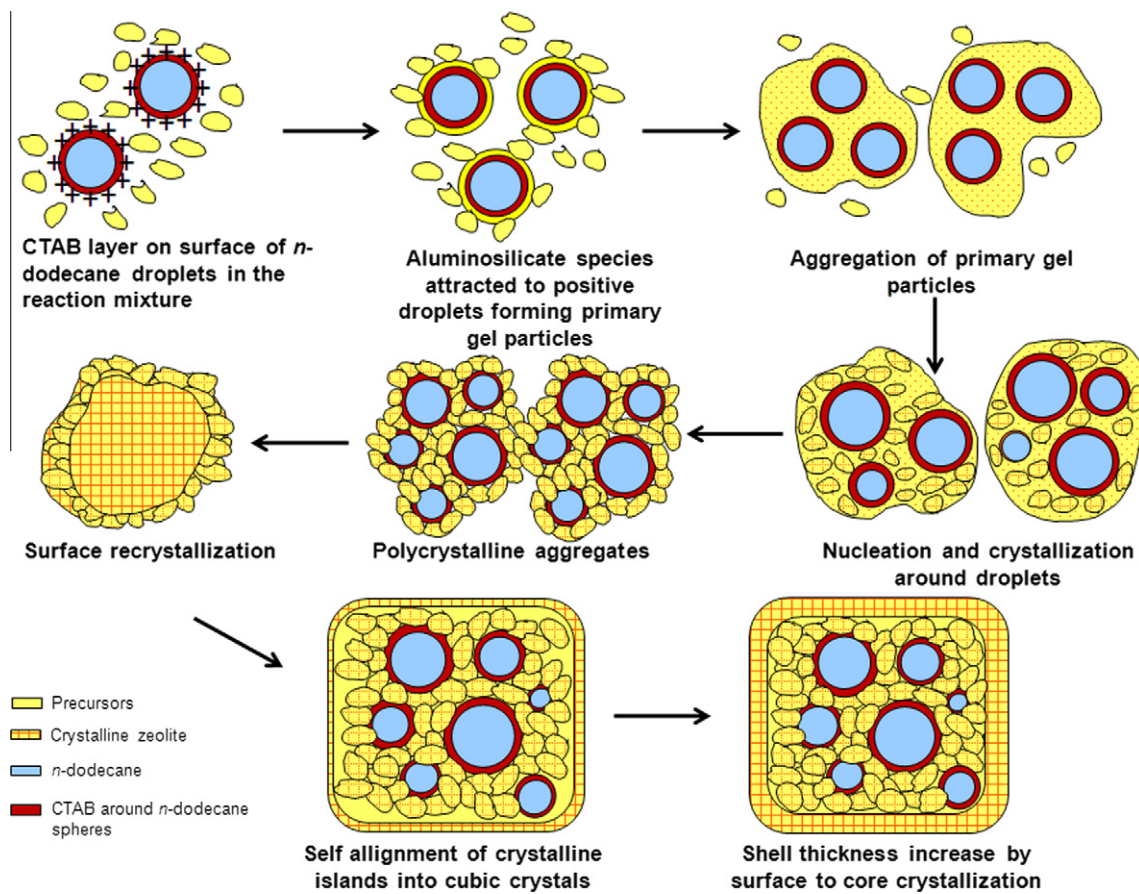
As the Na-A zeolite is non-adsorptive for N<sub>2</sub> at (−196 °C), the adsorption in this work was attributed to the mesopores which are represented by the voids between the aggregated crystallites. Thus, the appearance of large mesopores after 12 days which was enhanced after 14 days aging may be correlated to the size increase of the primary crystallites by Ostwald ripening within the polycrystalline aggregates, as was observed in SEM images in Fig. 9C [31].

In a complementary study, FTIR spectra were recorded for series of aliquots taken after different aging periods; 48 h and 6, 9 and 14 days (see Fig. S5 in Supporting information). As described

above, bands near 464, 556, 667 cm<sup>−1</sup> are the structure sensitive vibrations of LTA zeolite. These bands could not be observed on the spectrum of the sample taken after 48 h indicating the absence of LTA zeolite structure and suggesting that the sample is amorphous aluminosilicate gel [28]. Also, it was difficult to detect these bands clearly in the spectrum of the sample taken after 6 days aging in spite of the small diffraction peaks observed in the XRD pattern of the same sample (Fig. 10). However, with increasing the aging period to 9 and 14 days, the bands near 464, 556, 667 cm<sup>−1</sup> became sharper and can be distinguished easily indicating the presence of LTA zeolite structure. Further, evidence of the gel evolution and zeolite formation is the gradual disappearance of the band observed near 850 cm<sup>−1</sup>. This band is attributed to Si–OH bending vibration; therefore the simultaneous reduction of the intensity of this band with increasing the sharpness of LTA zeolite characteristics bands suggests increasing the number of atoms linked via oxygen to form LTA zeolite framework structure [28].

High temperature crystallization for the sample aged for 14 days does not show a noticeable increase in the intensity of the XRD peaks (Fig. 10E and F) which suggests no increase in the size of the particles. However, the BET surface area and the mesopore volume were increased with retaining the size of the large scale mesopores (Fig. 2, inset and Table S1). On the other hand, the range of the small mesopores was retained over the period from 9 to 14 days and even after the high temperature crystallization, but the size distribution was changed suggesting continuous local structural evolution.

Close observation by SEM of a particle in MZ-14d-cryst (Fig. 3B) shows a shell thickness of about 50 nm which is more than that ob-



**Scheme 1.** Proposed mechanism for the synthesis of Na-A zeolite crystals with multi-hollow polycrystalline core.

served in either MZ-12d or MZ-14d. The increase in the shell thickness accompanied with maintaining the size of the particles (as inferred from XRD and SEM results) suggests a reverse crystallization mechanism from surface to core. In some zeolites systems, spherical aggregates of nanoparticles are formed in the early stage of crystal formation followed by surface recrystallization which is extended reversely to the core [9,36,30]. Such a route was observed in analcime zeolite system and called NARS (nanocrystallites-aggregation-surface recrystallization-single crystal) [9]. Until recently the only growth mechanism that was recognized for zeolites crystals was based on so called Bravais–Friedel–Donnay–Harker (BFDH) law and Hartman–Perdok theory [9,10,36,30]. According to these theories, nuclei are formed and then grown slowly via atom by atom addition into layers resulting in monocrystalline zeolite [14,30].

LTA zeolite has demonstrated an aggregation–recrystallization growth mechanism in the presence of chitosan biopolymer. Chitosan molecules aggregated with LTA zeolite precursors forming spherical aggregation which then were crystallized into single cubes with amorphous core [10]. Longer synthesis time resulted in reverse crystal growth but the zeolite phase transformed from LTA to sodalite [36]. In contrast, in our work the nanoparticles within the aggregates were crystallized and grown forming polycrystalline aggregates prior to the surface recrystallization (as confirmed by XRD, SEM and TEM). We believe that probably the moderate crystallization conditions (room temperature) induce local crystallization and growth of each nanoparticle within the amorphous aggregates unlike the chitosan system where surface crystallization was faster than crystallite growth. Thus, the crystal growth mechanism in our system is probably more compatible with NARS route of core–shell and hollow icositetrahedra analcime zeolite [9]. However, the hollow formed in analcime crystals was due to reverse crystal growth while in our system was replicates of *n*-dodecane droplets as evidenced by the results obtained from TEM, Cryo-TEM and TGA. Thus, our work provides new insight into LTA zeolite crystallization by synthesizing monocrystalline cube-like Na-A zeolite shell with multi-hollow polycrystalline core.

In summary, the proposed crystal growth mechanism for the synthesis is shown in **Scheme 1** and can be described as follows: (1) attraction of the aluminosilicate species and tiny building blocks to the surface of *n*-dodecane droplets directed by the positive ammonium groups on the surface of the droplets (primary nanoparticles). (2) Simultaneous nucleation–crystallization and aggregation forming secondary aggregates. (3) Completion of nanoparticle crystallization forming polycrystalline aggregates. (4) Increase in the size of the crystallites by Ostwald ripening process. (5) Surface recrystallization forming thin islands of Na-A zeolite on the surface of the polycrystalline aggregates. (6) In some particles, these islands might be joined together and self aligned according to their crystallographic orientation forming cubic crystals of LTA zeolite with polycrystalline core. (7) Prolonging the aging/crystallization period induces surface to core crystallization which can be observed easily in the polycrystalline aggregates that are partially covered with the Na-A zeolite islands. The shell thickness increases by consumption of the nanocrystallites that attached to it by Ostwald ripening process. (8) Removing the CTAB layer and the *n*-dodecane droplets by calcination leaves hollows which are replicates to them inside the polycrystalline core.

#### 4. Conclusion

We have demonstrated that Na-A zeolite crystals consisting of thin crystalline polyhedral shell and multi-hollow polycrystalline core can be synthesized by conducting two step crystallization in the presence of emulsion droplets. The product also shows some par-

ticles which are multi-hollow polycrystalline aggregates that contain large mesopores attributed to voids among the aggregated crystallites. By systematic investigations of samples taken at different reaction stages, it is demonstrated that in presence of emulsion droplets, Na-A zeolite particles with multi-hollow polycrystalline core–shell structure can be grown according to aggregation–recrystallization approach in contrast to the classic growth mechanism. The presence of positive *n*-dodecane droplets within the zeolite reaction mixture enhances the formation of nanoparticle aggregates at the early stage of gel evolution and organization. By conducting the crystallization at room temperature, the aggregated nanoparticles are crystallized locally forming polycrystalline aggregates which then undergo a reversed crystal growth. The crystallization takes place on the surface of the polycrystalline aggregates and extends inward. This work demonstrates two points; the synthesis of new kind of mesoporous Na-A with multi-hollow polycrystalline morphology and also demonstrate, for the first time, formation of LTA zeolite crystal via reverse crystallization route while retaining the identity of LTA zeolite.

#### Acknowledgements

The authors acknowledge the financial support by the Australian Research Council (ARC). The authors also thank Dr. Eric Hansson from Bio21 Molecular Science and Biotechnology Institute - University of Melbourne for testing the samples by Cryo-TEM microscopy. Furthermore the authors also acknowledge the staff of Monash Centre for Electron Microscopy (MCEM), especially Tim Williams, Ellen Lovie, Flame Burgmann and Xi-ya Fang for their continuous support during the training on SEM and TEM.

#### Appendix A. Supplementary data

Supplementary data associated with this article can be found, in the online version, at <http://dx.doi.org/10.1016/j.micromeso.2012.05.002>.

#### References

- [1] Y. Li, J. Shi, Z. Hua, H. Chen, M. Ruan, D. Yan, *Nano Lett.* 3 (2003) 609.
- [2] L. Han, J. Yao, D. Li, J. Ho, X. Zhang, C.-H. Kong, Z.-M. Zong, X.-Y. Wei, H. Wang, *J. Mater. Chem.* 18 (2008) 3337.
- [3] V. Valtchev, S. Mintova, *Microporous Mesoporous Mater.* 43 (2001) 41.
- [4] X.D. Wang, Y. Tang, Y.J. Wang, Z. Gao, W.L. Yang, S.K. Fu, *Chem. Commun.* 21 (2000) 61.
- [5] H.-P. Lin, C.-Y. Mou, S.-B. Liu, C.-Y. Tang, *Chem. Commun.* 19 (2001) 1970.
- [6] X. Wu, Y. Tian, Y. Cui, L. Wei, Q. Wang, Y. Chen, *J. Phys. Chem. C* 111 (2007) 9704.
- [7] W. Li, X. Sha, W. Dong, Z. Wang, *Chem. Commun.* 20 (2002) 2434.
- [8] M. Fujiwara, K. Shiokawa, I. Sakakura, Y. Nakahara, *Langmuir* 26 (2010) 6561.
- [9] X. Chen, M. Qiao, S. Xie, K. Fan, W. Zhou, Y. He, *J. Am. Chem. Soc.* 129 (2007) 13305.
- [10] J. Yao, D. Li, X. Zhang, C.-H. Kong, W. Yue, W. Zhou, H. Wang, *Angew. Chem. Int. Ed.* 47 (2008) 8397.
- [11] J. Zhao, Z. Hua, Z. Liu, Y. Li, L. Guo, W. Bu, X. Cui, M. Ruan, H. Chen, J. Shi, *Chem. Commun.* 75 (2009) 78.
- [12] V.P. Valtchev, K.N. Bozhilov, *J. Am. Chem. Soc.* 127 (2005) 16171.
- [13] V.P. Valtchev, L. Tosheva, K.N. Bozhilov, *Langmuir* 21 (2005) 10724.
- [14] S. Mintova, N.H. Olson, V. Valtchev, T. Bein, *Science* 283 (1999) 958.
- [15] R.W. Thompson, K.C. Franklin, in: H. Robson, K.P. Lillerud (Eds.), *Verified Synthesis of Zeolitic Materials*, Elsevier, Amsterdam, 2001, p. 179.
- [16] V. Gramlich, W.M. Meier, in: M.M.J. Treacy, J.B. Higgins (Eds.), *Collection of Simulated XRD Powder Patterns for Zeolites*, Elsevier, Amsterdam, 2001, p. 215.
- [17] M. Kruk, M. Jaroniec, *Chem. Mater.* 13 (2001) 3169.
- [18] Y. Huang, K. Wang, D. Dong, D. Li, M.R. Hill, A.J. Hill, H. Wang, *Microporous Mesoporous Mater.* 127 (2010) 167.
- [19] K. Cho, H.S. Cho, L.C. De Menorval, R. Ryoo, *Chem. Mater.* 21 (2009) 5664.
- [20] L. Gora, *Zeolites* 18 (1997) 115.
- [21] D.W. Breck, W.G. Eversole, R.M. Milton, T.B. Reed, T.L. Thomas, *J. Am. Chem. Soc.* 78 (1956) 5963.
- [22] A. Aronne, S. Esposito, C. Ferone, M. Pansini, P. Pernice, *J. Mater. Chem.* 12 (2002) 3039.

- [23] E.M. Flanigen, H. Khatami, H. Szymanski, Molecular Sieve Zeolites-I, *Adv. Chem. Ser.*, vol. 101, American Chemical Society, Washington DC, 1971, 201p.
- [24] G. Engelhardt, in: H. Van Bekkum, E.M. Flanigen, P.A. Jacobs, J.C. Jansen (Eds.), *Studies in Surface Science and Catalysis*, vol. 137, Elsevier, Amsterdam, 2001. 387p..
- [25] J. Shi, M.W. Anderson, S.W. Carr, *Chem. Mater.* 8 (1996) 369.
- [26] M. Smaihi, O. Barida, V. Valtchev, *Eur. J. Inorg. Chem.* 24 (2003) 4370.
- [27] H.J. Butt, K. Graf, M. Kappl, *Physics and Chemistry of Interfaces*, Wiley, Germany, 2003. 246p..
- [28] V.P. Valtchev, K.N. Bozhilov, *J. Phys. Chem. B* 108 (2004) 15587.
- [29] D.P. Serrano, R. Van Grieken, *J. Mater. Chem.* 11 (2001) 2391.
- [30] W. Zhou, *Adv. Mater.* 22 (2010) 3086.
- [31] M. Choi, H.S. Cho, R. Srivastava, C. Venkatesan, D.H. Choi, R. Ryoo, *Nat. Mater.* 5 (2006) 718.
- [32] F.N. Gu, F. Wei, J.Y. Yang, N. Lin, W.G. Lin, Y. Wang, J.H. Zhu, *Chem. Mater.* 22 (2010) 2442.
- [33] J. Hua, Y. Han, *Chem. Mater.* 21 (2009) 2344.
- [34] Y. Tao, H. Kanoh, K. Kaneko, *Langmuir* 21 (2005) 504.
- [35] S.J. Gregg, K.S.W. Sing, *Adsorption Surface Area and Porosity*, Academic Press, New York, 1982. p. 111.
- [36] H. Greer, P.S. Wheatley, S.E. Ashbrook, R.E. Morris, W. Zhou, *J. Am. Chem. Soc.* 131 (2009) 17986.